



UNIVERSITÀ DELLA  
CALABRIA

UNIVERSITA' DELLA CALABRIA

Dipartimento di Ingegneria Civile

Dottorato di Ricerca in Ingegneria Civile e Industriale

CICLO

XXXIII


Probabilistic assessment of the seismic performance of two earth dams in Southern Italy  
using simplified and advanced constitutive models

Settore Scientifico Disciplinare ICAR/07

**Coordinatore:** Chiar.mo Prof. Enrico Conte


**Supervisore/Tutor:** Chiar.mo Prof. Roberto Cairo

**Co-Tutors:** Chiar.mo Prof. Paolo Zimmaro  
Chiar.ma Prof. Katerina Ziotopoulou

  
Firma oscurata in base alle linee guida del Garante della privacy

  
Firma oscurata in base alle linee guida del Garante della privacy

**Dottorando:** 

  
Firma oscurata in base alle linee guida del Garante della privacy



---

UNIVERSITÀ DELLA  
CALABRIA

UNIVERSITA' DELLA CALABRIA

Dipartimento di Ingegneria Civile

**Dottorato di Ricerca in Ingegneria Civile e Industriale**

---

**CICLO**

**XXXIII**

**Probabilistic assessment of the seismic performance of two earth dams in Southern Italy using simplified and advanced constitutive models**

**Settore Scientifico Disciplinare ICAR/07**

**Coordinatore:** Chiar.mo Prof. Enrico Conte

**Supervisore/Tutor:** Chiar.mo Prof. Roberto Cairo

**Co-Tutors:** Chiar.mo Prof. Paolo Zimmaro  
Chiar.ma Prof. Katerina Ziotopoulou

**Dottorando:** Dott. Gianluca  
Regina

*In memory of my dearest friend Emanuele*

*“The language of probability allows us to speak quantitatively about some situation which may be highly variable, but which does have some consistent average behavior. Our most precise description of nature must be in terms of probabilities.”*

*Richard Feynman*



## Abstract

The large majority of existing earth dams were designed with old standards, which often accounted for the effects of earthquakes in a simplified manner. Nowadays, safety assessment of these structures is becoming of great importance, particularly for dams suffering the effects of ageing. This study presents a fully probabilistic approach to evaluate the seismic performance of two critical earth dams in the Calabria region, a seismically active area in Southern Italy. One of them (the Farneto del Principe dam) is not susceptible to liquefaction, whereas the other dam (the Angitola dam) is founded on potentially liquefiable soils. Seismic input motions are derived from site-specific probabilistic approaches. Non-ergodic ground response is implemented within a probabilistic seismic hazard analysis (PSHA) framework for one of the two dam sites. This non-ergodic PSHA is derived from numerical amplification functions based on one-dimensional simulations. Such well-documented early application of non-ergodic PSHA for earth dams in Italy may encourage a transformational shift from years of past practices based on deterministic amplification functions merged with PSHA results by means of hybrid approaches. Simplified (i.e., using the Mohr–Coulomb failure criterion coupled with a simplified hysteretic procedure) and advanced (i.e., PM4Sand and PM4Silt) constitutive models are used to perform a comprehensive numerical simulation program for both dams. Field and laboratory geotechnical characterization data are used to calibrate these models. This calibration process is fully documented and potential issues discussed. Such fully-documented calibration process will enable future studies on similar infrastructure systems when advanced constitutive models are necessary. Shear strain and deformation patterns are analyzed and discussed, showing that for the Farneto del Principe dam (comprising non-liquefiable materials) both constitutive models provide similar results. However, when potentially liquefiable soils are involved, advanced constitutive models are necessary to capture the complexity and nuances of such materials. This effect is evident for the Angitola dam.

For both dams, seismic vulnerability is analyzed by means of analytical fragility functions for various damage mechanisms and intensity measures. Such fragility functions are based on nonlinear deformation analyses within the multiple stripe analysis framework. All fragility functions derived in this study are shown and main outcomes are illustrated by summary tables reporting mean and standard deviation

values of these curves. Finally, the efficiency and predictability of various ground motion intensity measures to predict different damage levels and mechanisms are calculated for both dams. Predictability of recent semi-empirical ground motion models is also calculated for all analyzed intensity measures. Overall, results from this analysis indicate that velocity-based ground motion properties, such as Peak Ground Velocity, Arias Intensity, Cumulative Absolute Velocity, and Cumulative Absolute Velocity after application of a  $0.05 \frac{m}{s^2}$  threshold acceleration provide good efficiencies in predicting damage. These intensity measures are the best in predicting damage states for both dams and all damage mechanisms. However, some of them are more predictable than others. After merging efficiency and predictability information, the best intensity measure to predict damage is the Cumulative Absolute Velocity, followed by the Arias intensity.

## Acknowledgements

I am deeply grateful to Prof. Giovanni Dente, who taught me the love for geotechnical engineering, gave me the opportunity to work on this research project, and gave me so many life lessons. I consider him my academic father, and I could have not done any of this without him.

I want to express my gratitude to Prof. Roberto Cairo, who inspired me during his lectures, accepted to be my supervisor for this Ph.D., and for his friendship.

I am truly thankful to Prof. Paolo Zimmaro, who reviewed part of this dissertation, and for the countless academic (and non-academic) discussions we had during these past four years.

I need to express my acknowledgments to Prof. Katerina Ziotopoulou, who accepted me in her research group at the University of California, Davis, gave me the opportunity to learn so many things, for reviewing part of this dissertation, and for her friendship.

I want to say thank you to Prof. Ernesto Ausilio, for his precious feedback and technical discussions we had in these past years. Also, a shout-out to Matteo as well, for his huge help in the geotechnical characterization of the Farneto del Principe dam.

I would like to express my gratitude to the “Consorzio di Bonifica Tirreno-Catanzarese” and in particular to engineer P. Cimbalo for providing the data of the Angitola dam. In addition, I want to thank Prof. Giuseppe Lanzo for the technical discussions we had about this dam.

I thank my family, because I could have not done this without their help. Special thanks goes to my brother, for his help in some computer-related issues.

A big thank you to all my friends and colleagues, near and far, for making these past years more enjoyable. Particular thanks goes to Florence, for her support during the first part of this Ph.D.

Special thanks goes to Ivette, for her precious support during these difficult months, and for the strength she gives me.

Finally, I want to thank Emanuele, my dearest friend, who is no longer with us, but he taught me so much, and he is still giving me strength.

## Contents

Abstract.....	4
Acknowledgements .....	6
Contents .....	7
List of Figures .....	11
List of Tables .....	25
1. Introduction.....	28
1.1 Background and scope of the work.....	28
1.2 Dissertation outline.....	32
2. Hazard analysis and seismic response of earth dams: state-of-the-art.....	34
2.1 PSHA: a brief review .....	35
2.1.1 The Uniform Hazard Spectrum computation.....	40
2.1.2 Disaggregation of the seismic hazard .....	41
2.2 Local vs global models and non-ergodic site response methodologies .....	42
2.3 Linking site response analysis results to PSHA.....	44
2.3.1 Implementation of the non-ergodic procedure into PSHA.....	46
2.3.2 Discussion.....	47
2.4 Seismic analysis of earth dams .....	49
2.4.1 Pseudo-static method .....	49
2.4.2 Newmark sliding block analysis .....	50
2.4.3 Shear beam methodology .....	53
2.4.4 Nonlinear Deformation Analysis (NDA) .....	55
2.5 Damage mechanisms in embankment dams .....	57
2.5.1 Global instability, internal erosion, and filters damage.....	59
2.5.2 Empirical methodologies for assessing deformations and cracks.....	63
2.5.3 Cyclic ground failure phenomena.....	66
3. The Farneto del Principe dam case study.....	78
3.1 Dam description .....	78

3.2	The 2015-2017 geotechnical investigation program.....	81
3.3	Boring logs, SPT, and CPT results .....	83
3.4	Geophysical investigation and laboratory test results .....	88
3.4.1	Invasive geophysical tests.....	88
3.4.2	Multichannel Analysis of Surface Waves (MASW).....	90
3.4.3	Seismic tomography and HVSR analysis.....	92
3.4.4	Laboratory test results .....	95
3.5	Analysis of the undrained shear strength.....	96
3.5.1	Fine grained-soils behavior .....	97
3.5.2	Consolidation tests.....	99
3.5.3	Isotropically-Consolidated Undrained triaxial tests .....	101
3.5.4	Direct Shear test results.....	103
3.5.5	Estimation of the undrained shear strength .....	103
4.	Non-ergodic hazard analysis for the Farneto del Principe dam site .....	113
4.1	Ground Motion selection and scaling.....	113
4.1.1	The Uniform Hazard Spectrum .....	114
4.1.2	The Conditional Spectrum.....	114
4.1.3	Ground motion selection algorithms .....	117
4.2	Seismic Ground Response Analyses.....	122
4.3	Amplification functions.....	124
4.4	Uncertainty analysis.....	126
4.5	Non-ergodic PSHA for the Farneto del Principe dam site .....	129
4.5.1	Non-ergodic hazard curves, CS, and CMS .....	131
4.5.2	Comparison with simplified methods.....	132
4.5.3	Disaggregation results .....	134
5.	The Angitola dam.....	137
5.1	Generalities.....	137
5.2	Geotechnical characterization of the secondary dam .....	140

5.5.1 Geotechnical properties of the dam body .....	142
5.5.2 Foundation layers characterization.....	145
5.5.3 Ambient noise measurements .....	151
5.3. Site-specific PSHA for the Angitola dam.....	152
5.4 Semi-empirical liquefaction resistance analysis.....	156
6. Numerical modeling of the Farneto del Principe and Angitola dams .....	159
6.1 Fast Lagrangian Analysis of Continua (FLAC).....	159
6.2 Constitutive models .....	161
6.2.1 PM4Sand .....	161
6.2.2 PM4Silt.....	165
6.3 Mesh generation and boundary conditions .....	168
6.4 The Farneto del Principe dam model .....	170
6.4.1 Generalities .....	170
6.4.2 Dynamic properties and material damping.....	173
6.4.3 Cyclic softening potential .....	176
6.4.4 PM4Silt calibration for the Farneto del Principe dam core.....	177
6.5 Numerical model of the Angitola dam .....	186
6.5.1 Generalities .....	186
6.5.2 Construction process and groundwater flow .....	188
6.5.3 Dynamic properties and material damping.....	191
6.5.4 PM4Sand calibration for the Angitola dam foundation .....	193
7. Nonlinear deformation analysis results .....	206
7.1 Introduction on analytical fragility functions .....	206
7.2 Analytical fragility functions for the Farneto del Principe dam.....	207
7.2.1 Ground motions, intensity measures, and damage measures.....	207
7.2.2 Numerical model results.....	210
7.2.3 Computed fragility functions.....	217
7.3 Analytical fragility functions for the Angitola dam .....	227

7.3.1 Ground motions, intensity measures, and damage measures.....	227
7.3.2 Numerical results and between-constitutive models differences .....	229
7.3.3 Computed fragility functions.....	235
7.4 Efficiency of ground motion intensity measures .....	250
Conclusion.....	261
References.....	263
Appendix A: Ground motions adopted for the Multiple Stripe Analyses .....	288

## List of Figures

Figure 2.1:	Seismogenic zonation ZS9. The 36 numbers reported in the map represent earthquake source zone IDs; the colors identify the mean seismogenic depth (in km); the superimposed shadings refer to the predominant focal mechanism (from Stucchi et al., 2011).....	37
Figure 2.2:	Examples of annual rate of earthquakes and Gutenberg-Richter laws to interpolate the data (adapted from Baker, 2013, and Zimmaro and Stewart, 2017).....	37
Figure 2.3:	Example of a GMM for a magnitude $m$ earthquake, and graphical representation of the probability of $PGA > 1g$ at a distance $r$ (from Baker, 2013).....	39
Figure 2.4:	Graphical representation of the UHS computation (from Baker, 2013).....	41
Figure 2.5:	Schematization of the seismic site response analysis and notation adopted.....	44
Figure 2.6:	Schematization of the pseudostatic approach for the seismic analysis of embankments. ....	49
Figure 2.7:	Schematization of the Newmark's sliding block method (Wilson e Keefer, 1985).....	51
Figure 2.8:	Variation of the normalized permanent displacements based on the yield acceleration ratio, for several magnitudes (Kramer, 1996).....	52
Figure 2.9:	Variation of the shear modulus in the earth dam in Dakoulas and Gazetas (1985) solution.....	53
Figure 2.10:	Effects of the erosion process in an embankment (from FEMA P-1032, 2015).....	61
Figure 2.11:	Longitudinal crack observed in Coihueco dam (from Séco and Pinto, 2015).....	62
Figure 2.12:	Schematization of the filters function (coarse material) which block the soil erosion from the above crack. The hydraulic gradient is reduced as the length of the blocked soil increases (U.S. Department of the Interior, Bureau of Reclamation, 2011). ....	63
Figure 2.13:	Incidence of transverse cracking and damage classes boundaries for earthfill dams in function of the seismic hazard (from Pells and Fell, 2002).....	65



Figure 2.14:	Schematization used by Swaisgood to define the Normalized Crest Settlement.....	65
Figure 2.15:	Estimated Normalized Crest Settlement (Swaisgood, 2014).....	66
Figure 2.16:	Normalized Crest Settlement for the case histories studied by Swaisgood (Swaisgood, 2014).....	67
Figure 2.17:	Lower San Fernando dam after the 1971 San Fernando earthquake (from Boulanger et al., 2015).....	68
Figure 2.18:	Fujinuma-Ike dam after the 2011 Tohoku earthquake (Matsumoto et al., 2011).....	68
Figure 2.19:	Grain size distribution-based criteria for liquefaction susceptibility for the Italian Building Code (from NTC18).....	70
Figure 2.20:	Correlations for cyclic resistance ratio from SPT data (from Idriss and Boulanger, 2010).....	73
Figure 3.1:	Location and aerial view of the Farneto del Principe dam (from Google earth, 2019).....	79
Figure 3.2:	Schematic cross section of the Farneto del Principe dam.....	80
Figure 3.3:	Locations of the tests performed at the Farneto del Principe dam site.....	83
Figure 3.4:	SPT results for the silty clay core of the Farneto del Principe dam.....	85
Figure 3.5:	SPT results for the alluvial and shells material of the Farneto del Principe dam.....	85
Figure 3.6:	Results of the SPCTu1 performed on the dam crest.....	85
Figure 3.7:	Results of the SCPTu2 performed on the dam crest.....	86
Figure 3.8:	Results of the SCPTu3 performed on the dam crest.....	86
Figure 3.9:	Results of the SCPTu4 performed on the dam crest.....	86
Figure 3.10:	Results of the CPTu1 performed on the dam crest.....	87
Figure 3.11:	Results of the CPTu2 performed on the dam crest.....	87
Figure 3.12:	Results of the CPTu3 performed on the dam crest.....	87
Figure 3.13:	Results of the CPTu4 performed on the dam crest.....	88
Figure 3.14:	Shear wave velocities in the core estimated from SCPTu tests.....	88

Figure 3.15:	Shear wave velocity profiles in the dam core measured using cross-hole tests. The first ID in the legend is the location of the source, while the second is the location of the receiver. ....	89
Figure 3.16:	Shear wave velocities evaluated from down-hole test in a free field area. The location of the borehole S1 is at the center of the alluvial foundation (a), while borehole S8 is at the left bank (b). ....	90
Figure 3.17:	Shear wave velocities in the dam shell and in the alluvial foundation.....	91
Figure 3.18:	Execution of the MASW test and positions of the receivers. ....	91
Figure 3.19:	(a) Dispersion curve and (b) inverted profile of shear wave velocity obtained at the Farneto del Principe dam crest using the MASW technique. ....	92
Figure 3.20:	Transversal profile of shear wave velocity evaluated from seismic tomography performed at the Farneto del Principe dam.....	93
Figure 3.21:	Longitudinal profile shear wave velocity evaluated from seismic tomography performed at the Farneto del Principe dam.....	93
Figure 3.22:	Microtremor HVSR results: (a) free field area; (b) inspection gallery; (c),(d),(e), and (f), dam crest. ....	94
Figure 3.23:	Ratio of the microtremor E-W horizontal component measured at various locations, divided by that measured in free-field conditions. ....	94
Figure 3.24:	Shear wave velocities estimated from laboratory tests with undisturbed specimens.....	95
Figure 3.25:	Shear modulus profile in the dam core estimated from the geophysical tests and Dakoulas and Gazetas law (1985). ....	96
Figure 3.26:	Shear modulus reduction and damping curves for the Farneto del Principe dam clay core.....	96
Figure 3.27:	Casagrande's chart for the clay core material and clay bed of the Farneto del Principe dam.....	97
Figure 3.28:	Geotechnical properties of the clay core material of the Farneto del Principe dam.....	98
Figure 3.29:	Geotechnical properties of the clay bed material of the Farneto del Principe dam.....	98
Figure 3.30:	Cyclic softening susceptibility for the Farneto del Principe dam core (a, b, and c) and clay bed (d, e, and f). ....	99

Figure 3.31:	Consolidation tests results for the clay core material of the Farneto del Principe dam.....	100
Figure 3.32:	Preconsolidation stress (a) and OCR profile with depth (b) for the clay core of the Farneto del Principe dam.....	100
Figure 3.33:	Results of the triaxial ICU tests performed on the clay core of the Farneto del Principe dam: deviatoric stress versus axial strain.....	101
Figure 3.34:	Results of the ICU tests performed on the clay core of the Farneto del Principe dam: excess pore water pressure versus axial strain.....	102
Figure 3.35:	Stress paths of the ICU tests performed on the clay core of the Farneto del Principe dam. Continuous lines are the ESPs, dashed lines are the TSPs, and the green line is the critical state failure envelope.....	102
Figure 3.36:	Results of the two DSS tests performed for the clay core of the Farneto del Principe dam.....	103
Figure 3.37:	Failure envelope for the Farneto del Principe dam core estimated from two DSS.....	104
Figure 3.38:	Mean failure envelopes as a function of (a) $sc'$ and (b) $\sigma fc'$ , and versus various consolidation stresses (c) and (d).....	107
Figure 3.39:	Variation of the undrained shear strength within the clay core of the Farneto del Principe dam.....	108
Figure 3.40:	Samples normalization of the five ICU tests performed.....	110
Figure 3.41:	Undrained shear strength profile with depth using SHANSEP methodology (a) and variation with the OCR (b).....	111
Figure 3.42:	Comparison between drained and undrained shear strength failure envelopes.....	111
Figure 3.43:	Comparison between the undrained shear strength profiles estimated from the SHANSEP and the Montgomery et al. methodology.....	112
Figure 4.1:	Ergodic Uniform Hazard Spectra for Farneto del Principe dam site, for four return periods.....	114
Figure 4.2:	Disaggregation results for various return periods vs mean (a) magnitude, (b) epsilon, and (c) Joyner-Boore distance.....	117
Figure 4.3:	Uniform Hazard Spectra and Conditional Mean Spectra for the return periods considered.....	117

Figure 4.4:	Selected response spectra using the UHS as target spectrum for the following return periods: (a) 1460 years, (b) 75 years, (c) 50 years, and (d) 30 years.....	120
Figure 4.5:	Schematic representation of the ground motion selection algorithm for CS as target spectrum (Adapted from Baker and Lee, 2017).....	121
Figure 4.6:	Results of the ground motion selection algorithm using the CS as target spectrum: (a) Monte Carlo simulated spectra; (b) Response spectra of selected motions; (c) Median of the selected motions; and (d) Standard deviation match. ....	121
Figure 4.7:	Measured and randomized shear waves velocity profiles of the alluvial foundation adopted for GRA. ....	123
Figure 4.8:	Grain size distributions for the alluvial foundation of Farneto del Principe dam.....	124
Figure 4.9:	Mean amplification functions for the alluvial foundation of the Farneto del Principe dam for the following intensity measures: (a) PGA, (b) Sa(0.03s), (c) Sa(0.1s), and (d) Sa(0.25s).....	126
Figure 4.10:	Variation across periods of parameters (a) $f_1$ and (b) $f_2$ .....	127
Figure 4.11:	Standard deviation of site amplification (a) Site-to-site standard deviation (b).....	128
Figure 4.12:	Variation of site-to-site standard deviation for different shear wave profiles and intensity measures. ....	129
Figure 4.13:	Source models used for the site-specific PSHA of the Farneto del Principe dam. (a) Area sources (b) Fault sources. (from Zimmaro and Stewart, 2017).....	130
Figure 4.14:	Logic tree used for the site-specific PSHA of the Farneto del Principe dam (adapted from Zimmaro and Stewart, 2017).....	130
Figure 4.15:	Ergodic and non-ergodic hazard curves for the Farneto del Principe dam site for the following intensity measures: (a) PGA,(b)Sa(0.1s), (c) Sa(0.25s), and (d) Sa(0.5s). ....	131
Figure 4.16:	Non-ergodic UHS for the following return periods: (a) 1460 years, (b) 75 years, (c) 50 years, and (d) 30 years.....	132
Figure 4.17:	Non-ergodic and ergodic UHS and CMS for the following return periods: (a) 1460 years, (b) 75 years, (c) 50 years, and (d) 30 years. ....	133

Figure 4.18:	Percentage differences between non-ergodic and ergodic spectra (positive values means that the non-ergodic spectrum is more intense than the ergodic one) for (a) UHS and (b) CMS. ....	133
Figure 4.19:	Comparison of hazard curves estimated from non-ergodic analyses and simplified methods. ....	134
Figure 4.20:	Comparison between non-ergodic and ergodic disaggregation results for the spectral acceleration at 0.25s. ....	135
Figure 4.21:	Non-ergodic magnitude-distance disaggregation of the Farneto del Principe dam site for a return period of 1460 years. ....	136
Figure 5.1:	Aerial view of the Angitola dam (from Google earth, 2021).....	139
Figure 5.2:	Cross section of the main dam (courtesy of Prof. Lanzo). ....	140
Figure 5.3:	Cross section of the secondary dam and location of the boreholes performed (courtesy of Prof. Lanzo).....	140
Figure 5.4:	Plan view of the Angitola dam area and location of all tests performed (courtesy of Prof. Lanzo).....	141
Figure 5.5:	Casagrande's and activity chart for the core and the foundation soils of the secondary dam (courtesy of Prof. Lanzo).....	142
Figure 5.6:	Failure envelope for the core of the secondary dam based on a triaxial ICU test (courtesy of Prof. Lanzo).....	142
Figure 5.7:	Shear wave velocity profile of core of the secondary dam (silty clay, and sandy layer) (courtesy of Prof. Lanzo).....	143
Figure 5.8:	MRD curved for the core of the secondary dam. ....	144
Figure 5.9:	Shear wave velocity profile adopted for the shells of the secondary dam.....	144
Figure 5.10:	Comparison of the grain size distribution curves of the Angitola dam shells with one of the range adopted by Menq (2003) for the development of the empirical MRD. ....	145
Figure 5.11:	Shear modulus reduction curves and damping curves for the shells of the secondary dam.....	145
Figure 5.12:	MRD curves for the silty clay foundation, and sigmoidal curve used in the numerical model. ....	146
Figure 5.13:	Shear modulus reduction curve used for the old alluvium. ....	147

Figure 5.14:	Shear modulus variation with mean effective stress. The black points refer to values calculated in free field conditions, while the blue points refer to locations beneath the dam. ....	148
Figure 5.15:	Shear modulus reduction curve adopted for the sandy layer and comparison with empirical curves.....	149
Figure 5.16:	Shear wave velocity profiles in free field conditions estimated from empirical relationships using (a) SPT data and (b) CPT data. ....	150
Figure 5.17:	Shear modulus reduction curve adopted for the alluvial sand layer and comparison with empirical curves.....	151
Figure 5.18:	Results of the HVSR performed on the crest: (a) H/V ratio vs frequency, (b) H/V time series, (c) HVSR polar plot, and (d) single component spectra. ....	153
Figure 5.19:	Results of the HVSR performed in free field conditions: (a) H/V ratio vs frequency, (b) H/V time series, (c) HVSR polar plot, and (d) single component spectra. ....	154
Figure 5.20:	(a) Hazard curves, and (b) UHS and CMS for the Angitola dam site.....	154
Figure 5.21:	Summary of disaggregation results for the Angitola dam site.....	155
Figure 5.22:	Magnitude-distance disaggregation for the Angitola dam site.....	156
Figure 5.23:	CRR estimated from SPT results (a) and CPT (b).....	158
Figure 6.1:	FLAC calculation scheme.....	160
Figure 6.2:	FLAC dynamic scheme for the boundary conditions. ....	169
Figure 6.3:	Aerial view of the Farneto del Principe dam (from Google Earth, 2019). ....	170
Figure 6.4:	Numerical mesh of the Farneto del Principe dam. ....	171
Figure 6.5:	Construction log of the Farneto del Principe dam. ....	171
Figure 6.6:	Vertical effective stresses after the application of the reservoir at the maximum level (Farneto del Principe dam).....	172
Figure 6.7:	Groundwater flow and saturation contours of the Farneto del Principe dam for the reservoir at the maximum allowable level. ....	172
Figure 6.8:	MRD curves for the shells and foundation of the Farneto del Principe dam, and sigmoidal curve used in the numerical model.....	175

Figure 6.9:	Comparison between the experimental modulus reduction and damping curves with single-element simulations in FLAC, for the core and shells of the Farneto del Principe dam. ....	175
Figure 6.10:	Rayleigh damping adopted in the numerical analyses of the two case studies. ....	176
Figure 6.11:	Profile of the CRR, CSR, and factor of safety for cyclic softening for the Farneto del Principe dam core based on the SHANSEP methodology. ....	178
Figure 6.12:	Flow chart for the calibration of the PM4Silt constitutive model calibration. ....	179
Figure 6.13:	Calibration of the $G_0$ parameter of the PM4Silt model based on the geophysical tests performed on the Farneto del Principe dam crest. ....	180
Figure 6.14:	Single-element simulations of undrained monotonic DSS for the lower part of the Farneto del Principe dam core. ....	181
Figure 6.15:	Stress-strain responses for undrained cyclic DSS simulation of the lower part of the core of the Farneto del Principe dam. ....	182
Figure 6.16:	Stress path responses for undrained cyclic DSS simulation of the lower part of the core of the Farneto del Principe dam. ....	182
Figure 6.17:	Experimental and numerical MRD from undrained strain-controlled cyclic DSS for the lower part of the Farneto del Principe dam core. ....	183
Figure 6.18:	Stress-strain responses for undrained cyclic DSS loading for several CSR for the lower part of the Farneto del Principe dam core. ....	184
Figure 6.19:	Stress path responses for undrained cyclic DSS loading for several CSR for the lower part of the Farneto del Principe dam core. ....	184
Figure 6.20:	Excess pore water pressure ratio variation for the lower part of the Farneto del Principe dam core. ....	185
Figure 6.21:	Cyclic stress ratio versus number of uniform loading cycles to cause 1%, 3%, and 5% shear strain in undrained cyclic DSS loading for the lower part of the core of the Farneto del Principe dam. ....	185
Figure 6.22:	Aerial view of the secondary dam and location of the boreholes performed (from Google earth, 2021). ....	187
Figure 6.23:	Numerical mesh of the Angitola dam used in FLAC. ....	187
Figure 6.24:	Construction log of the secondary dam and experimental reservoir (courtesy of Prof. Lanzo). ....	188

Figure 6.25:	Plane view, cross-section, and location of the piezometers installed in the secondary dam.....	189
Figure 6.26:	Downstream piezometer PzS3 measurements throughout the service life of the secondary dam.....	190
Figure 6.27:	Vertical effective stresses after the application of the reservoir at the maximum level (Angitola dam).....	190
Figure 6.28:	Groundwater flow and saturation contours of the Angitola dam for the reservoir at the maximum allowable level.....	190
Figure 6.29:	Results of the damped free oscillations of the Angitola dam with a shear modulus profile varying with mean effective stress.....	191
Figure 6.30:	Comparison between the experimental modulus reduction and damping curves with single-element simulations in FLAC, for the core and silty clay foundation of the Angitola dam.....	192
Figure 6.31:	Comparison between the experimental modulus reduction and damping curves with single-element simulations in FLAC, for the shells and sandy layer of the Angitola dam.....	192
Figure 6.32:	Flow chart for the calibration of the PM4Sand constitutive model calibration.....	194
Figure 6.33:	Coefficient of earth pressure at rest $K_0$ and static shear stress ratio $\alpha$ for the Angitola dam before applying the dynamic input.....	195
Figure 6.34:	Calibration of the $G_0$ parameter and profile of the shear modulus for three zones in the Angitola dam: alluvial sand (a) and (d); pit (b) and (d); beneath the dam (c) and (f).....	196
Figure 6.35:	Drained monotonic loading response of the sandy layer beneath the dam ( $D_R = 58.4\%$ ). Stress-strain response (a) and (b); volumetric strains vs shear strain (c).....	198
Figure 6.36:	Undrained monotonic loading response of the sandy layer beneath the dam ( $D_R = 58.4\%$ ). Stress-strain response (a) and (b); stress-path (c) and (d).....	198
Figure 6.37:	Drained cyclic loading response of the sandy layer beneath the dam for different confining pressures.....	199
Figure 6.38:	MRD from drained strain-controlled cyclic DSS loading in the sandy layer beneath the dam and comparison with well-known MRD found in literature.....	199



Figure 6.39:	MRD from drained strain-controlled cyclic DSS loading in the alluvial sand and comparison with well-known MRD found in literature.....	200
Figure 6.40:	Undrained cyclic DSS loading response for the sandy layer beneath the dam ( $D_R = 58.4\%$ ).....	201
Figure 6.41:	Excess pore water pressure ratio variation for the sandy layer ( $D_R = 58.4\%$ ) in undrained cyclic DSS loading. ....	201
Figure 6.42:	Stress path responses for undrained cyclic DSS simulation of the sandy layer ( $D_R = 58.4\%$ ).....	202
Figure 6.43:	Cyclic stress ratios versus number of equivalent uniform loading cycles in undrained DSS loading to cause $r_u=98\%$ or single-amplitude shear strains of 1% or 3% for the sandy layer ( $D_R = 58.4\%$ , $\sigma_c' = 3.5$ atm).....	202
Figure 6.44:	Excess pore water pressure ratio variation for the alluvial sand ( $D_R = 39\%$ ) in undrained cyclic DSS loading.....	203
Figure 6.45:	Undrained cyclic DSS loading response for the alluvial sand ( $D_R = 39\%$ ) with a vertical confining stress of 0.7 atm and no static bias.....	203
Figure 6.46:	Stress paths responses for undrained cyclic DSS simulation for the alluvial sand ( $D_R = 39\%$ ) with a vertical confining stress of 0.7 atm and no static bias.....	204
Figure 6.47:	Cyclic stress ratios versus number of equivalent uniform loading cycles in undrained DSS loading to cause $r_u=98\%$ or single-amplitude shear strains of 1% or 3% for the alluvial sand ( $D_R = 39\%$ , $\sigma_c' = 0.7$ atm).....	204
Figure 7.1:	Contours of ssi for time series ID5 (return period of 1460 years).....	212
Figure 7.2:	Contours of the horizontal displacements for time series ID5 (return period of 1460 years).....	213
Figure 7.3:	Contours of the vertical displacements for time series ID5 (return period of 1460 years).....	213
Figure 7.4:	Contours of the shear strain increment for time series ID3 (return period of 75 years).....	214
Figure 7.5:	Contours of the horizontal displacements for time series ID3 (return period of 75 years).....	214
Figure 7.6:	Contours of the vertical displacements for time series ID3 (return period of 75 years).....	215

Figure 7.7:	Locations of four control points within the dam core; excess pore water pressure ( $r_u$ ) time series for time series ID1-4 in four zones of the core of the Farneto del Principe dam: (a) upper core, (b) middle core, (c) lower core, and (d) central core.....	215
Figure 7.8:	Measured and estimated NCS for the Farneto del Principe dam and comparison with the limit states suggested by Silvestri and d’Onofrio (2014).....	216
Figure 7.9:	Typical results of the Multiple Stripe Analyses. The blue dots represent the damage observed and each stripe refers to a return period. The dashed vertical lines indicate the threshold used to define the damage measure and evaluate the fraction of ground motions that exceed that value.....	218
Figure 7.10:	(a) Plot of the damage measure versus significant duration showing larger damage for long earthquakes; (b) Plot of the damage measure versus the fundamental frequency of the ground motions.....	218
Figure 7.11:	Fragility functions for the Farneto del Principe dam using the PGA as Intensity Measure.....	219
Figure 7.12:	Comparison between fragility functions for the selected limit states: (a) Collapse Limit State; (b) Lower damage measures.....	220
Figure 7.13:	Collapse disaggregation for all DMs considered. The peak of these curves are used to evaluate PGA values contributing the most to the collapse of the dam. ....	221
Figure 7.14:	Filter displacement values versus AI for ground motions selected and scaled using PGA-based disaggregation results.....	222
Figure 7.15:	Fragility functions for the Farneto del Principe dam using the AI as IM. ....	223
Figure 7.16:	Comparison between fragility functions for the same limit state for (a) Collapse Limit State; (b) Lower damage measures.....	224
Figure 7.17:	Fragility functions for the Farneto del Principe dam using PGV as IMs. ....	225
Figure 7.18:	Comparison between fragility functions for the same limit state for (a) Collapse Limit State; (b) Lower damage measures.....	225
Figure 7.19:	Comparison between fragility functions for PGA and PGV for (a) filter displacement; (b) global instability. ....	226
Figure 7.20:	Locations of the Angitola dam where the excess pore water pressure ratio is calculated.....	229

Figure 7.21:	Contours of ssi for time series ID1 (return period of 1460 years).....	231
Figure 7.22:	Contours of the horizontal displacements for time series ID1 (return period of 1460 years).....	231
Figure 7.23:	Contours of the vertical displacements for time series ID1 (return period of 1460 years).....	232
Figure 7.24:	Contours of ssi for time series ID5 (return period of 75 years).....	232
Figure 7.25:	Contours of the horizontal displacements for time series ID5 (return period of 75 years).....	233
Figure 7.26:	Contours of the vertical displacements for time series ID5 (return period of 75 years).....	233
Figure 7.27:	Excess pore water pressure ratio $r_u$ time series for ground motions scales at the same PGA value, in four different zones of the model: (a) Pit, (b) sandy layer beneath the dam, sandy layer downstream, and alluvial sand.....	234
Figure 7.28:	Variation of the excess pore water pressure ratio $r_u$ in the pit, beneath the dam, in the sandy layer in free condition, and in the alluvial sand layer. The results refer to the set of ground motions scaled at a constant value of PGV. ....	234
Figure 7.29:	Shear stress vs shear strain showing the effects of the static shear stress ratio for time series ID6 at the following control zones: (a) pit, (b) sandy layer beneath the dam, (c) sandy layer downstream, and (d) alluvial sand.....	235
Figure 7.30:	Fragility functions for the Angitola dam using the PGA as Intensity Measure (Mohr-Coulomb dam model).....	237
Figure 7.31:	Fragility functions for the Angitola dam using the PGV as Intensity Measure (Mohr-Coulomb dam model).....	237
Figure 7.32:	Fragility functions for the Angitola dam using the AI as Intensity Measure (Mohr-Coulomb dam model).....	238
Figure 7.33:	Fragility functions for the Angitola dam using the CAV as Intensity Measure (Mohr-Coulomb dam model).....	238
Figure 7.34:	Fragility functions for the Angitola dam using the $CAV_5$ as Intensity Measure (Mohr-Coulomb dam model).....	239
Figure 7.35:	Collapse disaggregation for the Angitola dam for the Mohr-Coulomb dam model and the PM4Sand dam model.....	240

Figure 7.36:	Fragility functions for the Angitola dam using the PGA as Intensity Measure (PM4Sand dam model).....	241
Figure 7.37:	Fragility functions for the Angitola dam using the PGV as Intensity Measure (PM4Sand dam model).....	241
Figure 7.38:	Fragility functions for the Angitola dam using the AI as Intensity Measure (PM4Sand dam model).....	242
Figure 7.39:	Fragility functions for the Angitola dam using the CAV as Intensity Measure (PM4Sand dam model).....	242
Figure 7.40:	Fragility functions for the Angitola dam using the CAV <sub>5</sub> as Intensity Measure (PM4Sand dam model).....	243
Figure 7.41:	Variation of the excess pore water pressure ratio for the five IM adopted.....	244
Figure 7.42:	Fragility functions for the excess pore water pressure ratio $r_u$ for the Angitola dam using PGA as Intensity Measure.....	245
Figure 7.43:	Fragility functions for the excess pore water pressure ratio $r_u$ for the Angitola dam using PGV as Intensity Measure.....	245
Figure 7.44:	Fragility functions for the excess pore water pressure ratio $r_u$ for the Angitola dam using AI as Intensity Measure.....	246
Figure 7.45:	Fragility functions for the excess pore water pressure ratio $r_u$ for the Angitola dam using CAV as Intensity Measure.....	246
Figure 7.46:	Fragility functions for the excess pore water pressure ratio $r_u$ for the Angitola dam using CAV <sub>5</sub> as Intensity Measure.....	247
Figure 7.47:	Comparison between fragility functions for different damage mechanisms for the PM4Sand dam model for (a) PGA, (b) PGV, (c) AI, (d) CAV, and (e) CAV <sub>5</sub> .....	248
Figure 7.48:	Comparison between fragility functions at the collapse limit state for the Mohr-Coulomb dam model and the PM4Sand dam model.....	249
Figure 7.49:	Comparison between fragility functions at DMs for thresholds lower than the collapse state for the Mohr-Coulomb dam model and the PM4Sand dam model.....	249
Figure 7.50:	Ground Motion Intensity Measure Efficiency for the crest settlement (Farneto del Principe dam).....	252
Figure 7.51:	Ground Motion Intensity Measure Efficiency for the crest settlement for the PM4Sand dam model (Angitola dam).....	253

Figure 7.52:	Ground Motion Intensity Measure Efficiency for the $r_u$ in the pit for the PM4Sand dam model (Angitola dam).....	253
Figure 7.53:	Ground Motion Intensity Measure Efficiency for the crest settlement for the Mohr-Coulomb dam model (Angitola dam).....	254

## List of Tables

Table 2.1:	Overall statistics of embankment dam failures, large embankment dams, up to 1986 and excluding dams constructed in Japan pre 1930 and in China (adapted from Fell et al., 2014).....	60
Table 2.2:	Damage classes for embankment dams under earthquake loading (adapted from Fell et al., 2014). .....	64
Table 3.1:	Main characteristics of the Farneto del Principe dam. ....	80
Table 3.2:	Geotechnical characteristics of the materials tested prior and during the construction of the Farneto del Principe dam. ....	80
Table 3.3:	Mean percentage variation of the anisotropic undrained shear strength to the isotropic drained and undrained strength. A positive value means that the anisotropic undrained shear strength is higher. ....	108
Table 4.1:	Magnitude Distance Epsilon disaggregation results for spectral acceleration at period 0.25s for different return periods.....	117
Table 4.2:	Non-ergodic M-D- $\epsilon$ disaggregation results for the spectral acceleration at 0.25s for the Farneto del Principe dam.....	135
Table 4.3:	Differences between non-ergodic and ergodic disaggregation results for the spectral acceleration at 0.25s. ....	135
Table 5.1:	Main characteristics of the Angitola dam.....	139
Table 5.2:	Summary of the tests performed on the secondary dam.....	141
Table 5.3:	Summary of the properties used in the numerical analyses of the secondary dam.....	151
Table 6.1:	Primary parameters of the PM4Sand model.....	163
Table 6.2:	Secondary parameters of the PM4Sand model. ....	164
Table 6.3:	Primary parameters of the PM4Silt model. ....	166
Table 6.4:	Secondary parameters of the PM4Silt model.....	167
Table 6.5:	Summary of the fundamental periods of the Farneto del Principe dam estimated from different methods. ....	177

Table 7.1:	Magnitude-Distance-Epsilon disaggregation for the Farneto del Principe dam.....	208
Table 7.2:	Summary of the subset of ground motions for which results are shown in this section. ....	209
Table 7.3:	Fell damage classes for the Farneto del Principe dam.....	210
Table 7.4:	PGA that contribute the most to the collapse as evaluated from the collapse disaggregation.....	221
Table 7.5:	AI used in this study for the MSA.....	223
Table 7.6:	Peak Ground Velocities used for the Multiple Stripe Analyses.....	224
Table 7.7:	Median and standard deviations of the Farneto del Principe dam fragility functions for the collapse limit state. n.a. means that no settlements greater than the freeboard were observed. ....	227
Table 7.8:	Summary of the subset of ground motions for which results are shown in this section. ....	228
Table 7.9:	IMs adopted for the MSA of the Angitola dam.....	228
Table 7.10:	Fell damage classes for the Angitola dam. ....	229
Table 7.11:	Mean scale factors of the ground motions for the Intensity Measures used.....	236
Table 7.12:	PGA values contributing the most contribute to the collapse of the Angitola dam.....	239
Table 7.13:	Comparison between median and standard deviation values of the fragility functions for the MC dam model and PM4Sand dam model, for all considered collapse limit state (n.a. means that no exceedances were observed). ....	243
Table 7.14:	$\sigma_{\ln DM \ln IM}$ from regression analysis for several IM and DM for the Farneto del Principe dam.....	252
Table 7.15:	$\sigma_{\ln DM \ln IM}$ from regression analysis for various IM and DM, for the PM4Sand dam model of the Angitola dam. ....	254
Table 7.16:	$\sigma_{\ln DM \ln IM}$ from regression analysis for various IM and DM, for the Mohr-Coulomb dam model of the Angitola dam. ....	255
Table 7.17:	Efficiency, predictability, and total standard deviation for PGV, AI, CAV, CAV <sub>5</sub> , and S <sub>a</sub> (0.25s) for some well-known Ground Motion Models in literature. Farneto del Principe dam, MC dam model, Left crest displacement. ....	256

Table 7.18:	Efficiency, predictability, and total standard deviation for PGV, AI, CAV, $CAV_5$ , and $S_a(0.25s)$ for some well-known Ground Motion Models in literature. Farneto del Principe dam, MC dam model, Filter displacement. ....	256
Table 7.19:	Efficiency, predictability, and total standard deviation for PGV, AI, CAV, $CAV_5$ , and $S_a(0.2s)$ for some well-known Ground Motion Models in literature. Angitola dam, PM4Sand dam model, right crest displacement. ....	257
Table 7.20:	Efficiency, predictability, and total standard deviation for PGV, AI, CAV, $CAV_5$ , and $S_a(0.2s)$ for some well-known Ground Motion Models in literature. Angitola dam, PM4Sand dam model, filter displacement. ....	257
Table 7.21:	Efficiency, predictability, and total standard deviation for PGV, AI, CAV, $CAV_5$ , and $S_a(0.2s)$ for some well-known Ground Motion Models in literature. Angitola dam, PM4Sand dam model, excess pore water pressure in the pit zone. ....	258
Table 7.22:	Efficiency, predictability, and total standard deviation for PGV, AI, CAV, $CAV_5$ , and $S_a(0.2s)$ for some well-known Ground Motion Models in literature. Angitola dam, PM4Sand dam model, excess pore water pressure beneath the dam. ....	258
Table 7.23:	Efficiency, predictability, and total standard deviation for PGV, AI, CAV, $CAV_5$ , and $S_a(0.2s)$ for some well-known Ground Motion Models in literature. Angitola dam, MC dam model, right crest displacement. ....	259
Table 7.24:	Efficiency, predictability, and total standard deviation for PGV, AI, CAV, $CAV_5$ , and $S_a(0.2s)$ for some well-known Ground Motion Models in literature. Angitola dam, MC dam model, filter displacement. ....	259
Table 7.25:	Percentage variation of the total standard deviation for the Angitola dam between the two models. Positive values corresponds to larger $\sigma_{\ln DM \ln M,R,S}$ for the MC dam model. ....	260



## 1. Introduction

### 1.1 Background and scope of the work

Earth dams are essential infrastructure systems for the economy, our communities, and the society. Over the last century the global number of embankment dams rose almost exponentially (Penman, 1986), with Italy being no exception. There are more than 45,000 large embankment dams (dams taller than 15 m and/or impounding greater than 1.000.000 m<sup>3</sup> of water) worldwide (ICOLD 2020), 165 of which are located in Italy, a country almost entirely characterized by medium to high seismicity.

Most of the existing earth dams can be classified as “old structures”, as they have been in operation for more than 30 years. Thus, safety assessment of earth dams (under both static and dynamic conditions) is now becoming of great importance, particularly for dams suffering the effects of ageing. The geotechnical properties of the dam body materials may change over time (e.g. different grain size distribution in different zones of the dam – especially filters – due to seepage dragging forces) and the current characteristics can be remarkably different from those measured during the construction period. Foster (2000) showed that under static conditions, damage to earth dams occurs immediately after the end of construction, or several years later. For these reasons, the analysis and monitoring of the dam must be performed periodically, to ensure the functionality of the structure.

The above considerations are particularly true for seismic performance evaluations, as the majority of earth dams in Italy were designed with old codes/standards that often accounted for the effects of earthquakes only in a simplified manner. For instance, seismic conditions were typically treated using simplified methods where the seismic loading was represented as a pseudo-static force. Such methods fail to capture the actual nuances of the seismic behavior of earth dams (e.g. ignoring or oversimplifying excess pore pressure generation phenomena) and can only predict mass sliding failures. However, several case histories (Seed et al., 1969, 1975, Harder et al., 2011) showed that the actual failure mechanisms and damage types caused by earthquakes are associated to complex phenomena and should be analyzed using advanced methods. During the past four decades, several investigators worked on the evaluation of the seismic response of earth dams (e.g., Seed, 1981, Gazetas and Dakoulas, 1992, Mitchell, 2008, Boulanger et al., 2015). Such efforts led to new methods of analysis, which can capture nonlinear behavior

of soils, model the interaction between the dam and its foundation materials, and more faithfully reproduce the dynamic loading. As a result, the Italian National Authority for Dams recently issued new standards and requested the seismic re-evaluation of all old earth dams in the Italian territory (Italian Ministry of Infrastructures, 2004). The aforementioned methods require a substantial computational effort and advanced numerical models (typically using large strain finite element or finite difference methods) based on the dynamic characteristics of the materials. Thus, a key component of the seismic assessment of earth dams is represented by field and laboratory tests of soil.

The evaluation of the dynamic response of earth dams also depends on the choice of the seismic input to be used in the analysis. Input motions can be defined to be consistent with target response spectra derived from Probabilistic Seismic Hazard Analyses (PSHA), usually provided by a government agency and building codes (e.g., Norme Tecniche per le Costruzioni, NTC, 2018, in Italy). However, Zimmaro and Stewart (2017) showed that for critical infrastructure systems, ground motions should be chosen based on site-specific probabilistic hazard analyses. Such analyses can be undertaken adopting two levels of resolutions: (1) based on ground response effects estimated by means of proxies derived from global databases (ergodic approach), or (2) following a non-ergodic approach where such effects are estimated based on site-specific data (i.e., the site effect estimation will differ from the global average in a manner proportional to local site complexities). Seismic ground response analyses (GRA) can be used to quantify site-specific effects such as resonance, nonlinear behavior, and impedance contrast. Non-ergodic approaches improve the level of resolution of the analysis by means of an infusion of knowledge into the problem. Thus, such approaches reduce epistemic uncertainties related to site effects (e.g., Stewart et al. 2017; Zimmaro et al., 2017). Both approaches mentioned above account for ground response effects explicitly and within the PSHA hazard integral (using proxies from global data in approach 1 and site-specific information in approach (2)).

Once the input motions to be used for response history analyses are selected, two different approaches can be followed to assess the seismic performance of a structure, the uncoupled and the coupled approaches. In the former, the seismic input is derived from probabilistic approaches (e.g., PSHA results), while the dynamic response of the system is based on a certain number of deterministic

response history analyses. This approach meets the classic criteria of performance-based design procedures (Stewart et al., 2002; Krawinkler and Miranda, 2004) which give results (e.g., the permanent displacements of the embankment) that are consistent with a certain ground shaking intensity measure level (IM). However, such approach comprises two issues: (1) the information gathered from the probabilistic portion of the analysis are essentially lost as they remain confined in the hazard analysis part and uncertainties related to this step are not carried in the second step of the analysis, and (2) the results from deterministic analyses cannot be used to estimate the seismic risk related to the structure. These issues can be solved using a coupled approach where a fully probabilistic approach is used for both components of the analysis: hazard estimation and response history analysis of the structure (Tekie and Ellingwood, 2003; Lupoi and Callari, 2011). This goal can be achieved by the means of fragility functions, which, for any given level of seismic intensity, provide the probability that the structure reaches (or exceeds) a certain limit state. Presently, the number of seismic fragility functions for earth dams is very limited and always based on input selections performed using uniform hazard spectra (Jin and Chi, 2019, Vecchietti et al. 2019, both for rockfill dams). Padgett and Desroches (2007) showed that the most important source of uncertainty for the analysis of fragility functions is that arising from the choice or the inputs using different target spectra (e.g., uniform hazard spectra and conditional spectra), and therefore for seismic risk evaluation. Furthermore, additional considerations are necessary for earth dams, due to the effect of spatial and temporal variability of the geotechnical properties.

In this study, a non-ergodic probabilistic seismic hazard analysis for a zoned earth dam in Southern Italy (the Farneto del Principe dam) is presented. This study follows the work of Zimmaro (2015), who performed an ergodic site-specific hazard analysis of the dam objective of the study. Thus, one of the objective of this dissertation is to evaluate the differences between ergodic and non-ergodic PSHA results, and to identify which variables contribute to their differences.

The numerical model of the Farneto del Principe dam is built upon a comprehensive geotechnical characterization program performed by means of field investigation and laboratory tests. A series of invasive (cross-hole and down-hole) and non-invasive (multichannel analysis of surface waves, MASW) geophysical tests, in addition to traditional geotechnical field tests, such as cone penetration tests (CPTs),

standard penetration tests (SPTs), oedometric, grain size distribution, direct shear, and triaxial tests were performed to evaluate geotechnical characteristics of the dam. Several cyclic laboratory tests by means of resonant column tests were also performed on undisturbed specimens collected in the clay core of the dam. Such data formed the basis for developing a geotechnical model used to evaluate the seismic response of the dam.

In the second part of this study, Nonlinear Dynamic Analyses (NDA) are performed for two dams: (1) the Farneto del Principe dam, (2) the Angitola dam, for which geotechnical data are available. Both dams are located in the same area, characterized by high seismicity. However, they are built using different soil types. Thus, they are potentially vulnerable to different failure types and mechanisms. As a result, different constitutive models were used for these dams, and comparisons on their relative performance were made. The final goal of this comparison was to identify which dam types should be analyzed using advanced constitutive models, and when more simplified models are sufficient. This goal is accomplished performing a fully probabilistic approach where the performance of these structures are evaluated by means of fragility functions. Such fragility functions were derived for multiple intensity measures.

Fragility functions are useful tools to predict the performance of earth dams conditioned on the occurrence of a scenario event. However, this is not their only potential application. For instance, using fragility functions it is possible to perform rapid post-earthquake damage assessments. Such assessments can be performed using predicted IMs at the dam site (perhaps from readily available products such as ShakeMaps (e.g., Wald et al., 2005; Worden and Wald, 2016; Michelini et al., 2008), or recorded IMs if the dam is equipped with a monitoring system that includes ground motion recording stations. This goal can be achieved because fragility functions relate the probability of exceeding a certain damage level given the occurrence of an IM value. Once the IM of the event is known (e.g., from a recording at the dam site, or by means of predictive models), the probability of observing a certain damage can be readily computed. Armed with this information, the margin of safety (e.g., comparing if the probability is higher than an acceptable limit based on design standards) of the dam can be derived. This concept is strictly related to earthquake early warning systems (EEW, Pagano and Sica, 2012). Such systems are capable of predicting the incipient collapse based on the data

interpretation of a continuous monitoring of the dam. Some of the monitored parameters might be crest displacement, excess pore water pressure, accelerations, and seepage flow. Fragility functions can aid EEW systems by providing an estimate of the probability of observing a certain damage (e.g., excess pore water pressure ratio greater than 95%), thus calibrating the predictive model of cause and effect necessary implement an EEW system.

## 1.2 Dissertation outline

This dissertation comprises seven chapters. The introduction presented the problem, the purpose of this research, and an overall summary of the analysis performed.

Chapter 2 presents the current state-of-the-art for the following topics: (1) seismic hazard analysis, (2) dynamic analysis of earth dams, and (3) seismic performance of earth dams. A brief comparison between old and new methodologies to perform site-specific seismic hazard assessments is presented, with particular emphasis on non-ergodic probabilistic analysis. The chapter also discusses the current methods available to merge GRA results into hazard estimation procedures. In the second part of the chapter, methods to perform seismic analyses of earth dams are briefly discussed. Lastly, procedures to evaluate seismic performance of embankment dams is described. This is done analyzing various potential damage mechanisms and methods to assess them.

Chapter 3 illustrates one of the two earth dams analyzed in this dissertation: the Farneto del Principe zoned earth dam in Southern Italy and its geotechnical characterization program. Such program, partially performed during this study, comprises traditional and innovative field and laboratory tests. Results of these tests are then presented and analyzed. Particular emphasis was devoted to the dynamic behavior of the dam's materials and their strength characterization. Both items are particularly useful for the calibration of advanced constitutive models discussed in the remainder of this dissertation.

In the first part of Chapter 4, seismic ground response analyses for the Farneto del Principe dam site are illustrated. In this section, ground motion selection and scaling procedures for this dam are analyzed. Furthermore, a discussion of epistemic uncertainties is presented. In the second part of the chapter, a non-ergodic PSHA is presented and the differences in relation to more simplified methods to combine

ground response effects with PSHA are presented and discussed using a quantitative approach.

Chapter 5 presents a second case study for which geotechnical data were available: the Angitola dam. In this chapter, a brief description of the dam and its construction phases is presented and available geotechnical data are discussed. Interestingly, while the Farneto del Principe dam does not present any materials susceptible to liquefaction or cyclic softening phenomena, the Angitola dam comprises materials that may be susceptible to such pore-pressure induced failure mechanisms. As a result, particular attention is given to the characterization of foundation layers, potentially vulnerable to such cyclic phenomena. These results are later used to calibrate advanced constitutive models. Lastly, the results of a site-specific PSHA for this dam site are also illustrated.

In Chapter 6, the numerical modelling of the Farneto del Principe dam and of the Angitola dam is presented. The software used is FLAC 2D (Fast Lagrangian Analysis of Continua) which implements the explicit finite difference formulation for solving the dynamic equation of motion. Two constitutive models for earthquake engineering (PM4Sand and PM4Silt) are illustrated, and their calibration for the two dams of interest is presented.

Chapter 7 presents the results obtained from the NDAs of the Farneto del Principe and Angitola dams. The numerical analyses are performed using a Multiple Stripe Analyses (MSA) procedure. In this chapter, a brief review of fragility analysis and MSA procedures is conducted. Then fragility functions for both dams are presented. Several ground motion intensity measures (IM) and damage measures (DM) are used to estimate such fragility functions. The fitted fragility functions are then analyzed to evaluate the most efficient IM for a particular DM. In addition, the limit state that is more likely to be exceeded is estimated. For the Angitola dam, differences using two constitutive models are also presented.

The conclusion summarizes the main results obtained in this dissertation and provides an overview on future work that can be performed departing from the outcomes of this study.

## 2. Hazard analysis and seismic response of earth dams: state-of-the-art

Seismic analysis of any infrastructure system requires the knowledge of the ground shaking intensity level that can be expected (or exceeded) within a certain period of time at the site (i.e. seismic hazard). Seismic hazard analysis for critical infrastructure systems are typically performed using probabilistic approaches (i.e., PSHA) (e.g., Cornell, 1968; McGuire, 2004) as they provide results in terms of median/mean and associated uncertainty levels relative to return periods that have a clear meaning. An alternative to PSHA approaches is to use deterministic analysis. However, the latter approach relies upon judgement-based choices such as the arbitrary pre-selection of earthquake event scenarios and ground motion percentiles. As a result, in this section, we focus on probabilistic approaches.

The seismic intensity is a measure of the earthquake strength at a certain place, estimated based on its effects. Such measures are often referred to as macroseismic scales. The earlier empirical scales appeared in the 19<sup>th</sup> century and since 1883 (with the ten-degree Rossi-Forel scale) the seismic intensity prediction scales spread worldwide (Musson and Cekić, 2012). Sieberg (1932) proposed the Mercalli-Cancani-Sieberg scale, still widely used in Europe and Italy, while other famous intensity scales are the Medvedev–Sponheuer–Karnik (1964) and the European Macroseismic scale (1998). In earthquake engineering, a ground motion IM is needed for the analysis of the seismic response and design of a structure. Cancani (1904) and Sieberg (1923) developed a relationship to associate peak ground acceleration (PGA) values to each degree of the seismic intensity scale. However, more recent studies (Ambraseys, 1974; Trifunac and Brady, 1975; Decanini et al., 1995) showed that PGA and macroseismic intensities are poorly correlated, mainly because of the many different factors influencing the ground shaking.

Starting from the second half of the last century, as the number of strong-motion recordings increased, new models were proposed to evaluate the IM expected at the site of interest, leading to the development of tools for seismic design (Faccioli and Paolucci, 2005). The Deterministic Seismic Hazard Analysis (DSHA) procedure was one of the first models used in practice to estimate the ground motion at a given site (Kramer, 1996). In DSHA, the earthquake scenario (i.e. characterized by a certain magnitude and distance from the site) deemed the worst is considered and analyzed. The resulting ground motion is then believed to be the worst-case scenario (this was once known as Maximum Credible Earthquake or Maximum

Considered Earthquake, MCE). However, according to the committee on seismic risk (1984) of the Earthquake Engineering Research Institute (EERI), the use of the MCE or the maximum earthquake likely to occur in a 100-year interval (Maximum Probable Earthquake, MPE) is discouraged and misleading (Committee on Seismic Risk, 1984, Kramer, 1996). Baker (2008) shows how the DSHA is incapable of defining the true worst-case scenario, because a larger event, but still plausible, can always be determined.

It is interesting to notice that the high number of ground motion recording enabled the formulation of the intensity prediction models (thus, producing the inverse effect of the original formulation), based on magnitude, source-to-site distance, and site conditions (Cua et al., 2010). These equations relate hazard to seismic intensity, which in turn can be associated with seismic risk (Musson, 2000). Nonetheless, the only mathematical procedure that can explicitly and transparently account for uncertainty in ground motion from future earthquakes at a given location and time is the PSHA. The following section focuses mainly on the mathematical formulation and different levels of sophistication that can be introduced as part of PSHA approaches. More details on the state-of-the-art of the utilization of PSHA results for regional and site-specific applications in Italy and Europe are provided by Zimmaro (2015).

## 2.1 PSHA: a brief review

PSHA usually comprises the following four basic components, which are the fundamental principles of the methodology (every step can be refined to obtain a more precise and detailed model for the hazard estimation):

**(a) Earthquake source characterization;** in this step all of the seismic sources capable of producing considerable ground shaking at the site of interest are identified. The seismogenic zonation includes the definition of the geometry of finite faults, area sources, and/or background seismicity. Once the geometries of the faults in the area are identified, the probability distributions of source-to-site distance are defined. In Italy, the seismogenic zonation currently adopted in the Italian building code (Norme Tecniche per le Costruzioni, 2018) uses only area sources as shown in Figure 2.1 (MPS working group, 2004; Stucchi et al., 2011).

**(b) Earthquake recurrence relationships;** in this step the temporal distribution of earthquake magnitude is defined. The distribution can be created using



catalogues of historical and/or recorded events or based on geologic/paleoseismological information on long-term fault slip rates. The parameters defining this magnitude recurrence relationship can be estimated regressing historical data or using the slip rate values directly. In Italy, a catalogue developed by the CPTI working group (Catalogo Parametrico dei Terremoti Italiani, 1999, 2004) consisting of events from 217 b.c. to 2002 a.c. was used for the evaluation of the hazard maps. The simplest and most common recurrence relationship is the Gutenberg-Richter law, which describe the average rate of exceedance of a certain magnitude value using a simple power law:

$$\log \lambda_m = a - bm \quad (2.1)$$

where  $\lambda_m$  is the mean annual rate of earthquakes with magnitude greater than  $m$ ,  $10^a$  indicates the number of earthquakes per year with magnitude greater than 0, and  $b$  is the parameter that relates the likelihood of small and large earthquakes (i.e. the slope of the continuous line in Figure 2.2). The original Gutenberg-Richter relationship did not account for lower and upper magnitude bounds. Such assumption is physically incorrect, as the rupture size (directly related to earthquake magnitude) has always a maximum finite value. This issue can be solved by identifying a maximum magnitude based on the maximum event observed in the catalogue (or estimated based on geologic/paleoseismological evidences), while the minimum value depends on practical considerations. For the PSHA adopted in the Italian building code, a minimum magnitude of 4.645 was deemed sufficient, as smaller earthquakes do not modify significantly the hazard calculation at high intensity measure values (though it does effect the exceedance rates for small IMs). Furthermore, the computation time is increased if a broader range of magnitudes is used (Baker, 2013). Adding magnitude lower and upper bounds results in a modified bounded Gutenberg-Richter law. This law in turn relates to a cumulative distribution function (CDF) for earthquakes magnitude values within the specified range:

$$F_M(m) = \frac{1 - 10^{-b(m-m_{min})}}{1 - 10^{-b(m_{max}-m_{min})}} \quad m_{min} < m < m_{max} \quad (2.2)$$

Many other magnitude recurrence laws are available in the literature, such as that by Youngs and Coppersmith (1985), based on the model of the characteristic earthquake (Schwartz and Coppersmith, 1984).

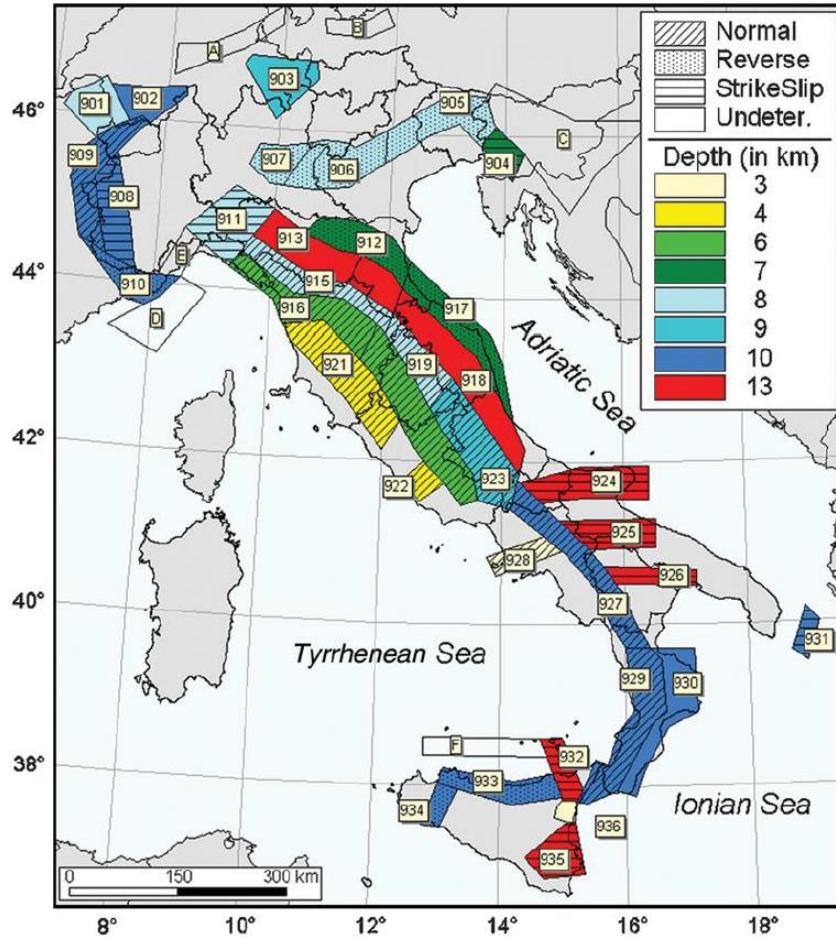


Figure 2.1: Seismogenic zonation ZS9. The 36 numbers reported in the map represent earthquake source zone IDs; the colors identify the mean seismogenic depth (in km); the superimposed shadings refer to the predominant focal mechanism (from Stucchi et al., 2011).

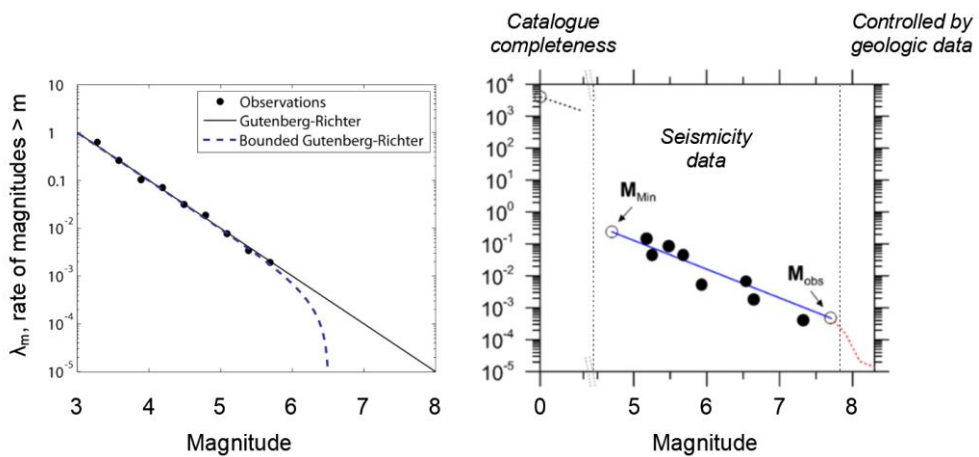


Figure 2.2: Examples of annual rate of earthquakes and Gutenberg-Richter laws to interpolate the data (adapted from Baker, 2013, and Zimmaro and Stewart, 2017).

This model assumes that some faults repeatedly generate earthquakes of similar magnitude, which implies a different distribution and relevance of the events observed in the database. Such model is typically used for faults capable of generating large earthquakes, such as the San Andreas fault in California. This model is not currently used for any faults in Italy.

**(c) Ground motion models (GMMs);** this step is one of the crucial aspect of the PSHA procedure. GMMs are semi-empirical relationships that estimate the ground motion produced at the site of interest by seismic events. Several ground shaking intensity measures can be calculated, such as PGA, the peak ground velocity (PGV), spectral accelerations at various periods, and earthquake duration. Usually, these quantities are log-normally distributed, thus GMMs are written in terms of the natural logarithm of the IM. A common functional form is comprised of four elements as shown in Equation 2.3 (Stewart et al., 2019):

$$\ln Z_{ij} = F_E(M_i, F_i) + F_P(M_i, R_{ij}) + F_S(S_j, x_{IMr,ij}) + \varepsilon \sigma_{\ln Z} \quad (2.3)$$

where  $Z_{ij}$  is the ground shaking intensity measure for event  $i$  and site  $j$ ,  $F_E$ ,  $F_P$ , and  $F_S$  are the event, path, and site terms, respectively. Subscript  $i$  refers to quantities depending on the event and on the source (i.e., magnitude  $M_i$  and focal mechanism  $F_i$ ).  $R_{ij}$  is the source-to-site distance,  $S_j$  is a vector depending on site parameters (e.g., the time-averaged shear wave velocity in the upper 30 m,  $V_{S30}$ ), and  $x_{IMr,ij}$  is an intensity measure of reference used to compute the nonlinear site response.  $\varepsilon$  is standard normal random variable, with a mean value of zero and standard deviation of one, and  $\sigma_{\ln Z}$  is the total standard deviation of  $Z$ .

GMMs are developed from regression of ground motion recordings made at different sites worldwide. Although such regressions would make GMMs only applicable within a relatively narrow parameter space (dictated by the range of input parameters used to perform the regression), it is desirable (and often necessary) to use GMMs outside of their parameter space. As a result, modern GMMs are developed to make such extrapolations possible as their functional forms are informed by expert judgement and/or simulations (e.g., Bozorgnia et al., 2014). Douglas (2019) reports over 461 empirical models for the prediction of PGA and 299 for the prediction of spectral acceleration values. Given the large number of available GMMs, appropriate criteria should be considered when selecting these models for site-specific applications. Several authors (Cotton et al. 2006; Bommer et

al. 2010; Scherbaum et al., 2010; and Stewart et al. 2015) proposed various procedures for the selection of suitable GMMs.

Once the probability distribution of the ground motion intensity measure is known, the probability of exceeding any value  $z$  can be computed as:

$$P(IM > z | \bar{s}) = 1 - \Phi\left(\frac{\ln z - \ln \overline{IM}}{\sigma_{ln}}\right) \quad (2.4)$$

where  $\Phi$  is the standard normal cumulative distribution function,  $IM$  is the intensity measure of interest (e.g. PGA),  $\bar{s}$  is a vector containing the parameters that define the scenario event (e.g., magnitude and distance) and it depends on the GMM predictor variables,  $\overline{IM}$  and  $\sigma_{ln}$  are the mean and logarithmic standard deviation of the GMM. A graphic depiction of this probability distribution is reported in Figure 2.3 (Baker, 2013).

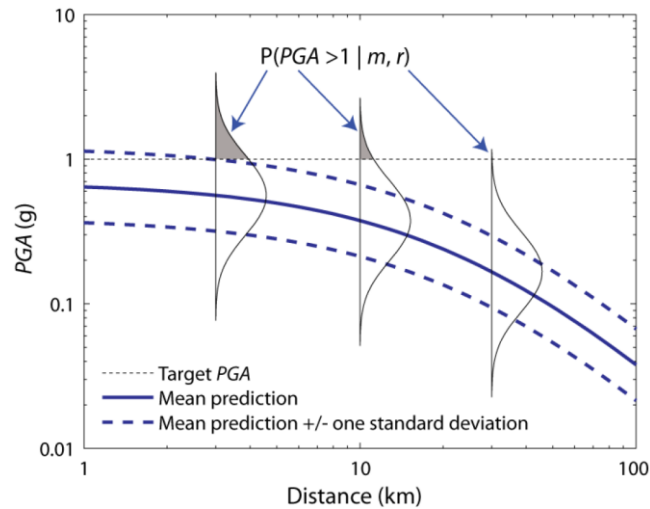


Figure 2.3: Example of a GMM for a magnitude  $m$  earthquake, and graphical representation of the probability of  $PGA > 1g$  at a distance  $r$  (from Baker, 2013).

#### (d) Probabilistic computation of seismic hazard curves;

The final step of a PSHA procedure is the computation of hazard curves, which combines all the information (and uncertainties) on earthquake size, location, and site conditions gathered in the previous steps. The hazard curve relates a ground motion intensity measure to the annual rate of exceeding different values of the

parameter of interest. For multiple seismogenic sources and for independent magnitude-distance events, the rates can be computed as:

$$\lambda(IM > z) = \sum_{i=1}^{N_{sources}} \lambda(M_i > m_{min}) \int_{m_{min}}^{m_{max}} \int_0^{r_{max}} P(IM > z | \bar{s}) f_{M_i}(m) f_{R_i}(r) dr dm \quad (2.5)$$

$f_M(m)$  and  $f_R(r)$  are the probability distribution functions for magnitude and distance,  $N_{sources}$  is the number of sources defined in the seismogenic zonation, and the other elements are defined above. Eq. 2.5 is the classical rate-based relationship (McGuire, 1995) to estimate the seismic hazard. However, an equivalent expression that uses the probability of rupture can also be formulated (Field et al., 2003) and it is implemented in the open source software OpenQuake (GEM, 2019, Pagani et al., 2014). In practice, a numerical integration is necessary to evaluate the rate of exceedance, thus the magnitude and distance variables are divided into suitable ranges. A smaller binning usually leads to more precise estimation, but heavily increase the computation time.

### 2.1.1 The Uniform Hazard Spectrum computation

Hazard curves can be used to evaluate the probability that a given ground motion parameter will be exceeded in a certain period. This requires a temporal distribution between occurrences of seismic event, which is typically assumed as Poissonian. The Poisson model is preferred because of its simplicity, for its proven methodology, and the poor results sensitivity to more complex distributions (further details are in Kramer, 1996). An alternative to Poissonian time-independent models is offered by so-called time-dependent models. Such models can be used when long-term event chronologies are available for a given fault and renewal models for their recurrence intervals can be applied (e.g., Field et al., 2015). These criteria are met by the well-known San Andreas and Hayward faults in California. No faults in Italy meet these criteria. As a result, in the remainder of this section, only Poisson-type time-dependent models are analyzed. The probability of exceedance is computed as:

$$P(IM > x) = 1 - e^{-\lambda t} \quad (2.6)$$

where  $\lambda$  is the rate of occurrence of events and  $t$  is the time period of interest. The reciprocal of  $\lambda$  is the return period  $T_R$ , which indicates the mean time between exceedances. For instance, a 2% probability of exceedance in 50 years corresponds to a return period of 2475 years.

The information of the PSHA and the Poisson model can be exploited to build a target response spectrum, by combining seismic hazard curves for spectral accelerations at various periods, but for the same return period. The result of this combination of multiple IMs at a common hazard level is the Uniform Hazard Spectrum (UHS). A single rate of exceedance is chosen (hence the name *Uniform*), then the corresponding spectral ordinates are evaluated; Figure 2.4 illustrates this procedure. However, as explained further in § 4.2.1, the UHS is the envelope of different spectral values from different hazard curves, whose acceleration ordinates may come from distinct seismic scenarios.

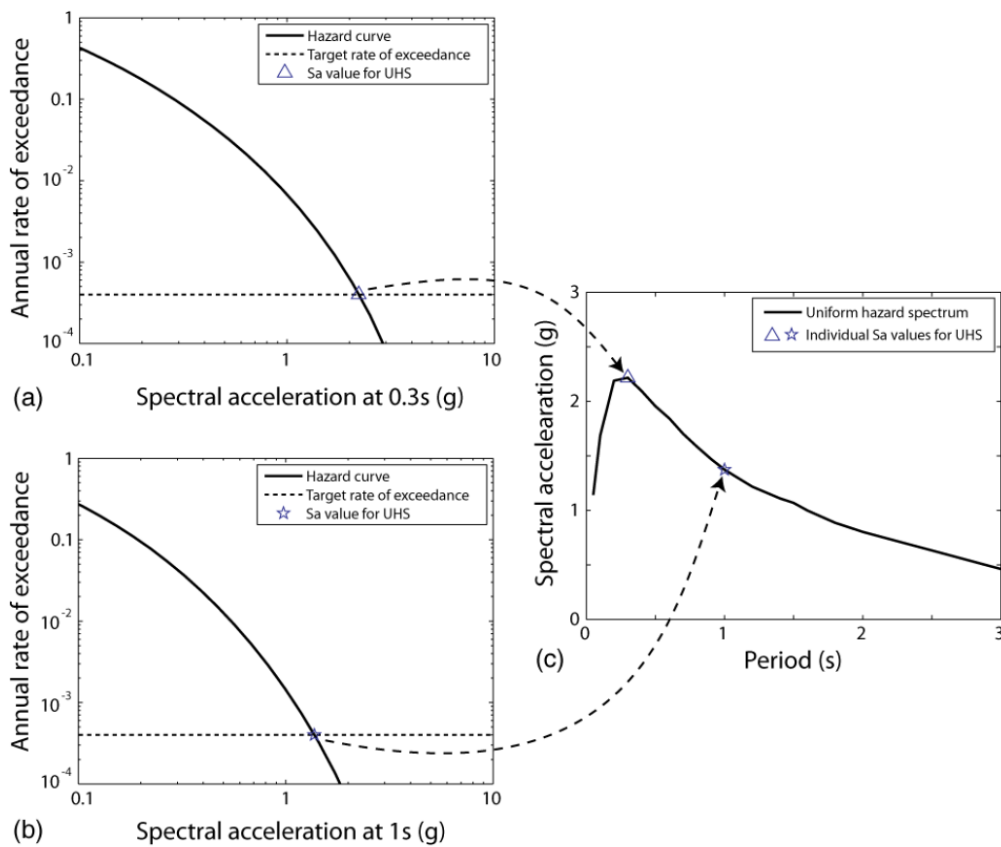


Figure 2.4: Graphical representation of the UHS computation (from Baker, 2013).

### 2.1.2 Disaggregation of the seismic hazard

The PSHA procedure computes the probability of exceedance of a ground motion intensity measure level, given the occurrence of one of the many potential seismic events (i.e. all possible magnitudes, their relative likelihoods, and distances are

considered). PSHA evaluates the following probability:  $P(IM > x)$  in  $t$  years. The disaggregation of the seismic hazard (Bazzurro and Cornell, 1999) identifies the probability of observing a seismic scenario (denoted  $\bar{s}$  previously) given the occurrence of a ground motion intensity measure exceedance.

This process implies the estimation of the relative contribution of all sources, magnitudes, and distances. From a probabilistic point of view, this means the evaluation of the quantity below:

$$P(\bar{s} | IM > x) \quad (2.7)$$

There are several ways of expressing the scenario  $\bar{s}$ ; for instance, magnitude-distance, and longitude-latitude tectonic region type, while some other disaggregation use the parameter  $\varepsilon$ , (§ 4.2.2.1). However, it should be noted that the disaggregation results vary for different scenario, IM type, and value. This is a proof that no single scenario earthquake rigorously defines the seismic hazard, but rather, it describes the most likely event that contribute the most to the overall hazard.

## 2.2 Local vs global models and non-ergodic site response methodologies

A common issue in PSHA applications is whether to choose global GMMs, built from larger database of events, or local models, which can capture local characteristics but lack the data necessary to cover the range of magnitude and distance of interest. For instance, the first accelerograph in Italy was installed in 1965 (Castellani and Faccioli, 2005); since then, few or no seismic events characterized by large magnitude values were observed in some regions (e.g. some portions of the Calabria region), even though it is known that some faults are capable of producing large earthquakes (e.g. the 1908 Messina earthquake)<sup>1</sup>. Recent studies (Stewart et al., 2012; Zimmaro et al., 2018) show that, even for site-specific applications in Italy it is desirable to use global models with regional adjustments. Such adjustments are the subject of studies focusing on how to make global models regionally applicable and on the geographical extent of regionalized models (e.g., Abrahamson and Gülerce, 2020; Parker et al., 2020).

Another challenge in the usage of GMMs for site-specific applications is the degree to which they are able to capture local site effects by only using globally-derived

---

<sup>1</sup> The author does not imply that large earthquakes in some regions are necessary; the purpose of this paragraph is to address the difficulties and uncertainties in seismic hazard estimations without local strong-motion recordings.

proxies (e.g.,  $V_{S30}$ ). This problem would hold even with a perfect knowledge of the rupture mechanism and propagation through the Earth's crust (which is rarely available anyway) since near the surface seismic waves will be scattered, refracted, diffracted, and damped due to site geology and nonlinear behavior of soils. Over the last decade, a significant effort was devoted to the development of efficient methodologies to account for site-specific conditions in PSHA applications and to reduce related epistemic uncertainties (e.g., Goulet and Stewart, 2009; Stewart et al., 2014). The most direct way of incorporating site response effects into PSHA applications is to multiply the hazard results (which are probabilistic in nature) by a deterministic site factor. This methodology is often referred to as hybrid approach (Cramer, 2003). In this approach, such deterministic site factor can be considered as ergodic (the site factor is derived from global ground motion and, even though it is conditioned on site response proxies – most often  $V_{S30}$  – it is not specific to the site being analyzed; Anderson and Brune, 1999). Results from hybrid approaches carry the undesirable issue of being related to an unknown hazard level (Stewart et al., 2017). A more sophisticated approach, is represented by the so-called convolution approach (Bazzurro and Cornell, 2004; Rathje et al., 2015). This approach relies upon a more robust modification of the rock hazard, but does not affect the original level of uncertainty associated with the results (i.e., which remains the same as that obtained using an ergodic PSHA). A third approach, referred to as non-ergodic approach, pervasively solves the issues present in the hybrid and convolution approaches. The non-ergodic approach modifies the GMMs being used in the PSHA process, substituting the original site term (and related standard deviation) with a new value based on either numerical simulations or empirical data from nearby or co-located recording stations.

Recalling Equation 2.3, a GMM provide the lognormal distribution of an intensity measure based on three elements: (1) source, (2) path, and (3) site term. With enough information (i.e. recordings and/or numerical simulations), all the elements of the model can be adjusted to be consistent with site-specific characteristics of the site. A modification of the source term is possible if specific knowledge about the energy released during the faulting mechanism is available. An adjustment of the path term reflects a different level of anelastic attenuation of seismic waves from source-to-site compared to the ergodic path term model. The site term modification is usually the easiest and most common enhancement made to GMMs, since its improvement is relatively feasible to exploit compared to the source and path term.



As a result, non-ergodic site response analysis has been applied to some recent critical projects (Rodriguez-Marek et al. 2014; Coppersmith et al. 2014; Vecchiotti et al. 2019). Due to reduction of the uncertainties, non-ergodic hazard analysis usually lowers the ground motion at long return periods (Stewart et al., 2017). Rodriguez-Marek et al. 2014 and Coppersmith et al. 2014 estimated the consequent hazard using the convolution approach (§2.3).

### 2.3 Linking site response analysis results to PSHA

There are several ways to merge site response analyses to PSHA (i.e. from ground motion hazard for reference site conditions to surface), but all of them require the definition of a probability density function for the amplification parameters. A lognormal distribution is typically used. Following the notation of Stewart et al. (2014), the ground surface motion is denoted  $Z$ , the input motion  $X$ , and the amplification  $Y$ ; Figure 2.5 illustrates the commonly used scheme and related symbology.

$$Y = \frac{Z}{X} \quad \text{or} \quad \ln Y = \ln Z - \ln X \quad (2.8)$$

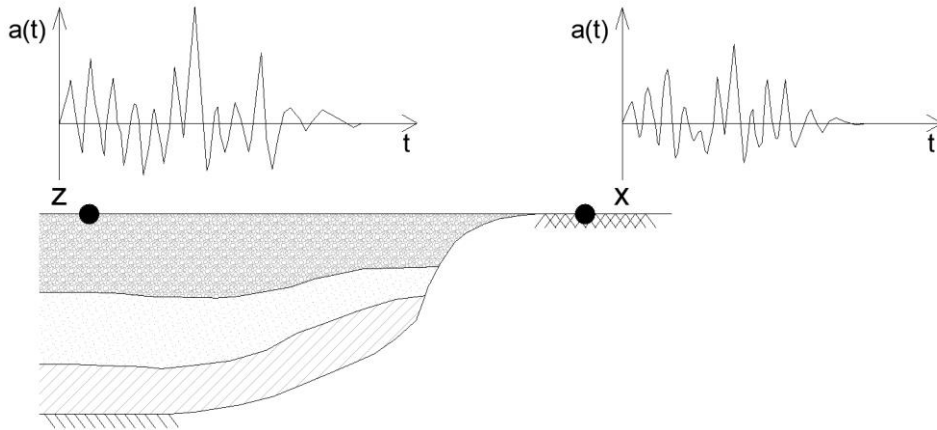


Figure 2.5: Schematization of the seismic site response analysis and notation adopted.

The amplification distribution can be represented as follows:

$$\ln \bar{Y} = f_1 + f_2 \ln \left( \frac{x_{IM,ref} + f_3}{f_3} \right) \quad (2.9)$$

where  $\bar{Y}$  is the mean amplification,  $x_{IM,ref}$  is the intensity measure for reference site conditions;  $f_1$  is the visco-elastic site amplification;  $f_2$  represents non linearity, and

$f_3$  is the value of intensity measure below which the amplification tend towards a constant value. Stewart et al. (2014) carefully reviewed the common methodologies for merging site response analysis in to PSHA; in this section, a brief summary of all methods mentioned in Section 2.2 is reported.

The hybrid method (Cramer, 2003) deterministically modifies the ground motion intensity measure of the reference site hazard curve by multiplying its value for the mean amplification function, conditioned on that ground motion. When the same IM is used to express surface motion  $Z$  and input motion  $X$  (i.e. amplification between equivalent intensity measures, such as PGA), the hybrid approach can be expressed as:

$$\ln Z = \ln X + \ln(\bar{Y} | x) \quad (2.10)$$

An issue for this approach is that the standard deviation used in the hazard computation for  $X$  is that for rock, so it is not appropriate for the actual site conditions. Moreover, the controlling sources for rock site are generally different from those for soil sites (the latter having greater contribution from distant sources). Since the hybrid approach simply modifies the hazard deterministically, the aforementioned effects are not considered in the analysis.

The convolution method incorporates the uncertainties in the site amplification function by computing the following hazard curve:

$$P(Z > z) = \int_0^{\infty} P\left(Y > \frac{z}{x} \mid x_{IMref}\right) f_X(x) dx \quad (2.11)$$

where  $P\left(Y > \frac{z}{x} \mid x_{IMref}\right)$  is the probability density function of the site amplification, which includes mean and standard deviation term  $\phi_{\ln Y}$ .  $f_X(x)$  is the absolute value of the slope of the rock hazard curve. Even though the convolution accounts for the site amplification standard deviation  $\phi_{\ln Y}$ , the hazard curve is still based on the standard deviation of the rock motion. In addition, the convolution approach shares the same controlling source issue of the hybrid approach.

An enhanced version of the hybrid approach was proposed by Goulet and Stewart (2009), called modified hybrid approach. The inherent philosophy is the same, but the mean amplification  $\bar{Y}$  is conditioned on the mean intensity measure of reference

for the magnitude and distance that most strongly contribute to the hazard (i.e., from disaggregation).

$$\ln Z = \ln X + \ln(\bar{Y} | \bar{X}_{IMref}(M, R)) \quad (2.12)$$

The modified hybrid approach is the least biased compared to fully probabilistic methods (Stewart et al., 2014). The only way to incorporate site amplification effects and to account for reduction of the standard deviation of GMMs is to modify the hazard integral by means of a fully non-ergodic approach (Stewart et al., 2017) as discussed in the following section.

### 2.3.1 Implementation of the non-ergodic procedure into PSHA

The hazard computation involves numerical integration of Eq. 2.5, where the probability of exceeding ground motion level  $Z$  given the occurrence of a scenario (typically described by magnitude and distance) is evaluated with a lognormal cumulative distribution function. The mean and standard deviation of the distribution are given by a GMM:

$$\ln Z_{ij} = (\mu_{\ln Z})_{ij} + \varepsilon \sigma_{\ln Z} \quad (2.13)$$

in which  $\mu_{\ln Z}$  is the mean value from a GMM in log units (i.e. the sum of the source, path, and site term reported in Eq. 2.3). The true ground motion, however, differs from the ergodic prediction by three elements:

$$\ln Z_{ij} = (\mu_{\ln Z})_{ij} + \eta_{E,i} + \eta_{P,ij} + \eta_{S,j} + \varepsilon \sigma_{\ln Z} \quad (2.14)$$

where  $\eta_{E,i}$ ,  $\eta_{P,ij}$ , and  $\eta_{S,j}$  are the non-ergodic event, path, and site term. The quantity  $(\mu_{\ln Z})_{ij} + \eta_{S,j}$  can be replaced by  $\ln \bar{X}_{ij} + \ln \bar{Y}_{ij}$  by exploiting the local site amplification function. Thus, the non-ergodic implementation can be represented as:

$$\ln Z_{ij} = \ln \bar{X}_{ij} + \ln \bar{Y}_{ij} + \eta_{E,i} + \eta_{P,ij} + \varepsilon \sigma_{\ln Z} \quad (2.15)$$

In Eq. 2.15,  $\sigma_{\ln Z}$  is the total uncertainty of ground motion, which now comprises the event, path, and site standard deviations. The partition of  $\sigma_{\ln Z}$  is necessary if the uncertainties reduction is to be considered in the hazard computation.

The uncertainties are divided into within-event (or intra-event,  $\Phi$ ) and between-event (or inter-event,  $\tau$ ) variability. The former represents the epistemic

uncertainty and it comprises the path, site, and amplification standard deviations (Eq. 2.16), while the latter reflects the aleatory variability of ground motion and it is site-independent.

$$\phi_{\ln Z} = \sqrt{\phi_{P2P}^2 + \phi_{S2S}^2 + \phi_{\ln Y}^2} \quad (2.16)$$

Strictly speaking, the term  $\phi_{\ln Y}$  represents the variability that remains when all the other effects are considered; however, it has been shown that this bias is dominated by site amplification uncertainties (Rathje et al., 2010; Li and Assimaki, 2011).  $\phi_{S2S}$  is the site-to-site standard deviation, which measure the variability of site response relative to ergodic models (typical values are 0.3-0.5, though it is regionally variable, Rodriguez-Marek et al. 2013), while  $\phi_{P2P}$  is the analogous for path term. The total standard deviation is evaluated as:

$$\sigma_{\ln Z} = \sqrt{\tau^2 + \phi_{\ln Z}^2} \quad (2.17)$$

It can be shown (Papaspiliou et al., 2012; Stewart et al., 2017) that if site amplification is expressed as Eq. 2.9, the within-event standard deviation is equal to:

$$\phi_{\ln Z}^2 = \left( \frac{f_2 x_{Im ref}}{x_{Im ref} + f_3} + 1 \right)^2 \phi_{\ln X}^2 + \phi_{\ln Y}^2 \quad (2.18)$$

in which  $\phi_{\ln X}^2$  is the within-event standard deviation of a GMM. In the non-ergodic implementation of a PSHA, the uncertainty is reduced by subtracting a fraction of the site-to-site variability from  $\phi_{S2S}$ .

$$\phi_{\ln Z}^2 = \left( \frac{f_2 x_{Im ref}}{x_{Im ref} + f_3} + 1 \right)^2 (\phi_{\ln X}^2 - F \phi_{S2S}^2) + \phi_{\ln Y}^2 \quad (2.19)$$

where F is a parameter representing the confidence that the amplification function, as per Eq. 2.9, actually evaluates site response (more details are in section 4.3 and 4.4).

### 2.3.2 Discussion

Probabilistic estimates of ground shaking from future earthquakes can be performed at several levels of resolution, which represent different degree of knowledge of the steps described in § 2.1.

(1) PSHA using published hazard maps (e.g. Italian building code, NTC 2018). These are the classical hazard results from government agencies and used in design standards;

(2) PSHA with pre-established source and ground motion models. These procedures, usually implemented in some PSHA software (e.g. OpenQuake) are based on models prepared by a research team;

(3) PSHA with pre-established source and ground motion models with novel features relevant to the specific site of interest (e.g. known local faults in the site proximity). Such analyses are ergodic and site-specific;

(4) PSHA with pre-established source with novel features relevant to the specific site of interest. In addition, the GMMs are customized for site-specific conditions (non-ergodic) if local characterization of site response or path effects is available. In this case, the median and standard deviation of ground motion are modified within the hazard integral, explicitly incorporating site effects.

According to the relevance of the project, PSHA should be performed at one of the above levels of resolution. For instance, PSHA for critical and strategic infrastructure should be site-specific and input ground motions should be selected to be consistent with the hazard of the site (levels 3 or 4). Such process involves critical analysis of GMMs and sources for the application region. This is accomplished by modelling all known faults that have relevance to the site of interest and to customize GMMs for site-specific conditions (i.e. non-ergodic applications). Actual site response, in fact, is different from that evaluated from a global database of recorded motions as captured using proxies such as  $V_{S30}$ . Ground motions depend on local morphology (e.g., topographic features and basins) and geology (e.g., stratigraphy). Some of these phenomena can be estimated by means of ground response analysis (GRA), in particular those regarding one-dimensional effects, such as impedance, soil nonlinearity, and resonance. Thus, information from GRA can be used to reduce epistemic uncertainties in ground motion predictions and be incorporated into PSHA applications. Another approach is to evaluate non-ergodic site response from recordings of regional earthquake events. This methodology is not addressed in this dissertation as the focus was given on simulations and site response analysis.

## 2.4 Seismic analysis of earth dams

This section briefly illustrates the most common methodologies to perform seismic analysis of earth dams. The methods differ in their overall complexity, their objectives, and their limitations. Hence, the choice of a suitable method should depend on the specific problem (e.g. stability or deformation analysis) and on the data available. Even though complex methods are more accurate, they need to be based on a quantity of reliable data that are not always available. In essence, there is no best way to perform seismic analysis of earth dams, but rather several methods that describe different behaviors of embankments subjected to dynamic loading. The methods described in the remainder of this section are reported in order of their overall complexity.

### 2.4.1 Pseudo-static method

The pseudo-static method is based on the rigid body assumption and it is used to evaluate the overall stability of the embankment. It is one of the simplest approach to perform seismic analysis of earth dams and it requires a reduced number of input data. The dynamic loading is treated as inertial forces in two directions and it is proportional to the soil weight, as shown in Figure 2.6.

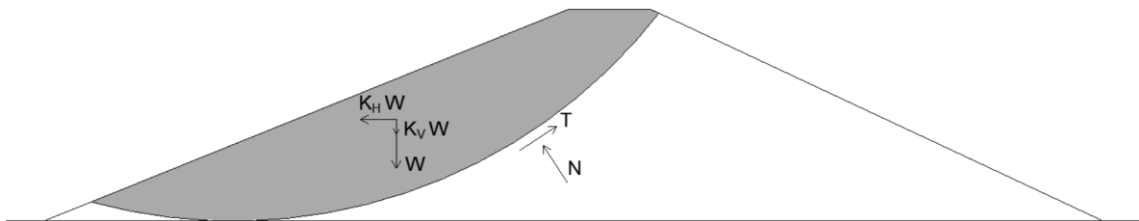


Figure 2.6: Schematization of the pseudostatic approach for the seismic analysis of embankments.

The inertial forces are expressed as:

$$F_h = a_h \frac{W}{g} = k_h W \quad (2.20a)$$

$$F_v = a_v \frac{W}{g} = k_v W \quad (2.20b)$$

where  $a_h$  and  $a_v$  are the horizontal and vertical accelerations,  $W$  is the weight of the soil mass, and the ratio  $\frac{a_h}{g}$  is called seismic coefficient. The accelerations are usually

given by building codes according to the site of interest, soil properties, and topographic features. The stability is evaluated by solving the equilibrium equations, using the classical methods of slope stability analysis, with the addition of inertial forces. A notable solution of the method is that by Sarma (1973), who found the seismic coefficient for which the safety factor is equal to one. The method has the following limitations: (1) the dynamic loading is not constant but varies in time and direction; (2) the soil properties remain constant (i.e. a rigid perfectly plastic constitutive model) while in reality they may change depending on the seismic intensity; (3) the method implies failure if the safety factor is less than one, but it actually changes over time; (4) the method is suitable to only analyze global stability failure mechanisms (Kramer, 1996). Despite these limitations, the method is still used to perform simplified analyses and to evaluate the safety factor.

#### 2.4.2 Newmark sliding block analysis

The Newmark method is a pseudo-dynamic analysis that removes limitations (1) and (3) of the pseudo-static approach discussed in the previous section. The purpose of this method is to estimate the displacements that occur due to dynamic loading and not the overall stability. The assumption is that when the inertial forces are greater than the soil resistance (i.e., when the safety factor is less than 1), permanent displacements occur. The resistance is expressed by the yield acceleration  $a_y$ , which is the acceleration that causes a safety factor of one (evaluated from limit equilibrium methods such as Sarma's). Then, the  $a_y$  is compared to the acceleration time history (hence the caption pseudo-dynamic method) to evaluate the relative velocity and displacement by integration. The last value corresponds to the permanent displacement of the embankment (Figure 2.7).

The limitations of the Newmark's method are: (1) it does not take into account the deformability of the soil (i.e. a rigid perfectly plastic model like the pseudo-static approach); (2) the assumption of rigid body implies displacements along the failure surface to be in phase; hence, the method cannot work for high-frequency ground motions; (3) if the soil is saturated possible excess pore water pressures are not taken in to account.

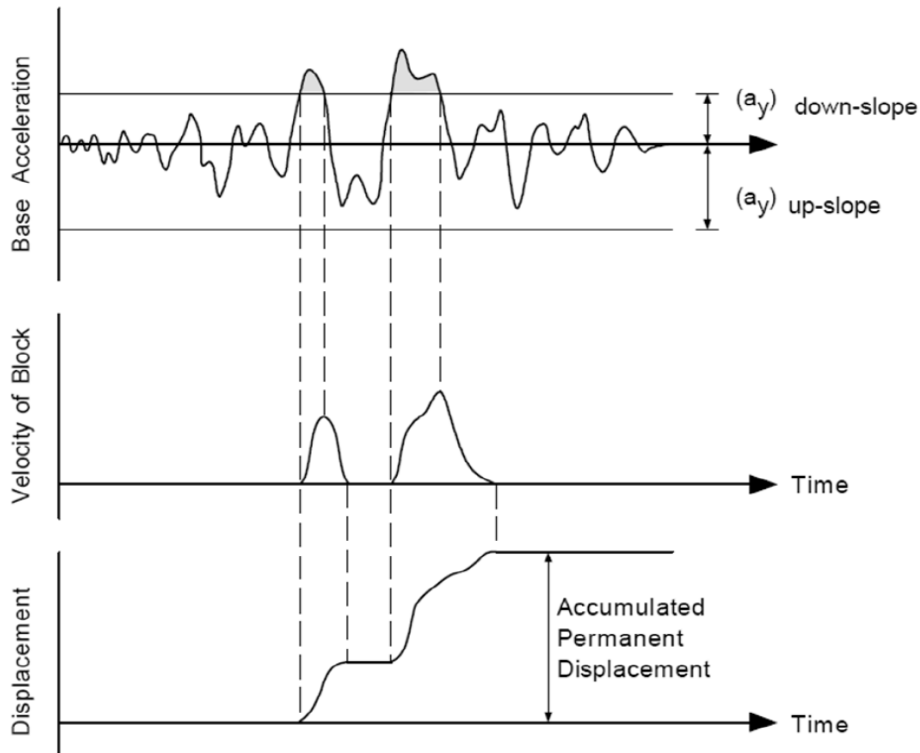


Figure 2.7: Schematization of the Newmark's sliding block method (Wilson e Keefer, 1985).

#### 2.4.2.1 Extensions and simplified Newmark methods

The deformability of earth dams has been taken into account by Seed and Martin (1966) and later by Makdisi and Seed (1978), who proposed a decoupled approach. First, a simplified dynamic analysis with a finite element software is performed to estimate the accelerations along the failure surface. Then, the accelerations are integrated as per the Newmark's method, to evaluate permanent displacements. Makdisi and Seed proposed a chart for the direct estimation of the displacements as a function of the ratio of the yield to the maximum acceleration, and of the fundamental period of the dam (Figure 2.8). However, Chopra and Zhang (1991) and Rathje and Bray (1999) show that the decoupled approach may lead to unconservative results. Other authors (e.g. Franklin and Chang, 1977, and Bray and Travararou, 2007) used the sliding block analysis to build an empirical relationship between the permanent displacements and several input motion parameters (e.g., significant duration and maximum acceleration). These equations can be used to calculate a rough estimate of the permanent displacements, but they should be used with caution.



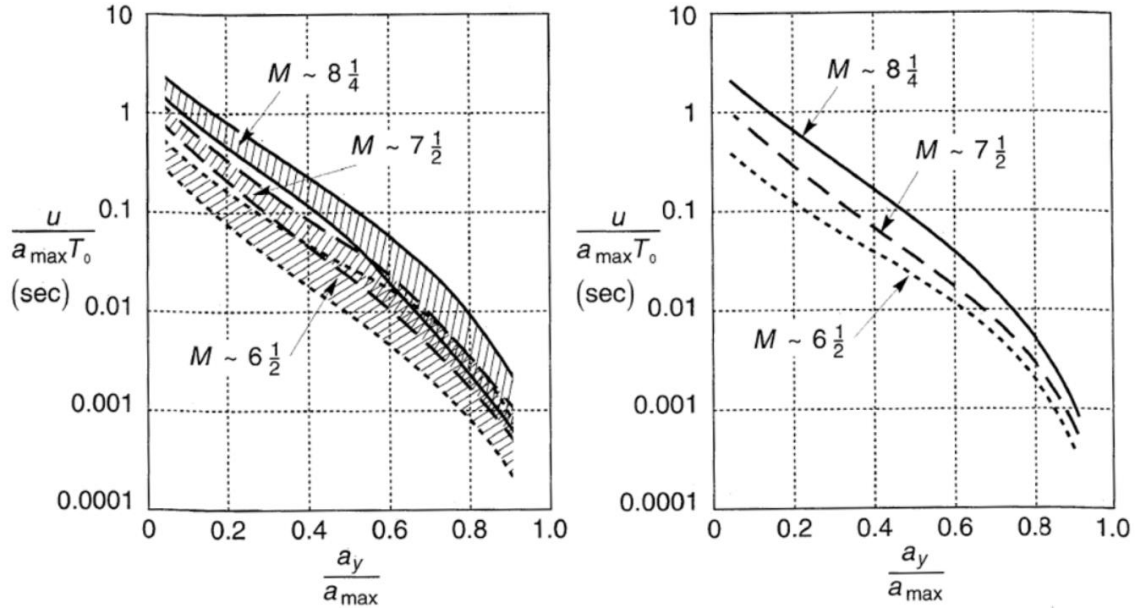


Figure 2.8: Variation of the normalized permanent displacements based on the yield acceleration ratio, for several magnitudes (Kramer, 1996).

The main limitations of these methods are: (1) high level of uncertainties in the cumulative displacement estimation using ground motion parameters, and (2) they are response displacement models based on a 1-D geometry. This is why in the last ten years efforts have been made to overcome issue (1), by adopting a probabilistic approach. Thus, instead of the single displacement value, we compute the probability that the displacement will be exceeded for a certain hazard level (i.e., the same concept behind the PSHA described in § 2.1). Rathje and Saygili (2011) proposed a pseudo-probabilistic approach to estimate the permanent displacements. In particular, their equation depends on the yield acceleration over PGA ratio, PGV, and magnitude, and are based on a large dataset of earthquake ground motions and computed displacements. More recently, Tropeano et al. (2017) proposed an uncoupled procedure to estimate permanent displacements of slopes in seismic condition. The authors adapted the approach proposed by Bray and Rathje (1998) for Italian events. Similarly, Gaudio et al. (2020) developed semi-empirical relationships to assess the seismic performance of slopes using an updated Italian strong-motion database. These two methods relies upon probabilistic approaches, which allow for the estimate of the probability that the permanent displacement will be exceeded for a certain hazard level. Hence, site-specific hazard curves can be constructed and the seismic risk can be estimated. The

advantage of these methods is that they require few seismic input parameters if compared against more complex models.

Such probabilistic versions of the method, however, are still based on models that can faithfully reproduce 1-D geometries. Overall, these methods are very useful for slope stability analyses, but for earth dams, they are sufficient only if the main damage mechanism is the global instability.

#### 2.4.3 Shear beam methodology

The previous family of methodologies provide useful information, but they do not explicitly take into account the dynamic behavior of the soil and input motion. An alternative is the shear beam method, which allows for: (1) the estimation of the fundamental periods of the dam in closed form solutions for different geometries; (2) the amplification functions between the dam crest and the base. A notable solution is given by Dakoulas and Gazetas (1985) for earth dams whose shear modulus changes with depth as:

$$\bar{G}(z) = G_b \left( \frac{z}{H} \right)^m \quad (2.21)$$

where  $G_b$  is the shear modulus at the base of the dam,  $H$  is the dam height plus an amount  $h$  given by a graphical construction (see Figure 2.9), and  $m$  is a coefficient of heterogeneity. The  $m$  value depends on the geometry and on the stiffness of the dam, and it usually varies between 0.3 and 0.8.

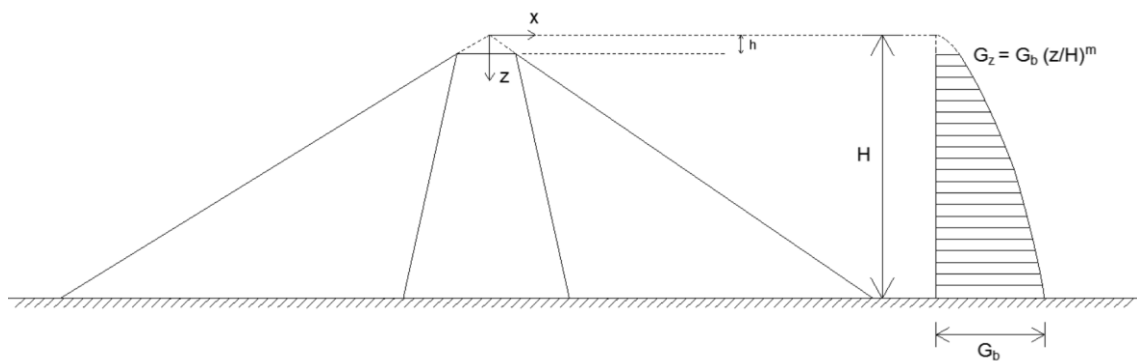


Figure 2.9: Variation of the shear modulus in the earth dam in Dakoulas and Gazetas (1985) solution.

Dakoulas and Gazetas (1985, 1987) provide a closed form solution of the wave equation for a 2D analysis of earth dams; the result is the horizontal displacements function along the vertical axis and during time. The solution depends on the modal

shapes  $\psi_n(z)$  and on  $I_n(t)$ , which is the single degree of freedom response of a system subjected to the input motion of interest.

$$u(z, t) = \sum_{i=1}^N \psi_n(z) I_n(t) \quad (2.22)$$

$$\psi_n(z) = \left(\frac{z}{H}\right)^{-\frac{m}{2}} J_q \left[ \beta_n \left(\frac{z}{H}\right)^{1-\frac{m}{2}} \right] \quad (2.23)$$

where  $J_q$  is the Bessel function of the first order and  $\beta_n$  is a parameter that depends on the coefficient  $m$ , given by the authors in tabular form. From the displacement solution, the amplification functions and fundamental periods can be derived as:

$$T_n = \frac{16\pi}{(4+m)(2+m)\beta_n} \frac{H}{\bar{V}_s} \quad (2.24)$$

where  $\bar{V}_s$  is the average shear wave velocity in the dam, estimated as:

$$\bar{V}_s = \frac{4}{4+m} \frac{1 - \lambda^{2+\frac{m}{2}}}{1 - \lambda^2} C_b \quad (2.25)$$

$C_b$  is the shear wave velocity at the base of the dam, and  $\lambda$  is the truncation ratio, calculated as the ratio  $\frac{h}{H}$  according to the graphical construction reported in Figure 2.9 above. These periods ( $T_n$ ) are typically underestimated if compared to numerical models (i.e. finite element methods or finite difference methods) but they still provide useful information if no direct measurements are available (e.g., Zimmaro and Ausilio, 2020). Furthermore, Gazetas and Dakoulas (1992) provides fundamental periods of 3D dams by considering dams located inside a canyon.

The main limitation of the shear beam approach is that it considers a 1D propagation of the wave and simplifies the stress distribution within the dam. In addition, closed form solutions are available only for a linear elastic or viscoelastic material. If nonlinearity is expected (e.g., when strong earthquakes affect the dam) numerical shear beam approaches should be considered (Elgamal et al., 1987b, Yiagos and Prevost, 1991b). These methods are based on numerical elasto-plastic analyses that uses advanced constitutive models (e.g., Prevost, 1977) that can estimate the nonlinear response of soil. However, the calibration of these models can be quite cumbersome and they do not always take in to consideration boundary problems

(e.g. complex interfaces between layers or complex geometry). Hence, in this case it is better to use numerical continuum approaches, such as the finite difference method or the finite element method. An application of these continuum approaches is the Nonlinear Deformation Analysis presented in the following section.

#### 2.4.4 Nonlinear Deformation Analysis (NDA)

In the past decade, Nonlinear Deformation Analyses (NDA) have become quite popular for seismic analyses of embankments dams (e.g., Boulanger et al., 2015, Boulanger and Beaty, 2016). Similar to the application of most advanced numerical modeling approaches, the choice of using NDAs depends on the specific problem at hand and the goal of the analysis, the data available, and on the constitutive model availability and applicability. NDAs are capable of providing numerous information regarding the dynamic behavior of earth dams. The main advantage is the ability to examine all the Potential Failure Modes (PFM) or damage mechanisms that an earth dam can suffer. In fact, PFM analyses have been used for several risk analyses (USACE, 2011) to identify site-specific damage mechanisms and their evolution in time. One of the main PFM that a NDA can examine is liquefaction- or strain softening-induced failure and the associated strain patterns. These phenomena are typically treated by using empirical correlations based on in-situ tests (e.g. Standard Penetration Test, SPT, and Cone Penetration Test, CPT, as described in §2.5.3) but such approaches do not consider the failure mode in its entirety. In fact, deformations due to liquefaction can affect the dam body as well as the foundation layers, and it is not trivial to analyze the failure mechanism and its progression. NDAs provide insights on the strain pattern, the influence of the progressive damage mechanism, the interaction between the embankment and other structures, and on the modification of the ground motion. In addition, NDAs can facilitate sensitivity studies, which have the potential to reduce some of the uncertainties. However, even though NDAs can theoretically provide more realistic responses compared to other methodologies, there are several concerns regarding their application. In fact, NDA results can vary greatly depending on the user, even if the tools used (numerical platform and constitutive model) are the same (Perlea and Beaty, 2010; Finn and Wu, 2013; Boulanger and Ziotopoulou, 2018). This is due to the numerous parameters and factors (technical and nontechnical) that affect the NDA process. Hence, the NDA method should be validated based on the tools and on the protocols used to perform the analysis. A summary and explanation of these factors is reported below, while more details can be found in Boulanger et al. (2015), and

Boulanger and Beaty (2016). In this dissertation, NDAs are exploited and the following factors are considered.

#### 1) Selection, validation, and calibration of the constitutive models

The choice of the constitutive model must be based on its capability to approximate the soil behaviors of interest to the problem at hand. The strength and limitations of each model adopted should be documented and taken into account when analyzing the results (e.g., a model could be well-suited for dynamic but not for static analysis).

The validation of the constitutive model concerns the physics of a problem and its underlying equations. Case histories and physical models are usually a good way to validate the model (i.e., the results should be consistent with observed field performances). For constitutive models for liquefiable materials, this means comparing single-element simulations with experimental and empirical relationships (e.g., Ishihara, 1996). If the results are in the range of responses observed, then the model can be considered capable of representing the physics of the problem. For earth dams susceptible to liquefaction, the interest lies in: (1) modulus reduction and damping curves, which control the dynamic behavior of the material before liquefaction; (2) excess pore water pressure generation (conversely the contractive behavior of the material), which affects the onset of liquefaction-induced deformations; (3) the accumulation of shear strains after liquefaction is triggered in dense-of-critical sands (cyclic mobility); (4) the residual shear strength after the earthquake and after liquefaction has occurred, which controls the post-seismic strains and stability.

The calibration process is essentially an iterative process wherein the constitutive model's parameters are varied until the desired response is obtained. It should be noted that the calibration and in-situ characterization are separate entities, and that any problem that may arise due to in-situ tests cannot be solved by the calibration process. Thus, the focus of the calibration should be placed on the uncertainty of the parameters and on the aspects that can be modeled. The analyst should carefully examine whether a model calibrated via single-element simulations can work well across the range of operating conditions in the broader system-level analysis (e.g. same soil under level and sloping ground, or same soil under varying overburden stresses). Depending on the ability of the model to perform well under a broad range of conditions or not, more calibrations may be warranted.

## 2) Numerical modeling and input ground motions

The results of NDAs strongly depend on the details of the numerical model and on the software (e.g. the choice of the boundary conditions and the way the software solves the equations amongst many others). In addition, dynamic analyses results depend on the initial state of stress, after the static analysis. Hence, the static phase procedure affects the overall results (e.g., how the pore water pressure distribution has been evaluated), so care must be taken in analyzing the initial state of stress. This is done by evaluating the vertical and horizontal effective stresses, the coefficient of lateral earth pressure  $K_0$ , and the static shear stress ratio  $\alpha$ . These quantities must be consistent with the variations across material zones and beneath the abutments.

The ground motions used should be hazard-consistent and sufficiently numerous (seven is a typical number) to estimate the average response. The method used to apply the ground motion at the base of the model can also influence the NDAs results (e.g. using outcrop motions with an elastic halfspace or within motions with rigid bedrock).

## 3) Site characterization and data uncertainty

The quality of the site characterization and geotechnical investigation will always influence the analyses, regardless of the method used. In NDAs, however, the effect is even more accentuated, because of the numerous parameters needed, the material nonlinearity involved, and the computation effort required. Ideally, the site investigation and the numerical solution should be informing each other. In fact, repeating NDAs for different site characterization values is both time consuming and can lead to different conclusions. Hence, NDAs should not be used without a comprehensive field investigation and a proper geotechnical characterization. In addition, even when several tests are available, the uncertainties in the data should be accounted for. For liquefaction analyses, this could mean estimating the cyclic strength and its variation due to the uncertainties in the field tests and in the empirical relationships (e.g. SPT energy correction and fines content of the soil).

### 2.5 Damage mechanisms in embankment dams

In this section, potential damage mechanisms of earth dams are briefly presented and their assessment is discussed. Particular emphasis is given to damage

mechanisms induced by dynamic actions, but damage mechanisms under static conditions are also analyzed. Seismic response of earth dams and their damage measure (DM) depend on the static stress state prior to the earthquake, thus three conditions should be addressed in the evaluation of the seismic performance of these structures: (a) pre-seismic; (b) seismic; (c) post-seismic phase. The problem is quite complex, because damage mechanisms are usually correlated and can occur in any on these three stages. For instance, if an internal erosion process begins shortly after construction, some cracks can occur during static conditions (but not causing any collapse). Then, an earthquake could generate large strains in the dam body and turn the cracks into even larger passageways for the water. Furthermore, the seismic shaking could produce excess pore pressure that dissipates over time, reducing the strength of the materials. All these factors could lead to total collapse in the post seismic stage. A risk analysis or seismic assessment of the embankment should consider their consequentiality and contemporaneity (this type of analysis is often called Potential Failure Modes Analysis, PFMA, Boulanger et al., 2015), despite being more convenient to treat the damage mechanisms by themselves. One way of doing so could be simulating the construction process of the dam, the groundwater flow, the dynamic action, and the pore pressure dissipation, while monitoring parameters such as crest displacement, strains, and pore pressure within the dam body. The most popular tool to perform these type of calculations is the Nonlinear Deformation Analysis (NDA). These types of analysis can describe complex soil behaviors by using simple and/or advanced constitutive models, thus giving insights into the deformation patterns and on the potential modes of failure of the dam.

The effects of ground motion shaking on earth dams can be grouped into three main categories: (1) permanent displacements; (2) internal erosion; (3) liquefaction-induced deformations. The following sections illustrate the effects of these damage mechanisms by considering some notable case histories. In addition, a brief description of the performance of earth dams is reported, set in the general framework of embankment performance. Guideline documents of several countries, including the NTD14 in Italy, list all the limit states related to earth dams, but they do not always provide precise and quantifiable criteria for safety assessment (Pagano et al., 2019). There is a certain freedom in assigning an exceedance of a limit state, based mostly on engineering judgement. However, this may be unavoidable,

as every dam is different and general criteria for limit states acceptability may not be consistent.

#### 2.5.1 Global instability, internal erosion, and filters damage

##### 2.5.1.1 Global instability

Slope instability and permanent displacements is probably the most common damage mechanism observed in earth dams after an earthquake (Pelecanos, 2013). Some of the dams that experienced global instability, but not complete failure, are: La Villita dam, El Infiernillo dams (Reséndiz et al., 1982, Sica et al., 2002), and Fategadh dam (Madabhushi and Haigh, 2001). Most of the times the displacements are concentrated in the upstream shell and crest, due to the lower effective stresses caused by the presence of the reservoir, and hence lower shear strengths. Slope instability can cause the loss of freeboard and differential settlements, which could lead to overtopping and cracks. Thus, one of the damage measure for global instability is the permanent displacement measured on a well-defined failure surface. There are no unique limits for the embankment admissible performance, but a typical value can be a one-meter displacement, defined by earlier documents (e.g., Franklin and Chang, 1977, Seed, 1979) as the typical thickness of filter thicknesses. In reality, the acceptable displacements depend on the specific dam type, geometry, and freeboard (Hynes-Griffin and Franklin, 1984).

##### 2.5.1.2 Internal erosion

Under static conditions, internal erosion is the most common failure mode of earth dams. Several authors (e.g., Foster et al., 2000a, Fell et al., 2014) analyzed dam failures for structures constructed between 1800 and 1986 and studied their statistics. They concluded that erosion is the cause of about half of earth dam failures where the cause of collapse is known. Temporally, half of all incidents have occurred after 5 years of operation, with the reservoir level at its maximum. Failures due to earthquakes comprises the 1.7% of their database; Table 2.1 reports the results obtained by the authors.

The erosion process takes place in two ways (1) erosion through the embankment; (2) erosion through the foundation. In general, each process can be divided into four steps: (1) the initiation, (2) continuation, (3) progression and pipe formation, and (4) initiation of a breach (Fell, 2014). The initiation concerns the beginning of soil erosion (e.g., a concentrated leak leading to uncontrolled seepage). Coarse graded



soils with a plasticity index less than 7 are the most vulnerable to erosion (Fell et al. 2008; Fell and Fry, 2013; Wan and Fell, 2004c, 2007, 2008). The continuation refers to transition zones within the dam that are capable of stopping the erosion (e.g., filters, as described later in this section). The progression concerns the pipe formation and its stability (Xu and Zhang, 2013). Foster and Fell (1999a) found that the most important factors for the pipe stability are fines content of the soil, degree of saturation, degree of compaction, and reservoir operation. The breach is the final step of the erosion process and can cause sinkholes, unravelling of the toe, and downstream slope instability. Figure 2.10 shows a schematization of the erosion process and the effects it can cause. The erosion through the embankment comprises the movement of soil particles caused by the groundwater flow, both in the dam body and in the adjacent structures.

*Table 2.1: Overall statistics of embankment dam failures, large embankment dams, up to 1986 and excluding dams constructed in Japan pre 1930 and in China (adapted from Fell et al., 2014).*

<b>Mode of failure</b>	<b>Number of cases</b>		<b>% Failures (where known)</b>		<b>Average probability of failure (<math>10^{-3}</math>)</b>	
	<b>All failures</b>	<b>Failures in operation</b>	<b>All failures</b>	<b>Failures in operation</b>	<b>All failures</b>	<b>Failures in operation</b>
Inadequate spillway capacity	46	40	36	34	4	3.5
Malfunction of gate	16	15	12	13	1.5	1.5
Subtotal overtopping and appurtenant failures	62	55	48	47	5.5	5
Internal erosion through embankment	39	38	30	33	3.5	3.5
Internal erosion through foundation	19	18	15	15	1.5	1.5
Internal erosion from embankment into foundation	2	2	1.5	1.5	0.2	0.2
Subtotal internal erosion(1)	59	57	46.5	48.5	5	5
Downstream slides	6	4	5	3.5	0.5	0.4
Upstream slides	1	1	1	1	0.1	0.1
Subtotal slides	7	5	6	4.5	0.6	0.5
Earthquake/liquefaction	2	2	1.5	1.5	0.2	0.2
Unknown mode	8	7				
Total no. of failures(1)	136	124			12	11
Total no. of failures (where mode of failure known)	128	117				
No. of embankment dams	11192	11192				
Notes:(1) Subtotals and totals do not necessarily sum to 100% as some failures were classified as multiple modes of failures						

Sherard (1973) and Fell and Fry (2013) suggest that hydraulic fracture can occur if the water pressure in the embankment is greater than the minor principal total stress plus the tensile strength:

$$u \geq \sigma_{min} + \sigma_t \quad (2.26)$$

If Eq. 2.26 is verified, the erosion process is initiated and usually it progresses from upstream to downstream. The erosion through the foundation can occur when the hydraulic gradient is high, and can cause piping at the dam toe. This results in the annulment of the effective stresses, leading to sinkholes and slope instability. Cut-off walls are typically used to avoid the groundwater flow beneath the dam body. The estimation of the critical hydraulic gradient is the classic way to evaluate the safety factor concerning piping.

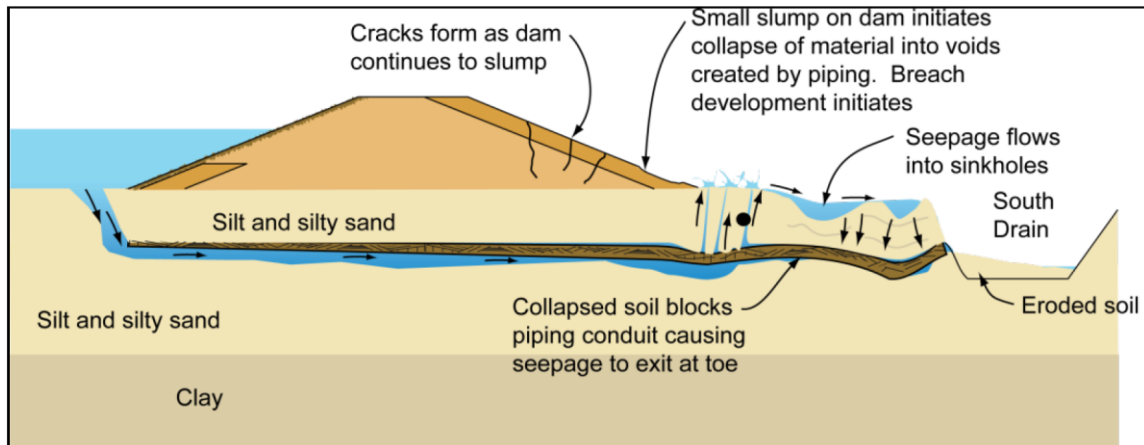


Figure 2.10: Effects of the erosion process in an embankment (from FEMA P-1032, 2015).

The statistics of Table 2.1 by themselves seem to suggest that the erosion is a static problem only. However, this is not the case, as the ground motion shaking can induce longitudinal and transverse cracking in the embankment (Figure 2.11). Earthquakes can cause differential settlements between the crest and the foundation, leading to the formation of cracking (Vick et al 1993). The cracks are caused by the low tensile strength of the embankment materials and are likely to open near area characterized by high stiffness contrasts (e.g., embankment and spillway structures). When this happens, the seepage inside of the embankment is modified and the erosion process begins. The evolution is the same as that described earlier in this section but in this case, the main cause is the ground shaking.



*Figure 2.11: Longitudinal crack observed in Coihueco dam (from Séco and Pinto, 2015).*

#### 2.5.1.3 Filters integrity

Dam filters are the elements of the embankment that control and stop soil particles movements due to flow-related dragging forces. The usefulness of filters and their design have been thoroughly assessed (Sherard and Dunnigan, 1985; Foster and Fell 2001). If modern design standards are used (e.g., U.S. Department of the Interior, Bureau of Reclamation, 2011) then the filters are perfectly capable of stopping the erosion and discharge the seepage flow without excessive build-up of hydraulic head. The filters are typically designed using grain size distribution curves, and they need to be fine enough to stop the erosion, and coarse enough to let the water flow (Figure 2.12). Under seismic conditions, however, modern standards suggest that the filter size should be at least twice the expected deformation. For existing dams, this would mean that the permanent displacement should be less than half the filter size. As an alternative, Seed (1979) suggested to use a limiting value equal to the filter size (typically 1m). If this condition is not verified, then the filter is damaged and it cannot perform its original task. In this case, the erosion continues to progress, leading to a breach. Hence, under seismic conditions, estimating the filters displacements is a good indicator for the erosion progress after initiation.

#### 2.5.1.4 Discussion and comments

A detailed analysis of the erosion phenomenon should take in to account the four steps of the process, described above, and its progression. However, some general and conservative considerations can be made.

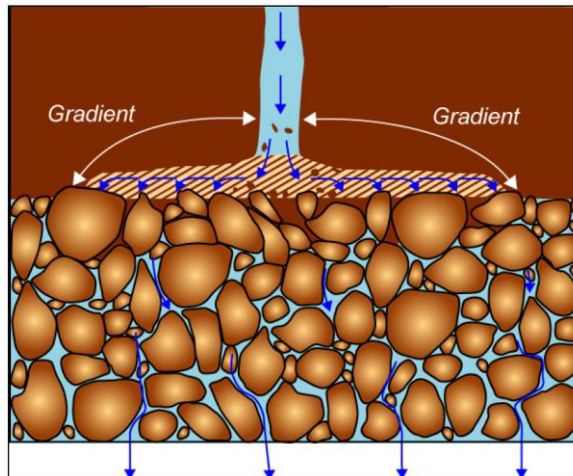


Figure 2.12: Schematization of the filters function (coarse material) which block the soil erosion from the above crack. The hydraulic gradient is reduced as the length of the blocked soil increases (U.S. Department of the Interior, Bureau of Reclamation, 2011).

If the erosion is initiated and it is not known if the process can be stopped (e.g., insufficient data), a breach event can easily be assumed (i.e., 46% of large dam failures were caused by piping and erosion). In this dissertation, the assessment of the erosion process is performed by estimating the filters integrity. If cracks are formed and the filters cannot stop the erosion, then a breach is assumed.

Overall, the performance of earth dams due to earthquakes is quite good (Ishihara, 2010, USSD, 2014; Seco e Pinto, 2015). On a global scale, the number of dams heavily damaged because of severe ground motions is limited (mostly tailings and hydraulics fill dams). However, these conclusions cannot be generalized, as the performance of the dam also depends on the material used, the dam type, the construction process, and the dam age. This is important in places where seismic hazard is continuously updated as new information about seismogenic sources are gathered (e.g., Italy). In this case, dams are subjected to seismic loadings that are more intense compared to those used in their original design (Lanzo, 2018).

### 2.5.2 Empirical methodologies for assessing deformations and cracks

There are several analytical methods to estimate deformations that occur in earth dams after and during an earthquake (§2.4). However, empirical methodologies based on real case histories can be extremely useful to obtain a quick estimate of the deformations. In addition, these methods allow for the estimation of the likelihood of occurrence and amplitude of various damage types. The most common empirical procedures are those by Fell et al. (2008) and by Swaisgood (2014). Both methods

are based on extensive investigations of damage observed in earth dams after an earthquake. However, both procedures are not valid if liquefaction occurs in the foundation or in the dam body. In that case, specific methods should be used to assess liquefaction induced deformations (e.g. §2.4.4, §2.5.3.1).

Pells and Fell (2002, 2003) gathered data from 305 dams, where 95 of them experienced longitudinal and transverse cracks. The authors used those case histories to define damage classes based on the crest settlement and to estimate crack widths. Table 2.2 reports damage class descriptions, while Figure 2.13 shows damage class boundaries as a function of the seismic hazard level. The methodology by Pells and Fell (2002) can be exploited in two different ways: (1) estimation of the damage class based on the seismic hazard (the damage class that the earth dam can experience is estimated from the expected magnitude and PGA, as per Figure 2.13), and (2) numerical results of NDA, which can compute the crest settlement of the site-specific dam. Then, this value is used to evaluate its corresponding damage class, as per Table 2.2. In this dissertation, method (2) is adopted to define fragility functions (§ 7.2.1).

Table 2.2: Damage classes for embankment dams under earthquake loading (adapted from Fell et al., 2014).

Damage Class		Maximum longitudinal crack width <sup>(1)</sup> [mm]	Maximum relative crest settlement <sup>(2)</sup> [%]
Number	Description		
0	None or slight	< 10	≤ 0.03
1	Minor	10 < w ≤ 30	0.03 - 0.2
2	Moderate	30 < w ≤ 80	0.2 - 0.5
3	Major	80 < w ≤ 150	0.5 - 1.5
4	Severe	150 < w ≤ 500	1.5 - 5
5	Collapse	> 500	> 5

(1): Maximum crack width is taken as the maximum width, in millimeters, of any longitudinal cracking that occurs.  
(2) Maximum relative crest settlement is expressed as a percentage of the maximum dam height (from general foundation to the dam crest).

The Swaisgood empirical methodology (1998, 2003, and 2014) is based on the case histories of seismic-induced settlement where the ground motion caused the dam body to deform according to Figure 2.14. The crest settlement is normalized by the dam height and foundation thickness as:

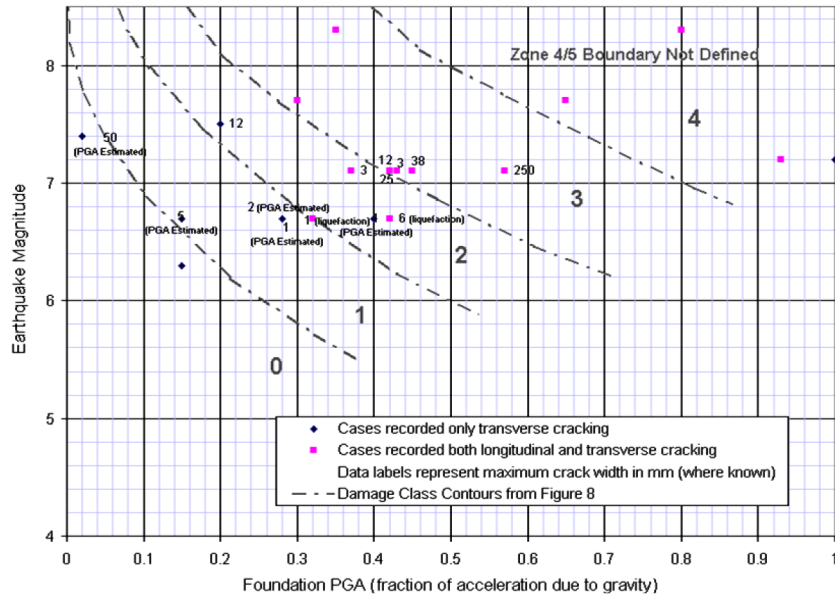


Figure 2.13: Incidence of transverse cracking and damage classes boundaries for earthfill dams in function of the seismic hazard (from Pells and Fell, 2002).

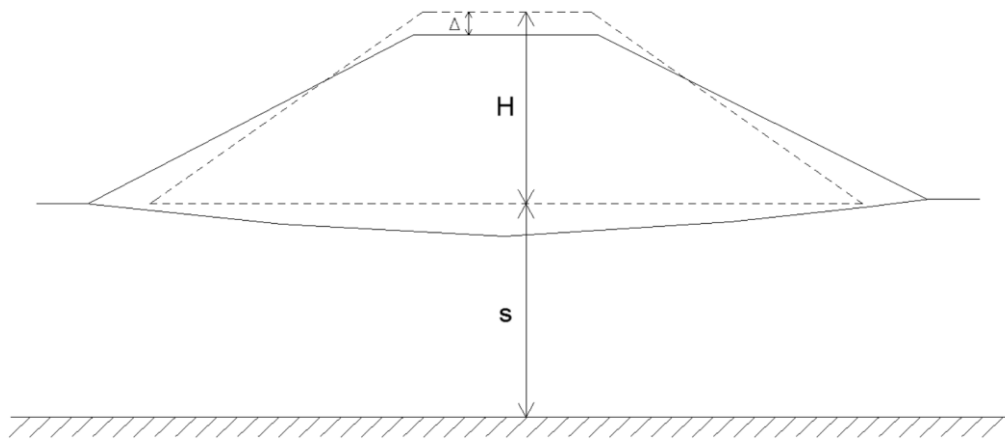


Figure 2.14: Schematization used by Swaisgood to define the Normalized Crest Settlement.

$$NCS = \frac{\Delta}{H + s} \cdot 100\% \quad (2.27)$$

where  $NCS$  stands for Normalized Crest Settlement,  $\Delta$  is the mean vertical settlement of the crest,  $H$  is the dam height, and  $s$  is the foundation thickness. As with the Fell methodology, the damage parameter is related to the seismic hazard (i.e. moment magnitude  $M_w$  and PGA) and it can be used in two ways. The first is a predictive equation (Figure 2.15):

$$NCS = e^{5.7PGA + 0.471M_w - 7.22} \quad (2.28)$$

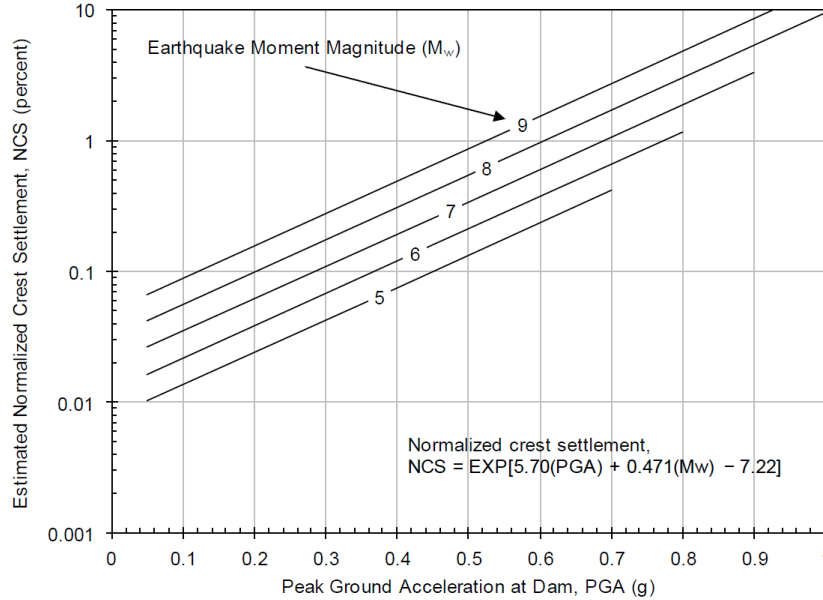


Figure 2.15: Estimated Normalized Crest Settlement (Swaisgood, 2014).

The second method is to compute the  $NCS$  from (Eq. 2.27) based on the results of the nonlinear deformation analyses. In this dissertation, this latter method is adopted. The limitation of this methodology is that there are no case histories of dam sites experiencing  $PGA$  greater than  $0.7g$  and  $NCS$  greater than  $5\%$ . The San Fernando, Masiway, and Hebgen dams reported in Figure 2.16 were subjected to liquefaction and they are not used for  $NCS$  predictions.

### 2.5.3 Cyclic ground failure phenomena

Liquefaction is one of the most dangerous ground failure phenomena that can occur in earth dams. Soil liquefaction causes the temporary reduction of shear strength and the development of deformations caused by excess pore water pressure build up. Damage mechanisms caused by liquefaction comprise all failure modes discussed in previous sections. In fact, shear strength reduction due to intense shaking can occur in the dam body, the foundation, and any surrounding areas that can affect the dam.



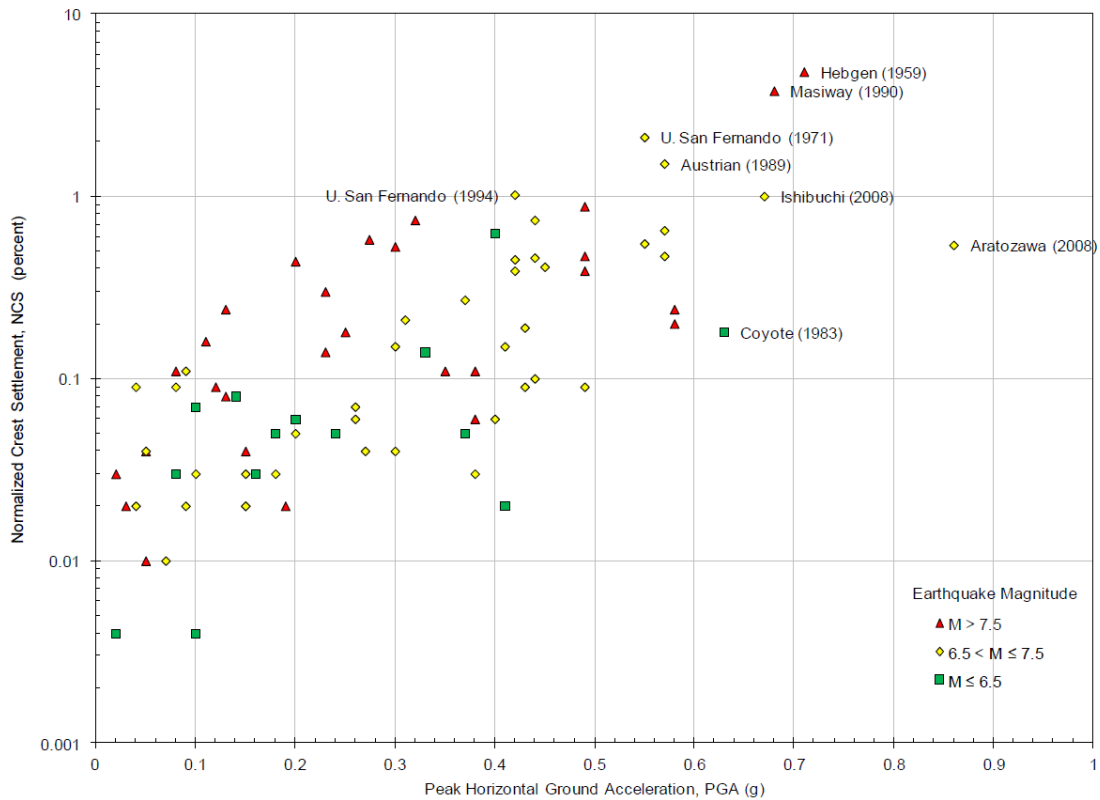


Figure 2.16: Normalized Crest Settlement for the case histories studied by Swaisgood (Swaisgood, 2014).

This can result in slope instability, crest settlement, and thus potential overtopping. However, even if the deformations are not sufficient to cause complete failure, they can still cause cracks and concentrated leaks, leading to erosion. The same considerations can be made if the liquefiable soil is the alluvial foundation. In that case, deformations can cause differential settlements and seepage along outlet works and spillways. Effects of liquefaction phenomena in earth dams were observed in several cases. The most famous case history of an embankment subjected to liquefaction is certainly the Van Norman dam (i.e. lower San Fernando dam, Figure 2.17) following the **M6.6** 1971 San Fernando, California earthquake. The dam experienced intense deformations but not total collapse, due to the reservoir level being low at that time (Seed et al. 1975; Beaty and Byrne, 2001; Chowdhury et al. 2018).

Other case histories comprise the Austrian dam, which experienced large cracks during the **M6.6** 1989 Loma Prieta, California earthquake (Boulanger, 2019), and the Sheffield dam failure during the **M6.8** 1925 Santa Barbara, California earthquake (Seed et al. 1969). More recently, the Fujinuma-Ike dam during the **M9.1** 2011 Tohoku earthquake in Japan experienced total collapse 20 minutes after the end of



the ground shaking (Figure 2.18). There are several reasons for the Fujinuma-Ike dam collapse (Pradel et al., 2013) but liquefaction and associated shear strength reduction played a major role (Ono et al., 2011).



*Figure 2.17: Lower San Fernando dam after the 1971 San Fernando earthquake (from Boulanger et al., 2015).*



*Figure 2.18: Fujinuma-Ike dam after the 2011 Tohoku earthquake (Matsumoto et al., 2011).*

Other liquefaction potential failures modes concern the aftermath of the earthquake. In particular, when excess pore water pressures are developed, they tend to dissipate after the end of the ground motion. This results in deformations that are added to those caused by the inertia-driven actions, leading to potential free board loss. In addition, delayed overtopping can occur if the deformations caused damage to the outlet works that control the reservoir level (e.g., repairs of the dam cannot be completed before the next flood). Furthermore, delayed effects may also be present when liquefaction-related void redistribution phenomena occur (Malvick et al., 2006).

It seems clear that if an earth dam has liquefaction potential, the effects can be catastrophic. Hence, liquefaction susceptibility, triggering, and consequences must always be assessed when performing seismic analysis of earth dams. Advanced methods of liquefaction analysis include the NDA (§ 2.4.4), but more simplified approaches can be used before performing complex numerical analyses. In addition, some of the parameters required by advanced constitutive models are based on liquefaction triggering semi-empirical methods; hence, their importance is prominent even when using advanced models. The following section briefly illustrates modern semi-empirical methodologies to perform liquefaction susceptibility and triggering analysis.

#### 2.5.3.1 Empirical methodologies for liquefaction susceptibility and triggering analysis

The first step of liquefaction potential analysis is to establish whether the soils being analyzed are actually susceptible to liquefaction. Several conditions need to be met in order to have the potential of soil liquefaction. Youd and Perkins (1978) report the likelihood of liquefaction for cohesionless sediments, based on the age and type of the deposit. Cohesive soils can also experience large deformations due to cyclic loading (e.g., sensitive clay deposits), but in this case the term cyclic softening is used instead of liquefaction. Both terms refer to the development of large strains caused by the excess pore water pressure, but they differ in the strength characteristics of the soils involved. Thus, geological setting information can give valuable information on the liquefaction potential of a deposit.

Nowadays, design standards provide criteria to assess liquefaction and cyclic softening susceptibility. For instance, according to the Italian Building Code (NTC 2018) further liquefaction analyses are not needed if one of the following conditions is met:

- 1) The maximum expected acceleration in free field condition is less than 0.1g;
- 2) The mean seasonal depth of the water table is greater than 15 m from the surface (for horizontal surfaces and shallow foundations);
- 3) The number of SPT for clean sand, corrected for energy and confinement stress ( $N_{160cs}$ ), is greater than 30; the cone tip resistance corrected for confinement stress ( $q_{C1Ncs}$ ) is greater than 180;
- 4) The grain size distribution curve is inside the range of soils susceptible to liquefaction (Figure 2.19).

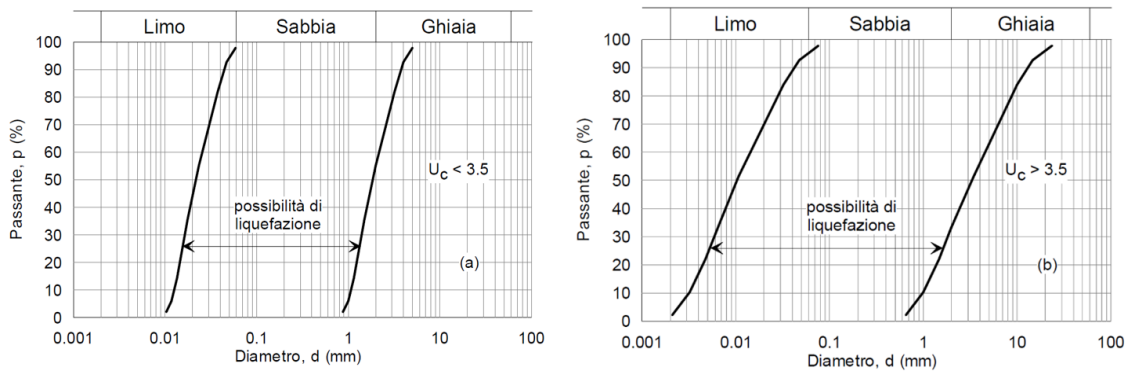


Figure 2.19: Grain size distribution-based criteria for liquefaction susceptibility for the Italian Building Code (from NTC18).

Liquefaction susceptibility criteria are often used to distinguish between soils that are potentially susceptible to liquefaction if shaken hard enough (i.e., sand-like) and soils that are not susceptible to liquefaction (i.e., clay-like). Cyclic ground failure phenomena can, however, also occur in clay-like materials even in presence of relatively high plasticity. In this case, the cyclic pore-pressure induced deformation phenomenon that can occur is less abrupt (more gradual) than liquefaction and it is commonly referred to as cyclic softening of clays. The first modern study on liquefaction susceptibility was performed in China by Wang (1979) using data the 1975 Haicheng and the 1976 Tangshan earthquakes. Wang (1979) observed that clay soils with  $< 15\text{--}20\%$  particles by weight smaller than 0.005 mm and having a water content to liquid limit ( $w/LL$ ) ratio larger than 0.9 can be classified as susceptible to liquefaction. Based on these observations, Seed and Idriss (1982) proposed that a material is deemed as susceptible to liquefaction if the following

conditions are met: (1) percent of particles less than 0.005 mm < 15%, (2) LL < 35, and (3) w/LL > 0.9. These criteria are known as “Chinese criteria.”

During the 1994 Northridge (California), 1999 Kocaeli (Turkey), and 1999 Chi-Chi (Taiwan) earthquakes, fine-grained soils that did not meet the Chinese criteria still liquefied. Bray and Sancio (2006) performed several cyclic tests on the soil retrieved in Adapazari that exhibited large strains during the 1999 Kocaeli earthquake and suggested the following liquefaction susceptibility criteria:

- The soil is susceptible if  $\frac{w}{LL} > 0.85$  and  $PI < 12$ ;
- The soil is moderately susceptible if  $\frac{w}{LL} > 0.80$  and  $PI < 18$  ;
- The soil is not susceptible if  $PI > 18$  (tests performed at low confining stresses).

They conclude, “...the agreement is sufficient to generalize the results from our comprehensive study of the Adapazari fine-grained soils to other fine grained soils.”

Boulanger and Idriss (2006) also performed laboratory-based studies. They developed liquefaction susceptibility criteria to distinguish between clay-like (or not susceptible) soils and sand-like (or susceptible) materials. The Boulanger and Idriss (2006) criteria define sand-like soils if  $PI < 7$  and the material plots below the A-line in the Atterberg limits chart. Clay-like soils are defined by Boulanger and Idriss (2006) as materials with  $PI > 7$ . These two modern criteria do not agree well. Furthermore, some differences in laboratory test protocols may also contribute to the differences. Chu et al. (2006) found that neither the Boulanger and Idriss (2006), not the Bray and Sancio (2006) methods are effective for the analysis of case histories from alluvial sites subjected to strong shaking during the 1999 Chi-Chi earthquake. That study showed that more advanced testing (such as strength normalization-based criteria) could lead to more accurate susceptibility assessments. However, these two susceptibility criteria still represent the state-of-the-art in liquefaction susceptibility.

Stress-based approaches are the most widely methods used to perform liquefaction triggering analysis (Seed and Idriss, 1971; Robertson and Wride, 1998; Idriss and Boulanger, 2008; Boulanger and Idriss, 2012 and 2016; Moss et al., 2006; Cetin et al., 2018; Kayen et al., 2013). The method works by comparing the earthquake induced shear stresses to the cyclic strength of the soil. The shear stresses are

usually normalized by the effective confining stress  $\sigma'_v$  to define a cyclic stress ratio (CSR). Seed and Idriss (1971) suggest the following expression to estimate the CSR:

$$CSR = \frac{\tau_{max}}{\sigma'_v} = 0.65 \frac{\sigma_v}{\sigma'_v} \frac{a_{max}}{g} r_d \quad (2.29)$$

$\tau_{max}$  is the maximum shear stress induced by the ground shaking,  $\sigma_v$  is the total vertical stress,  $a_{max}$  is the maximum horizontal acceleration at the ground surface, and  $r_d$  is a shear stress reduction factor (i.e. it takes in to account the deformation properties of the soil). The factor 0.65 is used to define the reference stress level, and it is related to the irregular acceleration time series (i.e. taking the 65% of the peak cyclic stress).

The cyclic resistance of soil is expressed as a cyclic resistance ratio (CRR) and can be estimated either in laboratory or with semi-empirical relationships. Laboratory tests, however, require field samples of the sand, obtainable by frozen sampling techniques, which are extremely expensive for regular applications. Hence, semi-empirical relationships are developed based on case histories where liquefaction was observed (or was not observed in liquefaction-prone areas), in relation to some *in situ* properties describing soil resistance (e.g., SPT, CPT, or  $V_s$  profiles). The most common tests used to estimate resistance characteristic of soil are the SPT, Cone Penetration Test (CPT), and geophysical tests to measure or estimate shear wave velocity profiles. As the number of case histories increases, so does the efficiency of the empirical relationships and the opportunity to define new site-specific correlations. The Next-Generation Liquefaction project (Brandenberg et al., 2019) is developing a new open-source and transparent database of liquefaction case histories (Zimmaro et al., 2019) that can be used, in the future, to build new and more reliable empirical or semi-empirical models.

Eq. 2.30 and 2.31 (Idriss and Boulanger, 2014) report the empirical relationships for standardized conditions of magnitude (7.5), confinement stress (1 atmosphere), and fines content (0%), while Figure 2.20 shows the limiting curve of liquefaction evidences using SPT data.

$$CRR_{M=7.5, \sigma'_v=1} = \exp \left[ \frac{(N_1)_{60cs}}{14.1} + \left( \frac{(N_1)_{60cs}}{126} \right)^2 - \left( \frac{(N_1)_{60cs}}{23.6} \right)^3 + \left( \frac{(N_1)_{60cs}}{25.4} \right)^4 - 2.8 \right] \quad (2.30)$$

$$CRR_{M=7.5, \sigma'_v=1} = \exp \left[ \frac{q_{c1Ncs}}{113} + \left( \frac{q_{c1Ncs}}{1000} \right)^2 - \left( \frac{q_{c1Ncs}}{140} \right)^3 + \left( \frac{q_{c1Ncs}}{137} \right)^4 - 2.8 \right] \quad (2.31)$$

$N_{160cs}$  and  $q_{c1Ncs}$  are the number of SPT for clean sands, corrected for energy and confinement stress and the cone tip resistance for clean sands corrected for confinement stress. They can be evaluated as:

$$(N_1)_{60cs} = (N_1)_{60} + \Delta(N_1)_{60} \quad (2.32)$$

$$q_{c1Ncs} = q_{c1N} + \Delta q_{c1N} \quad (2.33)$$

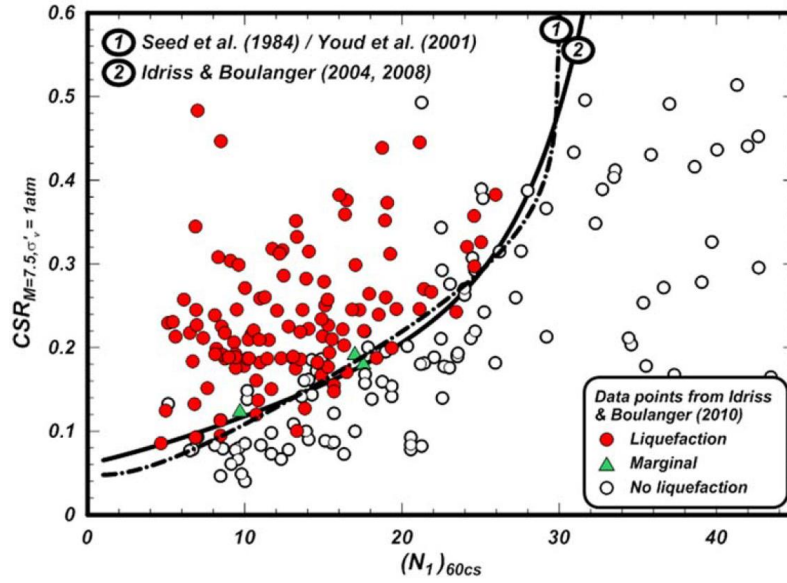


Figure 2.20: Correlations for cyclic resistance ratio from SPT data (from Idriss and Boulanger, 2010).

where  $\Delta(N_1)_{60}$  and  $\Delta q_{c1N}$  are the resistance increments due to the fines content,  $N_{160}$  is the number of SPT corrected for energy and confinement stress, and  $q_{c1N}$  is the cone tip resistance corrected for confinement stress. If the fines content of the soil increases, the liquefaction resistance curve shifts to the left. The increments can be estimated as:

$$\Delta(N_1)_{60} = \exp \left[ 1.63 + \frac{9.7}{FC + 0.01} - \left( \frac{15.7}{FC + 0.01} \right)^2 \right] \quad (2.34)$$

$$\Delta q_{c1N} = \left( 11.9 + \frac{q_{c1N}}{14.6} \right) \exp \left[ 1.63 + \frac{9.7}{FC + 2} - \left( \frac{15.7}{FC + 2} \right)^2 \right] \quad (2.35)$$

$FC$  is the fines content and it measure the clay fraction percentage. The  $N_{160}$  and  $q_{c1N}$  are determined as:

$$(N_1)_{60} = C_N N_{60} \quad (2.36)$$

$$q_{c1N} = C_N \frac{q_c}{p_a} \quad (2.37)$$

$C_N$  is the overburden correction factor,  $q_c$  is the measured tip resistance for unequal end area effects (Campanella et al., 1982), and  $N_{60}$  is the standardized value of the blow count.  $C_N$  can be determined from the Liao and Whitman (1986) relationship or from Idriss and Boulanger (2003b, 2008):

$$C_N = \left( \frac{p_a}{\sigma'_v} \right)^m \leq 1.7 \quad (2.38)$$

$$m = 1.338 - 0.249(q_{c1Ncs})^{0.264} \quad (2.39a)$$

$$m = 0.784 - 0.0768\sqrt{(N_1)_{60cs}} \quad (2.39b)$$

The  $m$  value estimated from Idriss and Boulanger (2008) requires an iterative procedure, while the Liao and Whitman (1986) relation uses a value of 0.5. The  $N_{60}$  value is usually the blow count corrected for the energy ratio, but additional correction factors may be needed (Idriss and Boulanger, 2010):

$$N_{60} = C_E C_B C_R C_S N_m \quad (2.40)$$

$C_E$  is the energy ratio factor and can be determined as  $\frac{ER}{60}$  where  $ER$  is the measured delivered energy ratio, which depends on the equipment and hammer. A typical  $ER$  value used in Italy is 75%.  $C_B$  is the borehole diameter factor,  $C_R$  is the rod length correction factor, and  $C_S$  is a sampler factor. For typical equipment and applications, these last three coefficients are equal to 1.

Lastly, the CRR is corrected for the proper magnitude with a magnitude scaling factor (MSF, more details in Idriss, 1999), for overburden stress with a coefficient  $K_\sigma$  (Boulanger, 2003), and for the presence of static shear stresses with a coefficient  $K_\alpha$ . The MSF takes into account the effect of shaking duration (and thus number of loading cycles) on the CRR and it is estimated as:

$$MSF = 6.9 \exp\left(-\frac{M}{4}\right) - 0.058 \leq 0.8 \quad (2.41)$$

The overburden correction factor  $K_\sigma$  can be evaluated as:

$$K_\sigma = 1 - C_\sigma \ln\left(\frac{\sigma'_v}{p_a}\right) \leq 1.1 \quad (2.42)$$



$$C_\sigma = \frac{1}{37.3 - 8.27 (q_{c1Ncs})^{0.264}} \leq 0.3 \quad (2.43a)$$

$$C_\sigma = \frac{1}{18.9 - 2.55 \sqrt{(N_1)_{60cs}}} \leq 0.3 \quad (2.43b)$$

The static shear stress coefficient  $K_\alpha$  (Seed, 1983) can be estimated according to Idriss and Boulanger (2003a):

$$K_\alpha = a + b \exp\left(\frac{-\xi_R}{c}\right) \quad (2.44)$$

$$a = 1267 + 636\alpha^2 - 634 \exp(\alpha) - 632 \exp(-\alpha) \quad (2.44a)$$

$$b = \exp(-1.11 + 12.3\alpha^2 + 1.31 \ln(\alpha + 0.0001)) \quad (2.45b)$$

$$c = 0.138 + 0.126\alpha + 2.52\alpha^3 \quad (2.46c)$$

$$\alpha = \frac{\tau_s}{\sigma'_{vc}} \quad (2.47d)$$

where  $a$ ,  $b$ , and  $c$  are coefficients that depends on the static shear stress ratio  $\alpha$ , defined as the ratio of the shear stress  $\tau_s$  and the vertical effective stress  $\sigma'_{vc}$ .  $\xi_R$  is an index describing the relative state parameter (Boulanger, 2003a) and can be computed from the penetration resistances as:

$$\xi_R = \frac{1}{Q - \ln\left(\frac{100(1 + 2K_0)\sigma'_{vc}}{3p_a}\right)} - \sqrt{\frac{(N_1)_{60}}{46}} \quad (2.48a)$$

$$\xi_R = \frac{1}{Q - \ln\left(\frac{100(1 + 2K_0)\sigma'_{vc}}{3p_a}\right)} - (0.478 (q_{c1N})^{0.264} - 1.063) \quad (2.48b)$$

where  $Q$  is the parameter introduced by Bolton (1986) to build the critical state line (CSL). In the previous expressions,  $\alpha$  and  $\xi_R$  are constrained by the following limits:

$$\alpha \leq 0.35 \quad (2.49a)$$

$$-0.6 \leq \xi_R \leq 0.1$$

Thus, the CRR for the site-specific condition is then computed:



$$CRR_{M,\sigma'_v} = CRR_{M=7.5, \sigma'_v=1} MSF K_\sigma K_\alpha \quad (2.50)$$

Hence, liquefaction is triggered if the CSR is greater than  $CRR_{M,\sigma'_v}$ . The effect of  $K_\sigma$  and  $K_\alpha$  in Eq. 2.50, however, are taken into account only in a simplified way. Advanced constitutive models (§ 6.2) can capture the effect of the overburden stress and static shear stress, providing a more consistent description of the phenomena.

### 2.5.3.2 Empirical methodology for cyclic softening triggering analysis

The potential of cyclic softening in clays and silts (i.e., the onset of significant deformations during undrained loading) can be estimated following a stress-based procedure similar to that used to evaluate liquefaction triggering in sand-like materials (Boulanger and Idriss, 2007). In this procedure, the cyclic strengths of soil are expressed as a cyclic stress ratio (CSR, Eq. 2.29), which is the dynamic shear stress divided by the vertical effective consolidation stress  $\sigma'_{vc}$ . The cyclic strength or cyclic resistance ratio (CRR) is defined as the CSR necessary to reach a failure criterion that describes the initiation of significant strains for a certain number of uniform cycles. For clays and plastic silts, CRR is usually defined in terms of the monotonic undrained shear strength ratio. This is useful when cyclic laboratory testing data is not available, and the CRR must be estimated empirically either from the undrained shear strength profile or from the consolidation stress history. In its most general form, the CRR can be expressed as:

$$CRR_M = C_{2D} \left( \frac{\tau_{cyc}}{s_u} \right)_{M=7.5} \frac{s_u}{\sigma'_{vc}} MSF K_\alpha \quad (3.11)$$

where  $C_{2D}$  is a correction factor to take in to account two dimensional cyclic loading and can be taken as 0.96 (Boulanger and Idriss, 2004).  $\frac{\tau_{cyc}}{s_u}_{M=7.5}$  is the ratio of cyclic stress to undrained strength for the number of equivalent uniform cycles for a magnitude 7.5 earthquake. Idriss and Boulanger (2004 and 2006) showed the relationship between CRR and number of uniform cycles and concluded that 30 cycles are a good approximation of a 7.5 magnitude earthquake. The authors suggest a  $\frac{\tau_{cyc}}{s_u}_{M=7.5}$  value of 0.83 based on cyclic strengths versus PI data for claylike soils, which show that the ratio is in relatively narrow range of values.  $\frac{s_u}{\sigma'_{vc}}$  is the monotonic undrained shear strength ratio, estimated from one of the available procedures in literature.  $MSF$  is the magnitude scaling factor that accounts for the variation of the

number of uniform cycles with magnitude (i.e., larger magnitude corresponds to greater duration, hence larger number of cycles). The  $MSF$  can be evaluated as:

$$MSF = 1.12 e^{-\frac{M_w}{4}} + 0.828 \quad (3.12)$$

$K_\alpha$  is a correction factor for the initial static shear stress and can be estimated as:

$$K_\alpha = 1.344 - \frac{0.344}{\left(1 - \frac{\tau_s}{s_u}\right)^{0.638}} \quad (3.13)$$

where  $\tau_s$  is the initial shear stress. The CRR for a given magnitude can thus be expressed as:

$$CRR_M = 0.8 \frac{s_u}{\sigma'_{vc}} MSF K_\alpha \quad (3.14)$$

By exploiting SHANSEP equation, the CRR can also be computed as:

$$CRR_M = 0.8 \cdot S \cdot OCR^m \cdot K_\alpha \quad (3.15)$$

This equation can be used to estimate the variation of the CRR with depth. Since all the terms are constants with the exception of OCR, the trend of  $CRR_M$  reflects the trend of OCR with depth.

### 3. The Farneto del Principe dam case study

#### 3.1 Dam description

Hazard analyses approaches and methods to assess the seismic performance of earth dams presented in the previous chapter are applied to the case study presented in this chapter: The Farneto del Principe dam (Figure 3.1). This structure is a zoned earth dam located in the Calabria region (Southern Italy). The Farneto del Principe dam (latitude 39.6515°N and longitude 16.1627°E) was designed in the '60s and built during the late '70s and early '80s and it is used for flow balancing and irrigation purposes. The dam is located in a seismically active region characterized by the presence of shallow crustal faults (predominantly extensional features) and deep seismicity related to the subduction zone of the Calabrian Arc. The dam height is 30 m and its length is more than 1200 m, while the crest elevation is at 144.20 m above sea level (a.s.l.) and the maximum allowable level of the reservoir is 141.70 m a.s.l. The central core comprises compacted, low permeability clay and silt. The shells are composed of mainly sand and gravel. Two filters (one meter each) protect the dam core, with grain size distributions similar to that of the adjacent soil, both upstream and downstream. The foundation of the dam comprises a shallower layer of high-permeability alluvial material (i.e., sand and gravel) which is in turn founded on a thick clay layer. The exact location of a compliant bedrock is unknown. The thickness of the alluvial material is not constant but varies lengthwise, with a maximum thickness of around 43 m in the central area of the dam. A cut-off wall is present throughout the length of the dam within the alluvial material and embedded for 3m into the clay bed, to prevent groundwater flow and possible seepage. The cut-off wall was built using two construction strategies: (1) two slurry walls formed by panels excavated in presence of bentonite mud, and (2) a double line of close piles with half-meter diameter, without injection of waterproof material. Downstream of the core is located an inspection tunnel, also used for collecting drained water coming from the dam. A representative cross section of the dam is shown in Figure 3.2.

During the design and construction phases of the dam, a comprehensive geotechnical laboratory program was performed on the material used to build the dam. This program included the following: consolidation tests by oedometer, grain size distribution, and permeability tests. A summary of the main geometrical characteristics and general information is reported in Table 3.1. Table 3.2 shows a

summary of geotechnical characteristics derived from laboratory tests performed prior to the construction and during the construction of the dam. Additional details on this data are provided by Ausilio et al. (2013, 2016).

A reliable evaluation of the seismic performance of a zoned earth dam requires a large number of details on the current geotechnical characteristics of the dam. Such data can be obtained by means on field and laboratory tests. In the remainder of this section, results obtained following a substantial geotechnical test program performed between 2015 and 2017 are presented. The resulting geotechnical model of the Farneto del Principe dam is based on these results and presented in a subsequent section.



Figure 3.1: Location and aerial view of the Farneto del Principe dam (from Google earth, 2019).

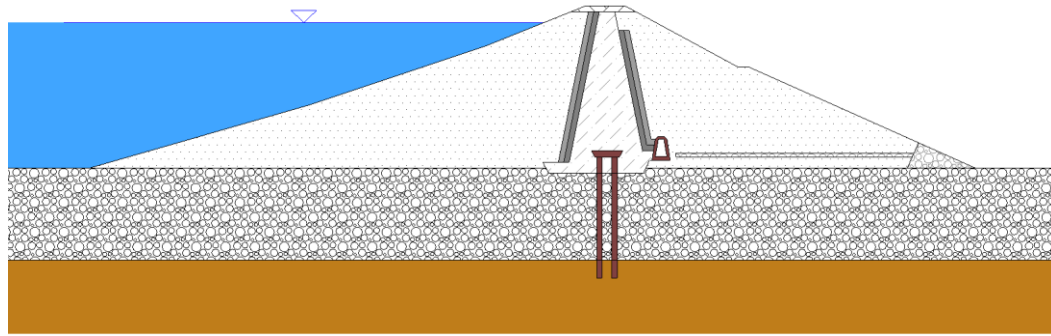


Figure 3.2: Schematic cross section of the Farneto del Principe dam.

Table 3.1: Main characteristics of the Farneto del Principe dam.

Geometrical property	Value
Water storage volume	46 Mm <sup>3</sup>
Average height (above the foundation)	27.7
Crest length	1240 m
Crest width	7 m
Freeboard (max level of the reservoir)	2.5 m
Current freeboard	8.1 m
Upstream face slopes	1:2.5, 1:3, 1:3.5
Downstream face slopes	1:1.185, 1:2.25
Crest elevation	144.20 m a.s.l.
Maximum allowable water level	141.70 m a.s.l.
Maximum authorized water level	136.30 m a.s.l.

Table 3.2: Geotechnical characteristics of the materials tested prior and during the construction of the Farneto del Principe dam.

Parameter	Description	Foundation		Dam body	
		Alluvium	Clay bed	Core	Shells
$c'$ [kPa]	Cohesion	0	180	80	0
$\phi'$ [°]	Friction angle	37.5	24	18	40
$c_u$ [kPa]	Undrained strength	-	450	202	-
$\gamma$ [kN/m <sup>3</sup> ]	Unit weight	24.1	21.12	21.31	25.1
$\gamma_d$ [kN/m <sup>3</sup> ]	Dry unit weight	-	17.98	18.07	24.04
$\gamma_s$ [kN/m <sup>3</sup> ]	Particles unit weight	-	27.3	27.3	27
$n$	Porosity	-	0.36	0.33	0.11
$e$	Void index	-	0.54	0.51	0.123
$S$ [%]	Degree of saturation	-	97.2	95.6	96.7
$w$ [%]	Water content	7.5	19.54	17.88	4.42
$w_L$ [%]	Liquid limit	-	41.51	45.4	-
$w_P$ [%]	Plastic limit	-	18.26	19.18	-
PI	Plasticity index	-	23.25	26.22	-

### 3.2 The 2015-2017 geotechnical investigation program

Available data on the dam material characterization, derived using results of the geotechnical investigation performed prior and during the construction of the dam, should be complemented by data providing information on the current geotechnical characteristics of the dam materials. There are two main reasons why new data should be acquired: (1) some of the material properties may be different (e.g., grain size distribution changed over time in different zones as a result of flow-related dragging forces), and (2) dynamic soil parameters are unknown (e.g., shear wave velocity profiles and modulus reduction and damping curves). The new geotechnical investigation program was specifically designed to fill these gaps. The field investigation program described in this study was performed between 2015 and 2017. It comprises the following test types:

- a) Boring logs with continuous sampling;
- b) Grain size distribution analyses and Atterberg's limits evaluation;
- c) Consolidation tests using the oedometer;
- d) Direct Shear test (DS);
- e) Triaxial tests (Consolidated Drained, Consolidated Undrained, and Unconsolidated Undrained);
- f) Standard Penetration Tests (SPT);
- g) Cone Penetration Tests with hydrostatic pore pressure evaluation (CPTu);
- h) Seismic Cone Penetration Tests (SCPTu);
- i) Seismic tomography;
- j) Down-hole and cross-hole tests;
- k) Multichannel Analysis of Surface Waves (MASW);
- l) Dynamic laboratory tests on undisturbed specimens (Resonant Column and Cyclic Torsional Shear tests);
- m) Microtremor Horizontal to Vertical Spectral Ratio (HVSr) analysis.

The locations of the aforementioned tests are reported in Figure 3.3. Fifteen boreholes were drilled during the field investigation, eight on the dam crest, three on the landside shell, one near the guardhouse, one by the lateral overflow spillway, and two in the landside, in free field condition. Grain size distribution analyses were performed for samples collected in each borehole, and Atterberg's limits were evaluated for samples collected in the core and the clay bed (S4, S5, S6, S11, PZ3, S1,

and S8). For these soils, consolidation, DS, CD, CU, and UU tests were performed to estimate soil mechanical behavior and static strength parameters.

SPTs were performed in ten of the fifteen boreholes (S1, S2, S3, S4, S5, S6, S7, S8, S12, S13), while five boreholes were equipped with Casagrande piezometers. The perforations were executed using a Teredo MN 900 drilling rig, which operated with a rods system and a Shelby tube sampler (101 mm of internal diameter). This sampler is usually suitable for cohesive soils up to a firm-to-stiff consistency and free from large particles. As a result, a thick wall sampler with a core catcher was used to drill boreholes S2 and S3 (in the downstream shells). The SPTs were performed following ASTM Standard procedures (D1586-11). Two enhanced versions of the CPT were performed, namely piezocone tests (CPTu, with pore pressure measurement), and seismic CPT with piezocone (SCPTu, with seismic wave velocity measurement). Eight seismic tomography tests were performed. Five of them capture the two-dimensional distribution of shear wave velocity along longitudinal profiles: one is located along the crest, one near the guardhouse, two along the inspection gallery, and one in a free-field area on the landside of the dam. The remaining three tomography tests are meant to characterize typical cross sections of the dam. One is located on the right bank (108 m long), one on the centerline (102 m long), and the last one on the left bank (96 m long). Additional tests (down-hole, cross-hole, and MASW) were performed to define shear wave velocity profiles of various zones of the dam. Five down-hole tests were performed: in boreholes S3 (landside shell), S4 (crest), S13 (guardhouse), and S1 and S8 (the last two in a free field area). The S4 down-hole reached a depth of 26 m, investigating the clay core up until the cut-off wall. The S3 down-hole extended for 40 m, crossing both the dam shell and the alluvial foundation, while S1, S8, and S13 reached the clay bed limit. Four cross-hole tests were performed, using three boreholes (S4, S5, and S6 – these boreholes have an inter-boring spacing of four meters). Two tests were performed, utilizing two different source-receivers permutations (i.e. one time the source was in S4 and the receivers in S5 and S6, then source in S5 and receivers in S4 and S6). An inclinometer probe was used to ensure the verticality of the boreholes. The depth reached by these tests is 26 m, which is roughly the location of the cut-off wall. The tests have been performed following the ASTM Standard procedures (D 4428). A MASW test was also performed on the dam crest, using 24 4.5 Hz-geophones. The distance between the source and the first receiver was 5 m, while the inter-geophone spacing was 2 m. Several dynamic laboratory tests on



undisturbed specimens were also conducted on the dam crest materials (the specimens were collected in the following boreholes: S4, S5, S6, S11, and PZ3 following the ASTM Standard procedures, D 4015). Resonant Column (RC) and Cyclic Torsional Shear (CTS) tests were used to estimate the shear modulus of the clay core, its variation with depth, and its reduction with increasing shear strain. CTS tests were performed using a frequency of 0.1 Hz and various number of cycles (ranging from 5 to 20). Microtremor Horizontal-to-Vertical Spectral Ratio (HVSr) analyses were also conducted on the dam crest, in a free-field area downstream of the dam, and in the inspection gallery. These tests were used to estimate the fundamental period of the dam. Data acquisition lengths ranged between 20 and 60 minutes. A portable Tromino 4 Hz seismometer with three receivers and a 24 bit digitizer was utilized. A summary of all tests performed is reported in Table 3.3.

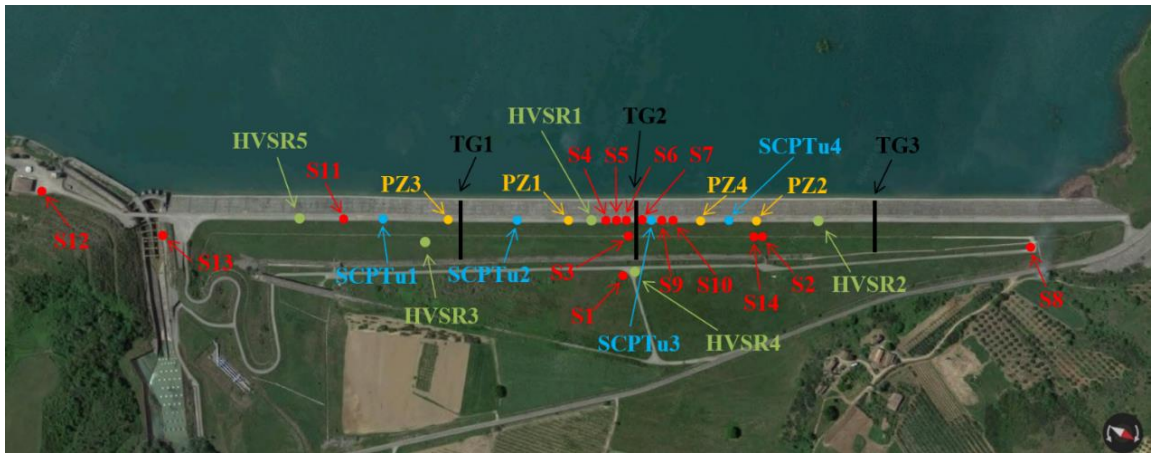


Figure 3.3: Locations of the tests performed at the Farneto del Principe dam site.

### 3.3 Boring logs, SPT, and CPT results

In this section, the results of SPT and CPT tests performed on the core, shells, and foundation of the dam are illustrated. Within the dam's core, the boreholes were mainly performed to retrieve undisturbed samples. Thus, a small number of SPT were conducted. Figures 3.4 and 3.5 show boring logs and SPT blow counts (both raw blow counts and energy- and fines-corrected values,  $(N_1)_{60cs}$  for boreholes S4, S5, S6, and S7 (relative to the core) and S1, S2, S3, and S8 (relative to the shells and foundation material), respectively.



Table 3.3: Summary of the tests performed at the Farneto del Principe dam site.

Test type	Number	Location
Borehole	15	Core, shells, foundation
Granulometry	29	Core, shells, foundation
Consolidation	8	Core, foundation
Direct Shear	2	Core
UU	6	Core, foundation
CU	7	Core, foundation
CD	1	Core
SPT	10	Core, shell, foundation
CPTu	4	Core
SCPTu	4	Core
Seismic tomography	8	Longitudinal and transversal profiles
Cross-hole	4	Core
Down-hole	5	Core, shell, foundation, guard house
MASW	1	Core
Resonant Column	14	Core
Cyclic Torsional Shear	8	Core
Microtremor HVSR	5	Core, inspection gallery, foundation

The high SPT blow count values (some of them reached refusal) are consistent with the sandy and gravelly material that constitute the shells and foundation of the dam. Within the core, SPT blow counts are consistent with values typical of compacted clayey soils. The results of the four CPTu and SPCTu performed on the crest and within the core are shown in Figures 3.6-3.13. These figures show that the soil behavior type index  $I_c$  of the core is consistent with the available boring log data. A mean  $I_c$  value of around 3.5 is representative of clayey silts and silty clay, which is the soil that constitute the core of the dam. Figure 3.14 shows the shear wave velocities measured by the four SCPTu, which are consistent with shear wave velocity profiles estimated using geophysical tests (§ 3.4). Overall, the results of SPT and CPT tests are consistent with the information obtained from the available boring logs and laboratory tests. This complementarity is an important aspect in the geotechnical characterization of earth dams, because it provides useful information when numerical models are built.

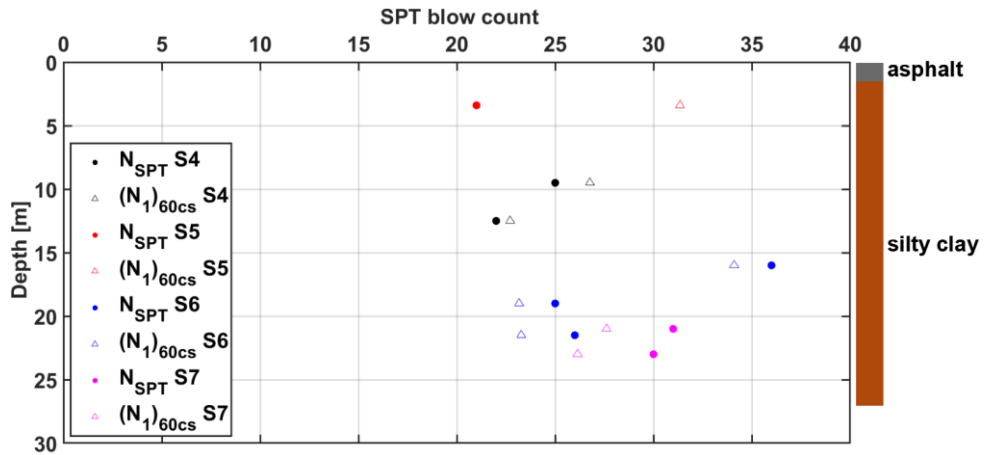


Figure 3.4: SPT results for the silty clay core of the Farneto del Principe dam.

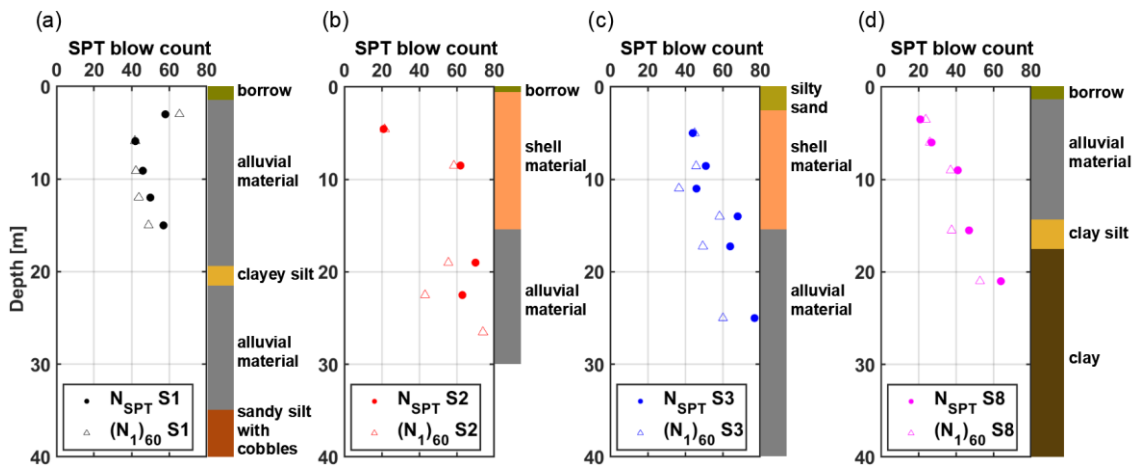


Figure 3.5: SPT results for the alluvial and shells material of the Farneto del Principe dam.

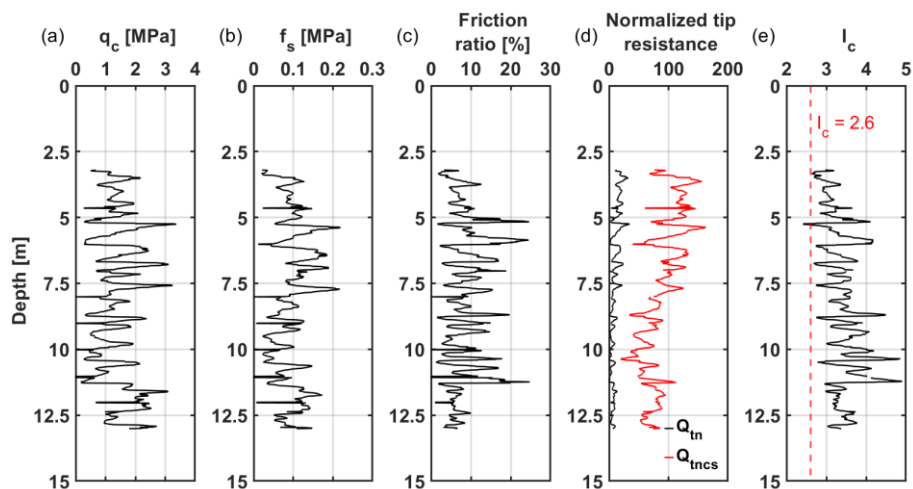


Figure 3.6: Results of the SPCTu1 performed on the dam crest.

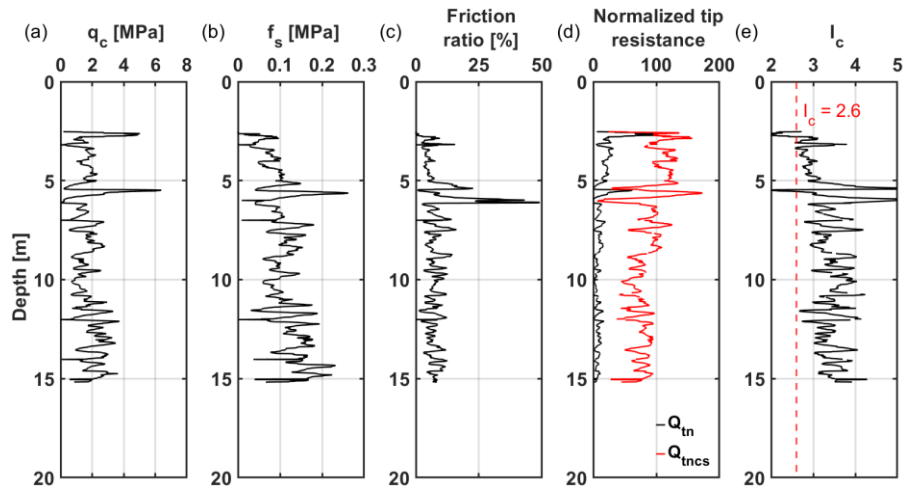


Figure 3.7: Results of the SCPTu2 performed on the dam crest.

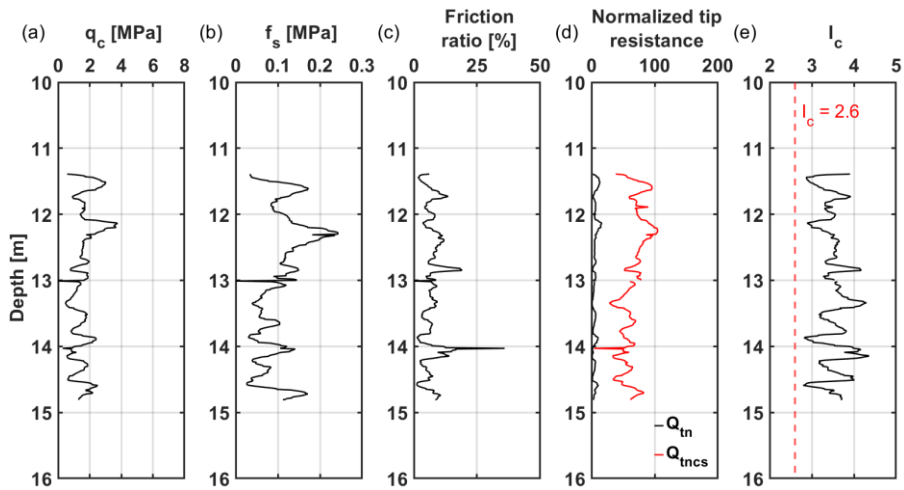


Figure 3.8: Results of the SCPTu3 performed on the dam crest.

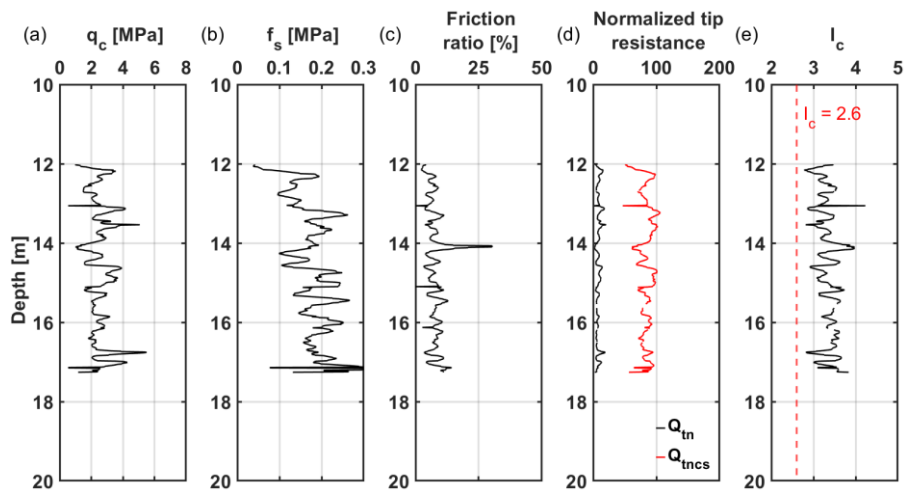


Figure 3.9: Results of the SCPTu4 performed on the dam crest.

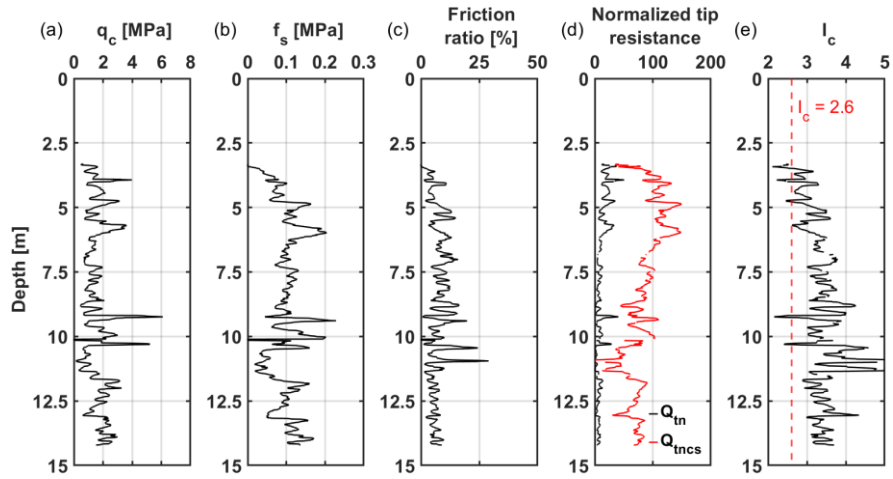


Figure 3.10: Results of the CPTu1 performed on the dam crest.

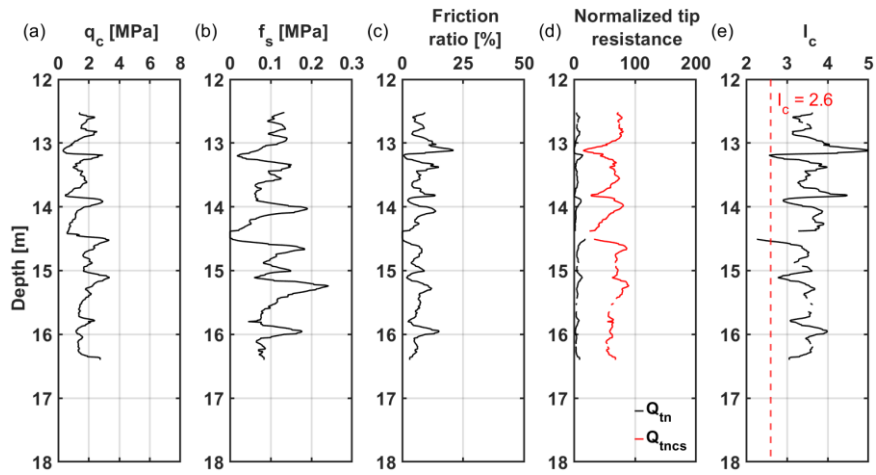


Figure 3.11: Results of the CPTu2 performed on the dam crest.

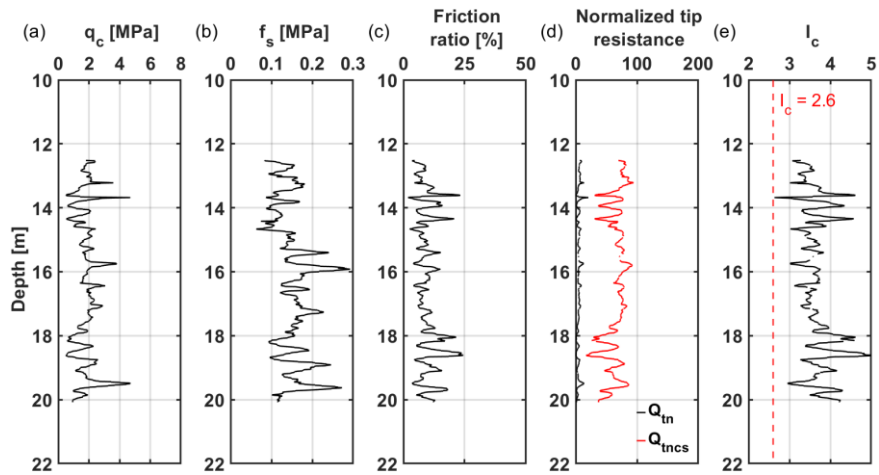


Figure 3.12: Results of the CPTu3 performed on the dam crest.

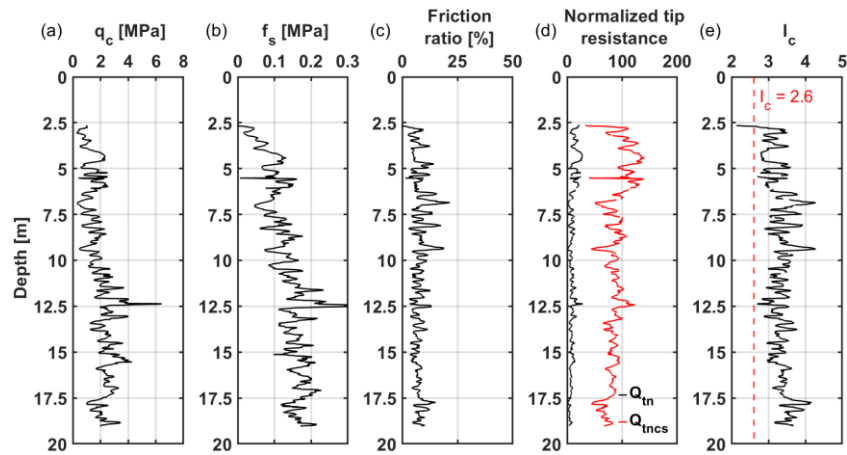


Figure 3.13: Results of the CPTu4 performed on the dam crest.

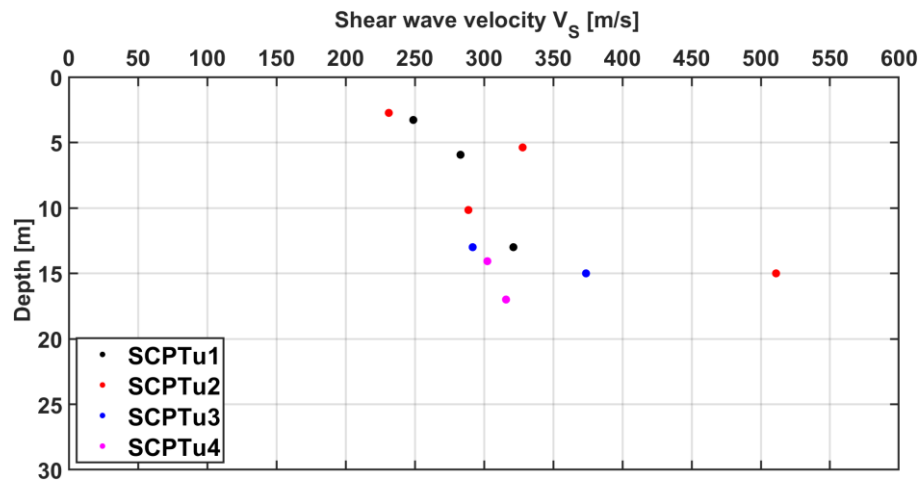


Figure 3.14: Shear wave velocities in the core estimated from SCPTu tests.

### 3.4 Geophysical investigation and laboratory test results

The following sub-sections illustrate the results obtained from geophysical and laboratory tests. A critical analysis is presented, explaining observed trends in the data and comparing measurements from this study with available data and empirical relationships in the literature. Differences between shear wave velocity profiles measured and/or estimated using different tests are also highlighted and discussed.

#### 3.4.1 Invasive geophysical tests

Four cross-hole tests were performed to estimate shear wave velocity profiles at various locations within the dam core. The results of these tests are presented in

Figure 3.15. There is some scatter in the data obtained using different source-receivers permutations. This can be related to at least two reasons: (1) heterogeneity over a short length of the core material, and/or (2) poor cementation of the boring casings. The latter is deemed more pervasive since the material used to build the dam is believed to exhibit negligible longitudinal variability. Figure 3.15 does not show results from a fourth cross-hole test, since its results are highly questionable, due to some issues in the data collection while in the field. If analyzed holistically, the shear wave velocity profiles shown in Figure 3.15 are somewhat consistent with previous studies on similar infrastructure systems (Kim et al., 2009, Park and Kishida, 2017). In particular, for a homogeneous clayey material, a monotonic increase of the shear wave velocity with depth is expected. This is consistent with the notion that the shear modulus (and consequently the shear wave velocity) increases with increasing mean effective stress. Down-hole tests were performed primarily to measure shear wave velocity profiles in the shells and in the alluvial foundation. A single test, however, was conducted inside borehole S4 (in the dam core), to compare it with cross-hole and MASW test results.

Figure 3.16 shows the shear wave velocity profiles at S1 and S8 (both in a free field area), measured by means of down-hole tests. These profiles are considered representative of the alluvial material on which the embankment is founded. The scatter in the data is related to the natural variability of this material and its intrinsic heterogeneity (Regina et al., 2019). Furthermore, the thickness of this material varies longitudinally. As such, these two profiles cannot be directly compared.

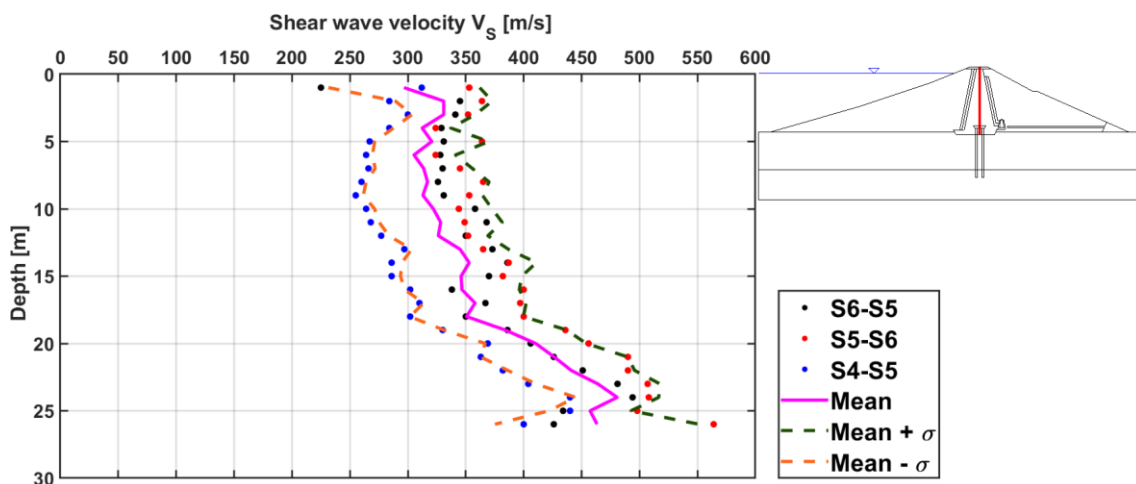


Figure 3.15: Shear wave velocity profiles in the dam core measured using cross-hole tests. The first ID in the legend is the location of the source, while the second is the location of the receiver.

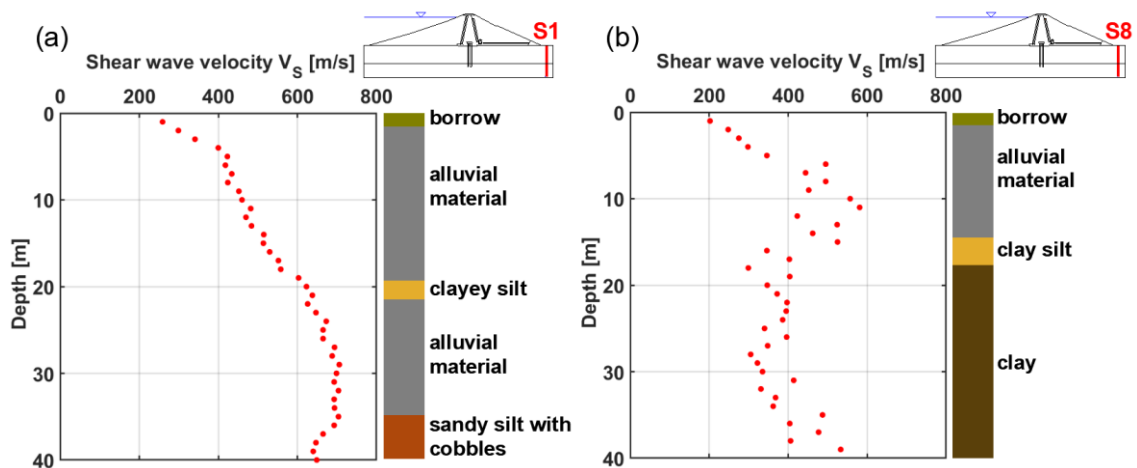


Figure 3.16: Shear wave velocities evaluated from down-hole test in a free field area. The location of the borehole S1 is at the center of the alluvial foundation (a), while borehole S8 is at the left bank (b).

Figure 3.17 shows shear wave velocity profiles in the dam shell and in the alluvial foundation (boreholes S3 and S1 respectively). In both cases, the shear wave velocity increases with depth, reaching a maximum value of 700 m/s in the alluvial material (at the bottom of the test). However, for down-hole S3 there is a small discontinuity in the profile at the boundary between the shell material and the alluvial foundation material. This transition is less abrupt in the data from S1. It is interesting to compare the absolute value of the shear wave velocity of the alluvial foundation material measured beneath the shells and in the free field areas. Figure 3.17 shows such comparison for down-holes S1 and S3. The shear wave velocity of the alluvial material beneath the dam is substantially higher than that in the free field area at the same elevation. In particular, it takes about 20 m for the shear wave velocity in the alluvial material in free field condition to reach the value measured in the same unit immediately beneath the dam. This comparison highlights the expected effect of overburden pressure on shear wave velocity profiles.

### 3.4.2 Multichannel Analysis of Surface Waves (MASW)

The Multichannel Analysis of Surface Waves (MASW) is a non-invasive method to estimate shear wave velocity profiles. One such test was performed on the dam crest to characterize the dam core. Figure 3.18 illustrates the position of the receivers on the dam crest.

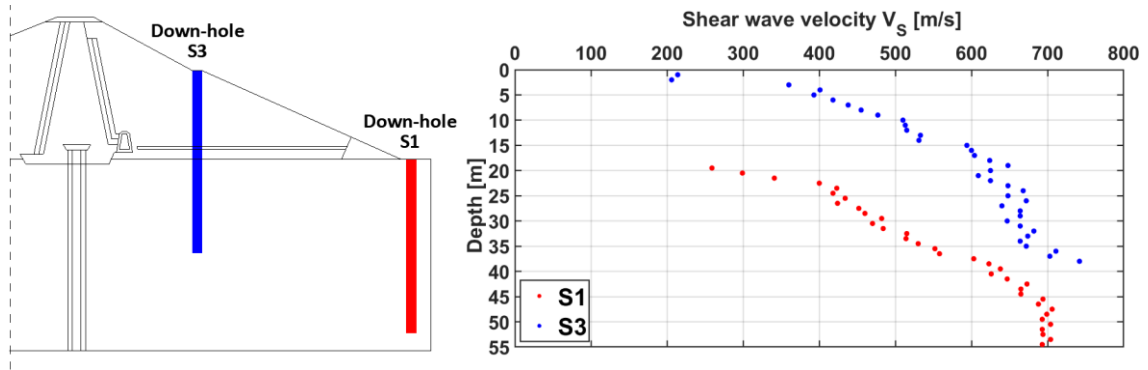


Figure 3.17: Shear wave velocities in the dam shell and in the alluvial foundation.



Figure 3.18: Execution of the MASW test and positions of the receivers.

Figure 3.19a shows the measured dispersion curve in terms of phase velocity versus frequency, while Figure 3.19b shows one inverted profile. The profile of Figure 3.19b represents one of the many potential inverted profiles. As a result, it carries a relatively high level of uncertainty. The inverted profile of Figure 3.19b is generally consistent with the profiles obtained in the same materials using invasive tests. It shows an initial value of 320 m/s in the upper 2m. This high value is representative of a 2m-thick sealing layer made of asphalt and concrete. After this layer, there is a visible inversion of the velocity profile, which then exhibits a trend of increasing velocity with depth. At a depth of 28m, the shear wave velocity value jumps to 700 m/s due to the presence of the concrete cut-off wall. Similar results were found for



dams in South Korea by Park and Kishida (2017). They observed that MASW results are in good agreement with invasive tests for depths up to 25 m in the clay core.

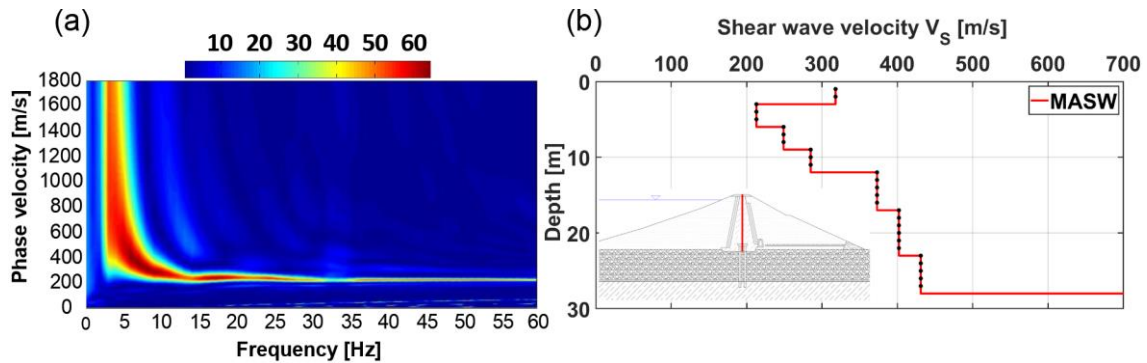


Figure 3.19: (a) Dispersion curve and (b) inverted profile of shear wave velocity obtained at the Farneto del Principe dam crest using the MASW technique.

### 3.4.3 Seismic tomography and HVSR analysis

Results from seismic tomography tests are useful to identify general trends of seismic waves velocities within the embankment. Furthermore, such tests can help identifying heterogeneities in the construction materials. The results of two transversal tomography tests are illustrated in Figure 3.20. Results from these seismic tomography tests do not show an evident stiffness contrast between the dam materials (core and shells) and the alluvial foundation. However, a shallow layer with low seismic wave velocity can be identified on both the upstream and downstream face of the dam, which indicates a low compaction level near the surface. This result is consistent with other tests (i.e. MASW) performed on the dam materials.

Figure 3.21 shows the result of the seismic tomography test for the longitudinal profile of the dam (performed on the dam crest). The profile is ~700 m long and shows a remarkable stiffness contrast between the dam body and the alluvial material. The clay bed shows velocities slightly higher than the alluvial material, although the stiffness contrast is not dramatic. These results are not consistent with what can be observed looking at the down-hole performed in boring S8. This may be a proof of the spatial variability of the alluvial foundation.

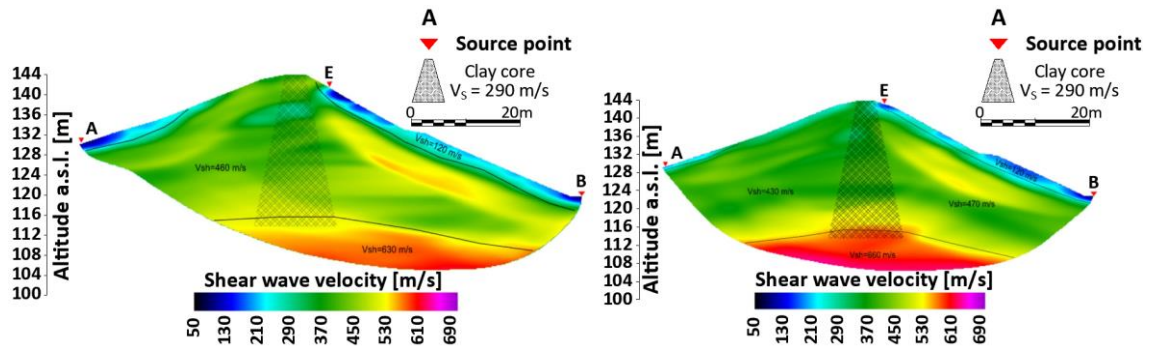


Figure 3.20: Transversal profile of shear wave velocity evaluated from seismic tomography performed at the Farneto del Principe dam.

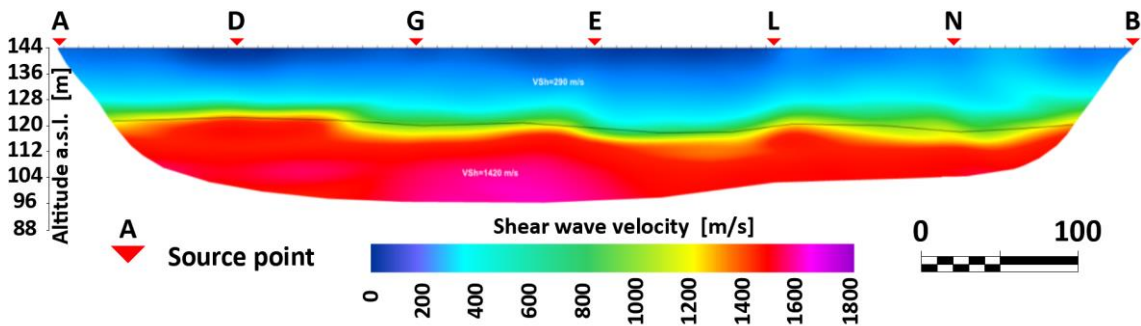


Figure 3.21: Longitudinal profile shear wave velocity evaluated from seismic tomography performed at the Farneto del Principe dam.

The results obtained from microtremor HVSR analysis are shown in Figure 3.22. The interpretation of these curves is not trivial, but some general considerations can be made. The spectral ratio curves evaluated in free-field condition and in the inspection gallery are almost flat (Figure 3.22a and 3.22b) indicating negligible impedance contrast in the soil profiles at these locations. This is consistent with the results of the down-hole in S1. These curves capture the behavior of the alluvial material on which the dam is founded. Four HVSR curves are available for the dam crest (Figure 3.11c-f). At the dam crest, the first spectral ratio peak seems to be in the frequency range 4-6 Hz (i.e. a period range of 0.17-0.25 s), indicating the fundamental frequency of the structure. Zimmaro and Ausilio (2020) performed a finite element method numerical modal analysis for this dam, estimating its fundamental period to be 0.25s. The results from the HVSR analysis presented here are roughly comparable to those provided by the numerical model. This is especially

so if considering that the numerical model ignored the effects of the reservoir, utilized a different water level in the embankment, and was based on approximate geotechnical parameters. Figure 3.23 shows the ratio of the E-W horizontal component measured at various locations, divided by that measured in free-field conditions. This figure shows that the first peak measured at the dam crest is not present in the inspection gallery. This is a further confirmation that the fundamental frequency of the dam should be in the range 3-5 Hz, and that at frequencies greater than 11 Hz the HVSR analysis shows a higher mode frequency. Similar conclusions can be drawn using the other horizontal component (N-S).

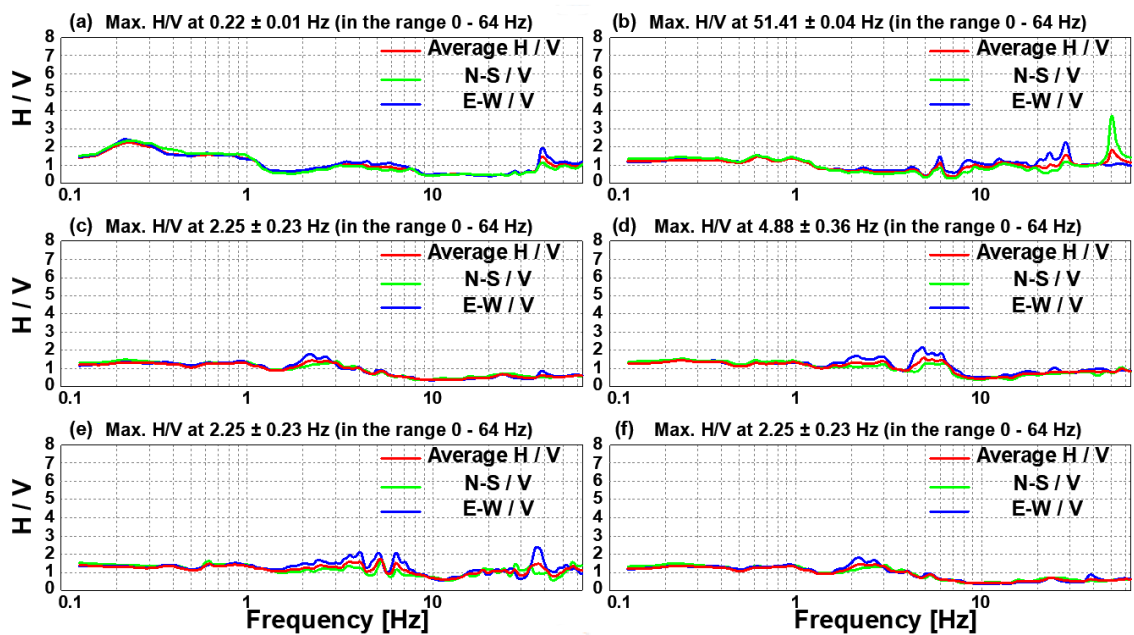


Figure 3.22: Microtremor HVSR results: (a) free field area; (b) inspection gallery; (c),(d),(e), and (f), dam crest.

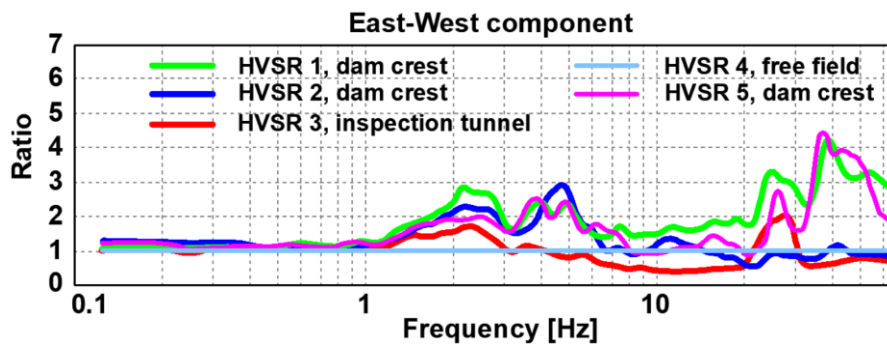


Figure 3.23: Ratio of the microtremor E-W horizontal component measured at various locations, divided by that measured in free-field conditions.

### 3.4.4 Laboratory test results

RC and CTS tests were used to evaluate the dynamic properties of the dam core material (i.e., shear modulus reduction and damping curves). Shear wave velocity of the specimens were also estimated based on the small strain shear modulus and the results are shown in Figure 3.24. Shear wave velocities estimated from CTS are 10% smaller compared to RC results. This is expected, as RC tests are conducted at high frequencies, which leads to a higher shear modulus and consequently shear wave velocity (Cavallaro et al., 1999).

The trend of increasing velocity with depth shown by field investigation data is captured by both laboratory tests. Figure 3.25 summarizes and compares the shear modulus values calculated for the Farneto del Principe dam core using in-situ test data and the same value as obtained using the expression provided by Dakoulas and Gazetas (1985). It appears that the analytical expression of Eq. 2.21 fits the data reasonably well. In this comparison, the value of the inhomogeneity factor  $m$  is 0.5. Shear modulus reduction and damping curves are shown in Figure 3.26, along with the mean curves fitting the data. The shear modulus reduction values are relatively constrained in a narrow range, while damping values are more scattered. These tests were performed on specimens taken at different depths (i.e., from 3 m to 21 m, with a 3 m interval). However, this data does not show an evident overburden stress effect on the modulus reduction and damping curves. Thus, while the small strain shear modulus does increase with depth, the variation with distortional strain is the same.

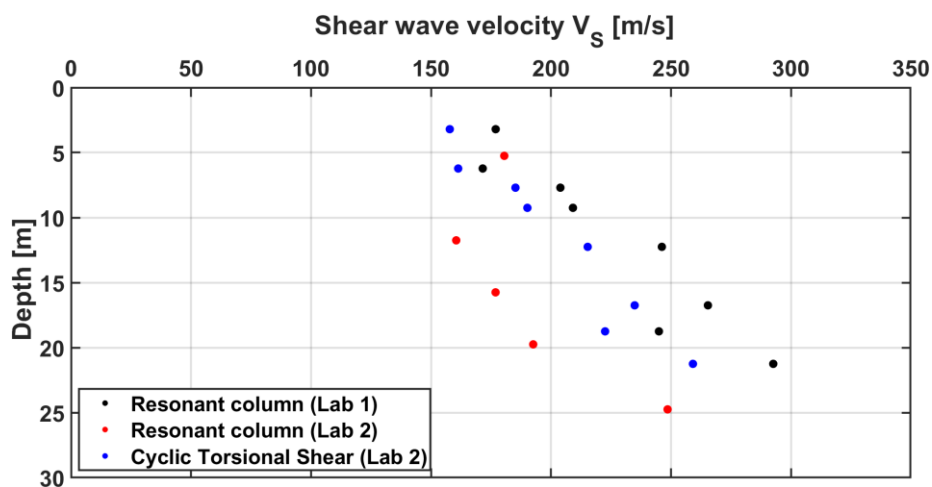


Figure 3.24: Shear wave velocities estimated from laboratory tests with undisturbed specimens.

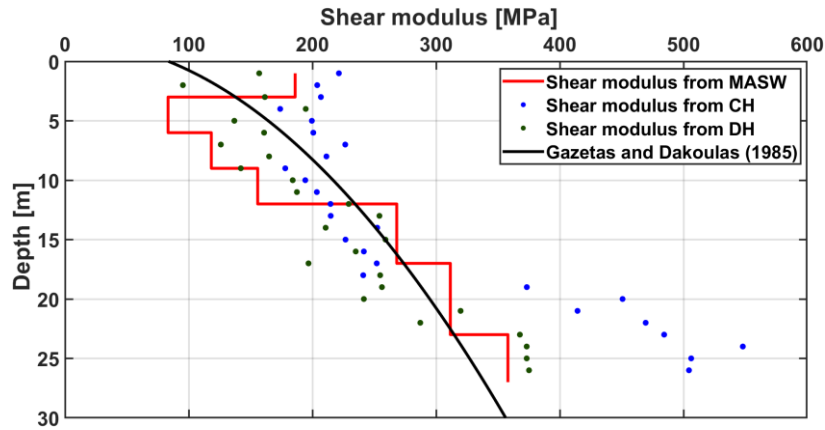


Figure 3.25: Shear modulus profile in the dam core estimated from the geophysical tests and Dakoulas and Gazetas law (1985).

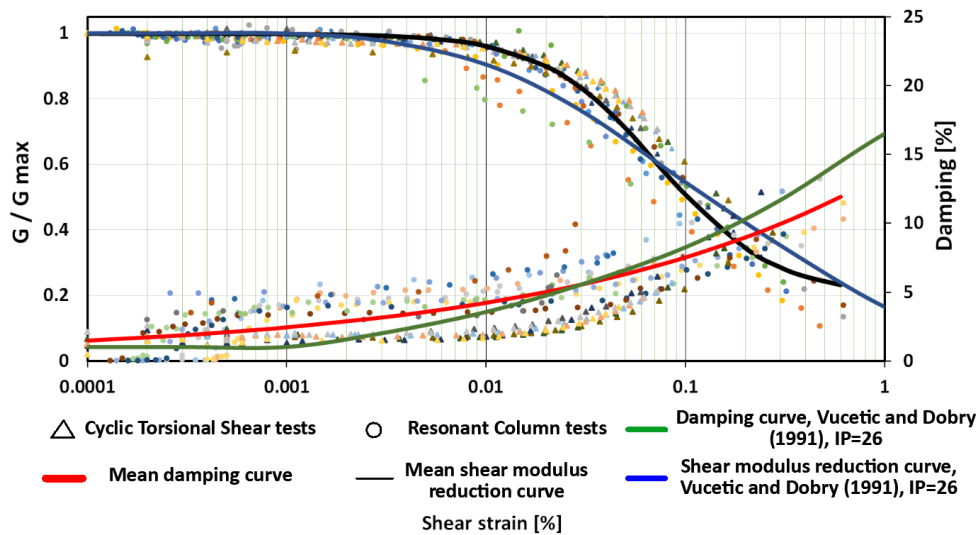


Figure 3.26: Shear modulus reduction and damping curves for the Farneto del Principe dam clay core.

### 3.5 Analysis of the undrained shear strength

Saturated fine graded soils exhibit an undrained behavior when subjected to rapid monotonic or cyclic loading. Thus, the assessment of the undrained shear strength becomes a crucial point for NDAs of dams. There are several methods to estimate the undrained strength of cohesive soils (Shewbridge, 2019). In this study, two methodologies are applied to the Farneto del Principe dam core, the Stress History And Normalized Soil Engineering Properties (SHANSEP, Ladd and Foot, 1974, Ladd and DeGroot, 2003) and the Duncan and Wright (2005). The above procedures are based on the results of oedometric and triaxial tests. In addition, information on the

soil properties such as plasticity index, Atteberg's limits and water content give insights on the overall behavior of a fine-graded soil. The results obtained for the case study are shown in the following sections.

### 3.5.1 Fine grained-soils behavior

Boulanger and Idriss (2006) showed that the behavior of silt and clays in undrained conditions varies in a narrow range of PI, ranging from sand-like ( $IP < 4$ ) to clay-like ( $IP > 7$ ), with a transition in between. The differences in cyclic behavior of sand-like vs clay-like soils determine a variety of possible failure mechanisms of earth dams. As a result, a thorough analysis of the type of cyclic failure that soils can undergo is extremely important when assessing the seismic behavior of such structures. As shown in Chapter 2, sand-like soils are generally susceptible to liquefaction, while clay-like soils are typically susceptible to cyclic softening mechanisms. Both phenomena have to do with the development of significant deformations and strength loss, sometimes leading to catastrophic consequences (Boulanger and Idriss, 2008). However, they are significantly different and can lead to different outcomes.

The core of the Farneto del Principe comprises fine grained plastic soils, with an average plasticity index of 23.3 Figure 3.27 shows how the core material and that found in the clay bed soil plot on the Casagrande's chart. In both cases, the behavior is clay-like, and it is far away from the transition zone of medium to low plasticity soils (zone CL-ML).

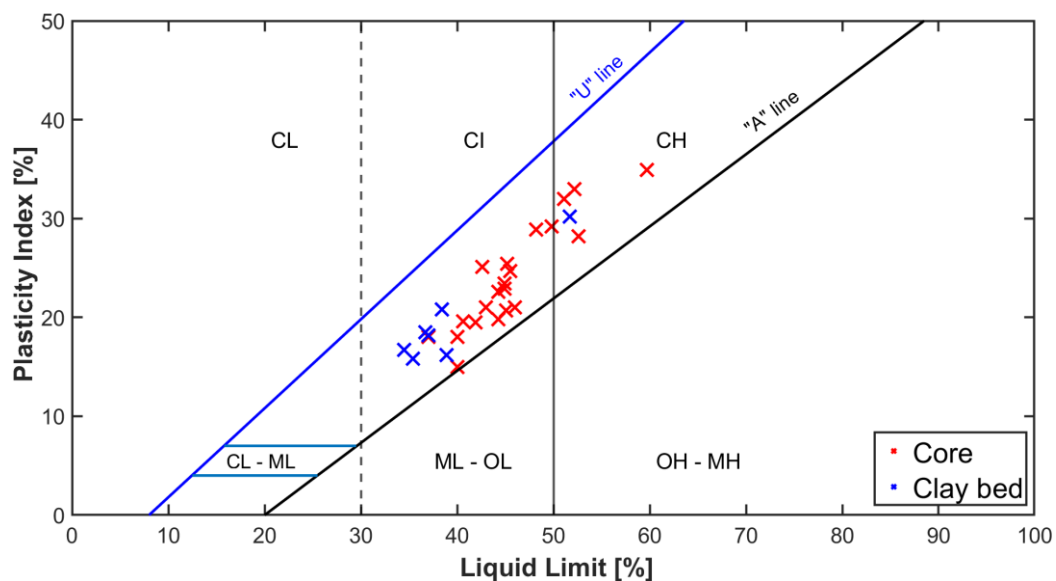


Figure 3.27: Casagrande's chart for the clay core material and clay bed of the Farneto del Principe dam.

Figures 3.28 and 3.29 illustrate the variation with depth of plasticity index, consistency index, water content, activity index, liquidity index, and clay activity in the core and clay bed. No evident trend with depth can be identified, suggesting relatively heterogeneous soils. The relatively high value of the consistency index is another indication of the strong plastic behavior of these soils.

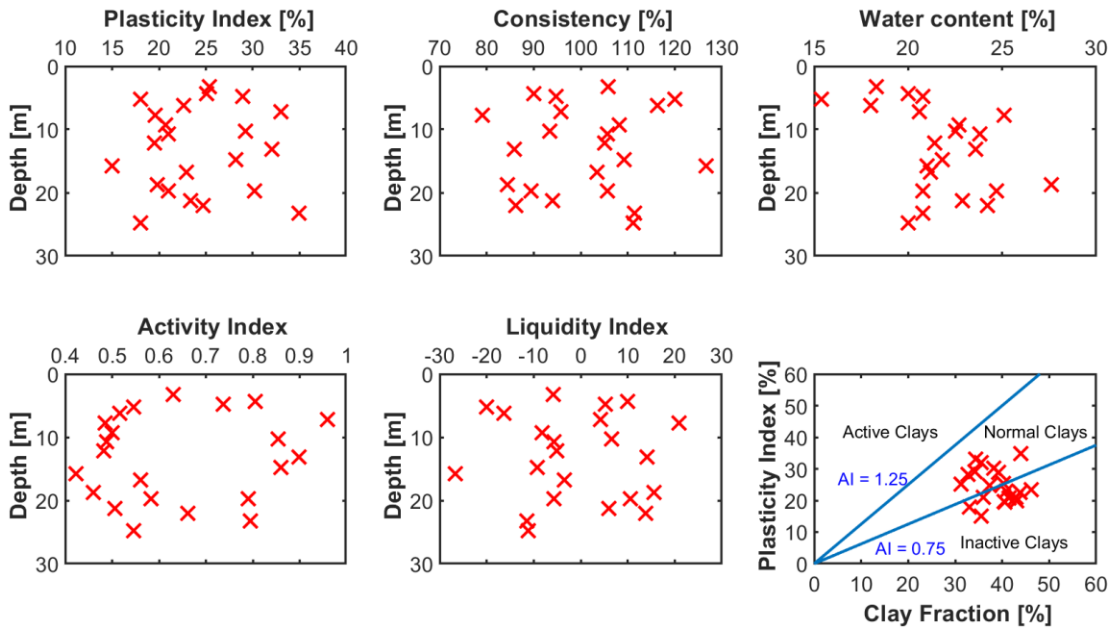


Figure 3.28: Geotechnical properties of the clay core material of the Farneto del Principe dam.

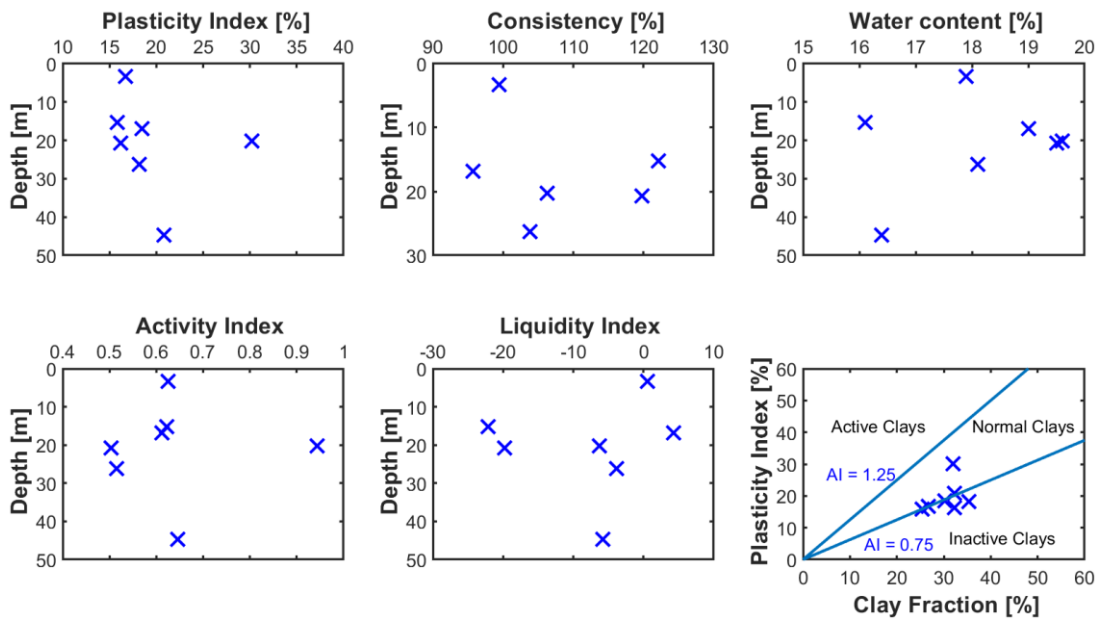


Figure 3.29: Geotechnical properties of the clay bed material of the Farneto del Principe dam.



The liquefaction susceptibility results obtained for the Farneto del Principe dam core and clay bed are shown in Figure 3.30. The clay bed has lower values of PI compared to the core, but it also behaves like a plastic soil and it is not susceptible to liquefaction (or clay-like) according to all analyzed susceptibility methods (i.e., Chinese criteria; Bray and Sancio, 2006; Boulanger and Idriss, 2006). No evident trends with depth can be identified, which is a consequence of the heterogeneous soil and the complex geological settings.

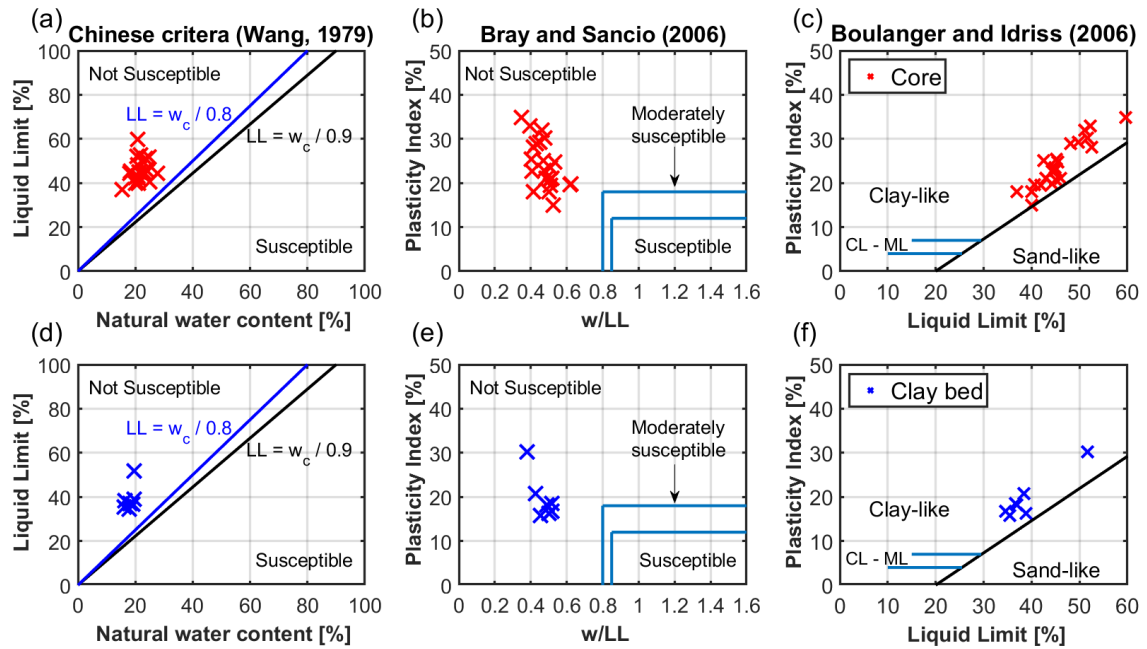


Figure 3.30: Cyclic softening susceptibility for the Farneto del Principe dam core (a, b, and c) and clay bed (d, e, and f).

### 3.5.2 Consolidation tests

Five consolidation tests were performed using the oedometer at the following depths within the dam's core: 4.75 m, 7.25 m, 10.25 m, 13.25 m, and 23.25 m to build the consolidation stress history profile (Figure 3.31). The Casagrande procedure was used to estimate the overconsolidation ratio of the soil, based on the in situ vertical effective stress evaluated from the 2D analysis of the dam. Figure 3.32 shows the profile of OCR with depth calculated from the consolidation test results as well as the OCR profile estimated from the empirical relationship of Lunne et al. (1997) and suggested by Ladd (2003), which is based on the results of CPTs:

$$OCR = k \frac{q_{net}}{\sigma'_{v0}} \quad (3.1)$$



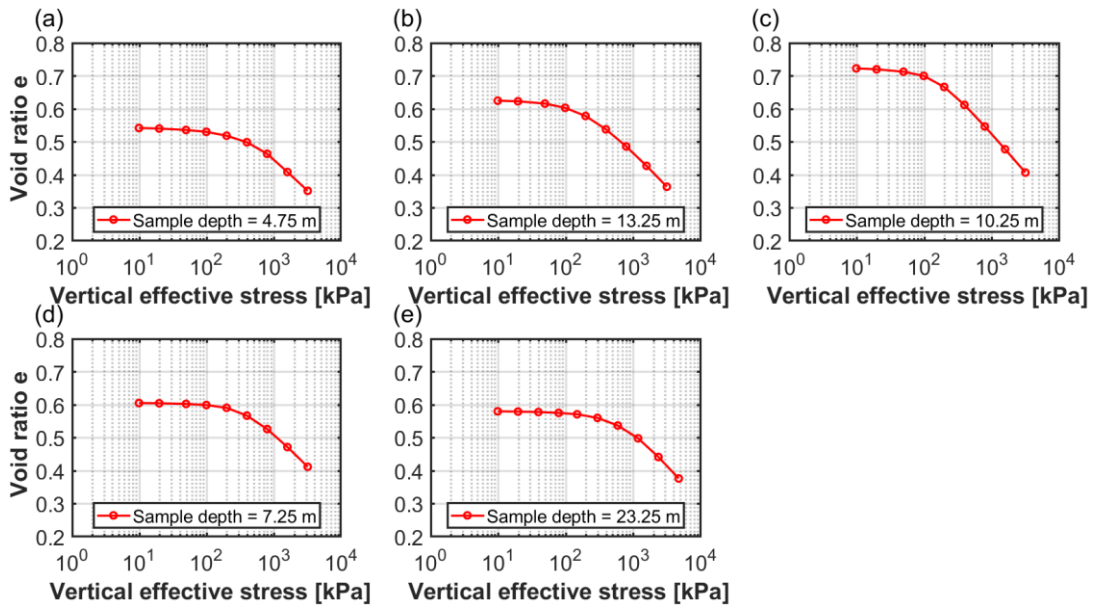


Figure 3.31: Consolidation tests results for the clay core material of the Farneto del Principe dam.

where  $q_{net}$  is equal to the corrected cone tip resistance  $q_t$  minus the total vertical stress, and  $k$  is usually taken as 0.3. In this case, the mean value  $q_t$  of all the CPT tests performed is used. The estimated OCR are quite similar particularly in the upper part of the core, while from 10 m below the crest, it becomes close to one. This is expected, as the dam was built by compacting each time the construction layer, making the lower portions of the core a normally consolidated soil. For shallower layers, the OCR is higher. This can be seen with the ICU tests results reported in the next section.

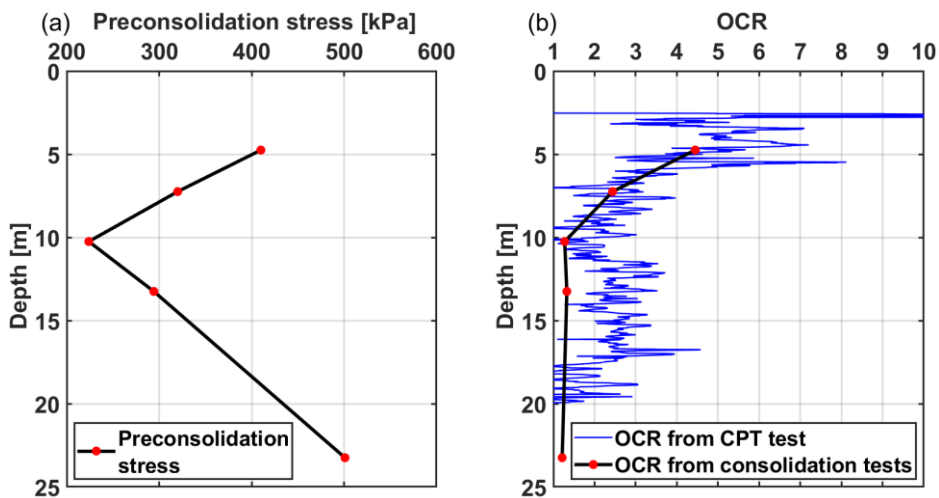


Figure 3.32: Preconsolidation stress (a) and OCR profile with depth (b) for the clay core of the Farneto del Principe dam.

### 3.5.3 Isotropically-Consolidated Undrained triaxial tests

Five isotropically-consolidated undrained (ICU) triaxial tests were performed within the core to estimate the undrained properties of the soil. The results of these ICU tests are shown in Figures 3.33-3.35. For each test, drained and undrained strength parameters are based on the failure criterion based on the maximum deviatoric stress. As shown in Figure 3.33, a large number of samples present a strain hardening behavior, with some of them needing large values of axial strain to reach the critical state condition. The excess pore pressures reported in Figure 3.34 are positive but they decrease at large strains, indicating an incrementally dilative soil behavior when the samples were sheared at high stresses. Figure 3.35 shows the effective stress paths (ESP) and total stress paths (TSP), in terms of stress invariants ( $q$  and  $p'$ ) obtained from three samples for each test. At low confining effective stress  $\sigma'_{3c}$ , the ESPs cross the critical state line (CSL), causing an increment in the mean effective stress, before reaching the failure condition. For higher confining stresses, the samples reach the CSL more regularly, meaning that the soil is closer to a normal consolidation condition. This type of behavior is expected as the soil is lightly over consolidated.

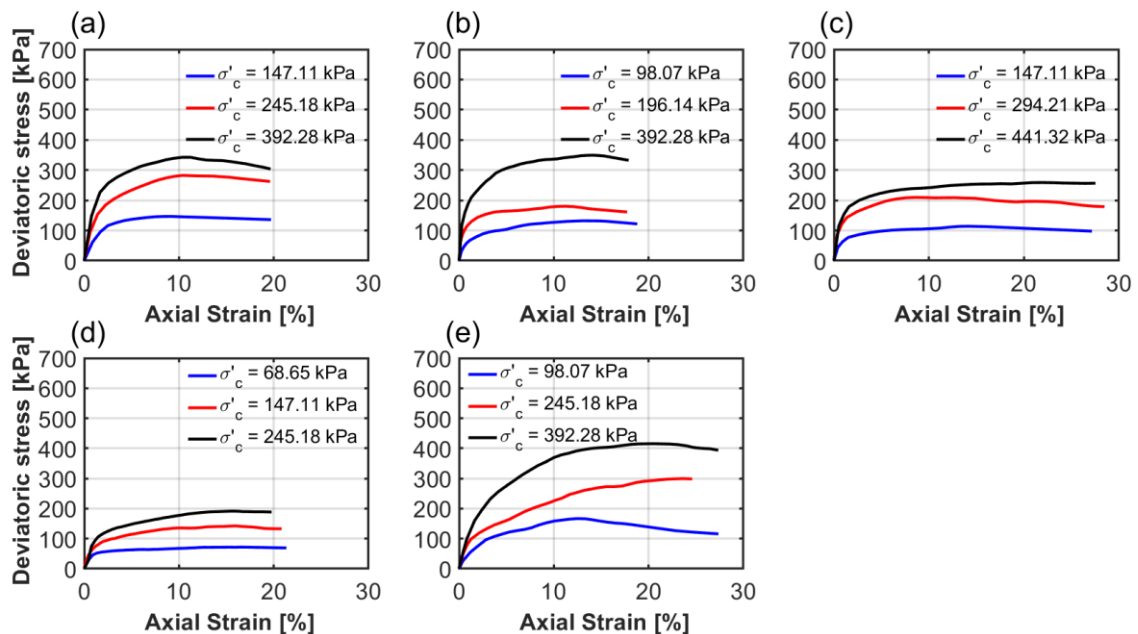


Figure 3.33: Results of the triaxial ICU tests performed on the clay core of the Farneto del Principe dam: deviatoric stress versus axial strain.

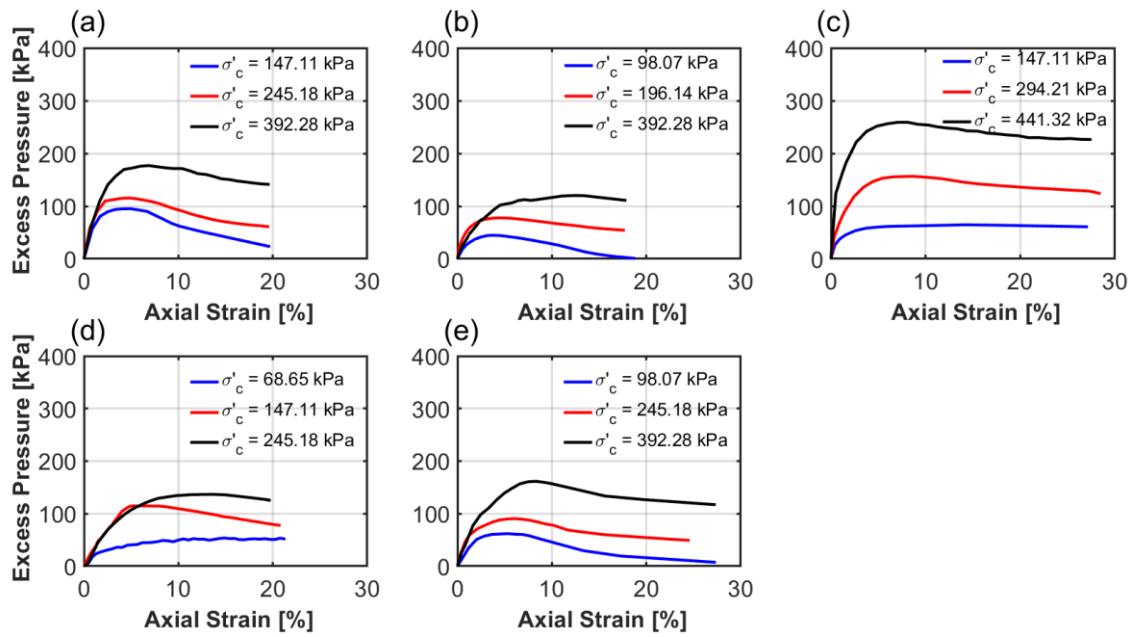


Figure 3.34: Results of the ICU tests performed on the clay core of the Farneto del Principe dam: excess pore water pressure versus axial strain.

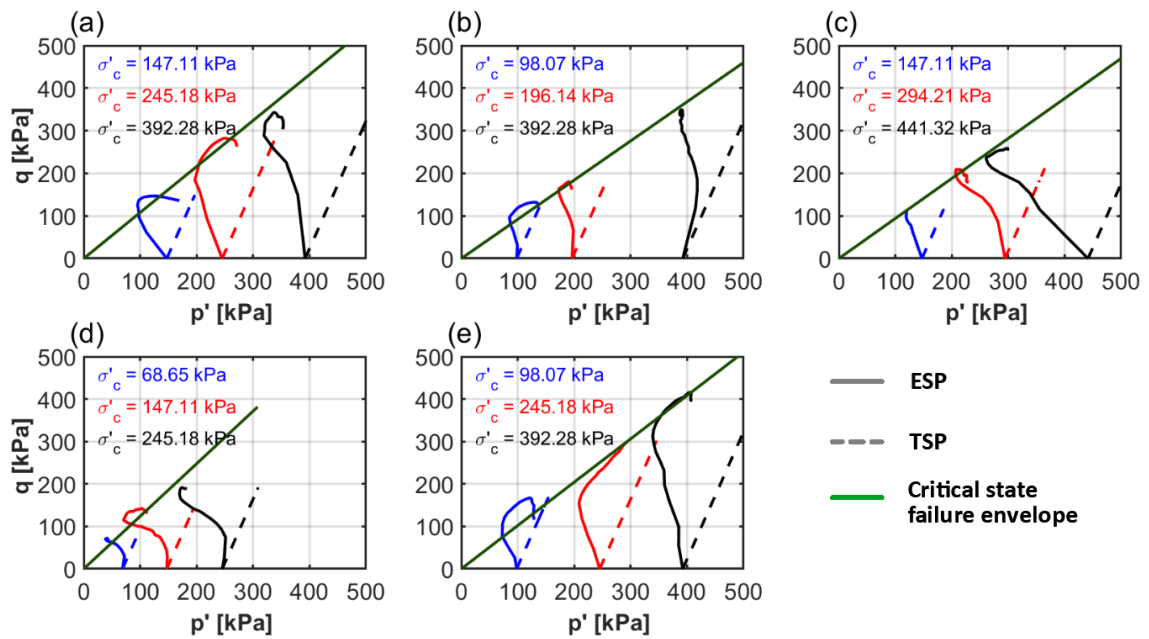


Figure 3.35: Stress paths of the ICU tests performed on the clay core of the Farneto del Principe dam. Continuous lines are the ESPs, dashed lines are the TSPs, and the green line is the critical state failure envelope.

### 3.5.4 Direct Shear test results

Two drained direct shear (DS) tests were performed on samples retrieved within the core of the Farneto del Principe dam to estimate drained strength parameters. Figure 3.36a-b presents results of these tests in terms of shear stress ( $\tau$ ) vs horizontal displacements ( $\delta_0$ ), while Figure 3.36c-d shows test results in terms of vertical ( $\delta_v$ ) vs  $\delta_0$ . Figure 3.36 shows that for low values of the vertical stress the material tends to dilate, while small displacements are observed for high values. The shear stress peak is not very pronounced, but can be well interpolated to obtain peak effective friction angle and cohesion (Figure 3.37). Despite not all the samples reach a well-defined critical state condition, an estimate of the critical state friction angle can be made by considering the last point of the test available. Figure 3.37 shows the failure envelopes are both characterized by a peak friction angle of about  $22^\circ$  and a critical state friction angle of  $21^\circ$ .

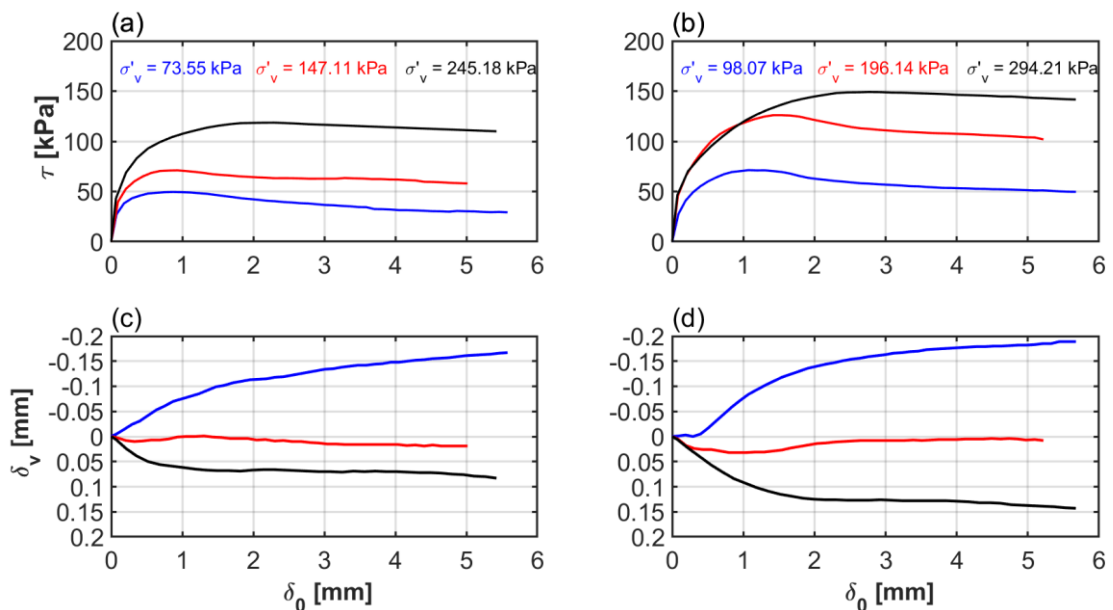


Figure 3.36: Results of the two DSS tests performed for the clay core of the Farneto del Principe dam.

### 3.5.5 Estimation of the undrained shear strength

The knowledge of the variation of the undrained strength with vertical effective consolidation stress is essential to evaluate the dynamic response of embankment dams. Boulanger (2019) shows that a good representation of the undrained shear strength in a numerical model can describe reasonably well the modes of failure of an earth dam.

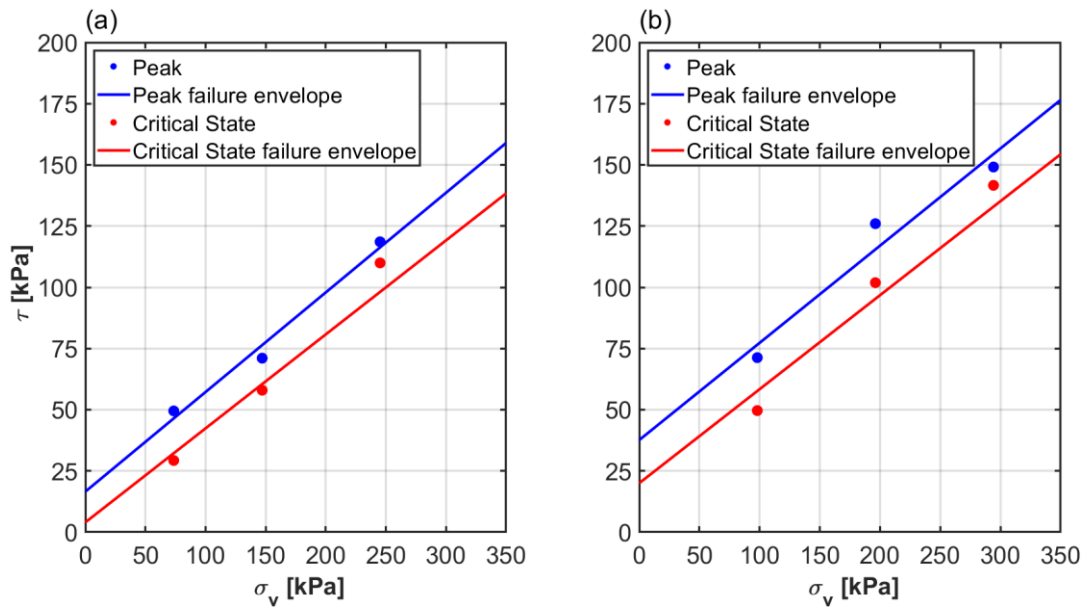


Figure 3.37: Failure envelope for the Farneto del Principe dam core estimated from two DSS.

### 3.5.5.1 Anisotropic undrained shear strength parameters methodology

The undrained shear strength of soils is usually determined from the results of isotropic consolidated tests. However, in most cases the in situ conditions are anisotropic, thus some adjustments are required to represent the proper state of stress. Often, the use of Anisotropically Consolidated Undrained tests (ACU) is not justified, as the precautions necessary to prevent the sample failure during consolidation are hard to achieve. Furthermore, ACU tests are more expensive than ICU tests. Several methods can be utilized to estimate ACU strengths from the results of ICU tests (e.g., Lowe and Karafiatah, 1959) but they usually refer to slope stability analyses by means of limit equilibrium method. Duncan et al. (1990) and Duncan and Wright (2005) show how to evaluate the ACU strength for rapid drawdown analyses by interpolating between the drained and undrained strength envelopes. Such analysis is part of the three-stage analysis proposed for the analysis of earth dam's rapid drawdown effects. This method is valid when a pre-defined failure surface is known, which is the case in limit equilibrium analyses. In NDA approaches, however, the failure surface is not available a priori. As a result, some adjustments to the method are necessary. Montgomery et al. (2014) show how to estimate ACU shear strengths for NDA of earth dams. The methodology can be summarized as follows:

1) The distribution of vertical effective stresses  $\sigma'_v$ , horizontal effective stresses  $\sigma'_h$ , and shear stresses  $\tau_{vh}$  of the 2D model before applying the dynamic input are evaluated;

2) The principal effective stresses at consolidation  $\sigma'_{1c}$  and  $\sigma'_{3c}$  are computed for the zones of interest as:

$$\sigma'_{1c} = \frac{\sigma'_v + \sigma'_h}{2} + \sqrt{\left(\frac{\sigma'_v - \sigma'_h}{2}\right)^2 + \tau_{vh}^2} \quad (3.2)$$

$$\sigma'_{3c} = \frac{\sigma'_v + \sigma'_h}{2} - \sqrt{\left(\frac{\sigma'_v - \sigma'_h}{2}\right)^2 + \tau_{vh}^2} \quad (3.3)$$

3) For each element, the consolidation stress ratio is defined as:

$$K_c = \frac{\sigma'_{1c}}{\sigma'_{3c}} \quad (3.4)$$

4a) Failure envelopes for  $K_c = 1$  (undrained shear strength) and  $K_c = K_f$  (drained shear strength, maximum limiting value of  $K_c$  for a condition corresponding to a state of drained failure) are computed as:

$$\tau_{ff, K_c=1} = d_R + \sigma'_c \tan \psi_R \quad (3.5a)$$

$$\tau_{ff, K_c=K_f} = c' + \sigma'_c \tan \phi' \quad (3.5b)$$

$\tau_{ff}$  is the shear stress on failure plane at failure,  $d_R$  and  $\psi_R$  are the intercept and slope of failure envelope estimated from regression analyses following the Duncan and Wright (2005) procedure, and  $\sigma'_c$  is a measure of consolidation stress.

4b) The parameters  $d_R$  and  $\psi_R$  can be estimated using the Duncan and Wright (2005) procedure. First, the shear stress on the failure plane at failure is estimated from the ICU tests as:

$$\tau_{ff} = \frac{\sigma'_{1f} - \sigma'_{3f}}{2} \cos \phi' \quad (3.6)$$

where  $\sigma'_{1f}$  and  $\sigma'_{3f}$  are the major and minor principal effective stresses at failure as computed from the ICU test (i.e., the points of the Mohr's circle at failure where  $\tau$  is equal to zero).

4c)  $\sigma'_c$  can be interpreted in different ways, such as the mean between the major and principal effective stresses,  $s'_c = \frac{\sigma'_{1c} + \sigma'_{3c}}{2}$ , or the stress on the failure plane assuming that no rotations of the principal axes occur during undrained loading  $\sigma'_{fc}$ . The latter, can be computed from Lowe and Karafiath (1960) as:

$$\sigma'_{fc} = \frac{\sigma'_{1c} + \sigma'_{3c}}{2} - \frac{\sigma'_{1c} - \sigma'_{3c}}{2} \sin \phi' \quad (3.7)$$

Montgomery et al. (2014) show the effects of interpolating the undrained shear strength with different stress consolidation measures, though there is no clear evidence on which measure is the best.

5) The value of the consolidation stress ratio at failure  $K_f$ , which refers to the condition of consolidating the sample at the highest possible value of  $K_c$ , can be estimated as:

$$K_f = \frac{\frac{\tau_{ff} - c'}{\tan \phi'} + \tau_{ff} \tan \phi' + \frac{\tau_{ff}}{\tan \phi'}}{\frac{\tau_{ff} - c'}{\tan \phi'} + \tau_{ff} \tan \phi' - \frac{\tau_{ff}}{\tan \phi'}} \quad (3.8)$$

where  $K_f$  is constant if the cohesion is zero.

6) The anisotropic undrained shear strength for the consolidation ratio  $K_c$  of interest is estimated by linearly interpolating between the two failure envelopes:

$$\tau_{ff, K_c} = \frac{\tau_{ff, K_c=K_f} - \tau_{ff, K_c=1}}{K_f - 1} (K_c - 1) + \tau_{ff, K_c=1} \quad (3.9)$$

When  $K_c$  is equal to  $K_f$  the drained failure envelope is obtained, while for  $K_c$  equal to 1 the formula returns the isotropic undrained strength.

The aforementioned procedure is applied to the core of the Farneto del Principe dam, based on ICU results. The initial static stress condition was evaluated using the 2D finite difference software FLAC (Itasca, 2019) before applying the dynamic input. Hence, the effects of the embankment construction and reservoir are taken into account. The ACU shear strength has been estimated using  $s'_c$  and  $\sigma'_{fc}$  as the consolidation stress measures. Figure 3.38a and 3.38b shows mean failure envelopes (computed from the mean values of  $c'$ ,  $\phi'$ ,  $d_R$ , and  $\psi_R$ ) estimated from the ICU tests, together with the anisotropic undrained strength failure envelope, for the

two consolidation stress measures. The differences in the range of interest of the consolidation stress are relatively small. Table 3.3 shows the mean percentage differences. The differences between anisotropic and isotropic strengths can also be seen in Figure 3.38c and 3.38d, indicated by the slopes of three connecting points.

Figure 3.39a and 3.39b show the variation of the anisotropic undrained shear strength and the ratio to the vertical confining stress. The strengths are essentially the same, so in this case it does not matter which profile to use. Montgomery et al. (2014) note that the analysis used to compute the  $K_c$  has a larger effect on the undrained shear strength. Hence, the interpolation measure does not affect the result. However, in the case of the  $s'_c$  as interpolation measure, the undrained shear strength envelope is above that for drained conditions for all the stresses of interest. This is not necessarily true, especially at high consolidation stresses.

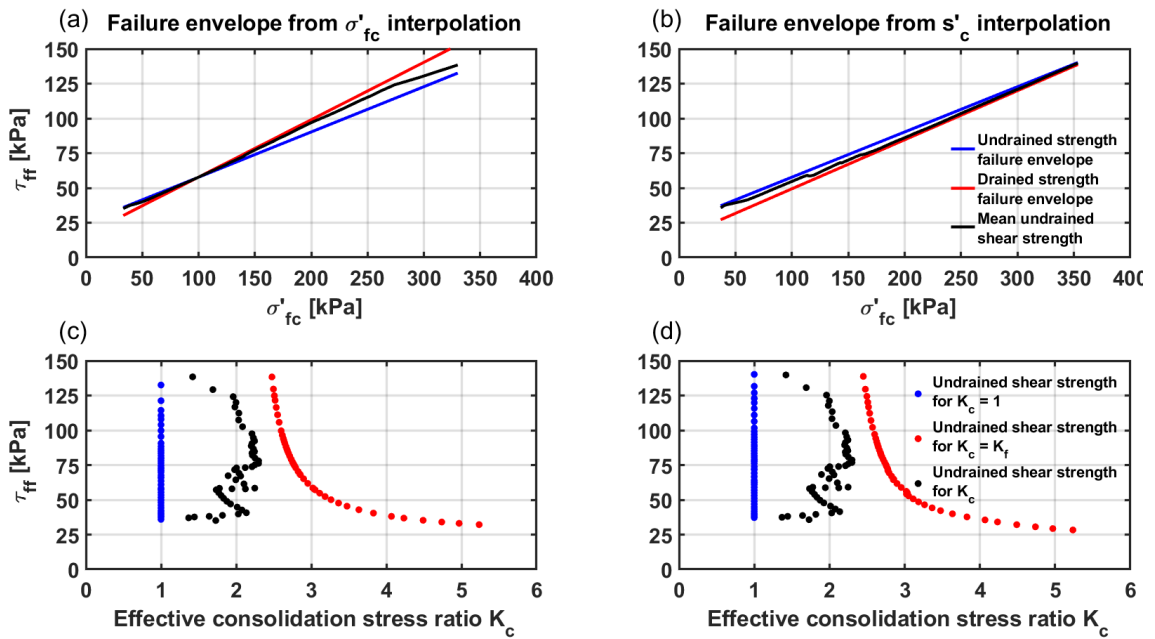


Figure 3.38: Mean failure envelopes as a function of (a)  $s'_c$  and (b)  $\sigma'_{fc}$ , and versus various consolidation stresses (c) and (d).

Finally, the undrained strength profiles for both isotropic and anisotropic cases are shown in Figure 3.39c and 3.39d. The differences are negligible for shallow depths. However, they become slightly more important at larger depths. This means that care must be taken when using anisotropic undrained shear strength values, because they could lead to slightly non-conservative results if compared to those obtained using isotropic strengths.



Table 3.3: Mean percentage variation of the anisotropic undrained shear strength to the isotropic drained and undrained strength. A positive value means that the anisotropic undrained shear strength is higher.

Interpolation from $s'_c$		Interpolation from $\sigma'_{fc}$	
Mean percentage variation in the consolidation stress of interest		Mean percentage variation in the consolidation stress of interest	
Drained strength (kc = kf)	Isotropic undrained strength (kc = 1)	Drained strength (kc = kf)	Isotropic undrained strength (kc = 1)
6.51	-4.87	0.19	2.47

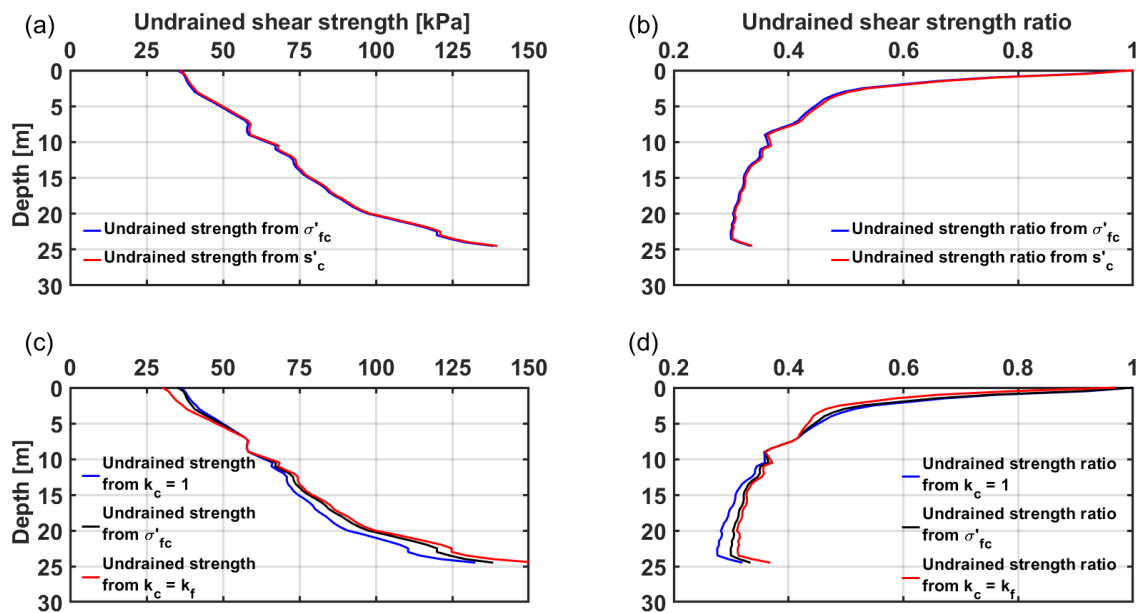


Figure 3.39: Variation of the undrained shear strength within the clay core of the Farneto del Principe dam.

### 3.5.5.2 SHANSEP procedure

The Stress History and Normalized Soil Engineering Properties procedure (Ladd and Foott, 1974; Ladd and DeGroot, 2003) can be used to estimate the variation of undrained shear strength with OCR. The method works well if the soil presents a normalized behavior, i.e., the ratio of the undrained strength to the vertical effective stress in situ is constant under normally consolidated conditions. Typical results of the SHANSEP procedure are shown in Ladd et al. (1977), where the authors estimate the variation of the undrained shear strength ratio with OCR for clays based on results of ACU triaxial tests. The SHANSEP procedure provides exact results if:

1) The preconsolidation history profile is well defined. This can be accomplished by performing several consolidation tests.

2) The samples are tested to pressures exceeding the in situ effective vertical stress.

However, the methodology does not work for sensitive clays, as their undrained strength does not increase with the consolidation pressure (Jamiolkowski, 1985). The results of this procedure are usually given in the form of the so-called SHANSEP equation, which relates the undrained shear strength ratio to OCR as follows:

$$\left(\frac{s_u}{\sigma'_v}\right)_{OC} = \left(\frac{s_u}{\sigma'_v}\right)_{NC} OCR^m \quad (3.10)$$

where  $\left(\frac{s_u}{\sigma'_v}\right)_{OC}$  and  $\left(\frac{s_u}{\sigma'_v}\right)_{NC}$  are the undrained shear strength ratio of the soil under normally consolidated (also known as  $S$ ) and overconsolidated conditions, respectively, and  $m$  is fitting parameter, with a typical value of 0.8.  $\left(\frac{s_u}{\sigma'_v}\right)_{NC}$  can be estimated from ICU triaxial tests when the confining pressure exceeds the in situ vertical effective stress. If the same specimen is subjected to several consolidation pressures, more details can be obtained regarding the disturbance and normalization of the sample. This can be done using the Coatsworth (1985) procedure, who suggests plotting the undrained strength ratio versus the ratio of the effective confining stress to the preconsolidation pressure. Figure 3.40 shows the results obtained for the Farneto del Principe dam core specimens used for the ICU tests. Of the five tests, four of them had a specimen subjected to a consolidation pressure greater than the preconsolidation stress. As such, it is not possible to get proper information about the soil normalization (more points with  $\frac{\sigma'_c}{\sigma'_p}$  greater than 1.5 per specimen would be necessary).

However, some considerations can be made about the undrained shear strength ratio by considering specimen depths. The S5C3 specimen taken at 19.75 m has the lowest values of the  $\frac{s_u}{\sigma'_v}$  ratio and the smaller variation with  $\frac{\sigma'_c}{\sigma'_p}$ ; this is probably due to the soil being almost normal consolidated at that depth (OCR of about 1.2). All specimens seem to have some disturbance, and only the S6C1 specimen seems to show strength normalization characteristics. Since there is not a consistent value of the  $\frac{s_u}{\sigma'_v}$  ratio, a conservative approach should be used in this case.

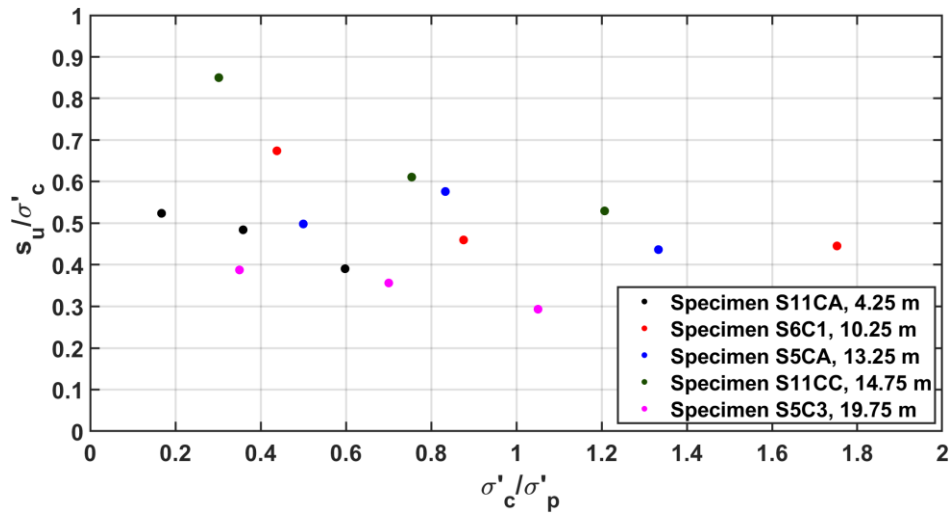


Figure 3.40: Samples normalization of the five ICU tests performed.

A constant value of 0.35 could be deemed appropriate. Another way of interpreting these results could be to create two different relationships for the undrained shear strength ratio (i.e. using different values of  $S$  at different depths). Figure 3.41 shows the undrained shear strength variation with depth using the SHANSEP procedure and the relationship with OCR. It can be seen that at 10 m depth the undrained strength reaches the minimum value, with slightly larger values at shallow depths. This is due to the value of OCR being as high as four in the upper part of the core. Figure 3.42 shows the Mohr-Coulomb envelope and the undrained failure envelope using the SHANSEP procedure. At low consolidation stresses, the drained strength is smaller than that under undrained conditions, while the opposite is true for high values of OCR. The condition of unitary OCR, and thus a normalization of the  $\frac{s_u}{\sigma'_v}$  ratio, can be identified when the  $s_u$  reaches a linear relationship to the effective consolidation stress.

### Comparison between the procedures to estimate the undrained shear strength

Figure 3.43 shows the undrained shear strength and the relative ratio estimated using the ACU (Montgomery et al., 2014) and SHANSEP procedures (Ladd and DeGroot 2003). The SHANSEP procedure is less conservative, though the  $\frac{s_u}{\sigma'_v}$  ratio is comparable for deeper layers. At shallow depths, the ratio can become too high due to the low consolidation stresses, hence, a limiting value of 1 should be used (Boulanger, 2019).

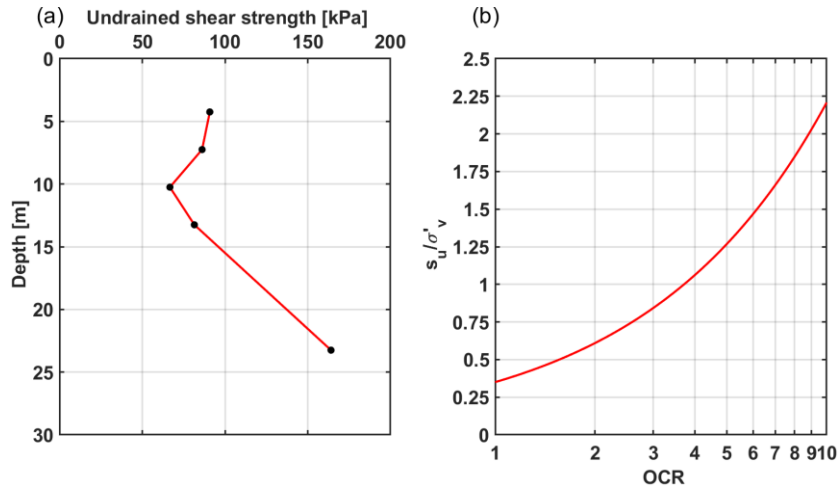


Figure 3.41: Undrained shear strength profile with depth using SHANSEP methodology (a) and variation with the OCR (b).

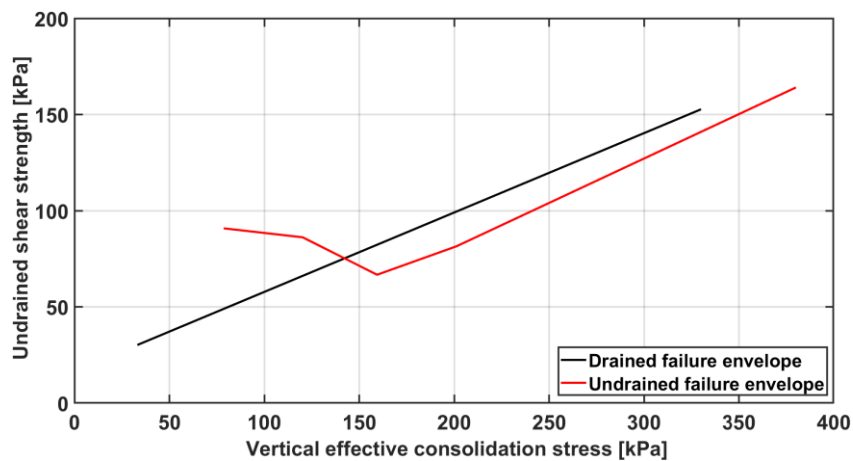


Figure 3.42: Comparison between drained and undrained shear strength failure envelopes.

The undrained strength, however, is higher at shallow depths, and it is not consistent with the ACU methodology, which implies a monotonic trend of  $s_u$  with depth. For these reasons, the final choice of the undrained shear strength ratio should be taken with care. If a well-detailed stress history profile is known and the soil presents a normalized behavior (that must be proved by means of several laboratory tests) then the SHANSEP methodology, despite providing non-conservative results, can be deemed a good representation of the site undrained strength. The ACU methodology, on the other hand, provides slightly conservative results (but that can be still non-conservative when compared to isotropic undrained strengths). In this case, more weight is given to the ACU procedure, hence

choosing a  $\frac{s_u}{\sigma'_v}$  value of 0.5 in the upper 10 meters, and a value of 0.35 in the bottom part for the entire core. However, if a large spatial variation is present, different relationships can be built based on the in-situ effective stresses or preconsolidation profiles, when they are available.

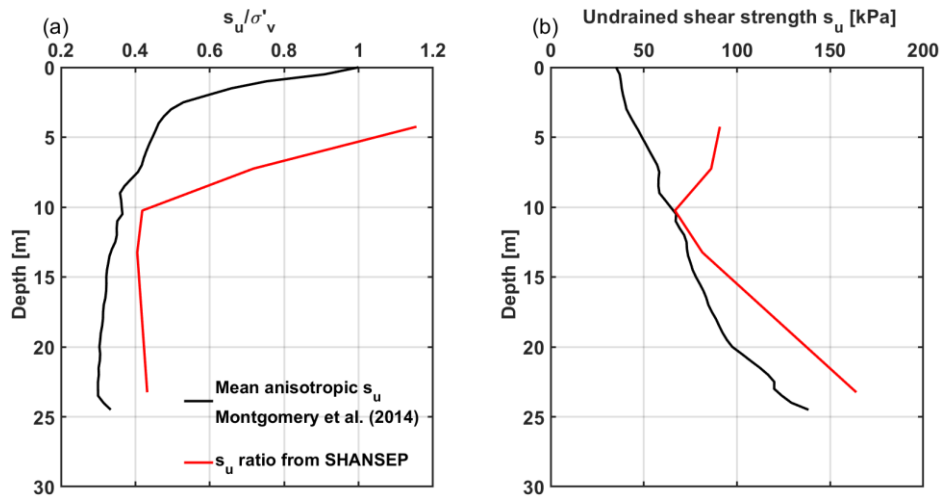


Figure 3.43: Comparison between the undrained shear strength profiles estimated from the SHANSEP and the Montgomery et al. methodology.

## 4. Non-ergodic hazard analysis for the Farneto del Principe dam site

The current Italian building code (NTC 2018) relies upon PSHA-based seismic hazard only based on areal sources. No finite faults or more modern distributed seismicity models are used in the fault source characterization model. This means that PSHA results are based on seismicity happening on large areas within which the seismic rate is assumed as homogeneous and based on historical information only (i.e., no geological or paleoseismological constraints are used). However, the Italian dam standards (Minister of the Infrastructure, 2014) requires site-specific PSHA if dams are located in an area of the country characterized by high seismicity (i.e., the PGA for a 475-year return period is  $> 0.1g$ ). Zimmaro and Stewart (2017) presented an ergodic site-specific hazard analysis for the Farneto del Principe dam site. To make the analysis non-ergodic, site-specific amplification functions are needed. In this chapter, such amplification functions are derived using 1D numerical ground response analyses (GRA). These analyses are based on ground motions selected and scaled to be consistent with PSHA-derived target spectra. Finally, the results of GRA in the form of amplification functions are used to modify selected GMMs. These modified GMMs are then used within a formal non-ergodic PSHA process (i.e., the hazard integral is computed using this modified GMMs).

### 4.1 Ground Motion selection and scaling

The choice of hazard-consistent ground motions is a key component of GRA and response history analyses. This is usually a three-step procedure: (1) a target spectrum for reference site conditions is defined, (2) time series are chosen to be consistent with tectonic regime, magnitude-distance, and local site conditions of the site of interest, (3) input motions are linearly scaled to be consistent with the target spectrum. As an alternative to linear scaling procedures, step 3 can be performed by modifying ground motions in the frequency domain. Such approach is commonly referred to as spectral matching. In this study, ground motions will be selected and scaled linearly in the time domain. According to Bozorgnia et al. (2010), the shape of response target spectra is also an important feature in ground motion selection procedures because it is linked to structural nonlinear response. As shown by Zimmaro and Stewart (2017), target spectra should be derived from site-specific PSHA in order to evaluate the seismic response of critical infrastructure systems. For these reasons, two different target spectra are considered in this study: (1) the Uniform Hazard Spectrum (UHS), and (2) the Conditional Spectrum (CS).

#### 4.1.1 The Uniform Hazard Spectrum

The UHS is used for many structural and geotechnical earthquake engineering applications. It is a spectrum comprising pseudo-spectral acceleration values at various periods having the same probability of exceedance (hence at a uniform hazard). The UHS is the result of a PSHA. As a result, it represents the contribution of multiple magnitude-distance scenarios and ground motion combinations. Hence, there is not a single earthquake associated to it. The UHS is a conservative target spectrum, as it implies that all spectral ordinates occur within a single ground motion (Baker, 2011). Figure 4.3 shows four different UHS are calculated at the following return periods: 1460, 75, 50, and 30 years, based on a site specific PSHA performed with the open source software OpenQuake (GEM, 2019). These return periods were selected based on the required return periods to evaluate the seismic performance of earth dams by the Italian dam standards (Minister of the Infrastructure, 2014).

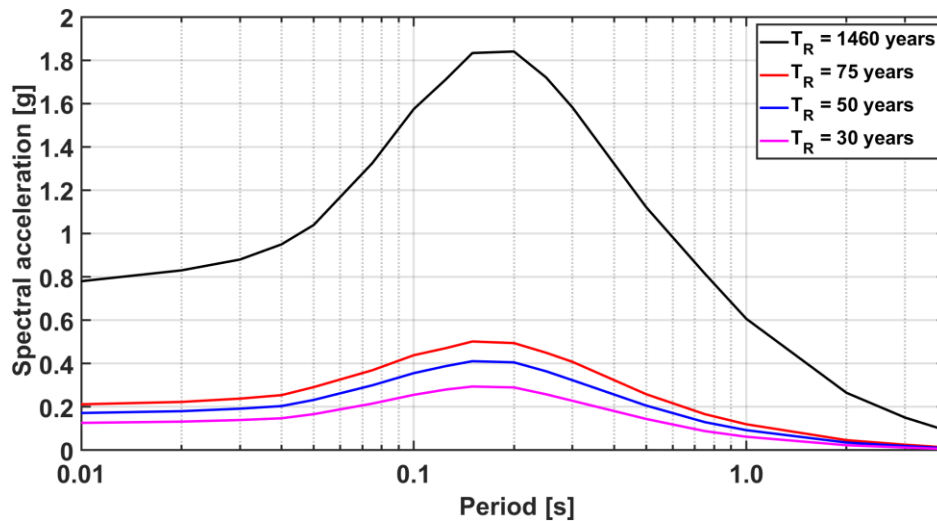


Figure 4.1: Ergodic Uniform Hazard Spectra for Farneto del Principe dam site, for four return periods.

#### 4.1.2 The Conditional Spectrum

As mentioned in the previous section, the UHS is a conservative target spectrum. An alternative target spectrum was introduced by Baker and Cornell (2006b) and Baker (2011): the Conditional Mean Spectrum (CMS). The CMS represents the mean of a statistical distribution called Conditional Spectrum (CS). The CS is the probability distribution of log spectral acceleration values, conditional on a given spectral value

at a conditioning period ( $T^*$ ). The CS distribution can be fully described by its means, standard deviations, and correlations. It is worth noting that “mean spectrum” refers to the logarithmic spectral accelerations. Hence, the CMS corresponds in reality to the median spectral value. However, the CMS calculation procedure involves calculation of mean logarithmic spectral ordinates, which is why the terminology “mean” is used. These types of response spectra are also called *scenario target spectra* (STS), as they are consistent with a scenario characterized by a certain magnitude, distance, and rate of occurrence. Spectral shapes of STS are more similar to those of ground motion response spectra. As a result, they also carry the benefit of requiring smaller scaling factors than UHS. Conditional Spectra can be obtained from databases or statistical procedures (i.e., Monte Carlo simulation) to be consistent with mean, standard deviation, and correlations of the CS probability distribution.

The definition of a CS requires the knowledge of the controlling scenario(s) for the site of interest. Such scenario can be identified using results of the so-called disaggregation of the seismic hazard (Bazzurro and Cornell, 1999). Disaggregation results can help identifying source, distance, and ground motion percentiles contributing to the hazard at the site. Source, distance, and ground motion percentiles are identified by magnitude, source-to-site distance (e.g., the Joyner-Boore distance), and a parameter called epsilon ( $\epsilon$ ), that defines how different a ground motion is from that implied by a GMM:

$$\epsilon(T) = \frac{\ln S_a(T) - \mu_{\ln S_a}(M, R, V_{s30}, T)}{\sigma_{\ln S_a}(M, R, V_{s30}, T)} \quad (4.1)$$

where  $S_a(T)$  is the spectral acceleration at the hazard level for which the disaggregation is computed and  $\mu_{\ln S_a}(M, R, V_{s30}, T)$  and  $\sigma_{\ln S_a}(M, R, V_{s30}, T)$  are the mean and standard deviation of logarithmic spectral accelerations (for a given magnitude and distance). These terms can be easily computed using a GMM. For the CMS computation, epsilon can be seen as the number of standard deviations by which a given mean logarithmic spectral value of the controlling scenario (for a given magnitude and distance) differs from the mean logarithmic value predicted by a target spectrum (e.g., the Uniform Hazard Spectrum). The Conditional Mean Spectrum can be computed as:

$$\mu_{\ln S_a(T_i)|\ln S_a(T^*)} = \mu_{\ln S_a}(M, R, V_{s30}, T_i) + \rho(T_i, T^*)\epsilon(T^*)\sigma_{\ln S_a}(M, R, V_{s30}, T_i) \quad (4.2)$$



where  $T^*$  is the conditioning period and  $\rho(T_i, T^*)$  is the correlation coefficient between the  $\epsilon$  at the two periods.  $T^*$  is usually taken as the first-mode excitation period of the structure, but multiple conditioning periods (i.e. multiple CMS) should be used if the behavior of the structure is also influenced by higher-modes. The CMS does not capture variability. As a result, a conditional standard deviation must be introduced to compute the CS:

$$\sigma_{\ln S_a(T_i) | \ln S_a(T^*)} = \sigma_{\ln S_a}(M, R, V_{s30}, T_i) \sqrt{1 - \rho(T_i, T^*)^2} \quad (4.3)$$

The CS calculation procedure is straightforward when a single GMM is used. However, PSHA usually utilizes multiple GMMs to capture epistemic uncertainties. There are several methods available to compute the CS when multiple GMMs are involved (Lin et al., 2013; Carlton and Abrahamson, 2014). In this study the procedure proposed by Carlton and Abrahamson (2014) named method 2.5 was used. This approach consists in combining all GMMs by identifying the controlling earthquake scenario using each GMM separately and then calculating the weighted average of  $\mu_{\ln S_a(T_i) | \ln S_a(T^*)}$  and  $\sigma_{\ln S_a(T_i) | \ln S_a(T^*)}$  for all GMMs using their logic tree weights. More details about the GMMs selected and used in this study are provided in §4.5.

In this study, disaggregation analyses were performed for the spectral acceleration at  $T = 0.25$  s (fundamental period of the dam-foundation system). Table 4.1 shows the disaggregation results in terms of magnitude-distance-epsilon for all hazard levels considered. It should be noted that the  $\epsilon$  reported here is the mean value from disaggregation and not the  $\epsilon(T^*)$  used to construct the CMS. Disaggregation analyses relative to  $S_a(0.25s)$  were also performed for various return periods, the mean results are plotted in Figure 4.4. It is worth noting that OpenQuake provides disaggregation distance outputs in terms of Joyner-Boore distance. However, the Zhao et al. GMM adopts the minimum source-to-site distance. Thus, a conversion between distances (Kaklamanos et al., 2011) was necessary to create Figure 4.4. The conditioning period adopted to calculate the CS in this study is the fundamental period of the system dam-foundation, which is 0.25 seconds. This value was estimated both from a modal analysis (Zimmaro and Ausilio, 2020) and with the study of free damped oscillations of the dam. A summary of all target spectra calculated for the four selected return periods is presented in Figure 4.5.

Table 4.1: Magnitude Distance Epsilon disaggregation results for spectral acceleration at period 0.25s for different return periods.

$T_R = 30$ years			$T_R = 50$ years			$T_R = 75$ years			$T_R = 1460$ years		
M	R [Km]	$\epsilon$	M	R [Km]	$\epsilon$	M	R [Km]	$\epsilon$	M	R [Km]	$\epsilon$
6.33	55.0	1.08	6.48	52.4	1.14	6.58	50.8	1.20	7.21	49.0	1.67

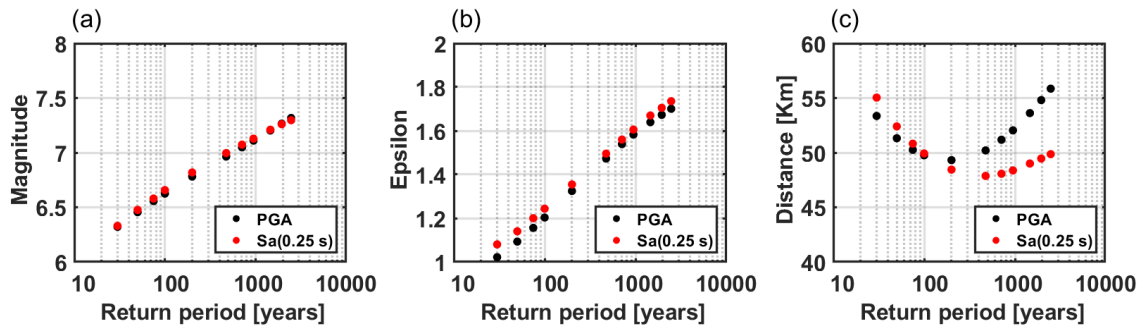


Figure 4.2: Disaggregation results for various return periods vs mean (a) magnitude, (b) epsilon, and (c) Joyner-Boore distance.

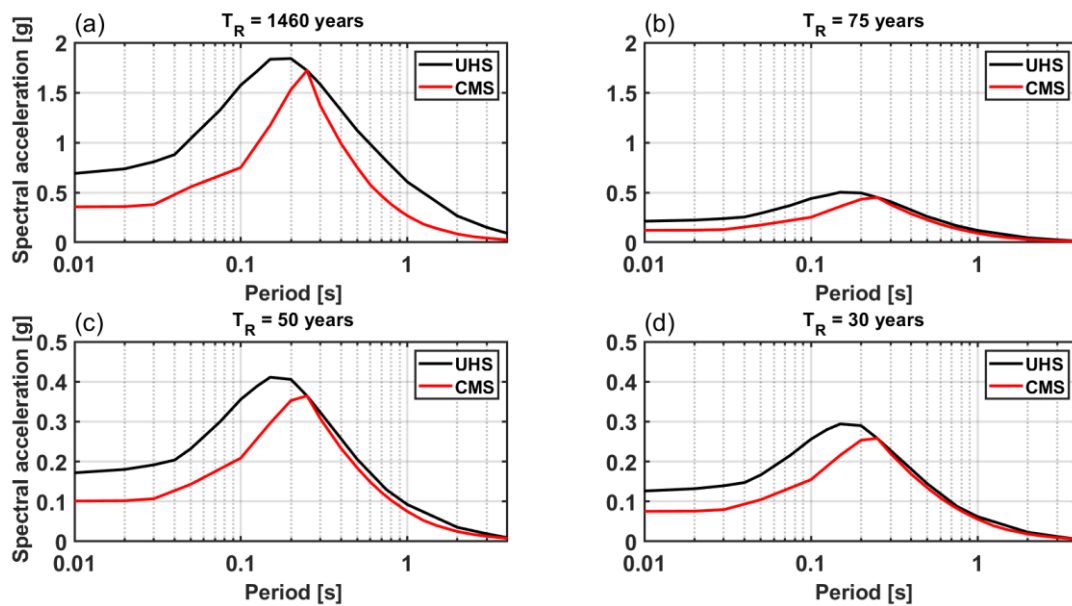


Figure 4.3: Uniform Hazard Spectra and Conditional Mean Spectra for the return periods considered.

#### 4.1.3 Ground motion selection algorithms

Once the target spectra are defined, input motions to use in GRA and response history analysis can be selected. There are several procedures for choosing a ground

motion sets consistent with a target spectrum (e.g. Naeim et al. 2004; Youngs et al. 2007; Jayaram et al. 2011). These methods usually involve ground motion scaling procedures, which are typically performed in the time domain to avoid any modifications to the frequency content of the motions. Some of these algorithms try to scale the ground motions to achieve a perfect match with a mean spectrum. According to Baker et al. (2017) and Jayaram et al. (2011) however, this approach is not suitable for all target spectra, because it does not include the response spectrum variability. Instead, the selected ground motion set should reflect the target distributions from predictive models (e.g., Lin et al. 2013b). The choice of an appropriate ground motion selection algorithm is one of the most important steps of dynamic analyses because it defines the input motions set.

Another crucial step is to guarantee the hazard-consistency of selected motions. This goal is achieved by ensuring that the selection is done selecting ground motions consistent with the hazard scenario evaluated from the disaggregation of the seismic hazard (i.e., the ground motion set is selected among recordings within a specific range of magnitude and source-to-site distance and for a given tectonic regime). Thus, the ground motions selected are consistent to the tectonic regime, magnitude, distance, and local conditions of the site. The ground motion database used in this study is the global Pacific Earthquake Engineering Research Center, Next Generation Attenuation (PEER) NGA West-2 Ground Motion Database (Ancheta et al., 2014). In this database, over 40% of recordings for normal fault mechanism comes from Italian earthquakes. The following additional criteria are used to screen a proper set of ground motions: (1) only one record for each seismic event is chosen; (2) the selected lowest usable frequency is 0.5; (3) no aftershock records are considered; (4) since almost all faults in the vicinity of the dam are normal fault, when possible, normal faulting style is favored; (5) the scale factor range adopted is 0.5-2.5; (6) the ground motion with response spectra far away from the mean are discarded, since they can bias the nonlinear response of the structure (Kramer et al., 2012).

#### 4.1.3.1 Ground motion selection algorithm for UHS as target spectrum

As discussed in §4.1.1, the UHS is the envelope of contributions from various magnitude-distance contributions with spectral ordinates that have the same rate of exceedance, as computed from PSHA. For each period, however, PSHA already accounts for variability in spectral accelerations, so adding any variance to the UHS

would modify the exceedance rate of spectral values (Jayaram et al. 2011). Such modification would be conceptually wrong. This could also imply that a selected ground motion record could exceed almost all spectral values of the UHS, which is unlikely to happen (e.g., Bommer et al., 2000; Naeim and Lew, 1995; Reiter, 1990). For these reasons, a ground motion set compatible with a UHS should have a mean response spectrum that is as close as possible to the target.

The spectral mismatch (i.e., the difference between the pseudo-spectral accelerations of the record and that of the target) can be measured using the Mean Squared Error (MSE) defined as follows:

$$MSE = \frac{\sum_i^N w(T_i) \{ \ln[Sa_{target}(T_i)] - \ln[f \cdot Sa_{record}(T_i)] \}^2}{\sum_i^N w(T_i)} \quad (4.4)$$

where  $Sa_{target}(T_i)$  and  $Sa_{record}(T_i)$  are the pseudo-spectral accelerations of the target and of the record at period  $T_i$ ,  $N$  is the number of points sampling the period range of interest,  $f$  is the scale factor and  $w(T_i)$  is a weight function that gives more weight to mismatches within a the period range of interest (technical report PEER). The algorithm adopted in this study follows all criteria listed above and scales ground motion sets until the minimal value of MSE is reached and the selected mean spectrum is consistent with the target in the period range that has relevance to the site (and structure) of interest. In this study, the period range selected to ensure this consistency is  $T = 0-1s$ . Within this period range a constant value of  $w(T_i) = 1$  is selected. Figure 4.6 shows the response spectra of all the input motions selected. This input motions will be used to perform 1D ground response analyses (GRA) as illustrated in §4.2 and response history analyses shown in Chapter 7.

#### 4.1.3.2 Ground motion selection algorithm for CS as target spectrum

Unlike the UHS, the CS is built to be consistent with a hazard scenario and explicitly represents the distribution from predictive models. There are several algorithms capable of selecting ground motions with some form of response spectral variability (Kottke and Rathje, 2008; Bradley, 2012; Ha and Han, 2016). In this study, the Baker and Lee algorithm (2017) was selected and used. This algorithm improves that by Jayaram et al. (2011). It selects ground motions from a database while ensuring consistency with response spectra distribution (i.e., mean, variance, and correlations of spectral ordinates at a selected range of periods).

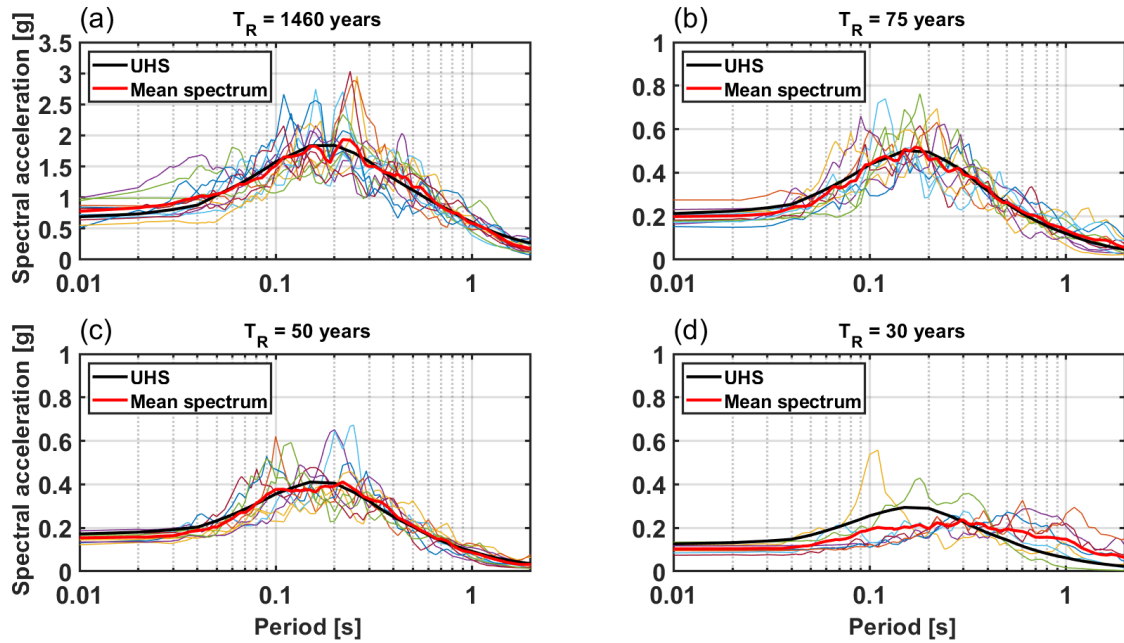


Figure 4.4: Selected response spectra using the UHS as target spectrum for the following return periods: (a) 1460 years, (b) 75 years, (c) 50 years, and (d) 30 years.

The key steps for this procedure are: (1) compute the target spectrum distribution, which is assumed multivariate normal (making it possible to fully describe it by means of means, standard deviations, and spectral ordinates correlations); (2) statistically simulate response spectra from the selected distribution using the Monte Carlo method; (3) screen out from the database ground motions that are not hazard-consistent and do not respect the general criteria presented in §4.1.3 (e.g., no aftershocks and low scale factor); (4) select ground motions whose response spectra is consistent with those obtained using Monte Carlo simulations; (5) run an optimization procedure to select ground motions to fit the target spectrum distribution (e.g., broaden range of input parameters). In this process, all additional criteria used for ground motion selection using the UHS (§4.1.3.1) are applied. A schematic illustrating the algorithm is shown in Figure 4.7 (adapted from Baker and Lee, 2017). Figure 4.8 shows the results obtained for the 1460-year return period. The total number of records shown in Figure 4.8 is 51.

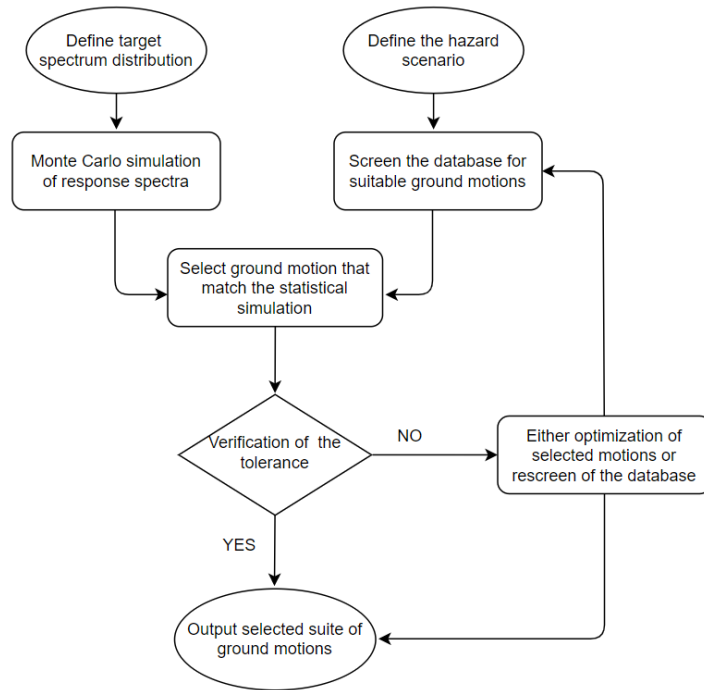


Figure 4.5: Schematic representation of the ground motion selection algorithm for CS as target spectrum (Adapted from Baker and Lee, 2017).

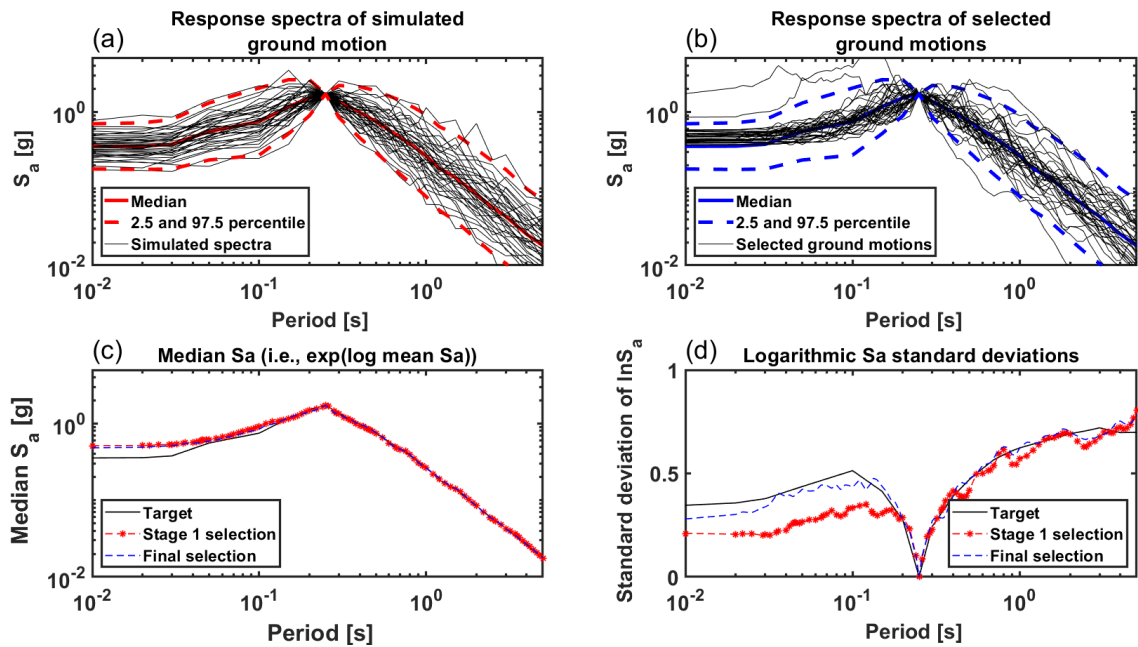


Figure 4.6: Results of the ground motion selection algorithm using the CS as target spectrum: (a) Monte Carlo simulated spectra; (b) Response spectra of selected motions; (c) Median of the selected motions; and (d) Standard deviation match.

## 4.2 Seismic Ground Response Analyses

Site response analysis is one of the most important components of seismic hazard analysis procedures. It consists in evaluating how ground motions are modified as they travel from the source through surficial rock and soil layers. Thus, the site geometry, topography, morphology, and stratigraphy, can substantially modify ground motions, and consequently, the seismic response of structures and infrastructure systems. Seismic site response can be subdivided into various components including: (1) basin effects, (2) topographic effects due to the presence of ridges, canyons, and/or slopes, and (3) stratigraphic effects. Basin and topographic effects can be analyzed with 2D and/or 3D models and/or inferred from the analysis of ground motion recordings. Stratigraphic effects are one-dimensional in nature and can be analyzed using 1D ground response analysis (GRA) simulations and/or free-field ground motion recordings. The evaluation of these effects and the analyses of the inherent variabilities and uncertainties associated to them are of great relevance for earthquake engineering. Since neither topographic irregularities, nor basin features are present at the Farneto del Principe dam site, in this section the focus will be on 1D ground response effects. Several factors influence such effects, such as: (1) soil nonlinearity, (2) the presence of impedance contrasts, and (3) resonance effects. These effects can all be quantified with GRA. Results from this analysis can be used to build amplification functions that can be incorporated into the PSHA framework. In this section, GRA performed at the Farneto del Principe dam site are illustrated. Such analyses are conducted considering the foundation soils in free-field condition. The numerical GRA model is built utilizing the results of the field investigation and laboratory tests shown in Chapter 3.

The field investigation test results presented in §3.4 show that there is a non-negligible variability in the shear wave velocity profiles measured from down-hole tests at boreholes S1 and S8. This inherent aleatory variability can be considered in GRA using  $V_s$  profile randomization procedures (e.g., Toro, 1995). Such randomization procedures are used to generate suites of statistically-based  $V_s$  profiles. In this study, this randomization procedure was used based on the information of down-hole tests. Figure 4.7 shows the available  $V_s$  profiles at S1 and S8, and three representative randomized profiles (mean, upper, and lower bound curves) obtained using the Toro (1995) approach. The generated randomized profiles are piecewise and are specifically calibrated to follow the general trend of



the available down-hole test data. In the numerical GRA model used in this study, the clay bed is modeled as an elastic half-space with a shear wave velocity of 450 m/s. This value is consistent with measured velocities shown in Chapter 3.

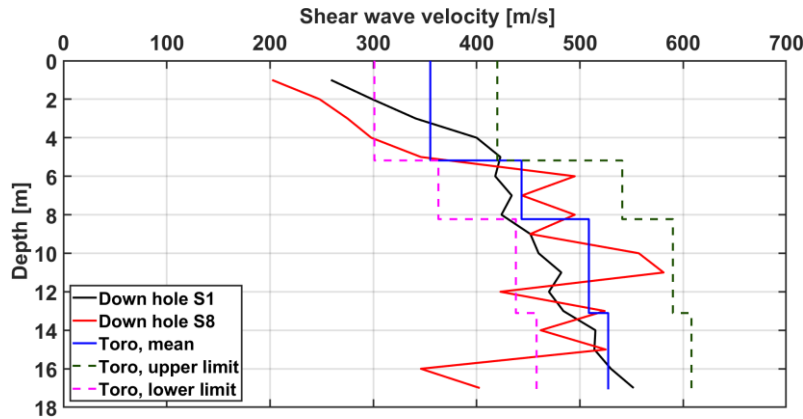


Figure 4.7: Measured and randomized shear waves velocity profiles of the alluvial foundation adopted for GRA.

All numerical GRA analyses are performed with the open source software DeepSoil version 6.1 (Hashash, 2016). This software implements both, fully nonlinear and equivalent linear seismic GRA of 1D soil columns. The appropriate method of analysis should be selected based on the expected level of strain (Kwok et al., 2007). According to Stewart et al. (2014) and Kim et al. (2016), a good indicator to select the method of analysis is the strain index, defined as the ratio of Peak Ground Velocity (PGV) of the outcropping input motion and the time-averaged shear wave velocity profile in the upper 30m ( $V_{s30}$ ). In general, as shear strain increases so does the nonlinearity of soil, and there is a strain threshold above which the equivalent linear method is no longer capable of predicting the actual site response faithfully (Kwok et al., 2007). Many authors attempted to propose a numerical value for this limiting threshold (e.g., Kaklamanos et al., 2015; Kim and Hashash, 2013; Assimaki and Li, 2012). In general, it is reasonable to assume this value as the reference shear strain (i.e., the strain that corresponds to a value of 0.5 in the modulus reduction curve). Since input motions selected and used in the GRA for this study (shown in §4.1.3) are expected to produce large strains, the General Quadratic Hyperbolic (GQH, Groholoski et al., 2016) nonlinear model was selected. This model is implemented in DeepSoil. It can model both small- and large-strain behaviors of soils.



Modulus reduction and damping (hereafter MRD) curves are evaluated using the Menq model (2003), which is suitable for coarse material. This model requires the following input parameters: uniformity coefficient  $C_u$  and median grain size  $D_{50}$ . A series of grain size distribution tests were performed on the alluvial material during the geotechnical investigation program (Figure 4.2) to characterize the dam foundation material. It was found that the variability in particle size distribution curves shown in Figure 4.8 does not affect appreciably MRD curves. As a result, the mean value of  $C_u$  and  $D_{50}$  are used in this study. A frequency-independent viscous damping formulation is used to model the small strain damping in this study. The hysteretic behavior is modeled with a non-Masing formulation implemented in DeepSoil (Phillips and Hashash, 2009) where the parameters are chosen to obtain a good fit with MRD curves.

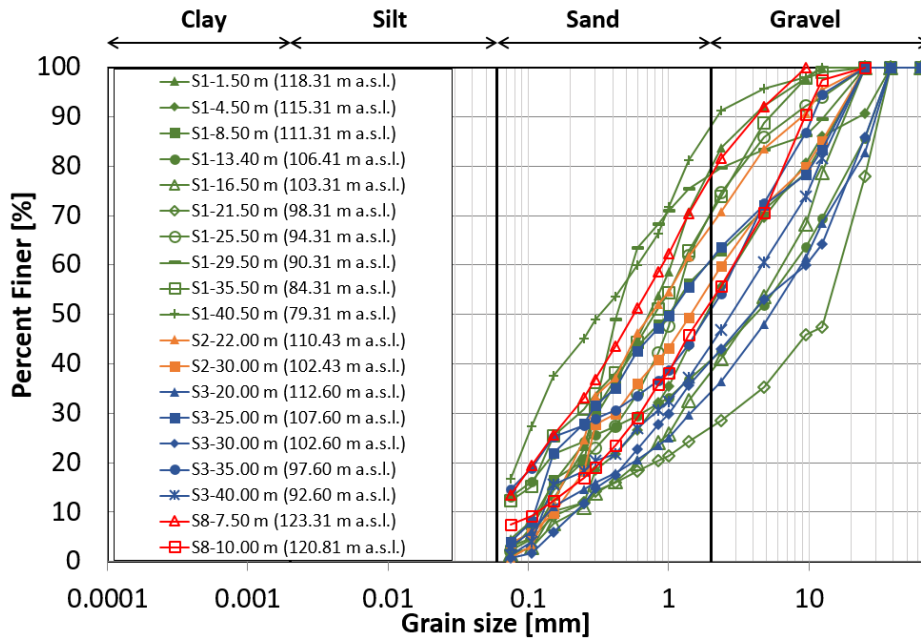


Figure 4.8: Grain size distributions for the alluvial foundation of Farneto del Principe dam.

### 4.3 Amplification functions

To generate a non-ergodic PSHA, GRA results need to be converted into amplifications functions. These functions are then used to modify GMMs that will be used in the modified PSHA hazard integral. To this end, GRA-related mean site amplification functions must be expressed following specific functional forms to be implemented in a GMM. A typical amplification function formulation is that

proposed by Seyhan and Stewart (2014) and implemented in the Boore et al. (2014) GMM:

$$\ln \bar{Y} = f_1 + f_2 \ln \left( \frac{x_{IM,ref} + f_3}{f_3} \right) \quad (4.5)$$

where  $\bar{Y}$  is the mean amplification;  $x_{IM,ref}$  is the intensity measure of reference used to define the amplification level;  $f_1$  is the weak motion amplification;  $f_2$  represents non linearity (i.e. the curve slope for high  $x_{IM,ref}$  values);  $f_3$  is the value of intensity measure that separates visco-elastic and nonlinear behaviors. The last three parameters are estimated regressing GRA results. In this study, amplification functions are built for a wide range of  $x_{IM,ref}$ , using 13 ground motions for each hazard level employed. For very low IM values, the ground motions consistent with a return period of 50 and 30 years were manually scaled to evaluate the amplification functions. Formally, these inputs are not associated with any rate of exceedance (though it is reasonable to assume that they happen frequently) but they are used to constrain the amplification function in the linear domain (low strains).

GRA are performed only in the period range where results are considered valid, which is usually up to two times the fundamental period of the site of interest (Stewart et al., 2014). However, in the case of the Farneto del Principe dam, the alluvial foundation overlays a clay deposit with shear wave velocity of about 450 m/s. This clay bed cannot be considered a proper compliant bedrock, whose real position is unknown and likely very deep (no borehole or geophysical test performed was able to identify it). For this reason, fundamental period of the site is not well defined and cannot be constrained by data. As a result, the period corresponding to the maximum amplification ( $T=0.1s$ ) was selected in this study and used in this application. The GRA-based amplification functions calculated for this site are the mean of seven amplification functions. Each of them was evaluated using one of the randomized shear wave velocity profiles calculated in §4.2. Figure 4.9 shows the GRA-based mean amplification functions obtained using both, the UHS and the CS, for various spectral ordinates. At short periods, mean amplification functions derived from the UHS have a more nonlinear trend than those obtained using the CS as target (Figure 4.9a-b-d). This is expected as when using the UHS as target, selected ground motions are more intense and determine higher strain levels. This in turn leads to large damping levels, higher nonlinearity, and an overall lower amplification. This effect is not visible for  $S_a(0.1s)$ . This is probably due to

resonance effects prevailing on other factors. The analyses were performed only for a limited number of periods, while for transition zone (zones of the plot between data points) an interpolation method proposed by Stewart et al. (2014) was used. For values greater than two times the site period the results of a semi-empirical model (Boore et al., 2014) were applied. At long periods, seismic quarter-wavelengths are longer compared to the profile thickness and no response can be realistically captured using a numerical model. This is evident in Figure 4.9d, where, for long periods, the amplification value is practically one. Figure 4.10 shows the parameters  $f_1$  and  $f_2$  and their variations across periods. Trends shown in Figure 4.10 highlights features exposed previously, with local peaks at  $T= 0.1s$  and values equal to a semi-empirical model beyond  $T = 0.25s$ . Parameter  $f_3$  is taken as constant in this study.

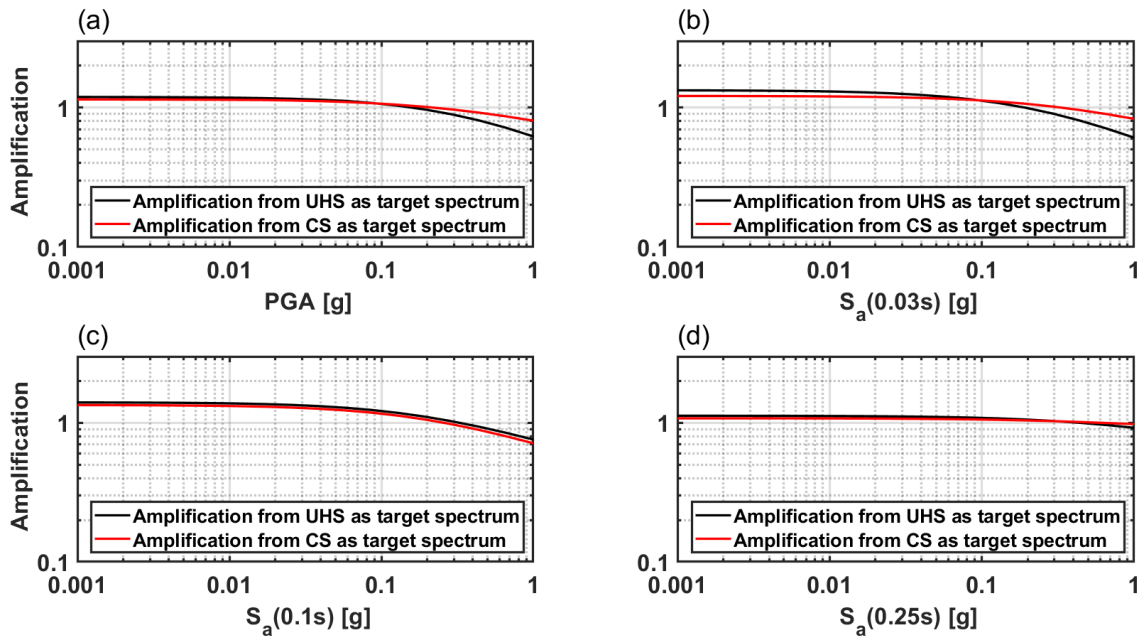


Figure 4.9: Mean amplification functions for the alluvial foundation of the Farneto del Principe dam for the following intensity measures: (a) PGA, (b)  $S_a(0.03s)$ , (c)  $S_a(0.1s)$ , and (d)  $S_a(0.25s)$ .

#### 4.4 Uncertainty analysis

One of the main benefits of GRA is to provide a better understanding of 1D local site response effects. Such infusion of knowledge results in a reduction of the epistemic uncertainties associated with the analysis being conducted. Following the concepts and notation illustrated in §2.3.1, in this section the standard deviation of a ground motion model (Boore et al., 2014) is partitioned into its various components.

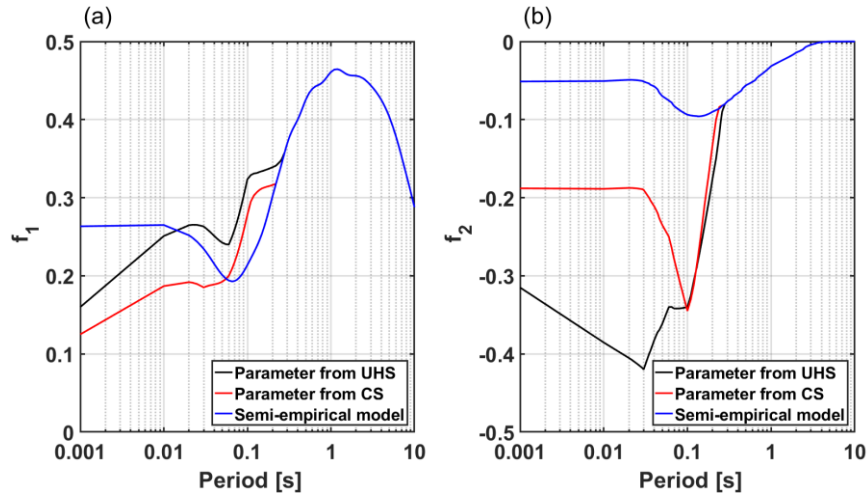


Figure 4.10: Variation across periods of parameters (a)  $f_1$  and (b)  $f_2$ .

The results of partition effort will then be used when GRA results are merged into GMMs that are ultimately going to be plugged in the PSHA hazard integral to perform a non-ergodic analysis. Local ground amplification ( $\phi_{lnY}$ ) uncertainties are quantified by considering several contributing sources. In this study, the following sources of uncertainties are explicitly considered: (1) shear wave velocities (by means of randomized profiles), (2) input ground motions (utilizing a large number of input recordings to perform the numerical analyses), (3) grain size distribution (considering the range of variability derived from laboratory data). Modulus reduction and damping curves were evaluated using the Menq (2003) model for coarse materials, which requires granulometry data. It was found that variability in grain size curves does not affect appreciably these curves. In the periods range where GRA is valid,  $\phi_{lnY}$  is relatively low, with CS amplifications less scattered (Figure 4.11a). Beyond this interval, empirical results can be adopted. Stewart et al. (2014) suggested to use values between 0.23 and 0.30. This low dispersion is probably due to the relatively homogeneous site and high  $V_s$  values.

Another important source of uncertainty is site-to-site variability, accounted for by means of a site-to-site standard deviation ( $\phi_{s2s}$ ), which represents the deviation of the observed amplification value at the site from the amplification predicted using a GMM. It was found that there is not a strong difference between site-to-site variability evaluated from UHS and CS ground motions (Figure 4.11b). Figure 4.12 shows  $\phi_{s2s}$  for different shear wave velocity profiles and various intensity measures.  $\phi_{s2s}$  is lower when GRA are performed on a profile with high impedance. In this case,

it is plausible to assume that higher impedance contrasts led to larger amplification values. Such effect dominated site response effects and masked between-recording variability due to inherent ground motions characteristics (e.g., their frequency content). However, this is not always the case and this conclusion cannot be generalized, as reported by Stewart et al. (2014).

Due to GRA limitations, it is unknown whether ground response from simulations actually estimates the “true” non-ergodic response. This is still an open question in literature (e.g., Stewart et al., 2017) and some of the results currently available in the literature provide mixed conclusions (e.g. Baturay and Stewart, 2003; Thompson et al., 2012). For these reasons, it is cautious to use different values of the parameter  $F$  in Eq. 2.19 (0 for ergodic analysis, 1 for fully non-ergodic) and to switch to ergodic results beyond the range where one-dimensional GRA fails to predict the actual ground response of the site.

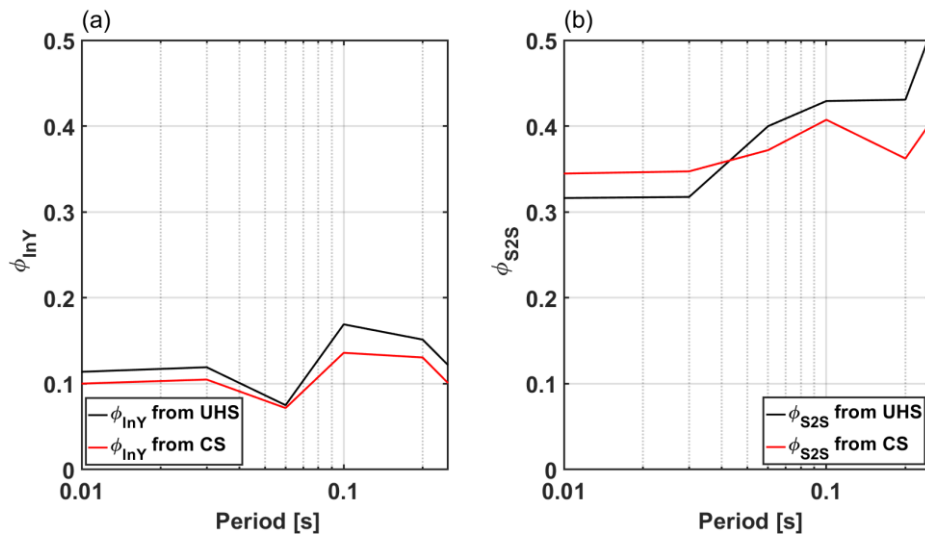


Figure 4.11: Standard deviation of site amplification (a) Site-to-site standard deviation (b).

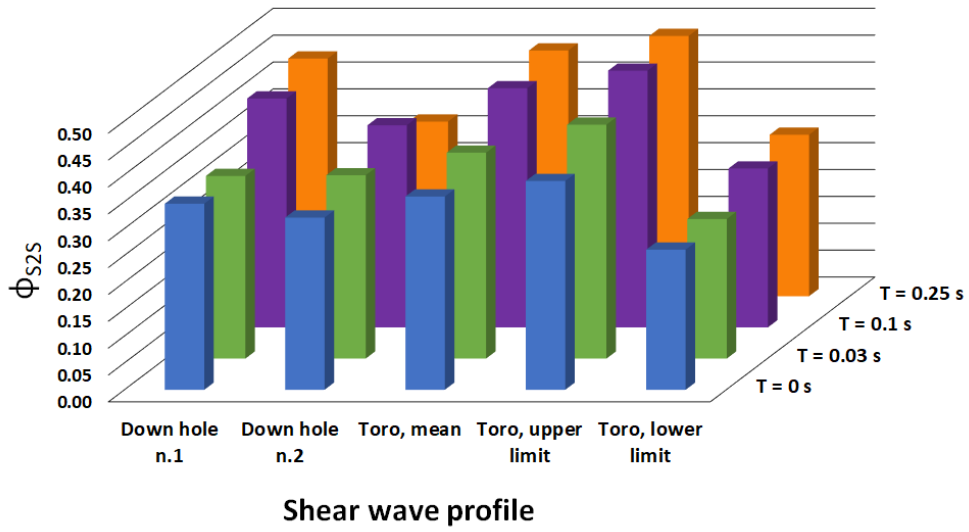


Figure 4.12: Variation of site-to-site standard deviation for different shear wave profiles and intensity measures.

#### 4.5 Non-ergodic PSHA for the Farneto del Principe dam site

In this section, a non-ergodic PSHA is performed for the Farneto del Principe dam site. The framework can be found in Stewart et al. (2017) and it is briefly summarized in §2.2. This section builds upon site-specific ergodic PSHA results presented by Zimmaro and Stewart (2017). In their study, Zimmaro and Stewart (2017) included area sources, fault sources, and background zones. They also modeled the Calabrian arc subduction zone and various shallow crustal faults not present in previous studies (Figure 4.13). The GMMs logic tree for active crustal regions and subduction zones (in-slab and interface) used by Zimmaro and Stewart (2017) is shown in Figure 4.14. In this study, the ergodic assumption on site effects was removed and a non-ergodic PSHA was implemented utilizing a modified version of the Boore et al. (2014) GMM. This model is partitioned in source,  $F_E(M_i, F_i)$ , path,  $F_P(M_i, R_{ij})$  and site term  $F_S(S_j, x_{IMr,ij})$  (Eq. 4.6):

$$\ln Z_{ij} = F_E(M_i, F_i) + F_P(M_i, R_{ij}) + F_S(S_j, x_{IMr,ij}) + \varepsilon \sigma_{\ln Z} \quad (4.6)$$

Where  $\ln Z_{ij}$  is the natural logarithm of the intensity measure being predicted,  $\varepsilon$  is the number of standard deviations of a predicted value away from the mean, and  $\sigma_{\ln Z}$  the total standard deviation. Based on the amplification functions evaluated for the alluvial foundation of the Farneto del Principe dam site, four different non-

ergodic PSHA were performed. In two of them, the GRA-based amplification functions were built on ground motions consistent with the CS for two different values of  $F$  (0.5 and 1). The remaining analyses are analogous but they use the amplification functions derived using the UHS as target spectrum. In the remainder of this section, the effects of these target spectra on the hazard results are illustrated, while the results for different  $F$  values show the sensitivity on the overall PSHA. The non-ergodic hazard curves are also compared against those estimated using simplified approaches.

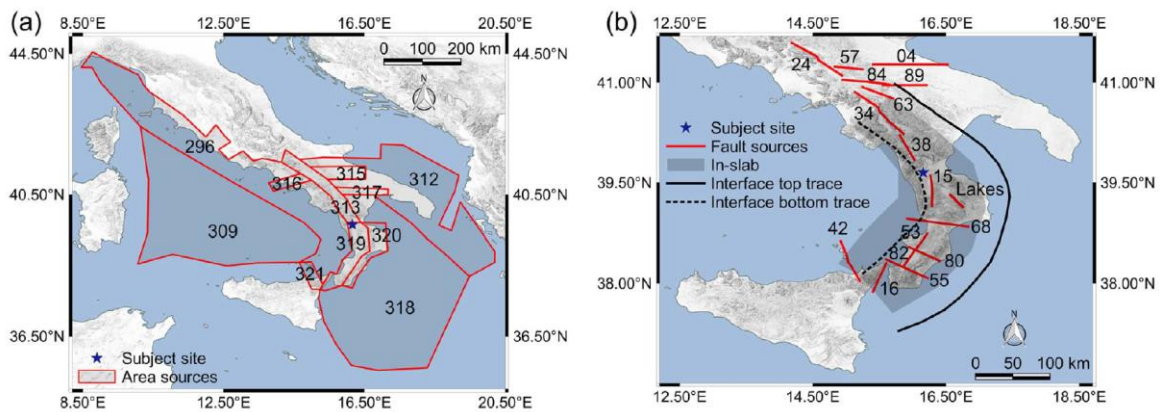


Figure 4.13: Source models used for the site-specific PSHA of the Farneto del Principe dam. (a) Area sources (b) Fault sources. (from Zimmaro and Stewart, 2017).

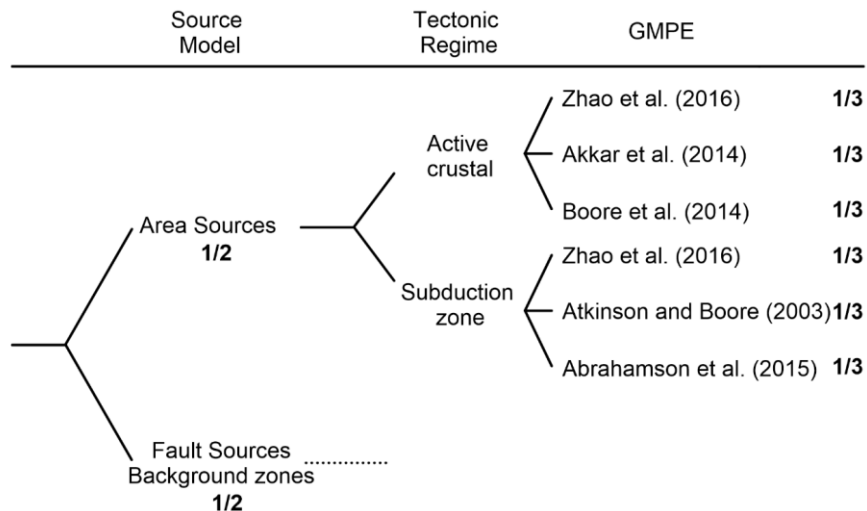


Figure 4.14: Logic tree used for the site-specific PSHA of the Farneto del Principe dam (adapted from Zimmaro and Stewart, 2017).



#### 4.5.1 Non-ergodic hazard curves, CS, and CMS

The four non-ergodic hazard curves for the Farneto del Principe dam site are shown in Figure 4.15, along with the ergodic curve produced using the model by Zimmaro and Stewart (2017). Figure 4.15 shows negligible differences among the non-ergodic curves. This may be due to the fact that the mean amplification functions are relatively similar. Hence, it should be noted that the four non-ergodic hazard curves are identical for periods greater than 0.25s. This is because the non-ergodic GMM is applied only up to that period. Beyond that value, semi-empirical parameters are used. The comparison between non-ergodic (surface) and ergodic (reference site conditions) hazard curves is more pronounced for the PGA and the fundamental period of the alluvial foundation, while for the other periods they are similar.

The low sensitivity of the results to the amplification function used can also be seen in the non-ergodic UHS and CS. The UHS derived from amplification functions built with UHS as target are slightly lower than those using the GRA derived from ground motions consistent to the CS (Figure 4.16). This difference is evident only for the 1460-year return period of 1460 years. Such difference is not evident for shorter return periods. This is expected and it is due to the greater nonlinearity and smaller amplifications at high strain levels (Figure 4.9). Beyond 0.25s, all spectra are equal. This is due to the fact that the modification of the GMM was done only in the period range where results are deemed as significant. The non-ergodic CS, instead, are all the same. This is because disaggregation results in this case are all the same (see §4.5.3).

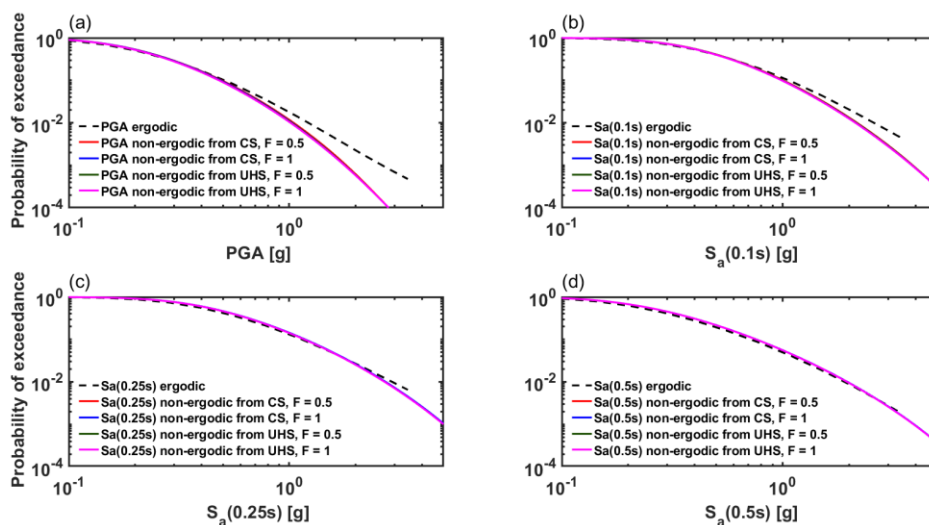


Figure 4.15: Ergodic and non-ergodic hazard curves for the Farneto del Principe dam site for the following intensity measures: (a) PGA, (b)  $S_a(0.1s)$ , (c)  $S_a(0.25s)$ , and (d)  $S_a(0.5s)$ .



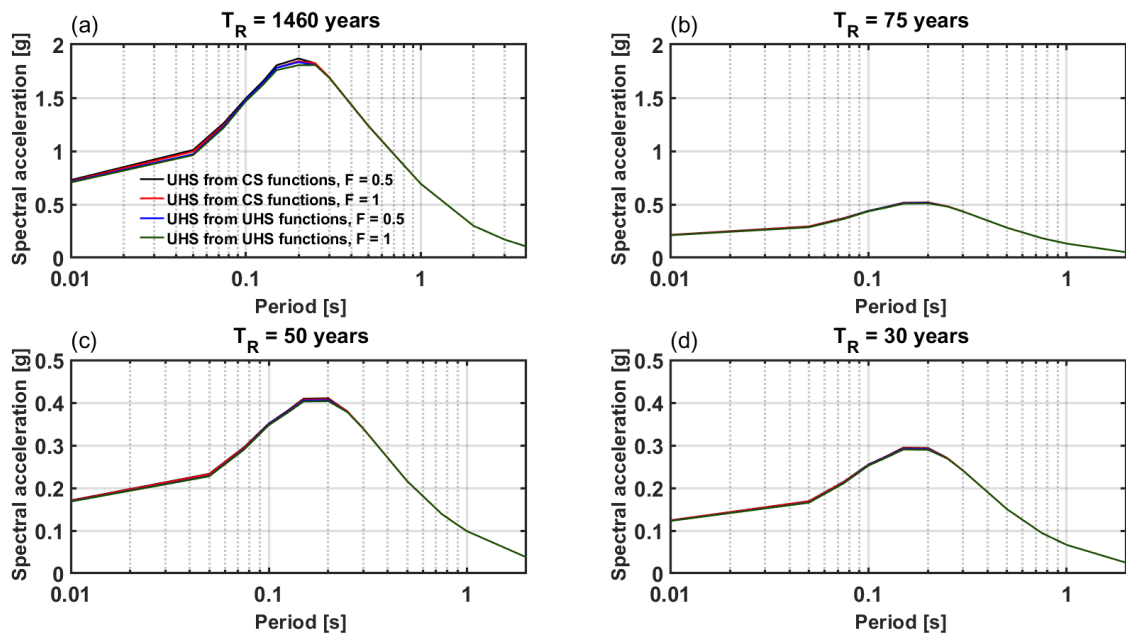


Figure 4.16: Non-ergodic UHS for the following return periods: (a) 1460 years, (b) 75 years, (c) 50 years, and (d) 30 years.

Figure 4.17 shows a comparison between non-ergodic UHS and CMS against their ergodic versions for the four return periods used in the GRA. The non-ergodic UHS shown in Figure 4.17 is that estimated from the amplification function based on the CS, with an  $F$  value equal to 1. The non-ergodic CMS are slightly more intense than the ergodic spectra. This is expected, as the non-ergodic spectra include the amplification effect of the alluvial material, while the ergodic spectra are derived for reference site conditions. The non-ergodic UHS, on the other hand, are less intense than the ergodic spectra only in a certain period range. In both cases, however, the differences between ergodic and non-ergodic spectra become smaller for lower return periods. This is evident in Figure 4.18, which shows the percentage difference of pseudo-spectral accelerations for the four return periods analyzed. Generally, the difference is greater for the range of periods adopted in the GRA, with some peaks at 0.25s for the CS.

#### 4.5.2 Comparison with simplified methods

Section 2.3 illustrated common methodologies to link GRA results to PSHA. In this section, results from these methods are compared. Hazard curves for the hybrid and modified hybrid methods, the convolution approach, and the non-ergodic hazard

method are shown in Figure 4.19. The implementation of the simplified method used in this study can be found in the electronic supplement of Stewart et al. (2014).

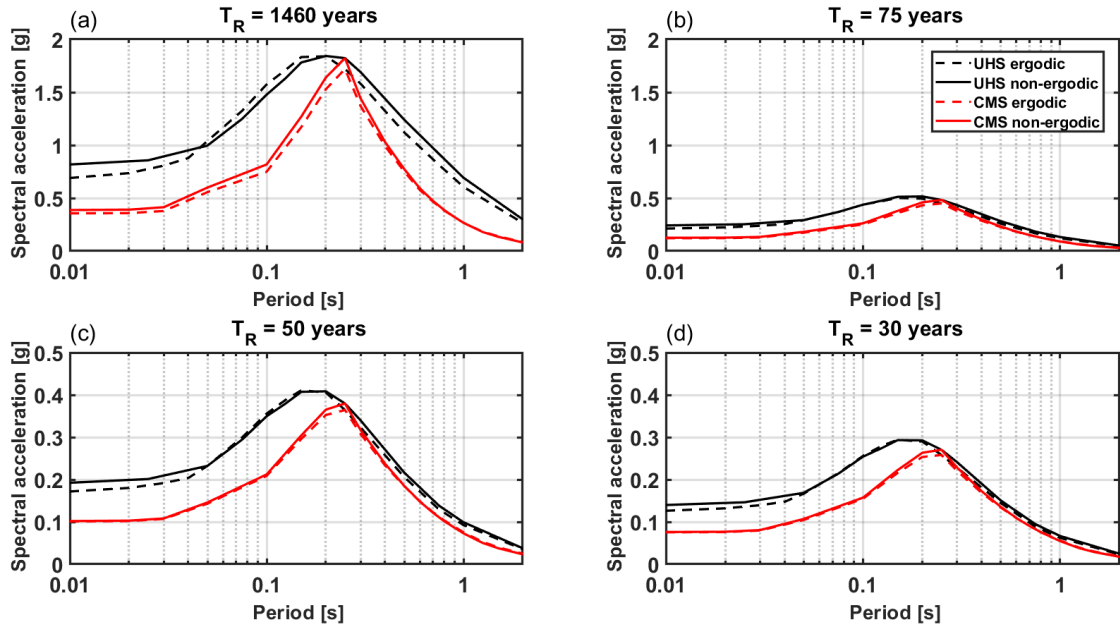


Figure 4.17: Non-ergodic and ergodic UHS and CMS for the following return periods: (a) 1460 years, (b) 75 years, (c) 50 years, and (d) 30 years.

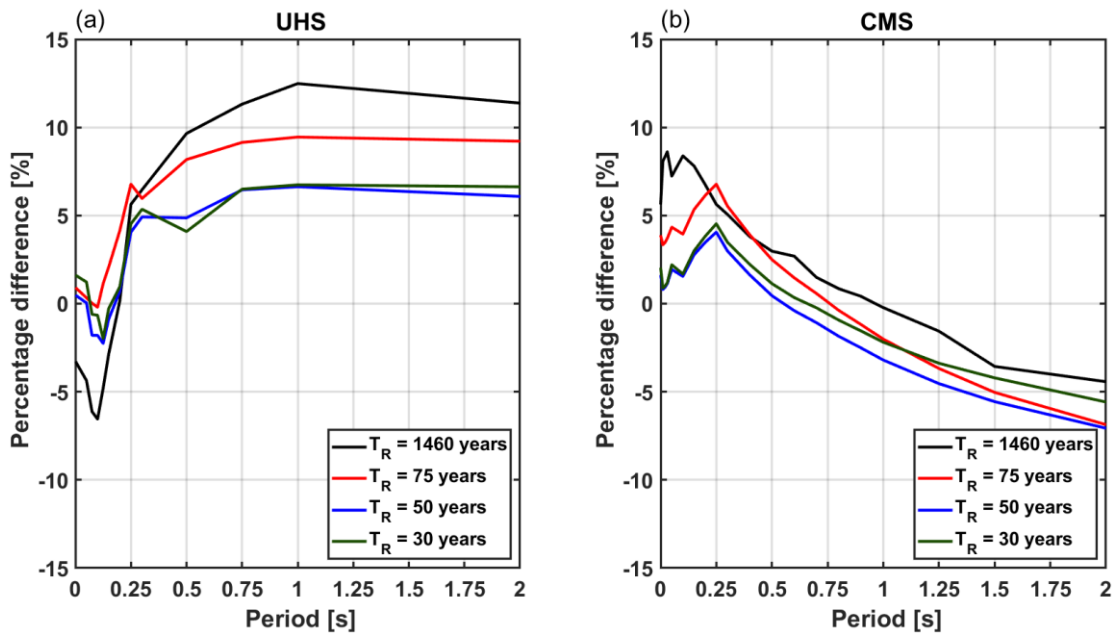


Figure 4.18: Percentage differences between non-ergodic and ergodic spectra (positive values means that the non-ergodic spectrum is more intense than the ergodic one) for (a) UHS and (b) CMS.

For PGA, all methods produce similar curves. For longer periods, only the modified hybrid approach seems to follow the same trend of the non-ergodic hazard curve. This is probably due to the inherent limitations of the other methods (see §2.3). The hybrid approach, for instance, does not take into account the variability in the amplification, nor that of the GMM. The convolution approach considers the amplification variability, but the total standard deviation used is still that for rock. The modified hybrid approach, however, can capture the non-ergodic trend (Stewart et al. 2014), probably because it exploits the disaggregation results for building the hazard curves.

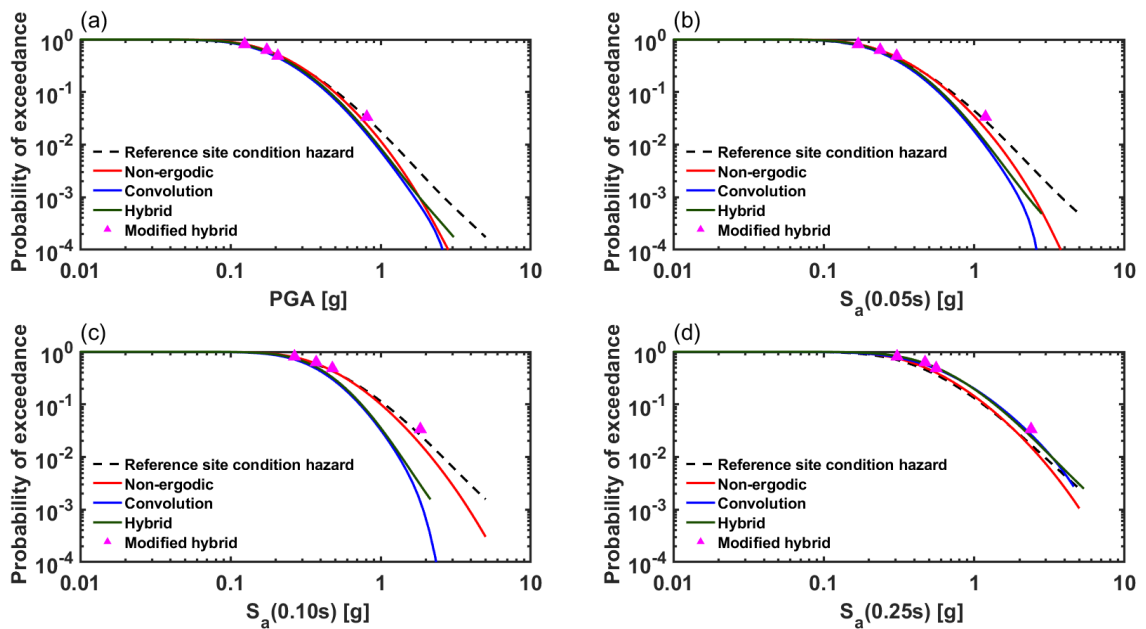


Figure 4.19: Comparison of hazard curves estimated from non-ergodic analyses and simplified methods.

#### 4.5.3 Disaggregation results

In this section, the disaggregation results of the non-ergodic hazard analyses are illustrated and compared to those from the ergodic approach. Table 4.1 shows the mean values of magnitude, distance, and epsilon for the four different analyses performed. The intensity measure being disaggregated is the spectral acceleration at the 0.25s. Table 1 confirms the poor sensitivity of the results on the different methods shown in Figure 4.15. Table 4.2 shows the comparison between ergodic and non-ergodic disaggregation results in terms of magnitude-distance-epsilon.

Aside from the return period of 1460 years, the mean distance and epsilon in the case of the non-ergodic analysis are greater, while the magnitude remains almost the same. A modest difference, instead, can be identified for  $T_R$  of 1460 years. This is probably due to the fact that the hazard curves shown are different mainly for low probability of exceedance, and thus high return periods (Figure 4.20).

Table 4.2: Non-ergodic  $M$ - $D$ - $\epsilon$  disaggregation results for the spectral acceleration at 0.25s for the Farneto del Principe dam.

$T_R = 1460$ , UHS $F = 0.5$			$T_R = 1460$ , UHS $F = 1$			$T_R = 1460$ , CS $F = 0.5$			$T_R = 1460$ , CS $F = 1$		
M	R [Km]	$\epsilon$	M	R [Km]	$\epsilon$	M	R [Km]	$\epsilon$	M	R [Km]	$\epsilon$
6.97	38.91	1.811	6.97	38.91	1.811	6.96	38.32	1.808	6.96	38.32	1.808

Table 4.3: Differences between non-ergodic and ergodic disaggregation results for the spectral acceleration at 0.25s.

	$T_R = 30$			$T_R = 50$			$T_R = 75$			$T_R = 1460$		
	M	R [Km]	$\epsilon$	M	R [Km]	$\epsilon$	M	R [Km]	$\epsilon$	M	R [Km]	$\epsilon$
<b>Ergodic</b>	6.33	55.0	1.08	6.47	52.4	1.14	6.58	50.8	1.20	7.21	49.0	1.67
<b>Non-ergodic</b>	6.31	57.5	1.13	6.43	54.0	1.20	6.52	51.5	1.26	6.96	38.3	1.81

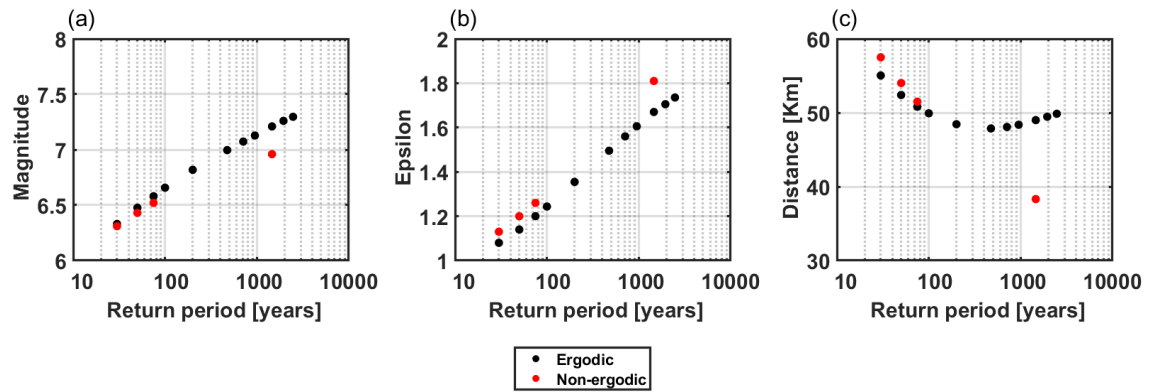


Figure 4.20: Comparison between non-ergodic and ergodic disaggregation results for the spectral acceleration at 0.25s.

Figure 4.21 shows the non-ergodic Magnitude-Distance disaggregation for the return period of 1460 years. It is evident that there are two large contributions, one from nearby faults (i.e., distances of  $\sim 10$  Km) and the other for faults that are more

distant (i.e., distances of  $\sim 50$  Km). Given the location of the Farneto del Principe dam, the latter contributor is probably the subduction zone of the Calabrian Arc (capable of producing magnitude larger than 8). The contributions of nearby faults are likely due to Crati valley fault (Figure 4.13), which is capable of producing magnitudes larger than 6. For these reasons, the choice of the dynamic inputs to be used in numerical analyses of the performance of the dam (Chapter 7) was made by selecting ground motions with a  $R_{jb}$  distance in the range 0-50 Km, thus considering both the contributions.

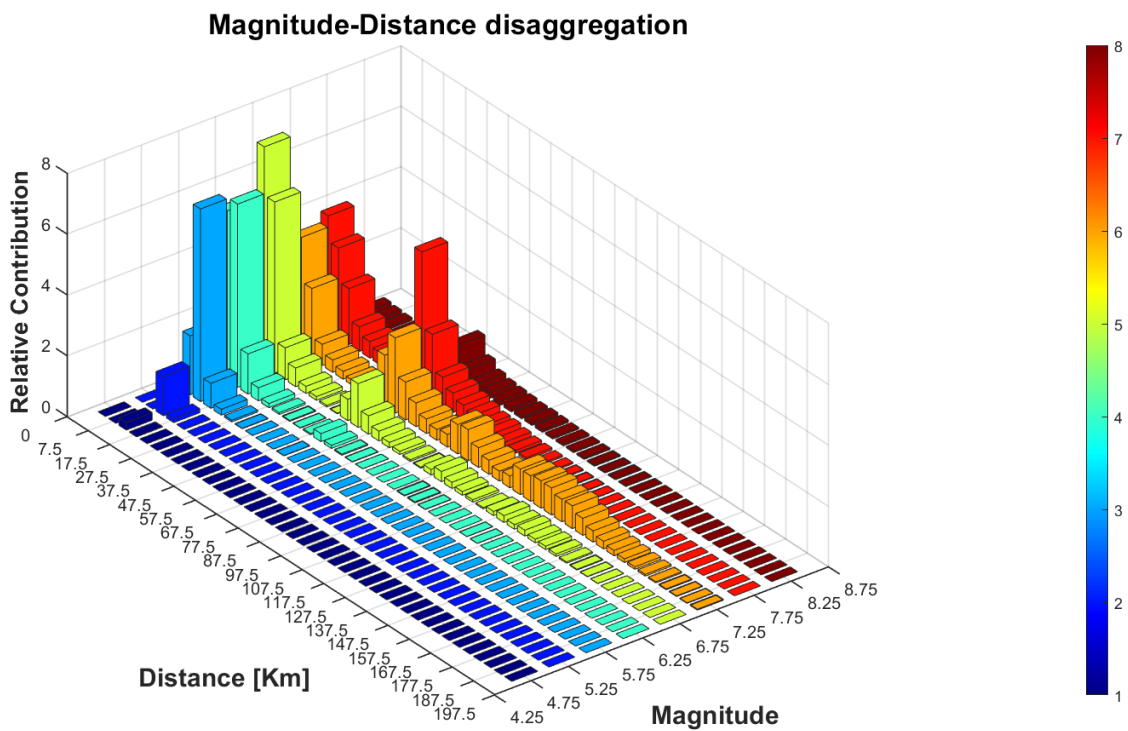


Figure 4.21: Non-ergodic magnitude-distance disaggregation of the Farneto del Principe dam site for a return period of 1460 years.

## 5. The Angitola dam

In addition to the Farneto del Principe dam, another dam in the same region was analyzed: the Angitola dam. This dam is located 130 km south of the Farneto del Principe dam, in a similar tectonically active environment. Whereas laboratory and field investigation results data were collected as part of this study, data for the Angitola dam were kindly provided by Professor Giuseppe Lanzo of the University of Rome “La Sapienza” who is gratefully acknowledged. Differently from the Farneto del Principe dam, the Angitola dam is founded on sandy soils that are potentially susceptible to liquefaction. This makes it an interesting case study to analyze the effects of different constitutive models on its seismic performance. For the purpose of this section, the focus is given to soils that are susceptible to liquefaction. The comparison between the results of MSA performed on a dam susceptible to liquefaction (the Angitola dam) and those on a dam that is not susceptible to liquefaction (the Farneto del Principe dam), can give insights into the various aspects of the seismic response of earth dams. For instance, deformations due to liquefaction can result in a different collapse mechanism of the dam. This is particularly relevant because understanding which limit state (or damage mechanism) is more likely to happen becomes critical to prioritize mitigation strategies.

### 5.1 Generalities

The Angitola dam (latitude 38.7486°N and longitude 16.2319°E) is a zoned earth dam located in the Calabria region, Southern Italy, in the same seismic context of the Farneto del Principe dam (the two dams are 130 km apart from each other). It was built in the period 1960-1966 and it has irrigation purpose. The structure is built around Mount Marellò and Colle Sant’Antonio on the Angitola river and it comprises two dams located on the two sides of the mountain (Figure 5.1). Table 5.1 reports the main characteristics of the two dams and of the reservoir, henceforth called main and secondary dam, respectively. The crest, maximum allowable water level, and freeboard elevations are the same for both the dams (48.30 m a.s.l., 46.40 m a.s.l., and 1.9 m, respectively). The crest length and height are 140.79 m and 29.80 m for the main dam, and 195.53 m and 27.75 m for the secondary dam. The height is defined according to the D.M. 26/06/2014 (the Italian Building Code for dams), which is the difference between the crest elevation and the lowest level of the shells. The core of the dams comprises medium plasticity silty sands, while the shells are

composed of sandy gravel taken from Mount Marelo during construction. There are two filters between the core and the shells; the internal filter, adjacent to the core, is 60 cm thick and is made up of sand and gravel (1 mm to 10 mm soil particles diameter). The external filter is 140 cm, with soil particles diameter up to 50 mm. On the downstream shell, draining layers comprising high permeability material are connected to the filters; they are one meter thick and placed every four meters. The core, shells, filters, and draining layers are similar for both dams. The watertightness of the main dam is assured with a 60cm-thick concrete cut-off that starts from the base of the core and is inserted for up to 3.5 m into the rock foundation. For the secondary dam, a cut-off wall ensures the watertightness of the dam in the Colle Sant'Antonio zone, which comprises more permeable materials, while in the other area near Mount Marelo the cut-off wall is 2m- thick and 3m high. These differences are due to the extreme variation of the foundation soils along the longitudinal section where the main and secondary dams are located. In addition, the foundation soil of the latter vary longitudinally, making it a very complex geological setting. The main dam is founded on alluvial soils (sandy gravel) which are laterally continuous (Figure 5.2). The secondary dam, however, is founded on four different layers, with very different geotechnical properties from those of the main dam. On the downstream side, there is a 5m-thick layer of sandy silts, which comprises the recent alluvial material. Beneath this layer, there is old alluvial material made up of gravel with sandy silt, together with tiny fractions of clay material. The dam lays on a pliocenic formation of consistent silty clay, whose thickness rises longitudinally from downstream to upstream. Beneath those layers, a heterogeneous sand layer (with soil particles comprising gravel, sand, silt, and clay) is present, coming from the weathering of the underlying rock foundation (sandy layer), which is made up of fractured gneiss. The intact rock is about 40 meters below the free surface, which is likely characterized by the same properties of the main dam. Figures 5.2 and 5.3 show the cross section of the two dams. The alluvial foundation of the main dam is characterized by a mean  $V_s > 500$  m/s, and by uncorrected SPT blow counts ( $N_{SPT} > 40$ ). The shells of both dams have a  $V_s$  that varies in the range 350-600 m/s, with  $N_{SPT}$  ranging from 20 to 40. Grain size distribution analyses have shown that the shells are made up of sandy gravel that are outside the bound of soils susceptible to liquefaction according to the Italian Building Code (NTC 2018). Furthermore, semi-empirical  $V_s$ - and SPT-based liquefaction triggering procedures, all agree on assigning high factors of safeties for these materials based on seismic scenarios



selected using PSHA results for all considered return periods. For all of the above reasons, the main dam is believed to be safe from experiencing deformation due to liquefaction and it will not be the focus of this chapter. The secondary dam, on the other hand, is founded on materials susceptible to liquefaction. As a result, it offers a better opportunity to analyze potential liquefaction-induced mechanisms. Thus, in the remainder of this chapter the secondary dam will be analyzed.

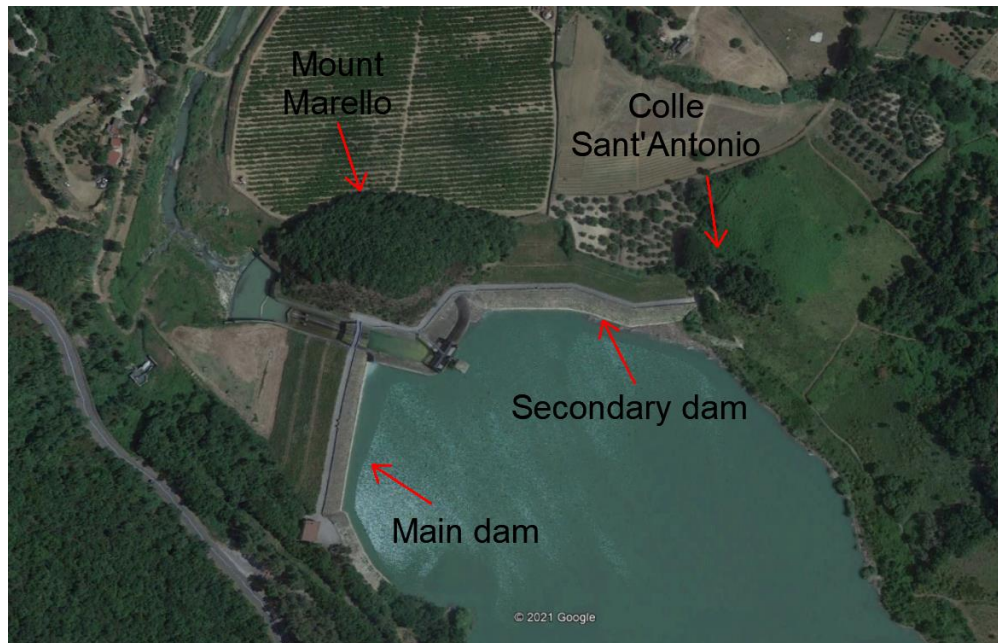


Figure 5.1: Aerial view of the Angitola dam (from Google earth, 2021).

Table 5.1: Main characteristics of the Angitola dam.

Property	Value	
	Main dam	Secondary dam
Water storage volume	21 Mm <sup>3</sup>	
Average height (DM 26/06/2014)	29.80 m	27.75 m
Crest length	140.79 m	194.52 m
Crest width	6 m	5 m
Freeboard (max level of the reservoir)	1.9 m	1.9 m
Upstream face slopes	1:1.75	1:1.75
Downstream face slopes	1:2, 1:2.3, 1:2.6	1:2, 1:2.3, 1:2.6
Crest elevation	48.30 m a.s.l.	48.30 m a.s.l.
Maximum allowable water level	46.40 m a.s.l.	46.40 m a.s.l.
Maximum authorized water level	44.20 m a.s.l.	44.20 m a.s.l.



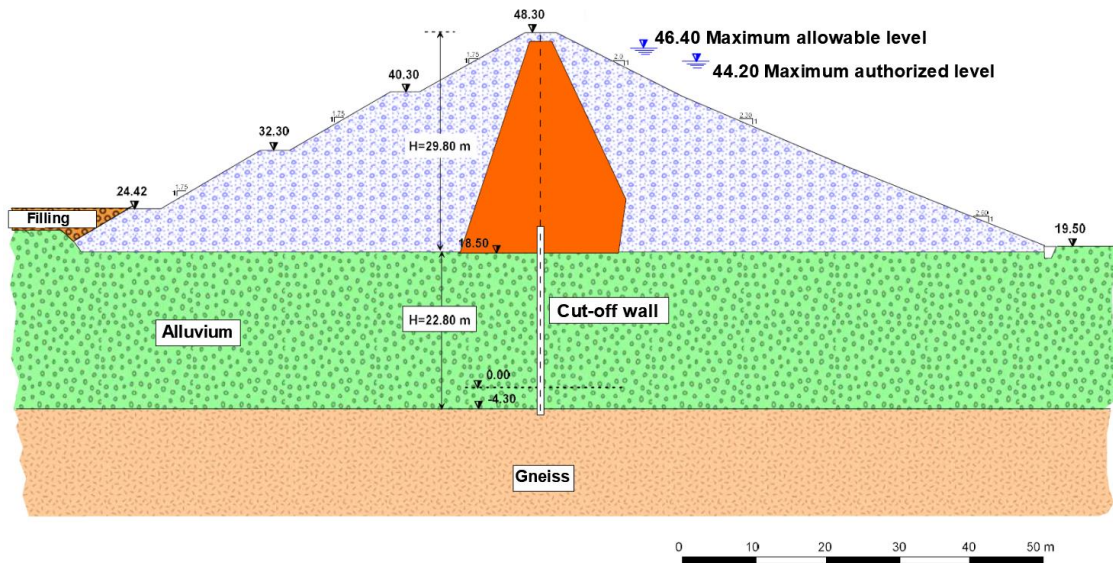


Figure 5.2: Cross section of the main dam (courtesy of Prof. Lanzo).

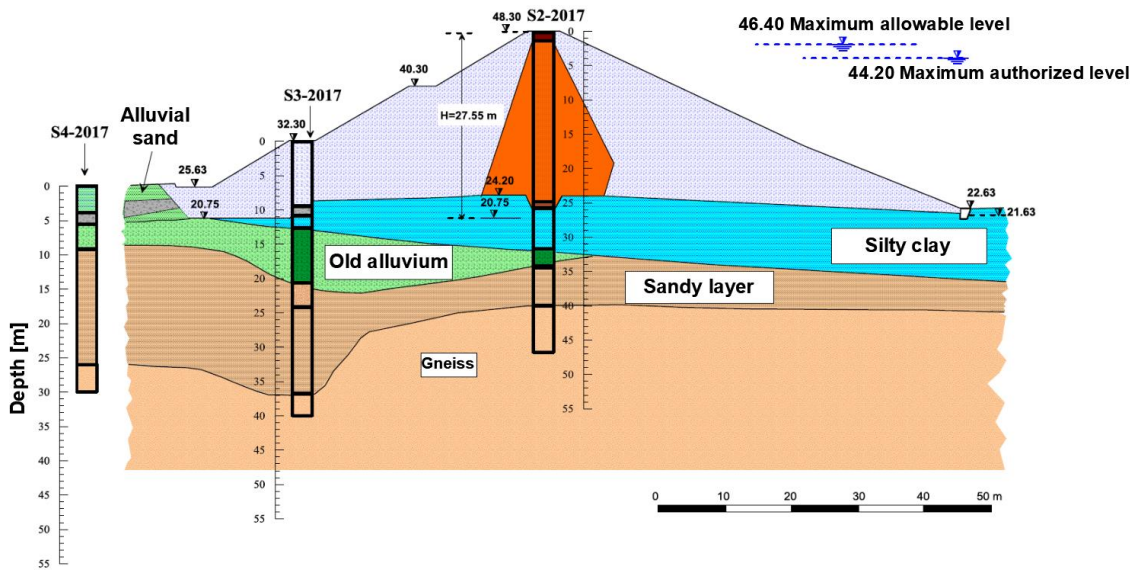


Figure 5.3: Cross section of the secondary dam and location of the boreholes performed (courtesy of Prof. Lanzo).

## 5.2 Geotechnical characterization of the secondary dam

The geotechnical properties of the Angitola dam are estimated from the construction logs and from a series of field investigation performed during various field investigation programs during the years 1999, 2015, and 2017. Several boreholes, identification tests, triaxial tests, direct shear stress, SPTs, CPTs, down-

holes, MASWs, and HVSR were performed on the dam body and on its foundation. Table 5.2 shows a list of all tests and their location, while Figure 5.4 shows the plan view of the dam area and the geographic locations of all tests. The results of these tests allowed for a comprehensive geotechnical characterization of the secondary dam. The geotechnical parameters shown in the following sections represent mean values from all available tests.

Table 5.2: Summary of the tests performed on the secondary dam.

Test type	Number	Location
Borehole	15	Core, shells, foundation
Granulometry	7	Core, shells, foundation
Oedometric	1	Foundation
Direct Simple Shear (DSS)	2	Core, foundation
Cyclic DSS	3	Core, foundation
UU	2	Core, foundation
CU	7	Core, foundation
CD	2	Core, foundation
SPT	50	Core, shell, foundation
CPTu	9	Foundation
SCPTu	1	Core
Seismic tomography	9	Longitudinal and transversal profiles
Down-hole	5	Core, shells, foundation
Microtremor HVSR	3	Crest, downstream

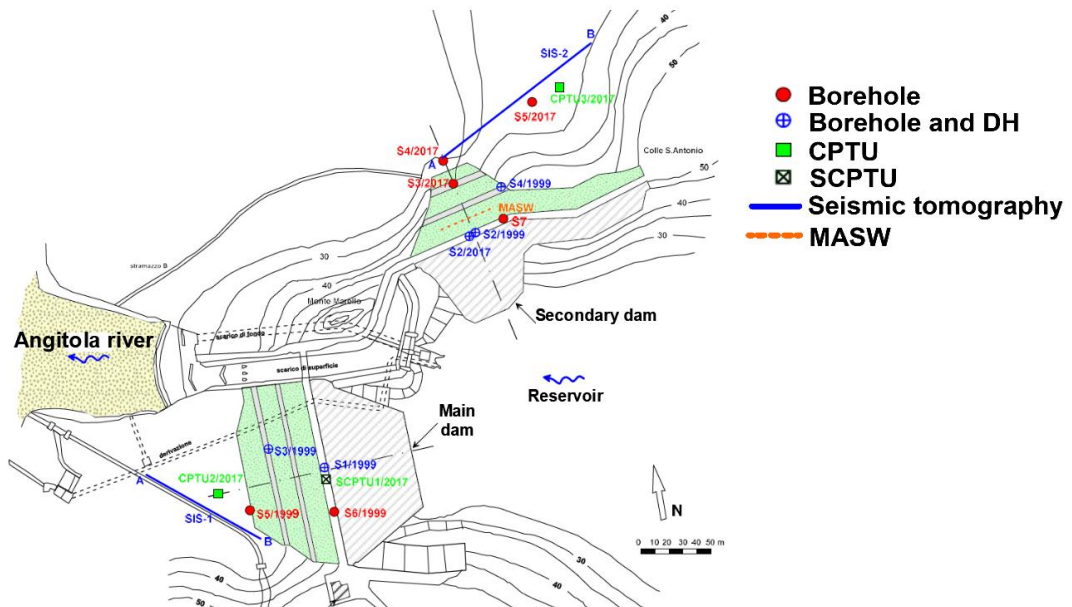


Figure 5.4: Plan view of the Angitola dam area and location of all tests performed (courtesy of Prof. Lanzo).

### 5.5.1 Geotechnical properties of the dam body

For the core, the soil and dry unit weights are  $20.36 \frac{kN}{m^3}$  and  $17.70 \frac{kN}{m^3}$ , respectively. The water content is 17.3% and the void ratio is 0.497. The plasticity index and liquid limit are 20.9 and 41.3%, thus the soil is classified as a medium plasticity inorganic clay according to the Casagrande's chart. According to Bray and Sancio (2006) and Boulanger and Idriss (2006), these soils are not susceptible to liquefaction. The strength parameters were estimated from direct shear and triaxial tests. The mean value of cohesion is 10 kPa and that of the friction angle is  $26^\circ$ . Figures 5.5 and 5.6 show relevant results obtained for the materials of the core and the foundation.

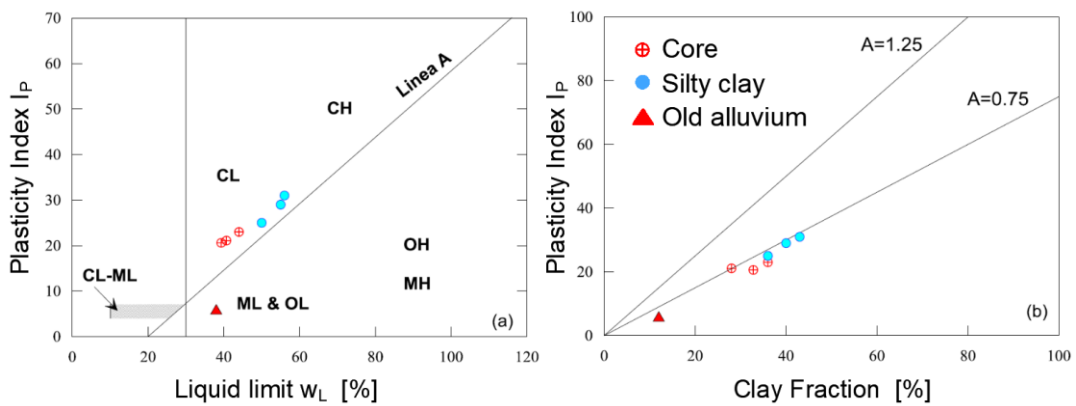


Figure 5.5: Casagrande's and activity chart for the core and the foundation soils of the secondary dam (courtesy of Prof. Lanzo).

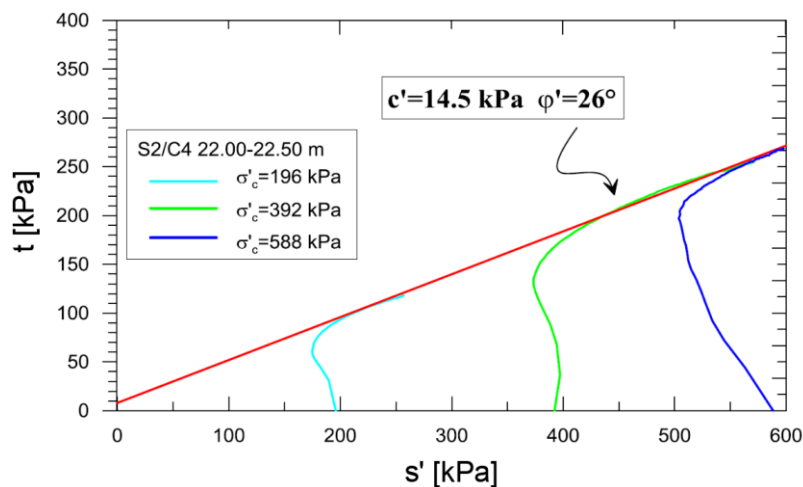


Figure 5.6: Failure envelope for the core of the secondary dam based on a triaxial ICU test (courtesy of Prof. Lanzo).

The small strain shear modulus in the core was estimated from a down-hole test performed during the 2017 field investigation program. A power law was used to fit the data and establish a variation of the shear modulus with depth. Figure 5.7 shows the  $V_s$  profile, which is consistent with that of the Farneto del Principe dam.

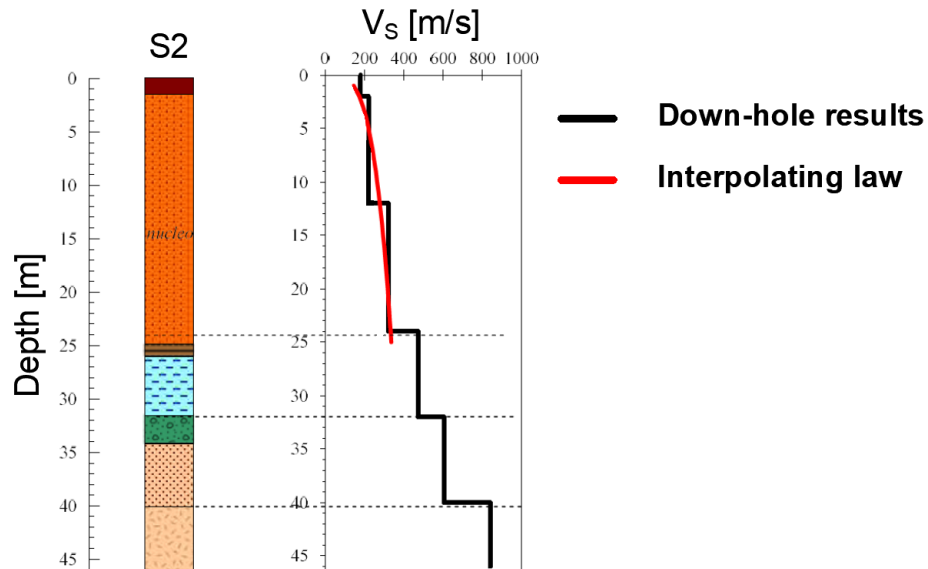


Figure 5.7: Shear wave velocity profile of core of the secondary dam (silty clay, and sandy layer) (courtesy of Prof. Lanzo).

The MRD curves are evaluated from a cyclic direct shear test for two confinement stresses (250 and 500 kPa). The results show that there is no dependence of the MRD curves on the confinement stress. As a result, a single curve was used in the numerical analyses. Figure 5.8 shows the experimental curves, as well the interpolating sigmoidal curve used in FLAC to fit the experimental data (more details on the numerical model set up and calibration are provided in § 6.5).

The shells were modeled as a pure frictional material, with a friction angle of  $40^\circ$ , estimated from a drained consolidated triaxial test. The soil unit weight, dry unit weight, and permeability available are those from the pre-construction data and construction logs ( $21.92 \frac{kN}{m^3}$ ,  $20.99 \frac{kN}{m^3}$ , and  $1.9 \cdot 10^{-7} \frac{m}{s}$ ). The stiffness of the shells was estimated from a down-hole performed on the landside shell at 40.30 m a.s.l., which showed a  $V_s$  in the range of  $350\text{-}600 \frac{m}{s}$ . A power law was used to fit the shear wave velocity with depth (Figure 5.9), with a minimum value of  $250 \frac{m}{s}$  for the first 2 meters.

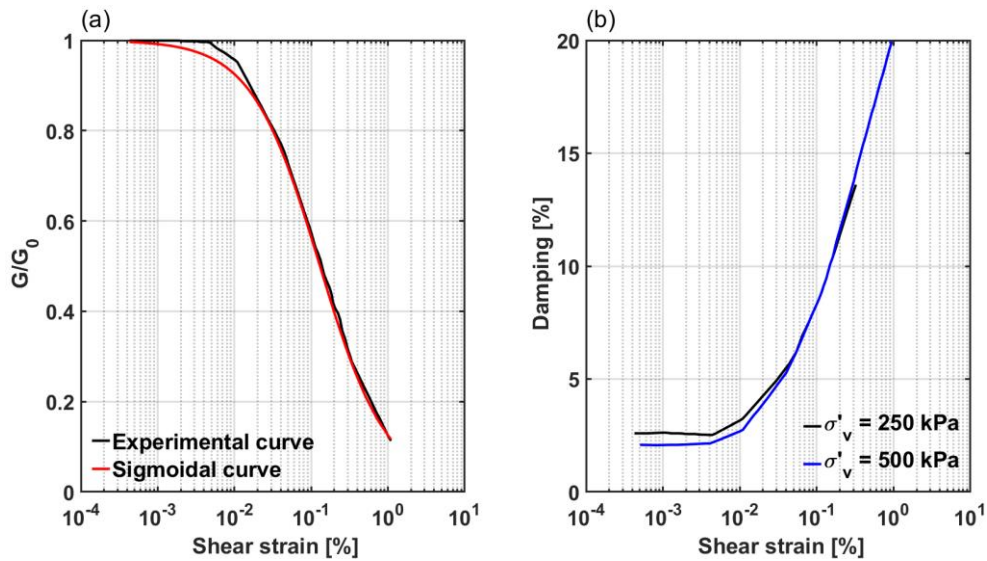


Figure 5.8: MRD curved for the core of the secondary dam.

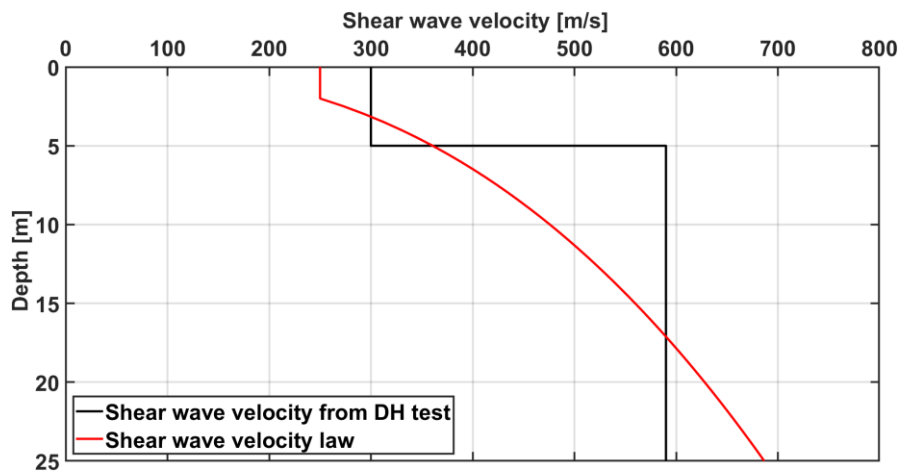


Figure 5.9: Shear wave velocity profile adopted for the shells of the secondary dam.

There are no experimental data on the MRD curves for the shells. As a result, the empirical model proposed by Menq (2003) for cohesionless soils is used in this study. This model is largely based on available grain size distribution data. Figure 5.10 shows the comparison between the grain size distribution of the shell and one of the grain size distribution ranges analyzed by Menq (2003). This model (Menq, 2003) accounts for the variation of MRD curves with confinement stresses. For the levels of stress of interest for the secondary dam, there is a slight variation of the MRD curves with confining stress (Figure 5.11).



A mean sigmoidal curve was used to fit the empirical curves. For the filters, the same mechanical properties of the shells are considered, but with the hydraulic conductivity estimated from the design documents, which is around  $5.5 \cdot 10^{-6} \frac{m}{s}$ .

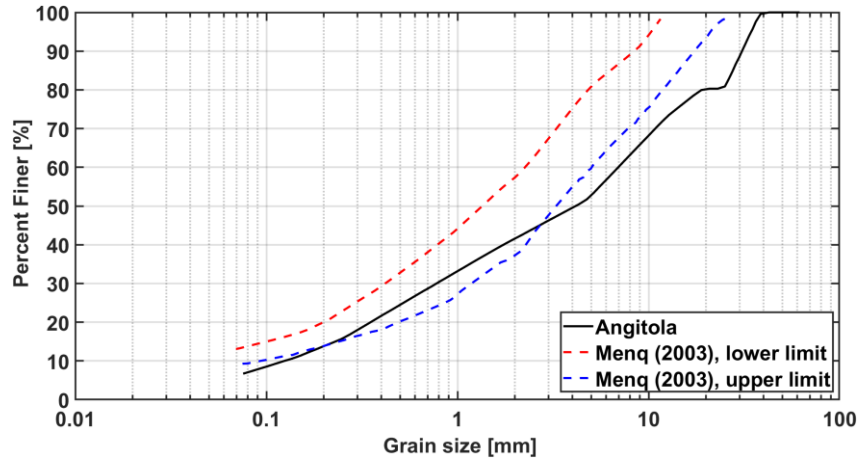


Figure 5.10: Comparison of the grain size distribution curves of the Angitola dam shells with one of the range adopted by Menq (2003) for the development of the empirical MRD.

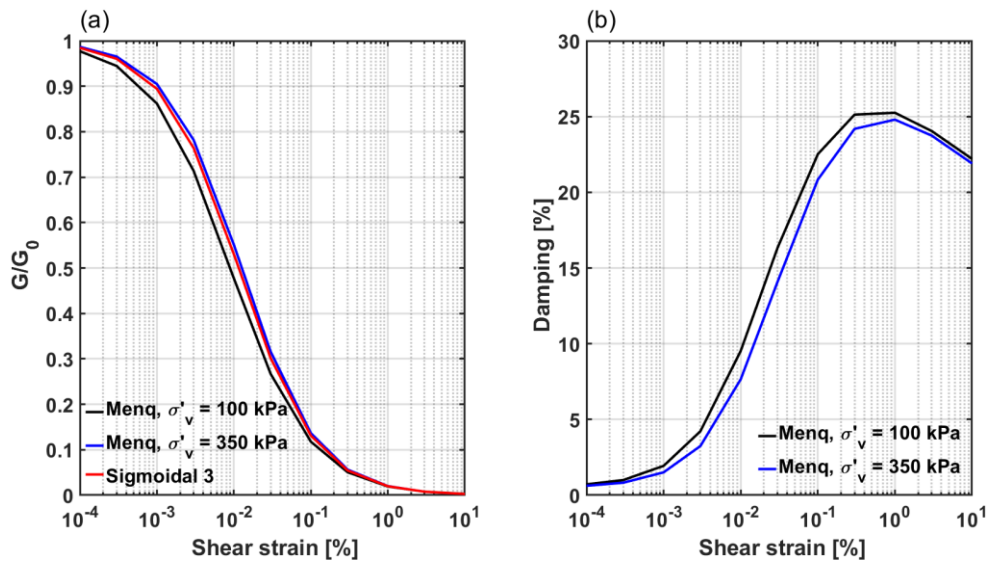


Figure 5.11: Shear modulus reduction curves and damping curves for the shells of the secondary dam.

### 5.5.2 Foundation layers characterization

The foundation layers of the secondary dam are characterized by a complex stratigraphy. For the clayey silts that are immediately beneath the dam, the mean soil unit weight is  $18.25 \frac{kN}{m^3}$ , with a hydraulic conductivity of  $1 \cdot 10^{-9} \frac{m}{s}$ . The liquid

limit and plasticity index are 54% and 28, respectively, indicating a medium to high plastic, inorganic clay according to Casagrande's chart. The strength parameters are evaluated from a direct shear test, which resulted in post-peak values of 48 kPa for the cohesion and  $24^\circ$  for the friction angle. The stiffness is estimated from the down-hole performed on the crest of the dam, which showed a mean value of  $480 \frac{m}{s}$ . The MRD curves are based on two cyclic direct simple shear tests for a confinement stress of 300 and 400 kPa. These results indicate a slight dependence on the confining pressure. Due to the moderate thickness of the foundation layer, and thus of the modest variation of the effective stresses in the clayey silt, only one fitting curve was used (Figure 5.12). For the old alluvium there are limited data available, so typical values from the literature are assumed for most of the geotechnical parameters within this layer. In particular, a soil unit weight of  $18.5 \frac{kN}{m^3}$  and a hydraulic conductivity of  $1 \cdot 10^{-7} \frac{m}{s}$  were used. For the MRD curves, the mean results of the Rollins (1998) model for gravel were used.

For the stiffness of the foundation materials, three empirical relationships based on a limited number of available SPT blow counts were used. Two correlations are based on the recommendations of Wair et al. (2012), while the third is that by Andrus and Stokoe (2000):

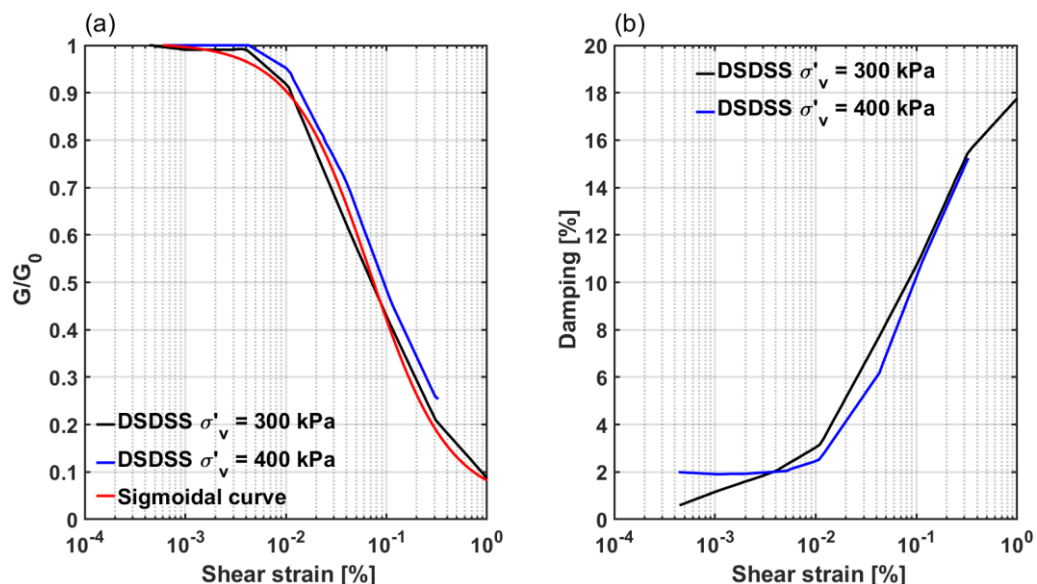


Figure 5.12: MRD curves for the silty clay foundation, and sigmoidal curve used in the numerical model.

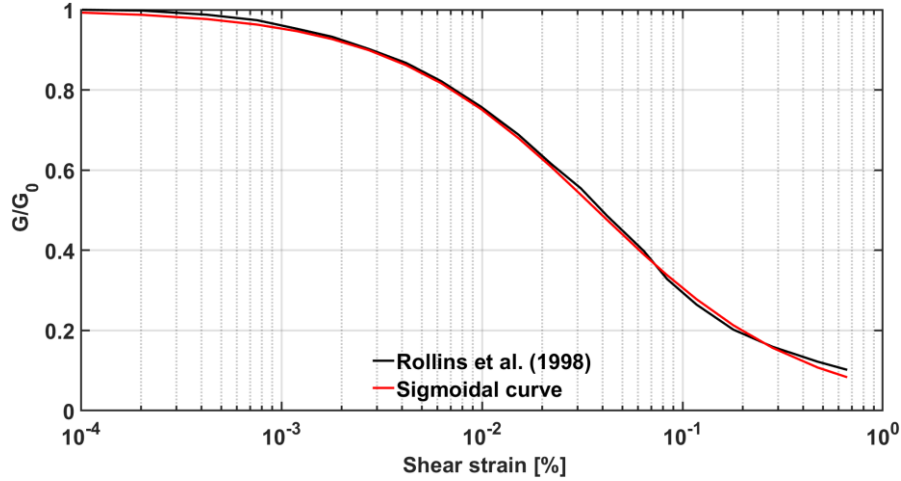


Figure 5.13: Shear modulus reduction curve used for the old alluvium.

$$V_S = 30 N_{60}^{0.215} \sigma_v'^{0.275} \quad (5.1)$$

$$V_S = 30 N_{60}^{0.23} \sigma_v'^{0.23} \quad (5.2)$$

$$V_S = 85[(N_1)_{60} + 2.5]^{0.25} \quad (5.3)$$

$N_{60}$  is the  $N_{SPT}$  value corrected for energy efficiency, while  $(N_1)_{60}$  is also corrected for overburden stress, and  $\sigma_v'$  is the vertical effective stress. The first and third equations are valid for all type of soils, while the second is sand specific. This choice is based on the fact that the foundation layer does not comprise clean sands, since the boreholes showed a fraction of both fine and coarse graded soils. The mean  $V_s$  value based on the above-mentioned SPT-base relationships for the old alluvium is  $231 \frac{m}{s}$ . For this layer, a CPTu is also available and the  $V_s$  profile was also estimated using the following relationships (Robertson, 2009, Mayne, 2006, and Piratheepan, 2002):

$$V_S = \left[ 10^{(0.55Ic+1.68)} \frac{q_t - \sigma_v}{p_a} \right]^{0.5} \quad (5.4)$$

$$V_S = 118.8 \log(f_s) + 18.5 \quad (5.5)$$

$$V_S = 25.3 q_c^{0.163} f_s^{0.029} D^{0.155} \quad (5.6)$$

where  $Ic$  is the soil behavior type index,  $q_t$  is the corrected tip resistance,  $\sigma_v$  is the total vertical stress,  $p_a$  is the atmospheric pressure,  $q_c$  is the cone tip resistance,  $f_s$  is the sleeve friction, and  $D$  is the depth. For the old alluvium, a mean value of  $226 \frac{m}{s}$



is obtained, which is almost the same as that obtained using SPT data. In-situ tests were also performed on the landside shell and in free field condition, downstream of the dam (Figure 5.4). The soil in this free field area, however, despite being the same material (i.e. gravel with silty sand) does not have the same stiffness properties of that beneath the dam. Hence, it is not recommended to use the same shear modulus for the entire layer, because of the overburden stress effect generated by the presence of the dam. The same effect was observed looking at field investigation test results for the Farneto del Principe dam (Figure 3.17). The shear wave velocities in the alluvial foundation estimated from the down-hole starting from the downstream shell, were higher than those measured in free field conditions. For these reasons, the spatial variation of the stiffness in the foundation layers were modeled adopting a mean effective stress dependence:

$$G(x, z) = G_0 p_a \left( \frac{p'(x, z)}{p_a} \right)^m \quad (5.7)$$

where  $G_0$  and  $m$  are fitting parameters,  $p_a$  is the atmospheric pressure, and  $p'$  is the mean effective stress. This relationship was used throughout the foundation layers that are mildly influenced by the dam body up to the gneiss, such that the mean shear modulus is obtained in the center of the layer. Beyond a mean effective stress of 220 kPa, a linear relationship was used (Figure 5.14).

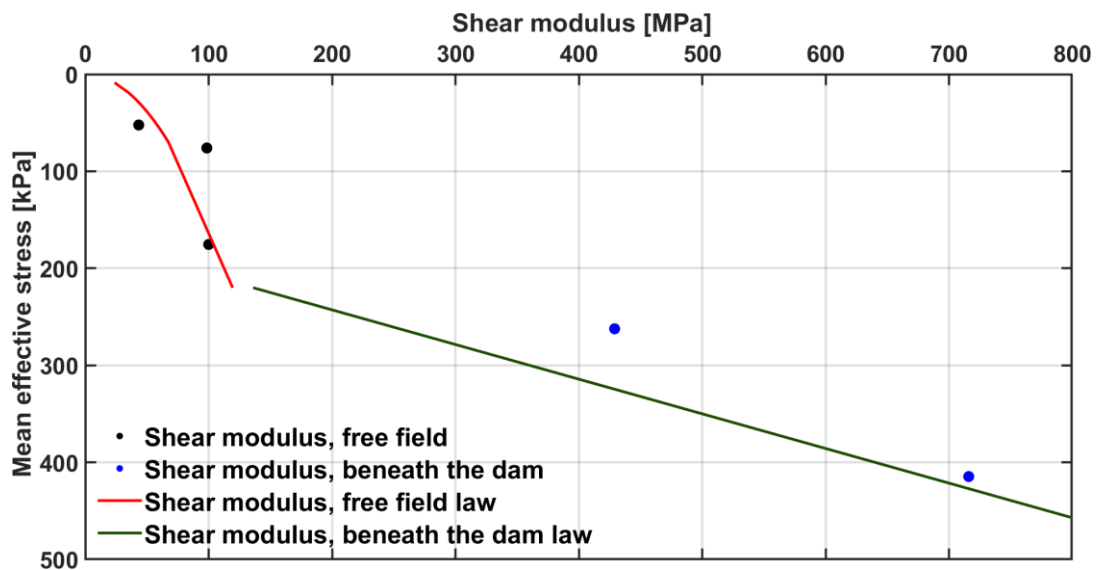


Figure 5.14: Shear modulus variation with mean effective stress. The black points refer to values calculated in free field conditions, while the blue points refer to locations beneath the dam.

This refinement was necessary to avoid unrealistic impedance contrasts between the dam body and its foundation system. The friction angle was estimated using the Mayne (2006) relationship, based on Hatanaka and Uchida (1996), which gave a mean value of over  $40^\circ$ . However, due to the heterogeneous nature of the layer, a conservative value of  $35^\circ$  was selected.

For the sandy layer, reasonable values of the soil unit weight and hydraulic conductivity are assumed ( $19.5 \frac{kN}{m^3}$  and  $10^{-7} \frac{m}{s}$ , respectively). For the stiffness, the same spatial variation of the shear modulus shown above was assumed (Eq. 5.7). The mean  $V_s$  of the sandy layer beneath the dam was estimated with data from the available down-hole test performed on the crest ( $V_s = 600 \frac{m}{s}$ , see Figure 5.7). For the soil in free field conditions, the three SPT-based empirical relationships for are used (Eqs. 5.1-5.3). The mean value of the  $V_s$  is  $225 \frac{m}{s}$ . The friction angle was estimated using the De Mello (1971) and Mayne (2006) relationships, providing a mean value of  $34.5^\circ$ . The MRD curves are based on the upper bound of Seed and Idriss (1970), because the sandy layer is not a clean sand. This shear modulus reduction curve is also consistent with the Electrical Power Research Institute, EPRI (1993) curve valid in the range 15-36 m of depth, which is the range where the sandy layer is located (Figure 5.15).

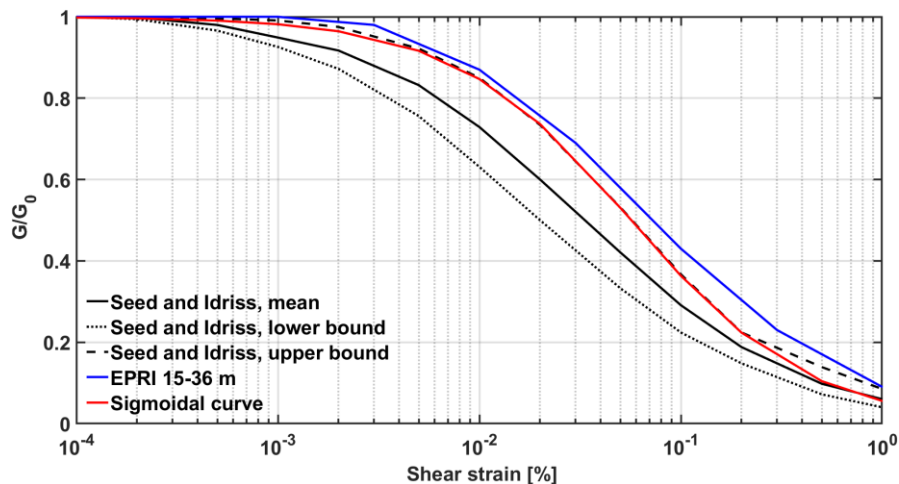


Figure 5.15: Shear modulus reduction curve adopted for the sandy layer and comparison with empirical curves.

For the alluvial sand, two boreholes with SPT one CPTu are available. The soil unit weight was assumed as  $18.5 \frac{kN}{m^3}$ , while the other parameters were estimated using SPT- and CPT-based empirical relationships (Equations 5.1-5.6). The mean  $V_s$  value for the alluvial sand layer ranges between  $151 \frac{m}{s}$  and  $149 \frac{m}{s}$ , using the SPT- and CPT-based relationships, respectively. Figure 5.16 shows the  $V_s$  profile obtained for the SPT and CPTu relationships. These  $V_s$  profiles are coherent with seismic refraction data available downstream of the dam.

The friction angle of this material was taken as  $36^\circ$ , which is the lower value estimated from SPT- (Mayne 2001) and CPT-based (Kulhawy and Mayne, 1990) empirical relationship. The hydraulic conductivity was estimated from the following CPT-based relationship (Robertson, 2010):

$$k = 10^{0.952-3.04I_c} \quad \text{for } I_c \leq 3.37 \quad (5.8a)$$

$$k = 10^{-4.52-1.37I_c} \quad \text{for } 3.27 < I_c < 4 \quad (5.8b)$$

which give a mean value of  $6.5 \cdot 10^{-5} \frac{m}{s}$ . The MRD curve is the average curve by Seed and Idriss. This curve is similar to that by EPRI (1993) for sands from 0-6 m (Figure 5.17). These comparisons between empirical relationships are useful since grain size distribution data available, and the boring logs showed that there are fractions of silts in the upper layer. The use multiple relationships, based on different tests, can somewhat compensate to the epistemic uncertainties due to the paucity of laboratory tests.

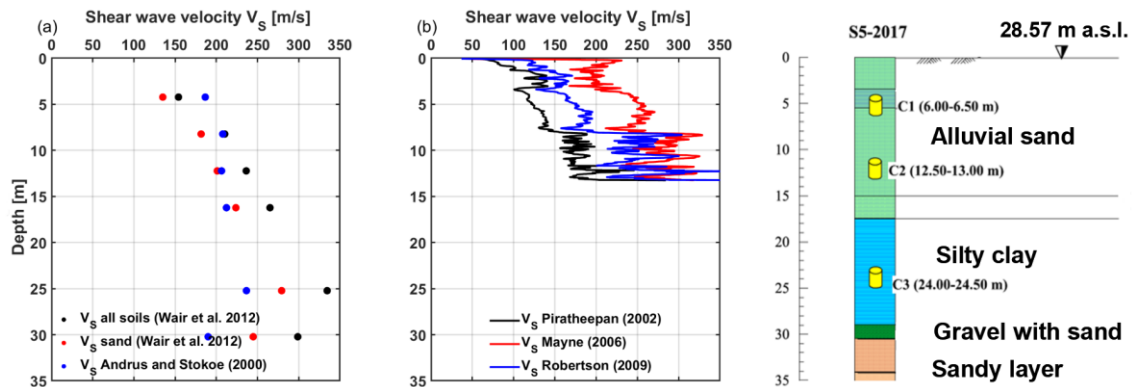


Figure 5.16: Shear wave velocity profiles in free field conditions estimated from empirical relationships using (a) SPT data and (b) CPT data.

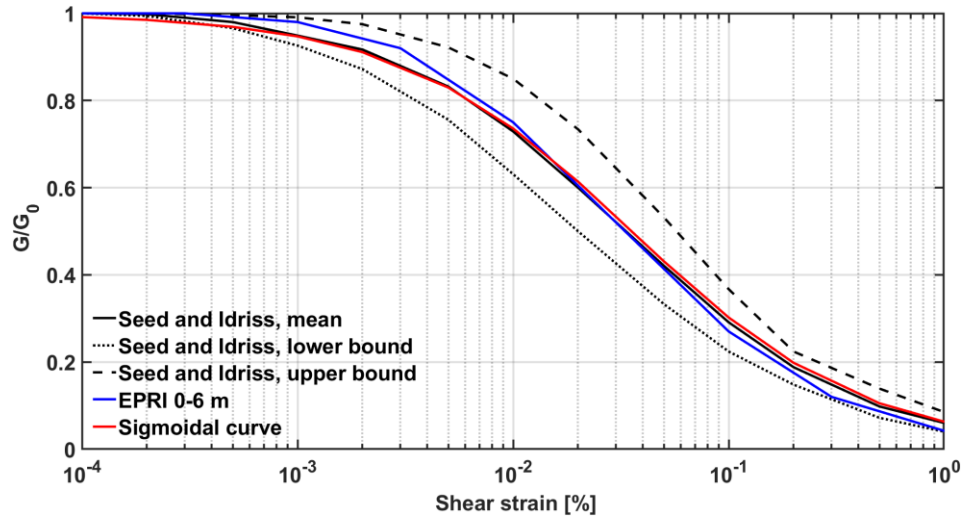


Figure 5.17: Shear modulus reduction curve adopted for the alluvial sand layer and comparison with empirical curves.

The rock layer, which consist of slightly fractured gneiss, was modeled as an elastic material, with a  $V_s$  of  $1440 \frac{m}{s}$  and a Poisson ratio of 0.35. These values are based on seismic refraction tests in free field conditions performed in the secondary dam area, and on a down-hole test performed on the main dam (this can be done as the rock material is persistently present in the whole area and is spatially continuous). Table 5.3 shows a summary of the properties of the dam body and of the foundation layers used in the dynamic analyses.

Table 5.3: Summary of the properties used in the numerical analyses of the secondary dam.

Property	Core	Shells	Clayey Silt	Old alluvium	Sandy layer	Alluvial sand	Fractured Rock
$\gamma$ [ $kN/m^3$ ]	20.36	21.92	18.25	18.5	18.5	19.5	25.5
$c'$ [ $kPa$ ]	10	0	48	0	0	0	-
$\phi'$ [ $^\circ$ ]	26	40	24	35	34.5	36	-
$k$ [ $m/s$ ]	$5 \cdot 10^{-10}$	$1.9 \cdot 10^{-7}$	$1 \cdot 10^{-9}$	$6.5 \cdot 10^{-5}$	$1 \cdot 10^{-7}$	$6.5 \cdot 10^{-5}$	$1 \cdot 10^{-10}$
$G$ [ $MPa$ ]	$G(z)$	$G(p')$	$G(p')$	$G(p')$	$G(p')$	$G(p')$	1880
$\nu$	0.39	0.33	0.33	0.33	0.33	0.33	0.35

### 5.5.3 Ambient noise measurements

Three Microtremor HVSR were performed on the secondary dam (one on the crest and two downstream, in free field conditions), using a three-component Micromed Tromino® (Moho s.r.l., 2021). The sampling interval was around 20 minutes, with measurement every 30 seconds. The short duration of the measurement may have some impact on the clarity of the data, especially for low frequencies that can only

be resolved if longer measurement durations are utilized (e.g., SESAME, 2004; Gospe et al., 2020). However, this aspect should not affect the identification of the fundamental frequency of the dam-foundation system that, given the geotechnical and geophysical properties of the dam and its foundation, is believed to be at relatively high frequencies ( $>1\text{Hz}$ ). The peak on the mean curve is then used to estimate the fundamental period of the dam (Nakamura, 1989). In addition, H/V polar diagrams (i.e., series of H/V curves evaluated by varying the horizontal component direction in the range  $0^\circ\text{-}180^\circ$ ) were calculated to find any potential peak polarization effects (which is typical for elongated topographic features, such as embankment dams). For the crest, the North was taken as the parallel direction to its longitudinal axis. Figure 5.18 shows the results obtained for the HVSR performed on the crest. Here, a well-defined peak cannot be identified. The HVSR performed downstream in free field conditions (Figure 5.19) show higher amplitudes and two peaks at around 3Hz and 5Hz. The second peak (5Hz) seems to be the most likely candidate as a clear peak as its amplitude is higher and it clearly stands out from neighboring frequencies. This would indicate a fundamental period of the dam of around 0.2 s. This is consistent with numerical results presented in section 6.5.3. Figure 5.19c shows the HVSR polar plot at this location. This plot shows a clear polarization of the H/V ratio in the azimuth range  $90^\circ\text{-}120^\circ$ . This direction is consistent with the longitudinal direction of the dam.

### 5.3. Site-specific PSHA for the Angitola dam

In this section, site-specific PSHA and disaggregation results for the Angitola dam site are illustrated. The model used to perform the site-specific PSHA is the same used for the Farneto del Principe dam site. The seismic hazard for the Angitola dam was computed for a  $V_s$  of 800 m/s, as the layer beneath the foundation of the dam comprises intact rock. Figure 5.20a shows the mean hazard curves obtained for PGA and the spectral accelerations at 0.1, 0.2, 0.5s, and 1 s. The annual rates of exceedances of the  $S_a$  (0.2s) and  $S_a$  (0.1s) are the greatest, which is reflected in the shape of the UHS (Figure 5.20b). Figure 5.20b shows the UHS and CMS for the four return periods used in the dynamic analyses (75, 475, 710, and 1460). The CMS are built following the approach used for building those at the Farneto del Principe dam site as reported in § 4.2.2.1. The conditioning period for the CMS is 0.2s, which is the fundamental period of the dam-foundation system. The differences between the two spectra are more pronounced for high return periods and in the period range 0-1s.

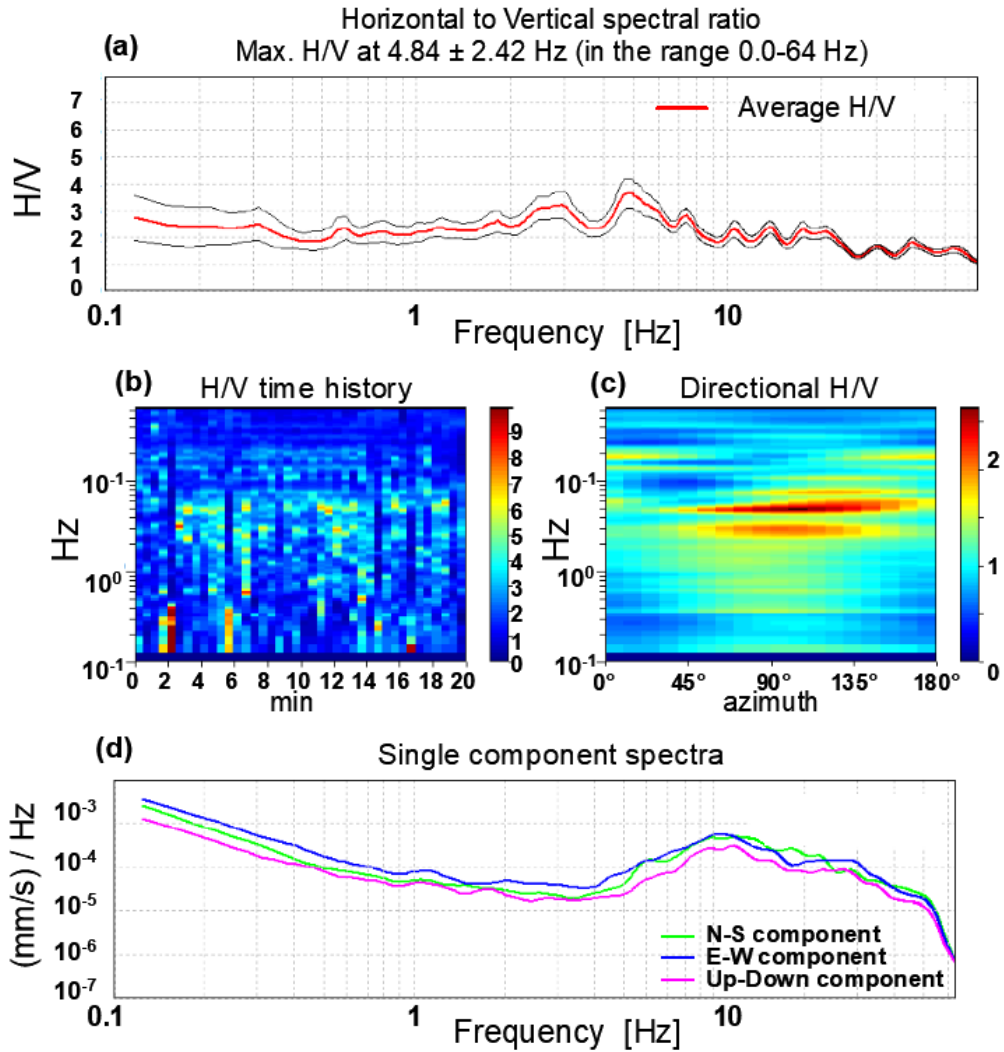


Figure 5.18: Results of the HVSR performed on the crest: (a) H/V ratio vs frequency, (b) H/V time series, (c) HVSR polar plot, and (d) single component spectra.

The CMS are built based on disaggregation results for Sa(0.2s). Figure 5.21 and Table 5.4 show magnitude and epsilon values with the highest contribution to the hazard at the site for all return periods and PGA and Sa(0.2s). Figure 5.22 shows the magnitude-distance disaggregation plot. The differences between the PGA and Sa(0.2s) disaggregation results are only visible the distances for high return periods, with higher distances contributing more to the PGA. Magnitude-distance results are similar to those produced at the Farneto del Principe dam site with local, smaller magnitude faults, and high-magnitude events from the subduction of the Calabrian Arc dominating the hazard.

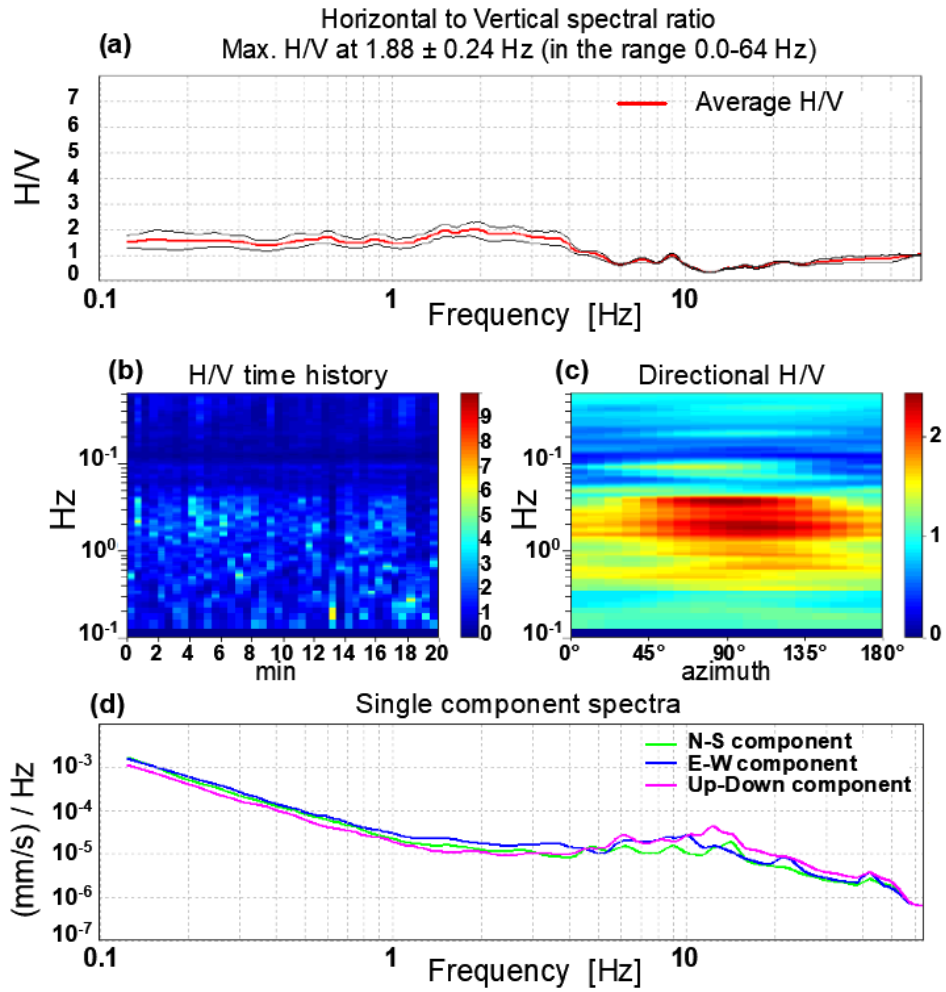


Figure 5.19: Results of the HVSR performed in free field conditions: (a) H/V ratio vs frequency, (b) H/V time series, (c) HVSR polar plot, and (d) single component spectra.

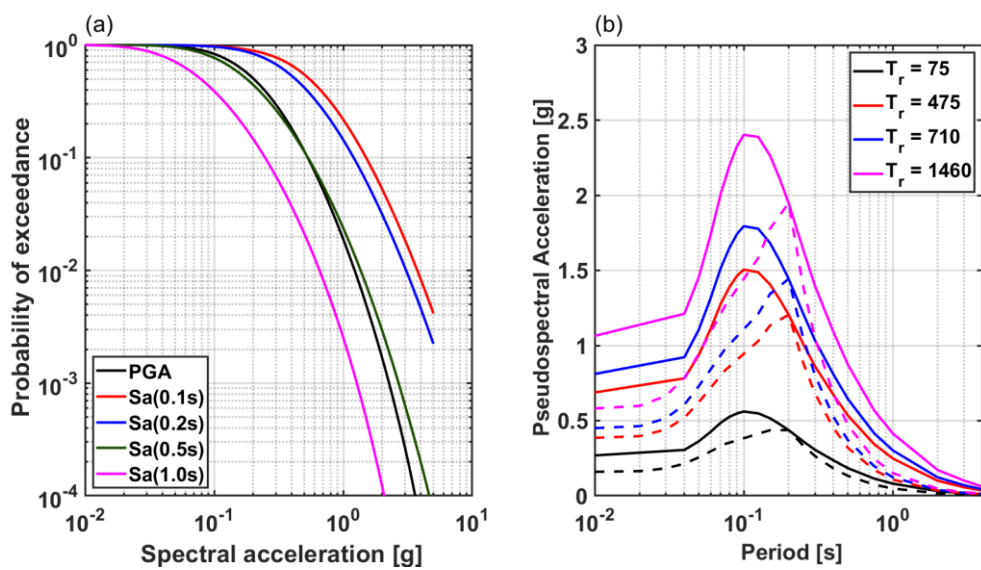


Figure 5.20: (a) Hazard curves, and (b) UHS and CMS for the Angitola dam site.



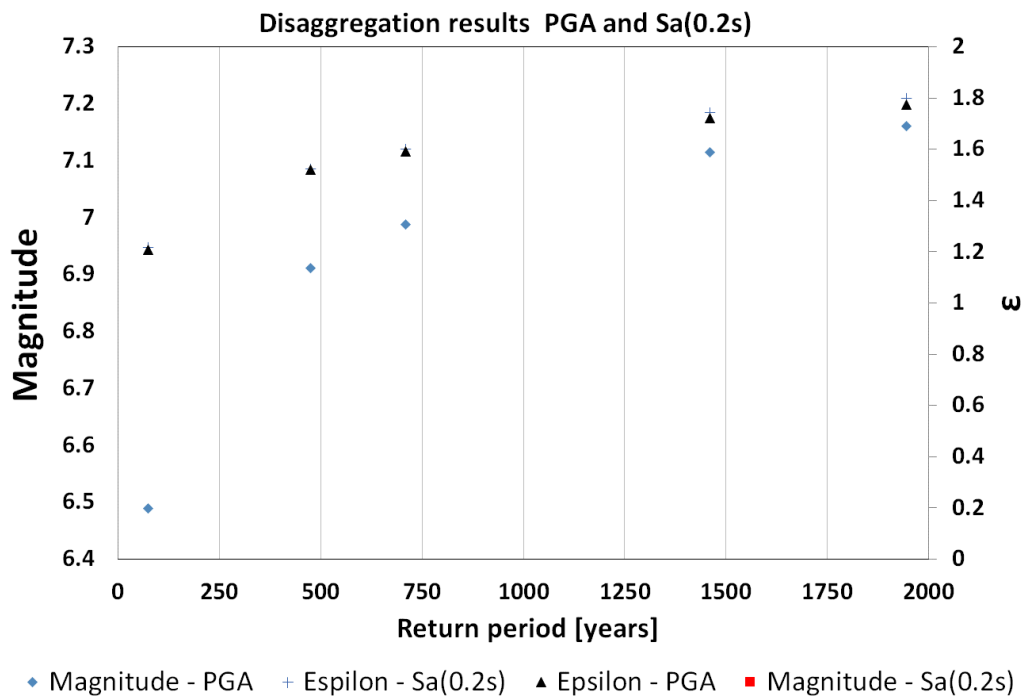


Figure 5.21: Summary of disaggregation results for the Angitola dam site.

Table 5.4: Summary of disaggregation results for the Angitola dam site.

Return period	Magnitude		Distance [Km]		Epsilon	
	Sa(0.2 s)	PGA	Sa(0.2 s)	PGA	Sa(0.2 s)	PGA
75	6.489	6.530	50.77	50.80	1.22	1.21
475	6.911	6.937	45.51	49.27	1.52	1.52
710	6.988	7.003	44.80	49.47	1.60	1.59
1460	7.115	7.103	43.65	49.90	1.74	1.72
1946	7.161	7.138	43.19	50.06	1.80	1.77
2475	7.198	7.166	42.78	50.17	1.84	1.82

Figure 5.23 illustrates the magnitude-distance disaggregation for a return period of 1460 years. The chart shows that there are two main contributions: one is due to nearer faults and short distances, while the other is due to long distances, most likely related to the subduction slab and interface.



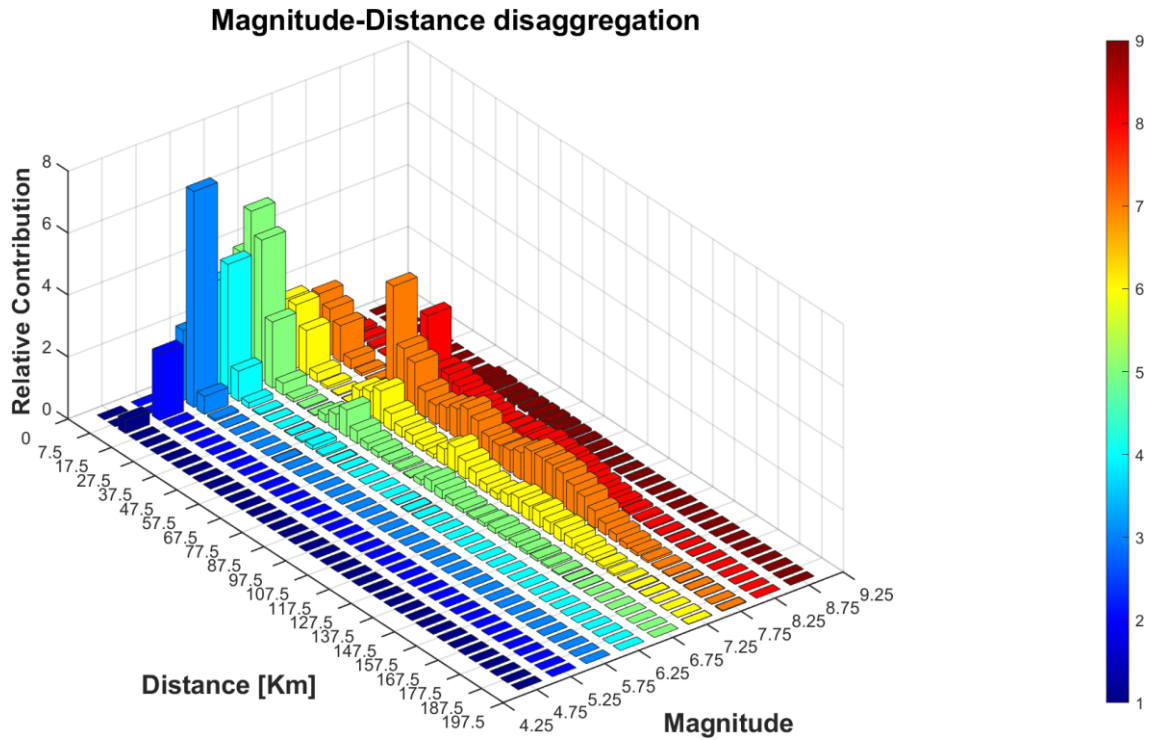


Figure 5.22: Magnitude-distance disaggregation for the Angitola dam site.

#### 5.4 Semi-empirical liquefaction resistance analysis

This section illustrates the analysis of liquefaction susceptibility and triggering of the foundation layers of the Angitola secondary dam foundation layers. As reported in § 5.2.1, the dam body is not susceptible to liquefaction (for the shells). Particular attention, however, must be given to foundation layers; in fact, large deformations beneath the embankment can cause severe damage to the above structure. For the secondary dam, the two layers of interest are the sandy layer and the alluvial sand layer (labelled as old alluvium in Figure 5.3). The former comprises heterogeneous fine silty sand, while the latter comprises mildly loose silty sands. This information obtained by the two available boring logs shown in Figure 5.3 is the only detail about grain size distributions within these layers. For this reason, the percentage of fines in these layers was treated using a conservative approach, as it is a main component of the liquefaction susceptibility of soil.

Given the lack of laboratory tests on the materials of these layers, the materials will be treated as susceptible to liquefaction. As a result, a liquefaction triggering analyses were performed using data from the two available SPTs (one from the landside shell and one downstream) and one CPTu (Figure 5.4) and following semi-

empirical procedures by Idriss and Boulanger (2014) and successive modifications (Boulanger and Idriss, 2016). Four blow counts are available in the sandy layer for both SPT performed on the landside shell and downstream. These N values were corrected for the energy ratio delivered to the samples (in Italy practice, it is usually 75%) and for the overburden stress. The other correction factors (e.g. borehole diameter, rod length, and sampler) are equal to one. The overburden correction factor  $C_N$  is estimated from the vertical effective stresses calculated from a numerical static analysis of the dam. The stress state beneath the dam cannot be considered as geostatic. In addition, the construction process of the dam, and the groundwater flow, influence the state of stress in the foundation layers. All of these phenomena were analyzed in the numerical model as reported in § 6.5.2. The same consideration can be made for the N values downstream, though the overburden stress effect due to the presence of the dam is practically negligible (i.e., the state of stress is close to geostatic conditions). The adjustment of the blow counts for clean sands is done by using a Fines Content value of 10%. This is probably a conservative value, though it does provide a light contribution to resistance. The cyclic resistance ratio (CRR) is then estimated as:

$$CRR_{M,\sigma'_v} = CRR_{M=7.5,\sigma'_v=1} MSF K_\sigma K_\alpha \quad (5.9)$$

where MSF is the Magnitude Scaling Factor,  $K_\sigma$  is the overburden correction factor,  $K_\alpha$  is the correction factor for static shear stresses, and  $CRR_{M=7.5,\sigma'_v=1}$  is the CRR for clean sands and reference conditions of magnitude and confinement (7.5 and 1 atmosphere). In this case, the magnitude used is that producing the highest contribution to the hazard (from disaggregation analysis results) for a return period of 1460 years, which is 7.1. The mean CRR in the sandy layer beneath the dam is 0.161, while in free field conditions is 0.246. These values will later be used to calibrate the advanced constitutive model PM4Sand for these materials. For the alluvial sand, the same calculations were performed for the available SPT, and for a fine content of 10%. In this layer, the CRR is around 0.223, though the variability due to overburden stress and fines content is more important than that in the sandy layer. This is because below a  $\sigma'_v$  of 40kPa, the dependence of  $K_\sigma$  is not validated (Boulanger and Idriss, 2014). For these reasons, and because there is only one blow count available, the CRR of the alluvial sand was estimated from the CPTu test. Table 5.5 shows a summary of the main results obtained for the SPT tests. Figure 5.23a shows the CRR trend with depth, which highlights the effect of the overburden stress

on the liquefaction resistance (i.e. CRR does not monotonically increase with depth). The CRR estimated from the CPTu is shown in Figure 5.23b, whose trend reflects that of the cone tip resistance. The boring log co-located with this CTPu showed that only the first 3 meters are made up of silty sands. Beyond this depth, there is a layer of clay with silt. Thus, the mean value of the CRR adopted is that in the range 1-3 m, which is 0.19. The first meter was excluded because of soil disturbances. This value is more conservative than that estimated from the SPT test, and it is averaged throughout the layer.

Table 5.5: Summary of the results obtained from the SPT tests and CRR for liquefaction triggering.

Quote a.s.l. [m]	Depth [m]	$N_{SPT}$	$N_{160}$	$N_{160 CS}$	$K_{\sigma}$	$CRR_{M, \sigma'_v}$
<b>SPT from landside shell, sandy layer</b>						
7.08	25.23	20	13.3	14.5	0.86	0.145
3.08	29.23	28	19.0	20.1	0.81	0.187
0.07	32.23	23	14.2	15.4	0.84	0.148
-2.93	35.23	27	16.6	17.8	0.81	0.163
<b>SPT in free field condition, sandy layer</b>						
13.46	12.23	22	24.2	25.4	0.95	0.315
10.46	15.23	19	18.9	20.1	0.93	0.214
6.46	19.23	21	19.0	20.2	0.90	0.208
<b>SPT in free field condition, alluvial sand</b>						
22.46	3.23	10	10.6	17.9	1.1	0.223

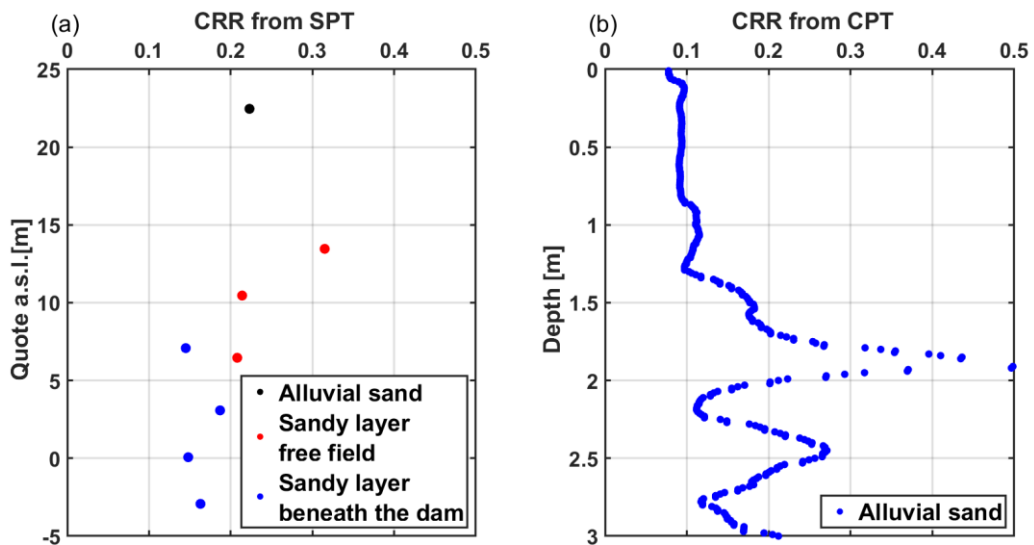


Figure 5.23: CRR estimated from SPT results (a) and CPT (b).

## 6. Numerical modeling of the Farneto del Principe and Angitola dams

This chapter presents the numerical models of the two case studies, the Farneto del Principe dam and the Angitola dams. After a brief introduction of the software used, the general recommendations for modeling an earth dam are presented. Then, the constitutive models PM4Silt and PM4Sand, developed for geotechnical earthquake engineering applications, are briefly introduced. The Farneto del Principe dam numerical model and the calibration of PM4Silt are presented. Lastly, the Angitola dam model is presented, along with the several PM4Sand calibrations performed for the foundation layers.

### 6.1 Fast Lagrangian Analysis of Continua (FLAC)

The numerical modeling of the two case studies was carried out with the 2-Dimensional finite difference commercial software platform FLAC (an acronym for Fast Lagrangian Analysis of Continua, Itasca 2019), specifically developed for geotechnical and mining engineering. The materials are represented by elements, or zones, which form a grid that can be modified depending on the particular geometry of the problem. Each zone behaves according to a selected stress-strain relationship (constitutive model) provided by the user. If the material yields and the analysis is set for large strain calculations, the grid deforms consequently and moves with the material that is represented (hence the name Lagrangian Analysis of Continua).

The FLAC formulation is based on the explicit, time-marching method to solve the equations of motion, where the governing differential equations are replaced by algebraic expressions using an appropriate time discretization. In each step, the finite difference equations are updated, thus no matrices are formed and large 2-D calculations can be made without excessive memory requirements. In addition, no iterations are necessary to follow a highly nonlinear stress-strain law. The drawback of time-marching explicit programs is that a small timestep is usually necessary to ensure numerical stability. FLAC uses the dynamic equations of motion even for static problems, to avoid issues connected to physical instability (i.e. an unstable system may still be numerically stable, so that the collapse progression can be estimated). The calculation performed by FLAC for each step is described by the loop in Figure 6.1.

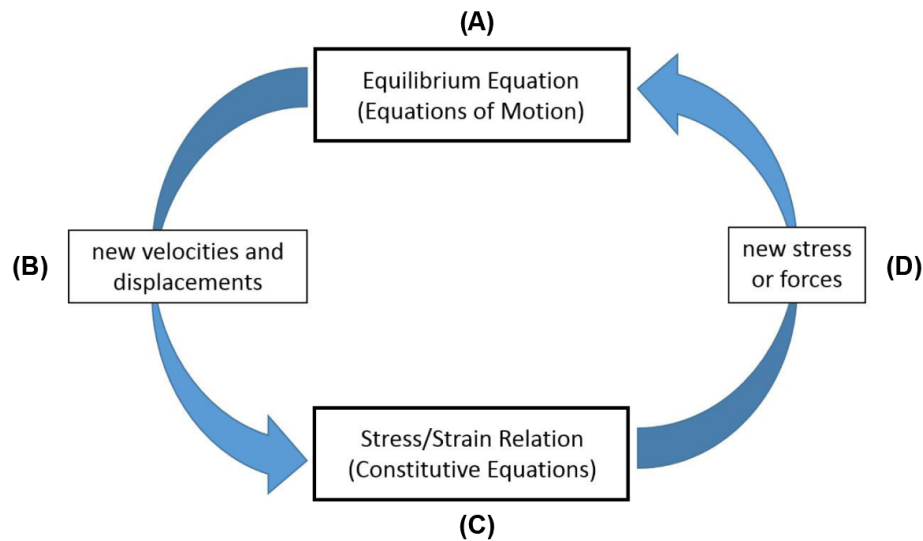


Figure 6.1: FLAC calculation scheme.

Starting from the dynamic equation of motion, new velocities and displacements are derived based on the initial conditions of stresses and/or forces. The velocities are used to derive strain rates, which are then combined with constitutive models to evaluate new stress increments. Every cycle around the loop corresponds to one timestep, wherein every grid variable is updated from known values that remain fixed. For instance, phase C takes the set of velocities already calculated, and for each element computes new stresses. The velocities are assumed to remain constant for operation C (i.e., the newly calculated stresses do not affect the velocities), so the variation of velocity in a single time step is null. This may seem unreasonable considering that a stress change in one zone will influence its neighbors and change their velocities. However, the timestep is chosen so small that information will not physically pass from one zone to another in that interval. All materials have some maximum speed at which information can propagate; the main concept of the explicit method is that the calculation wave speed must be greater than the physical wave speed. After several cycles of the loop, disturbances can propagate across several elements, just as they would propagate physically.

The strength of the software lies in several capabilities and tools, such as the possibility of dealing with problems characterized by complex geometries. FLAC has a built-in programming language (FISH for FLACish), which allows defining new functions, variables, and constitutive models (see later for alternative option for implementing user-defined constitutive models as dynamic link libraries).

## 6.2 Constitutive models

This section presents the background of the advanced constitutive models adopted in the numerical analyses. The focus of this section is to provide the reader with the general idea behind these models, while for a more in-depth description the reader is referred to the corresponding manuals (Boulangier and Ziotopoulou, 2017, 2019). As explained in § 2.4.4, one of the main concerns about the use of more complex plasticity models is the calibration procedure. This is usually achieved by performing single-element simulations for the range of loading paths important for an earth dam (e.g. simulating the rate of pore pressure generation, Boulangier and Ziotopoulou, 2015). However, due to the nature of the models, it is not possible to calibrate them to represent all the stress strain behaviors of interest. For instance, the undrained monotonic response in a single element simulation is usually stiffer than the laboratory one. If this behavior is prioritized, it could lead to an erroneous evaluation of the shear modulus reduction curves. Hence, sometimes it might be necessary to perform different calibrations to represent different behaviors. In addition, the single-element calibration should be done by considering all the in-situ stress-state conditions (e.g. several confinement stresses) or the user should check that the model is capable of capturing the broad range of applicable conditions with just one set of calibration parameters. Section 6.4.3 and 6.5.4 illustrate the procedure used to calibrate the PM4Silt and PM4Sand models for two earth dams, taking into account all of the above considerations.

### 6.2.1 PM4Sand

PM4Sand v3.1 (Ziotopoulou, 2014, Boulangier and Ziotopoulou 2017) is a plane strain stress ratio-controlled, critical state compatible, bounding surface plasticity model that follows the framework of Dafalias and Manzari (2004). The model is developed and calibrated at the equation level to approximate the stress-strain responses of coarse-grained soils in geotechnical earthquake engineering applications. In particular, the dynamic behaviors of interest of PM4Sand are the triggering of liquefaction and the deformations that occur. The model calibration targets at honoring the broader set of design correlations (empirical and semi-empirical) known in literature and experimental test results, such as:

- The variation of the Cyclic Resistance Ratio (CRR) with number of uniform loading cycles, which reflects the response of the soil to earthquakes characterized by irregular loading cycles. In the simplified liquefaction

triggering procedure, this is accounted for with the use of a Magnitude Scaling Factor;

- The effect of overburden stress on the CRR. The model is able to approximate the cyclic strength variation with effective confining stresses and for different relative densities, which is illustrated by the parameter  $K_\sigma$  in liquefaction analyses (Idriss and Boulanger, 2008). The CRR reduces with increasing overburden stress, with a less pronounced effect for loose sands. This is a consequence of the tendency of the soils to dilate or contract according to their position to the Critical State Line;
- The effect of initial static shear stresses on cyclic strength, illustrated by the parameter  $K_\alpha$  (Boulanger 2003a). The model is calibrated such that higher static shear stress ratio  $\alpha$  results in higher CRR for dense-of-state sand and lower for loose-of-state. This is again attributed to the critical state behavior of the soils, upon which the model is based on;
- The progressive accumulation of shear strains following the triggering of liquefaction. This is accomplished mainly by extending the fabric tensor of Dafalias and Manzari (2004) to also measure its cumulative absolute value as an indirect metric of damage such that the model can attain larger strains without locking up in a repeating loop;
- Shear modulus reduction and damping curves, which control the dynamic behavior of the soil for low to medium shear strains before the onset of liquefaction;
- Drained and undrained monotonic stress-strain responses, as illustrated by experimental results by Ishihara (1993), and Lee and Seed (1967). The peak friction angles obtained from the model honor Bolton's relation (1986);
- Volumetric strains due to post-liquefaction reconsolidation.

The PM4Sand model incorporates a fabric-dilatancy tensor (Dafalias and Manzari, 2004) that *“macroscopically model the effect that microscopically-observed changes in sand fabric during plastic dilation have on the contractive response upon reversal of loading direction.”*

The model has a set of primary variables that must be chosen and/or calibrated by the user and a set of 21 secondary parameters, where default values are provided based on the model’s generalized calibration but can be adjusted if site-specific data is available. The parameters and a brief description are reported in the tables below.

Table 6.1: Primary parameters of the PM4Sand model.

<b>Primary parameters<sup>2</sup></b>		
<b>Input parameter</b>	<b>Default value</b>	<b>Description</b>
$D_R$	-	<i>Required</i> Apparent relative density (expressed as a decimal). Primary variable controlling dilatancy and stress-strain response characteristics.
$G_o$	-	<i>Required</i> Primary variable controlling the small strain shear modulus.
$h_{p0}$	-	<i>Required</i> Contraction rate parameter. Primary variable that adjusts contraction rates and hence can be adjusted to obtain a target cyclic resistance ratio.
$p_A$	101,300 Pa	Atmospheric pressure in the unit set being used.
First call	0	Flag used to re-set the back-stress ratio history terms equal to the current stress ratio, and to erase all fabric terms.
PostShake	0	Flag used during post-shaking portion of a simulation to improve modeling of post-liquefaction reconsolidation strains.

<sup>2</sup> The reader is referred to Boulanger and Ziotopoulou (2017) for more details



Table 6.2: Secondary parameters of the PM4Sand model.

Secondary parameters		
Input parameter	Default value	Description
$h_o$	$\frac{0.25 + D_R}{2}$	Variable that adjusts the ratio of plastic modulus to elastic modulus. It was chosen to provide reasonable shear modulus reduction curves.
$e_{max}, e_{min}$	0.8 and 0.5	Maximum and minimum void ratio. Refinements in these parameters may not be necessary, as the calibration of other parameters will have a stronger effect on monotonic or cyclic strengths.
$n^b$	0.5	Parameter that regulates dilatancy and thus also the peak effective friction angles.
$n^d$	0.1	Parameter that controls the stress-ratio at which contraction transitions to dilation.
$A_{do}$	0.8	Default value is computed based on Bolton's dilatancy relationship at the time of initialization.
$z_{max}$	$f(D_R)$	May require varying if the relationship between $D_R$ and cyclic strength is significantly different from that implied by the liquefaction correlations of Idriss and Boulanger (2008).
$c_z$	250	Parameter that controls strain levels at which fabric affects become important.
$c_\epsilon$	$f(D_R)$	Parameter that can be used to adjust the rate of strain accumulation in undrained cyclic loading.
$\phi'_{cv}$	33°	Critical state friction angle.
$\nu_o$	0.3	Poisson ratio.
$C_{GD}$	2	Parameter that controls the degradation of the small-elastic modulus with cumulative plastic deviatoric strains.
$C_{DR}$	$f(D_R)$	Parameter that controls the rotated dilatancy surface and is applied to reduce the rate under which dilatancy is increasing.
$C_{kaf}$	$f(D_R)$	Parameter that controls the effect that sustained static shear stresses have on plastic modulus.
$Q$	10	Default value is 10 for quartzitic sands per recommendations of Bolton (1986).
$R$	1	Default value for quartzitic sands is 1 per recommendations of Bolton (1986).
$m$	0.1	Parameter used for reasonable modeling and numerical stability.
$F_{sed,min}$	$f(D_R)$	Controls the minimum value the reduction factor of the elastic moduli can attain during reconsolidation.
$p'_{sed,o}$	$-\frac{p_A}{5}$	Mean effective stress up to which reconsolidation strains are enhanced in post-shaking analysis.
$cr_{hg}$	0.005	Nominal plastic shear strength ratio used to compute $c_{hg}$ at the time of initialization.
$c_{hg}$	$f(cr_{hg}, p')$	Nominal plastic shear strength assigned at initialization.

### 6.2.2 PM4Silt

PM4Silt is a bounding surface plasticity model for low-plasticity silt and clays that is stress-ratio-controlled and critical state compatible (Boulanger and Ziotopoulou, 2018). The model was built upon the PM4Sand model and with the purpose to evaluate the undrained monotonic and cyclic behavior of low plasticity fine grained soils. Several engineering correlations and stress-strain responses known from literature were considered in the model framework, such as:

- Stress history normalization of the monotonic undrained shear strength, as illustrated in the SHANSEP procedure (§ 3.5.5.2);
- The development of excess pore water pressure in both low and high plasticity soils, which leads to a huge rate of shear strain accumulation;
- The shape of the cyclic resistance curve for cyclic softening. In particular, the variation of cyclic strength ratios with the number of uniform cycles is flatter compared to the CRR of sands. The overburden stress effects are accounted for in the relation between the monotonic undrained shear strength and the OCR;
- The variation of shear modulus reduction and damping curves for fine grained soils varying with plasticity index and confining stress.

The model formulation and its implementation in the numerical software FLAC are reported in Boulanger and Ziotopoulou (2018). Just as PM4Sand, the PM4Silt model uses the fabric-dilatancy tensor to control the shear strain rate accumulation.

The model requires a set of primary and secondary parameters. The former are required and they define the main characteristics of the fine grained soils, while the latter have default values (based on a generalized calibration under a range of loading paths) but they can be adjusted if site-specific data are known. A summary of the primary and secondary parameters is reported in Tables 6.3 and 6.4 (further details are given in Boulanger and Ziotopoulou, 2018).

Table 6.3: Primary parameters of the PM4Silt model.

Primary parameters		
Input parameter	Default value	Description
$s_{u,cs,eq}$ or $\frac{s_{u,cs,eq}}{\sigma'_v}$	-	<i>Required</i> Undrained shear strength at critical state under earthquake loading rates. It is used to position the critical state line to obtain the specified undrained shear strength at critical state for the current void ratio.
$G_o$	-	<i>Required</i> Primary variable controlling the small strain shear modulus.
$h_{p0}$	-	<i>Required</i> Contraction rate parameter. Primary variable that adjusts contraction rates and hence can be adjusted to obtain a target cyclic resistance ratio.
$F_{su}$	1	Undrained shear strength reduction factor. Primary variable that can be used to reduce the $s_{u,cs}$ value relative to the value at the time of initialization.
First call	0	Flag that is used to set the back-stress ratio history terms equal to the current stress ratio, erasing all fabric terms.
$p_A$	101,300 Pa	Atmospheric pressure in the unit set being used.

Table 6.4: Secondary parameters of the PM4Silt model.

Secondary parameters		
Input parameter	Default value	Description
$n_G$	0.75	Shear modulus exponent. It controls the small strain shear modulus variation with confining stress.
$h_o$	0.5	Variable that adjusts the ratio of plastic modulus to elastic modulus. It was chosen to provide reasonable shear modulus reduction curves.
$e_0$	0.9	Initial void ratio. It affects how volumetric strains translate into changes in state parameter.
$\lambda$	0.06	Slope of the critical state line in $e$ - $\ln(p)$ space.
$\phi'_{cv}$	32°	Critical state friction angle.
$n^{b,wet}$	0.8	The degree to which the peak $s_u$ may exceed the critical state $s_{u,cs}$ increases with decreasing $n^{b,wet}$ .
$n^{b,dry}$	0.5	Controls peak effective friction angles for dense of critical state conditions, and thus influences undrained cyclic loading behaviors.
$n^d$	0.3	Parameter that controls the stress-ratio at which contraction transitions to dilation.
$A_{do}$	0.8	Default value provides approximate consistency with stress dilatancy relationships.
$r_{u,max}$	$f(p')$	Excess pore water pressure ratio based on the mean effective stress. It is different from the form commonly used to interpret DSS tests (which is based on $\sigma'_{vc}$ );
$z_{max}$	$f\left(\frac{S_u}{\sigma'_v}\right)$	Can be adjusted to improve approximation of site-specific laboratory test data.
$c_z$	100	Parameter that controls strain levels at which fabric effect become important.
$c_\epsilon$	$f\left(\frac{S_u}{\sigma'_v}\right)$	Parameter that can be used to adjust the strain accumulation in undrained cyclic loading.
$C_{GD}$	3	Parameter that controls the degradation of the small-elastic modulus with cumulative plastic deviatoric strains.
$C_{kaf}$	4	Parameter that controls the effect that sustained static shear stress has on plastic modulus and hence cyclic strength.
$\nu_o$	0.3	Poisson ratio.
$cr_{hg}$	0.005	Nominal plastic shear strength ratio used to compute $c_{hg}$ at the time of initialization.
$c_{hg}$	$f(cr_{hg}, p')$	Nominal plastic shear strength assigned at initialization.
PostShake	0	Flag that can be used during post-shaking simulations to improve modeling of post-liquefaction reconsolidation strains.
$C_{GC}$	2	Factor by which the estimated elastic modulus for 1D reconsolidation is degraded.

### 6.3 Mesh generation and boundary conditions

The accuracy of a numerical model strongly depends on the mesh size and on the choice of the boundary conditions. For embankment dams, four general criteria should be taken in to account when building a numerical model (although they can be extended to every structure):

#### 1) Accuracy of the seismic wave transmission

Kuhlemeyer and Lysmer (1973) suggest that the accuracy of wave transmission in a numerical model depends on the frequency content and material properties. In particular, the maximum zone size should be less than 10 times the wavelength corresponding to the maximum frequency:

$$l_{max} < \frac{\lambda}{10} \quad (6.1)$$

In other words, the mesh size controls the maximum frequency that can be transmitted accurately in a numerical model. Eq. 6.1 can be also written as:

$$l_{max} < \frac{V_s}{10f_{max}} \quad (6.2)$$

where  $V_s$  is the minimum shear wave velocity and  $f_{max}$  the maximum frequency that needs to be transmitted in the model. The  $f_{max}$  depends on the acceleration time series and can be found with a Fourier analysis.

#### 2) Geometrical details of the dam

Earth dams usually have a complex geometry and particular construction details (e.g. cut-off wall, filters). Even if the maximum zone size from the Kuhlemeyer and Lysmer relationship is large, sometimes it is not necessary to model the geometric details of the dam. This is also very important when modelling zones where a high gradient of stresses and deformations is expected (i.e. stiffness contrast in tiny layers, such as filters and inspection tunnels).

#### 3) Boundary conditions

One of the main aspects of numerical models is the choice of boundary conditions and their distance from the center. In geotechnical earthquake engineering problems, the motion of the soil is different near the structure and far from it. Seed

et al. (1975) proposed that the extension of the dam boundaries should be around half the width of the embankment such that wave absorption is ensured. However, beyond a certain distance, the motion should be representative of free-field conditions (i.e. not influenced by the structure); in dynamic problems, this is not always modeled. In FLAC, this is accomplished by enforcing the free-field boundary condition on the sides with a 1D column that simulates the extended medium (free-field boundary).

At the base of the model, the elastic half-space usually represents very well the condition that the medium extends indefinitely. This is modelled with viscous dashpots (quiet boundary in FLAC) as described by Lysmar and Kuhlemeyer (1969). Figure 6.2 shows a representative scheme of the boundary conditions used in the numerical models of the two case studies. As reported by the FLAC manual, when the quiet boundary is used, a shear stress time history is applied at the base of the model.

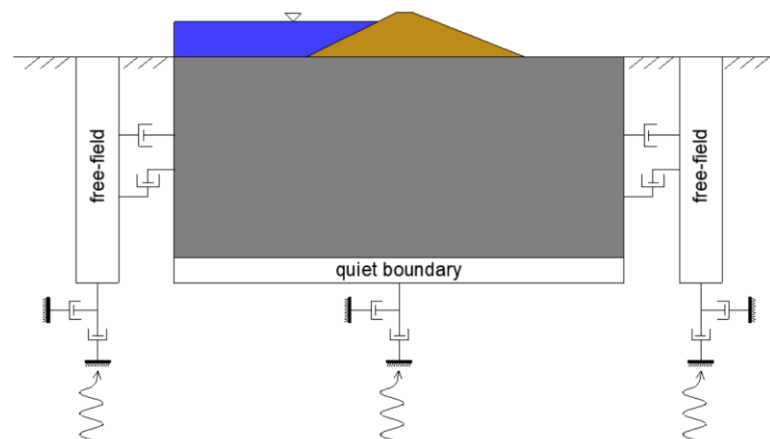


Figure 6.2: FLAC dynamic scheme for the boundary conditions.

#### 4) Computational effort

Nonlinear Deformation Analyses can be quite computationally expensive, especially for a very fine mesh. As long as the three criteria aforementioned are observed, the machine time can be reduced by adopting a slightly less conservative mesh size. Calibration and sensitivity analyses are helpful to understand how much time can be saved with a more efficient mesh. When numerous NDAs are necessary, the time spent in sensitivity analyses is surely gained with less machine time. In the

numerical models of the Farneto del Principe and the Angitola dams, the four criteria mentioned above were observed.

## 6.4 The Farneto del Principe dam model

### 6.4.1 Generalities

In this section, the Farneto del Principe dam numerical model is presented. The dam has a length of over 1200 m and a height of 30 m, thus the plane-strain assumption is justified. In the numerical analyses, the middle section (as indicated in Figure 6.3) is considered, as it can reliably be considered representative of the overall behavior. However, as reported in Chapter 3, the thickness of the foundation layers varies longitudinally, with a maximum value of about 40 m at the center. Sensitivity analyses were performed also in a different section, with a foundation thickness of 20 m. The differences were negligible, hence only the results of the middle section will be presented in the following chapter.

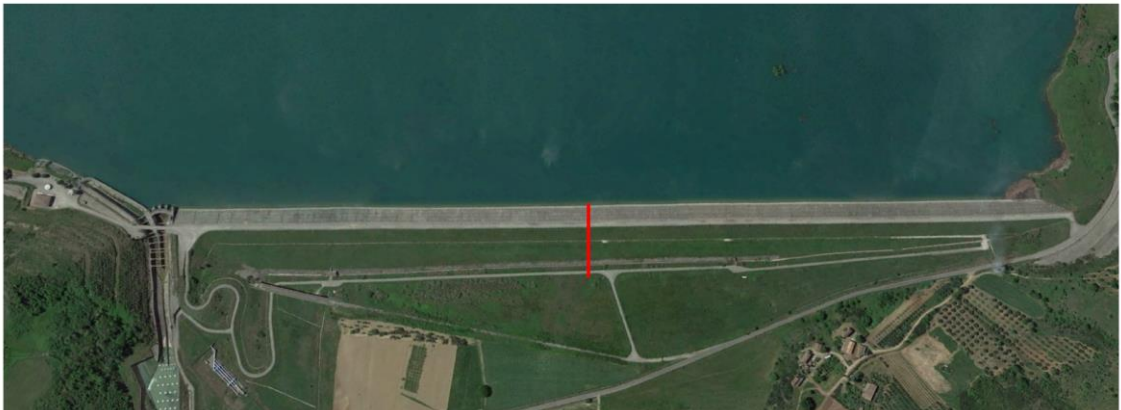


*Figure 6.3: Aerial view of the Farneto del Principe dam (from Google Earth, 2019).*

The dam width is around 142 m, thus the model was extended for 70 m to ensure a good representation of the free-field conditions. In addition, the free-field boundary in FLAC is used to prevent reflected spurious waves into the model. At the base, the clay bed extends for hundreds of meters so it can be considered as an elastic halfspace. The quiet boundary is used to model the clay bed and prevent the reflection of the waves back in the foundation layer. This is important, because there is not an impedance contrast between the foundation and clay bed (as shown by geophysical tests). Hence, the quiet boundary is appropriate to model the energy

absorption of the elastic halfspace. The mesh geometry is coarser near the boundaries, but finer in the center, to model the construction details (e.g. inspection tunnel and cut-off wall). Figure 6.4 shows the mesh of the Farneto del Principe dam model. The Mohr-Coulomb model is used for the alluvial foundation and the dam body, and an elastic material for the cut-off wall and inspection tunnel.

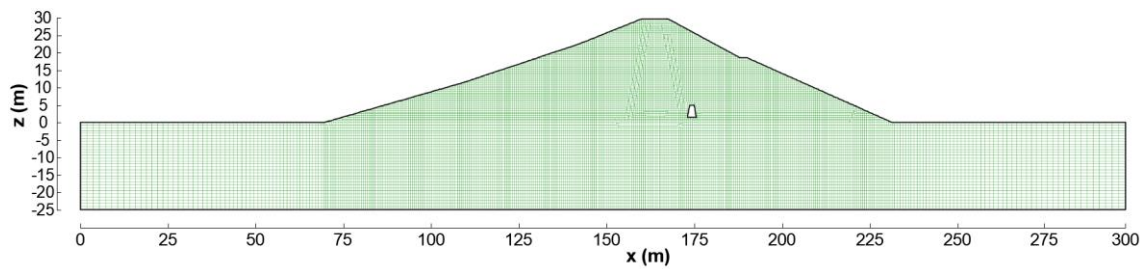


Figure 6.4: Numerical mesh of the Farneto del Principe dam.

The geotechnical modelling is based on the extensive field investigation performed during 2015 and 2017 (§ 3.2 and § 3.4). In particular, the soil properties adopted in the model are the mean of the various tests conducted (e.g. soil unit weight, void index, permeability). For the stiffness, a variation of the shear modulus is assumed in the core, shells, and foundation, as shown in Figures 3.15, 3.16, and 3.17. The construction process of the dam is illustrated in Figure 6.5, where six steps can be identified. Thus, the initial stress state is evaluated with a six-stage process. The deformations monuments measures did not give significant results during construction, so there is no available information on the settlements experienced by the dam body.

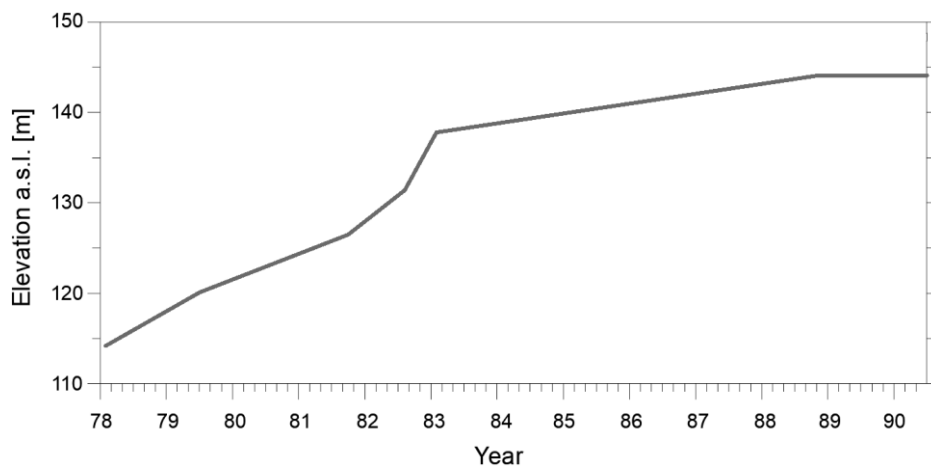


Figure 6.5: Construction log of the Farneto del Principe dam.



The groundwater flow in the dam body is monitored by five Casagrande's piezometers in the core, two standpipe piezometers in the downstream shell, and four in free-field condition away from the dam. The measurements indicate that the reservoir level does not influence substantially the water table depth in the dam core. This is due to the very low permeability of the core material (around  $5 \cdot 10^{-11} \frac{m}{s}$ ). The standpipes piezometers downstream, instead, show a correlation of the water table depth (with a mean value of 5 meters below the free surface) with rainfall events. The standpipe piezometers in the downstream shell (at depths 16 and 25 meters) never found water, which implies that all the water is drained in the inspection tunnel. More details about the piezometric monitoring are in Ausilio et al., 2013 and 2016. Calibration analyses are performed with several reservoir levels to verify the numerical model against the piezometers data available. The results are consistent with the measurements, which means that the analyses performed with the reservoir at the maximum level are also reliable. Figures 6.6 and 6.7 show the initial stress-state and the groundwater flow in the dam body and in the foundation layer.

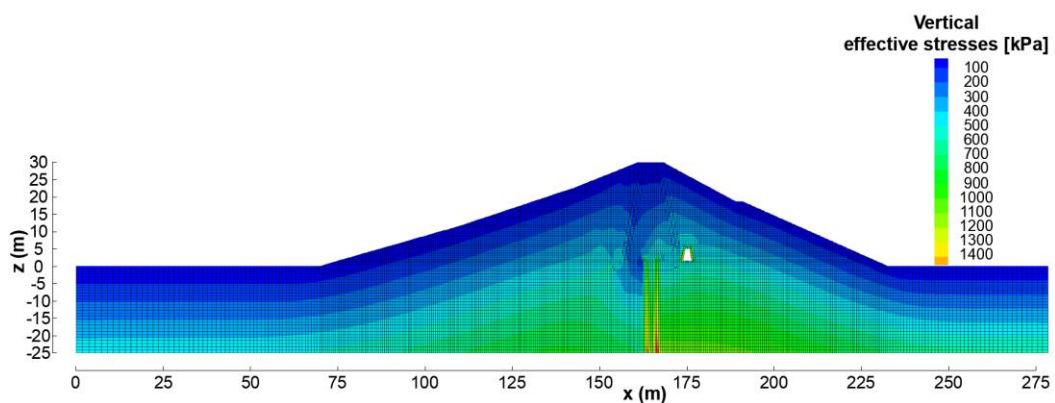


Figure 6.6: Vertical effective stresses after the application of the reservoir at the maximum level (Farneto del Principe dam).

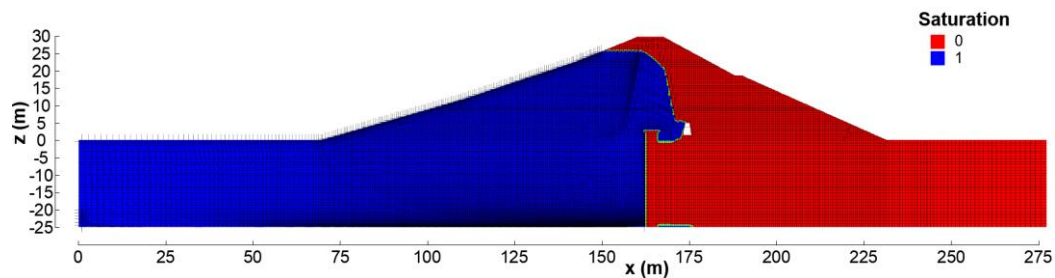


Figure 6.7: Groundwater flow and saturation contours of the Farneto del Principe dam for the reservoir at the maximum allowable level.

#### 6.4.2 Dynamic properties and material damping

The evaluation of the dynamic behavior of embankments dams require the knowledge of the material damping and fundamental period of the structure. For the Farneto del Principe dam, the hysteretic damping formulation (Itasca 2019) has been used for the Mohr-Coulomb type materials. In essence, for each timestep and zone, the shear strain is calculated and a multiplier is applied to the shear modulus. This multiplier is estimated from a fitted shear modulus reduction curve. In this case, sigmoidals curves are chosen to fit the experimental and empirical MRD (§ 3.3.4). The Menq (2007) formulation is used for the shells and alluvial foundation, while for the core the mean experimental curve is fitted. The Menq MRD curves are estimated as:

$$\frac{G(\gamma)}{G_{max}} = \frac{1}{1 + \left(\frac{\gamma}{\gamma_r}\right)^\alpha} \quad (6.3)$$

$$\alpha = 0.86 + 0.1 \cdot \log\left(\frac{\sigma'_0}{p_a}\right) \quad (6.4)$$

$$\gamma_r(\%) = 0.12 C_u^{-0.6} \cdot \left(\frac{\sigma'_0}{p_a}\right)^{\phi_2} \quad (6.5)$$

$$\Phi_2 = 0.5 C_u^{-0.15} \quad (6.6)$$

where  $p_a$  is the atmospheric pressure,  $\sigma'_0$  the mean effective stress, and  $C_u$  the uniformity coefficient. The relationship for the damping is the following:

$$D(\gamma) = D_{min} + b D_M(\gamma) \left[\frac{G(\gamma)}{G_{max}}\right]^{0.1} \quad (6.7)$$

$$D_{min} = 0.55 C_u^{0.1} D_{50}^{-0.3} \left(\frac{\sigma'_0}{p_a}\right)^{-0.08} \quad (6.8)$$

$$b = 0.6329 - 0.0057 \ln(N) \quad (6.9)$$

$$D_M(\gamma) = c_1(D_{M,\alpha=1}) + c_2(D_{M,\alpha=1})^2 + c_3(D_{M,\alpha=1})^3 \quad (6.10)$$

$$c_1 = 0.2523 + 1.8618\alpha - 1.1143\alpha^2 \quad (6.11)$$

$$c_2 = -0.0095 - 0.0710\alpha + 0.0805\alpha^2 \quad (6.12)$$

$$c_3 = 0.0003 - 0.0002\alpha - 0.0005\alpha^2 \quad (6.13)$$

$$D_{M,\alpha=1}(\gamma) = \frac{100}{\pi} \left[ 4 \frac{\gamma - \gamma_r \ln\left(\frac{\gamma + \gamma_r}{\gamma_r}\right)}{\frac{\gamma^2}{\gamma + \gamma_r}} - 2 \right] \quad (6.13)$$

where  $D_{50}$  is the mean grain size,  $b$  is a scale coefficient,  $N$  the number of cycles, and  $D_M(\gamma)$  the Masing damping (with  $\gamma_r$  equal to 0.03%). However, it should be noted that FLAC estimates the damping as the area of the hysteresis loop. Thus, the damping relationships can only be used for calibration analyses.

Figure 6.8 shows the fitted sigmoidal curve with the Menq MRD curves for the foundation and shells. There is a slight variation of the MRC with the effective stress range of interest. However, a mean curve is used for simplicity throughout the shells and alluvial foundation. As explained in § 3.4.4, there is not a correlation between MRC and overburden stress; hence, for the whole core the mean curve is adopted.

In addition, Figure 6.9 shows the single-element simulations performed in FLAC for two zones, one in the core and the other in the shells. The numerical damping is slightly overestimated compared to the empirical and experimental data.

A small portion of Rayleigh damping is used to remove high frequency noise. FLAC uses a single control frequency approach, thus the damping can be represented as:

$$\xi_i = \frac{1}{2} \left( \frac{\alpha}{\omega_i} + \beta \omega_i \right) \quad (6.14)$$

where the coefficients  $\alpha$  and  $\beta$  are equal to:

$$\alpha = \xi_{min} \omega_{min} \quad (6.15)$$

$$\beta = \frac{\xi_{min}}{\omega_{min}} \quad (6.16)$$

The  $\xi_{min}$  is taken as 0.5%, and the  $\omega_{min}$  as 18.85 rad/Hz, which corresponds to 3 Hz. For the Farneto del Principe dam, this frequency was chosen to be representative of the fundamental period of the structure and of the input motion.

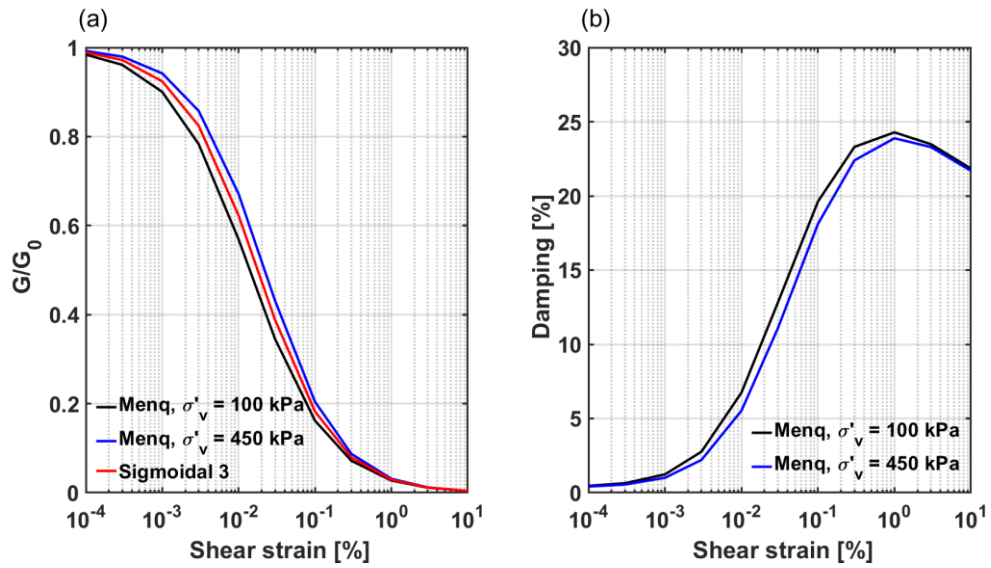


Figure 6.8: MRD curves for the shells and foundation of the Farneto del Principe dam, and sigmoidal curve used in the numerical model.

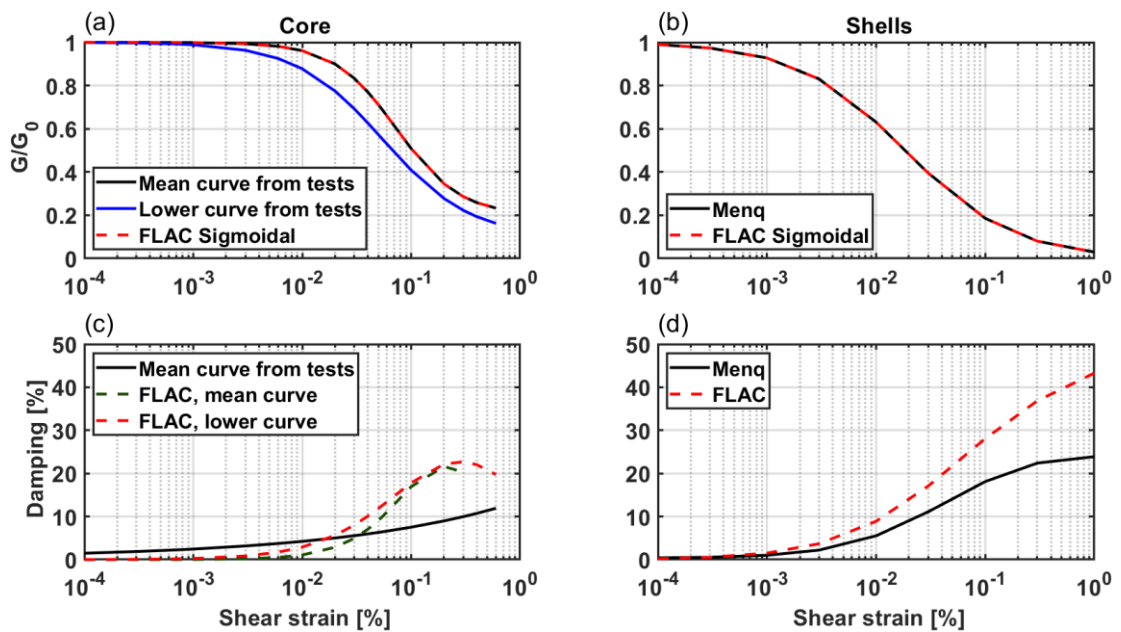


Figure 6.9: Comparison between the experimental modulus reduction and damping curves with single-element simulations in FLAC, for the core and shells of the Farneto del Principe dam.

In particular, the damping is as constant as possible in the range of frequencies deemed important in the analyses (the soil damping is frequency independent). Figure 6.10 shows the Rayleigh damping variation.

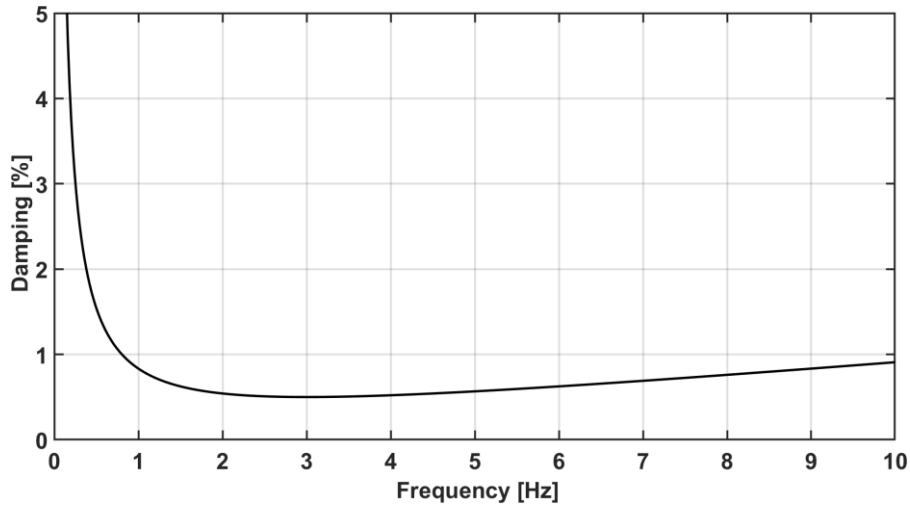


Figure 6.10: Rayleigh damping adopted in the numerical analyses of the two case studies.

The fundamental period of the dam has been estimated in four different ways: 1) from HVSR analyses (§ 3.4.3); 2) from numerical analyses (i.e. free damped oscillations); 3) from analytical solutions (i.e. Gazetas and Dakoulas, 1985); 4) from a modal analysis (Zimmaro and Ausilio, 2020). The microtremor analyses are not perfectly clear, but they show a fundamental period in the range 0.2 s – 0.35 s. The damped free oscillation gave a value of around 0.3 s, consistent with the values estimated from HVSR analyses. In addition, the fundamental period is estimated from the Gazetas and Dakoulas (1985) analytical solution:

$$T_n = \frac{16\pi}{(4 + m)(2 + m)\beta_n} \frac{H}{\bar{V}_s} \quad (6.17)$$

where the shear wave velocity at the base is taken as 415 m/s, the heterogeneity coefficient  $m$  is 0.5, and  $\beta_n$  is given by the analytical solution in function of  $m$ . The fundamental period is found to be 0.135 s, slightly lower compared to the direct measurements. However, the underestimation of the period compared to numerical analyses is also pointed out by Gazetas and Dakoulas (1985). For these reasons, and based on the HVSR, the damped free oscillation analyses, and the modal analysis, the fundamental period of the dam is taken as 0.25 s. Table 6.5 summarizes the results obtained from the various methods used herein.

#### 6.4.3 Cyclic softening potential

In this section, the potential of cyclic softening of the Farneto del Principe dam core is estimated.

Table 6.5: Summary of the fundamental periods of the Farneto del Principe dam estimated from different methods.

Fundamental periods of the Farneto del Principe dam [s]					
Mode of vibration	Method				
	Shear beam (Gazetas and Dakoulas, 1985)	HVSR	Modal analysis (Zimmaro and Ausilio, 2020)		Free damped oscillations
	Fixed base		Fixed base	Flexible base	Flexible base
1	0.135	0.20-0.35	0.197	0.240	0.290
2	0.065	/	0.097	0.126	/

The theoretical background is illustrated in § 2.5.3, while the results used to perform the calculations are based on the undrained shear strength and OCR mentioned in § 3.5.2 and § 3.5.6. The static shear bias is taken into account by considering the mean value in the lower and upper part of the core. The magnitude used to estimate the MSF is the one obtained from the disaggregation analysis, which is equal to seven. The CRRs calculated from Eq. 3.14 are equal to 0.264 and 0.388 for the lower and upper part of the core respectively. These are relatively high values, but they are expected, as the monotonic undrained shear strength ratio are also high. Eq. 3.14 can be rearranged by exploiting SHANSEP equation, the CRR can also be computed as:

$$CRR_M = 0.8 \cdot S \cdot OCR^m \cdot K_\alpha \cdot MSF \quad (6.18)$$

This equation can be used to estimate the variation of the CRR with depth; since all the terms are constants but OCR, the trend of  $CRR_M$  reflects the trend of OCR with depth. Figure 6.11 shows the variation of the CRR, CSR, and factor of safety for cyclic softening. Based on this analysis, cyclic softening phenomena are unlike to happen, as the factor of safety is always  $> 1$ .

#### 6.4.4 PM4Silt calibration for the Farneto del Principe dam core

The present section illustrates the PM4Silt calibration process for the Farneto del Principe dam core. There are several ways to calibrate the PM4Silt model based on the available data and the behaviors of interest. However, the general calibration process always comprises an iterative procedure. Figure 6.12 shows the procedure used in this work to perform this type of calibration (the reader is referred to Boulanger et al., 2018, and Boulanger and Wijewickreme, 2019, for more details about the calibration procedure).

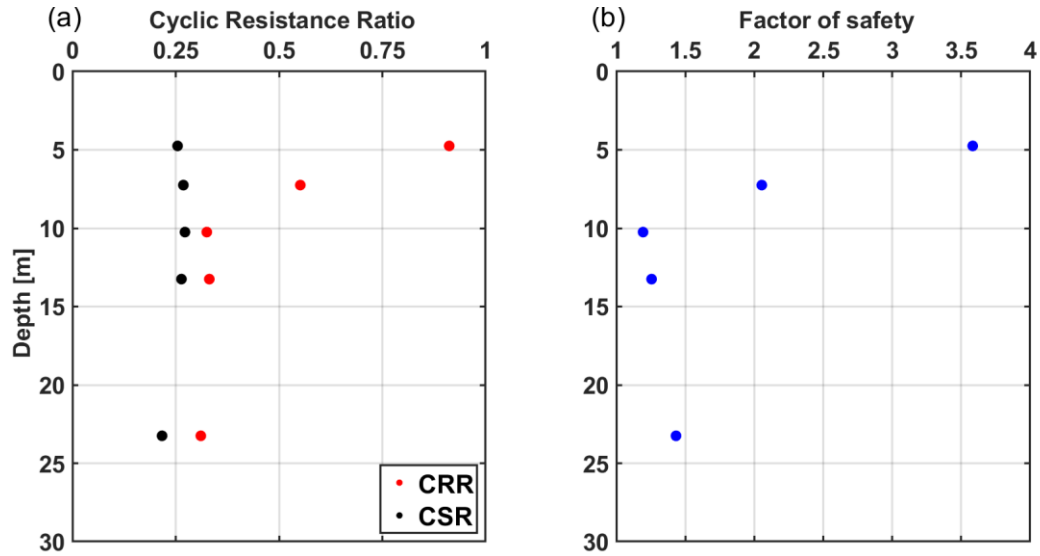


Figure 6.11: Profile of the CRR, CSR, and factor of safety for cyclic softening for the Farneto del Principe dam core based on the SHANSEP methodology.

The calibration should initially be based on the absence of static shear bias, to make sure that the model gives reasonable responses. However, the final calibration should consider the initial static shear stresses, as they can reduce the CRR for loose-of-critical soils.

Step 1: the undrained shear strength  $s_u$  or undrained shear strength ratio  $\frac{s_u}{\sigma'_v}$  is estimated from one of the procedures reported in § 3.4. The calibration of this parameter has many levels of resolution, depending on the laboratory or in-situ testing available (i.e. lower level being a single laboratory test such as UU or empirical correlation from CPT data, and higher level being based on the interpretation of ICU tests or SHANSEP methodology). Either way, the uncertainties in the undrained shear strength should always be accounted, as the  $s_u$  is a primary parameter of the model. Based on the results of Figure 3.43, two different values of the  $\frac{s_u}{\sigma'_v}$  ratio are used, 0.55 for the upper part of the core, and 0.385 below.

Step 2: the shear modulus coefficient  $G_o$  is evaluated from the in-situ data available. The PM4Silt functional form for the shear modulus  $G$  is based on the mean effective stress:

$$G = G_o p_A \left( \frac{p'}{p_A} \right)^{n_G} \quad (6.19)$$

If shear wave velocity measurements are available, the  $G_0$  parameter can be estimated as:

$$G_0(z) = \frac{\rho V_s^2(z)}{p_A \left( \frac{p'(z)}{p_A} \right)^{n_G}} \quad (6.20)$$

The exponent  $n_G$  can be varied to obtain a better fit of the small strain shear modulus. Note that the  $G_0$  can be either constant or variable with depth (in the latter case, the primary and secondary parameters would change with depth), as long as a good fit is reached. Figure 6.13 shows the results for a calibration based on all the geophysical tests available:

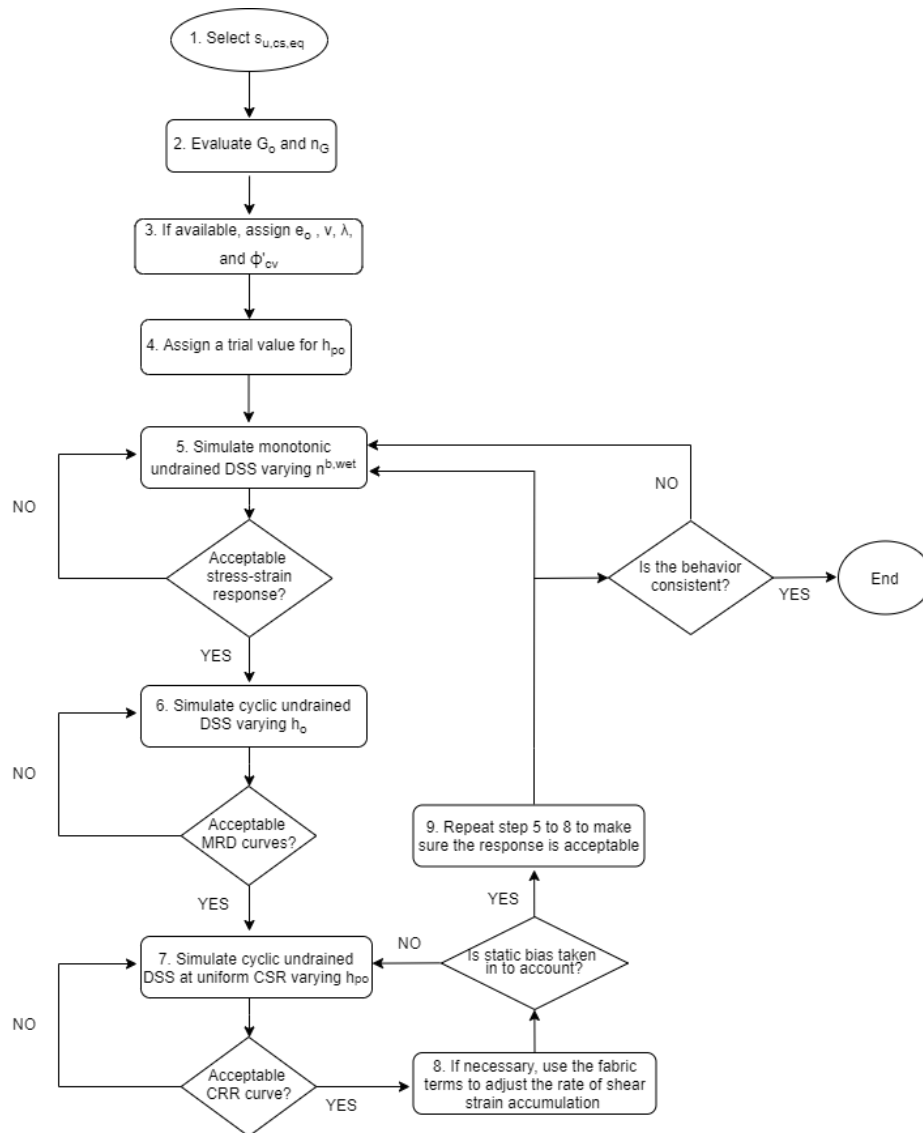


Figure 6.12: Flow chart for the calibration of the PM4Silt constitutive model calibration.



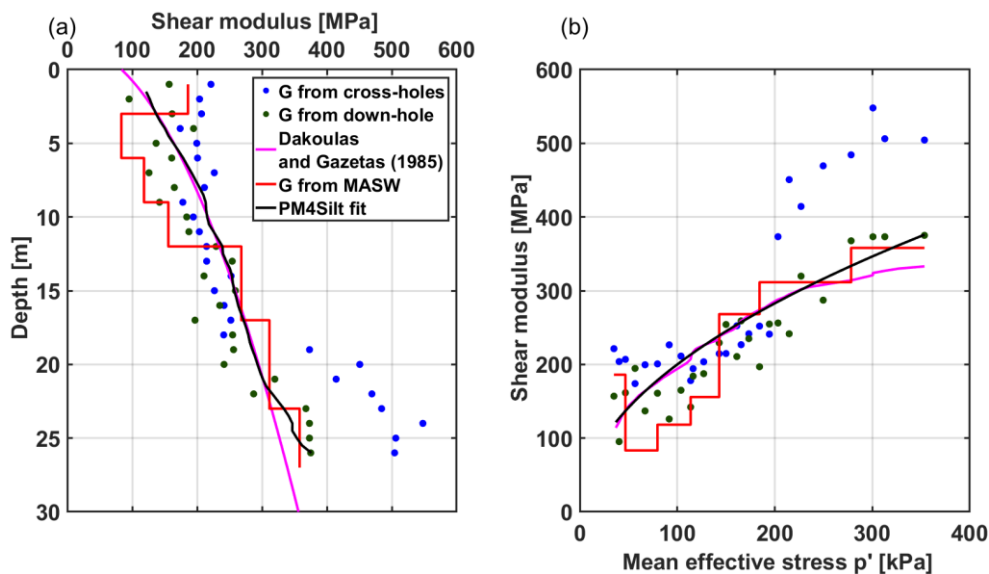


Figure 6.13: Calibration of the  $G_0$  parameter of the PM4Silt model based on the geophysical tests performed on the Farneto del Principe dam crest.

The fitted value of  $G_0$  is 1375, while  $n_G$  is equal to 0.95. The value of  $n_G$  was chosen as close to one (implying a linear dependence with mean effective stress) because it provides a reasonable fit to the shear wave velocities. In addition, the 0.95 value minimizes the effect of confining stress in shear modulus reduction curves, which was not observed in the cyclic laboratory tests (Figure 3.26). Different combinations of  $G_0$  and  $n_G$  can be used to obtain a good fit; hence, the final choice depends on how these parameters influence the overall behavior. Sometimes, multiple calibrations are necessary to represent different behaviors of the soil (Boulanger, 2019).

Step 3: the secondary parameters  $e_0$ ,  $\nu$ ,  $\lambda$ , and  $\phi'_{cv}$  are assigned; these quantities are usually based on specific laboratory tests.  $\phi'_{cv}$  can influence the degree of the dilatancy behavior, while modifying the void index and compressibility  $\lambda$  has little effect on the overall response. The values used for the Farneto del Principe dam are the mean values obtained from all the laboratory tests.

Step 4: a trial value for  $h_{po}$  is assigned (e.g. 50). Calibration of this parameter must be done last, because its value depends on the other parameters.

Step 5: simulate the monotonic undrained response and modify the secondary parameter  $n^{b,wet}$  to adjust the peak shear strength. If the soil has strain softening behavior (i.e. a pronounced post-peak drop in undrained strength) then  $n^{b,wet}$

should be lower compared to its default value. The Farneto del Principe dam core has a strain hardening behavior, thus the default value was retained. Figure 6.14 shows typical results of the simulation. The stress-strain curve is monotonic and tends to the measured shear strength at high strains, which is a consequence of the  $\frac{s_u}{\sigma'_v}$  at critical state being an input parameter. As expected, at low values of strains, the stiffness is extremely high.

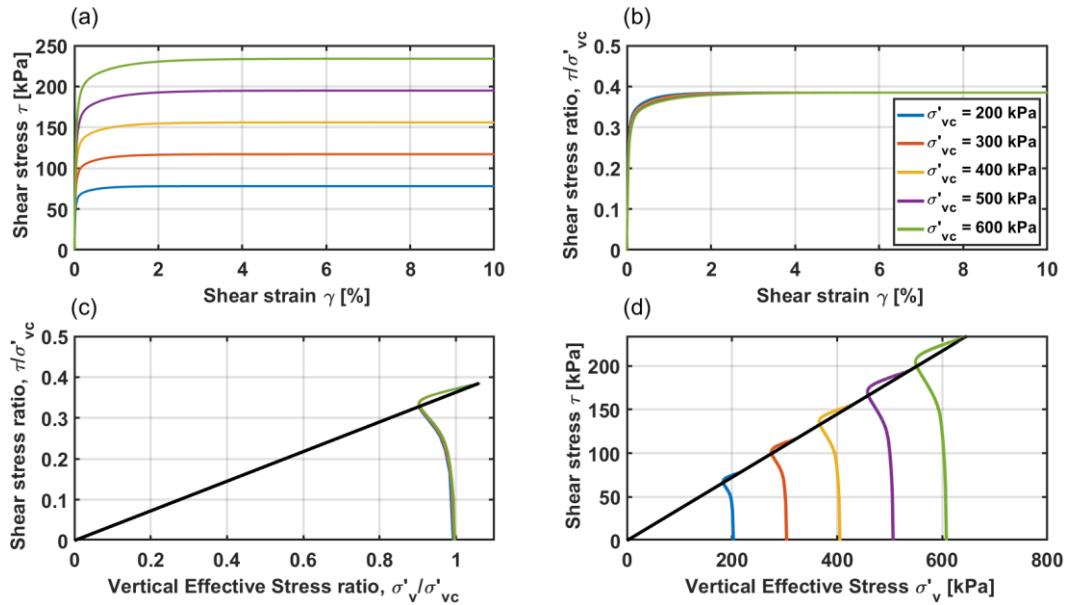


Figure 6.14: Single-element simulations of undrained monotonic DSS for the lower part of the Farneto del Principe dam core.

Step 6: the  $h_0$  parameter is modified until a reasonable fit of the shear modulus reduction and damping curves is obtained. Simulations of undrained cyclic loading at different shear strains are performed to achieve this type of calibration. A higher value for  $h_0$  means a stiffer material, which is reflected in the shape of the loops (Figure 6.15). This also implies a very stiff monotonic undrained stress-strain response. This type of behavior is similar to a Mohr-Coulomb material, where the shear modulus at high strains is underestimated due to an overshooting of the loops (i.e. huge variation of the slope of the loops in a very small range of shear strain). The damping is usually overestimated at high strains, though this is a known drawback of this type of models. In this case, large damping is due to the huge area of the loops. Furthermore, varying  $h_0$  leads to a different CRR curve, with higher strengths if  $h_0$  increases. For these reasons, prioritizing the shear modulus reduction

curves calibration might lead to a different behavior of the soil not encountered in laboratory tests (e.g. monotonic undrained response). Thus, depending on the most important aspect that needs to be modeled, different calibrations might be needed. Figures 6.15-6.17 show the results obtained. The vertical effective stress ratio did not even reach the value of 0.9, meaning that the soil did not experience cyclic softening and significant excess pore pressure. This is expected, as the soil is very stiff and not susceptible to cyclic softening.

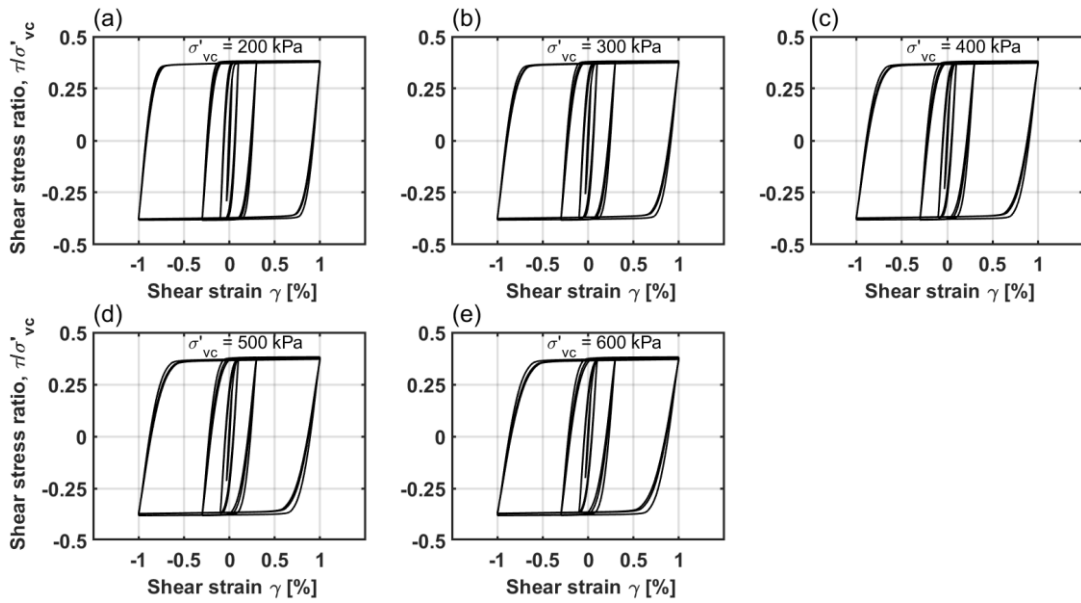


Figure 6.15: Stress-strain responses for undrained cyclic DSS simulation of the lower part of the core of the Farneto del Principe dam.

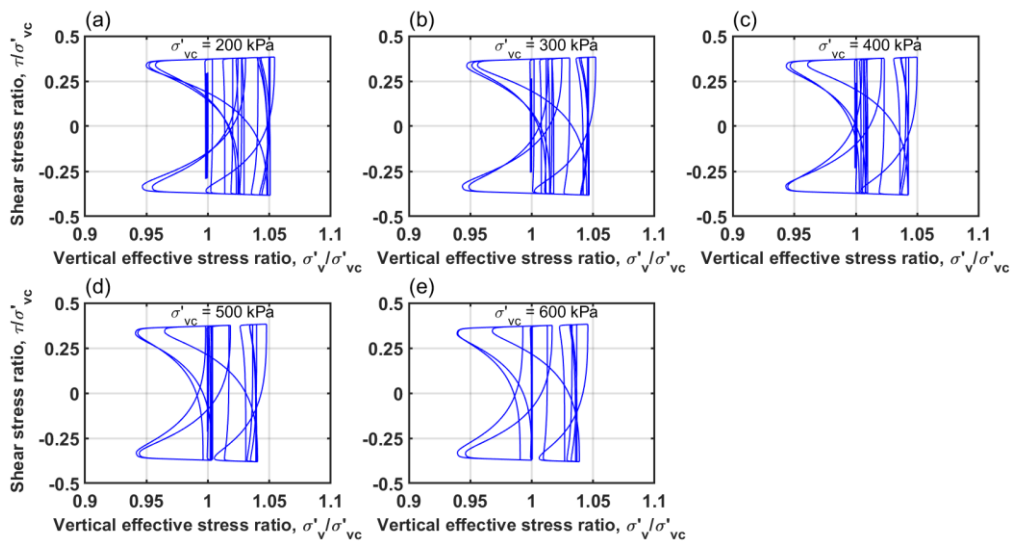


Figure 6.16: Stress path responses for undrained cyclic DSS simulation of the lower part of the core of the Farneto del Principe dam.

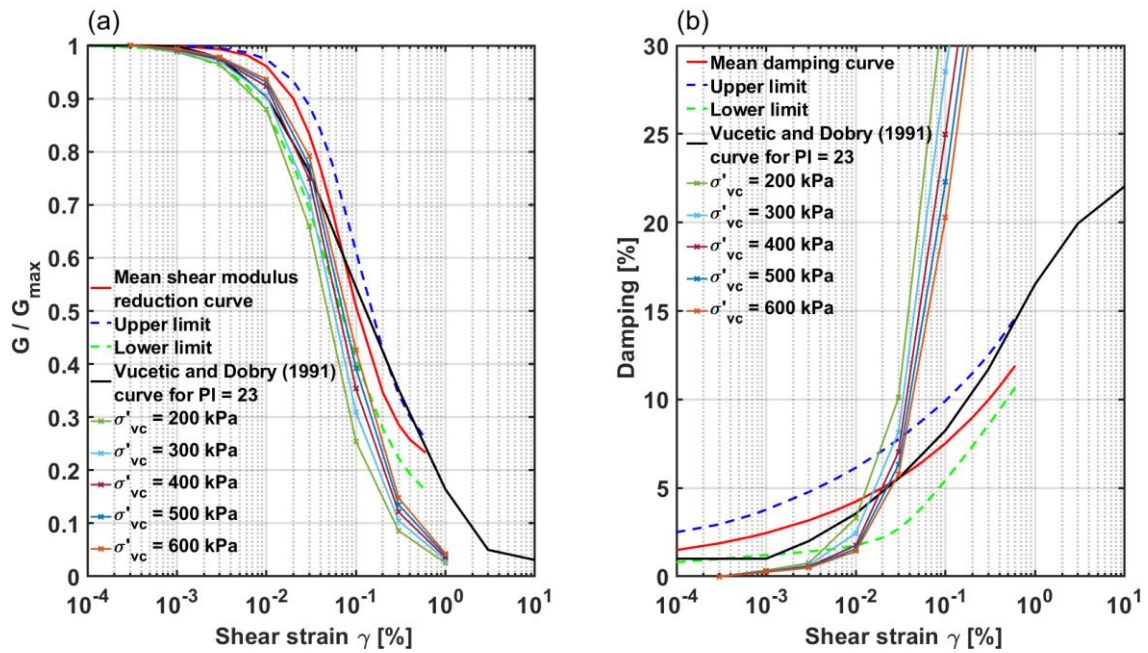


Figure 6.17: Experimental and numerical MRD from undrained strain-controlled cyclic DSS for the lower part of the Farneto del Principe dam core.

Step 7: simulate cyclic undrained DSS loading at uniform CSR for different consolidation stresses. The primary parameter  $h_{po}$  is varied until the simulated cyclic resistance curve fits the experimental one. The CRR curve is estimated by computing the CSR and number of uniform cycles necessary to cause a peak shear strain of 3%. Different failure criteria can be chosen to define liquefaction and cyclic softening (e.g. when the excess pore pressure is equal to one) but they are generally consistent with the onset of significant deformations. If the experimental CRR curve is not available,  $h_{po}$  is varied until the empirical cyclic strength, which corresponds to 30 uniform loading cycles, matches the simulated curve. Figures 6.18-6.21 show the results obtained for the Farneto del Principe dam in the lower part of the core, where a CRR of 0.264 was estimated (§6.4.3), and taking in to account the presence of an initial static shear bias.

Step 8: the stress-strain response obtained from the cyclic undrained DSS simulations are analyzed. If laboratory data are available (e.g. results from a DSS or a cyclic triaxial tests) then the secondary parameters such as  $r_{u,max}$ ,  $n_G$ , and the fabric terms can be used to adjust the rate of shear strain accumulation. Thus, the shape of the simulated loops can be consistent with the experimental ones.

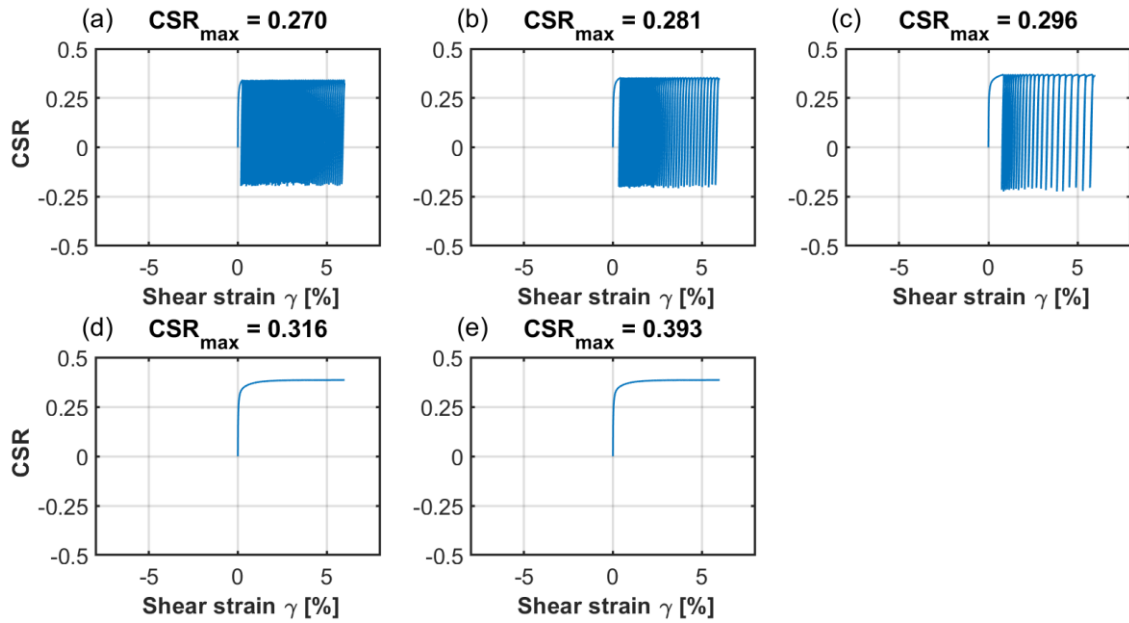


Figure 6.18: Stress-strain responses for undrained cyclic DSS loading for several CSR for the lower part of the Farneto del Principe dam core.

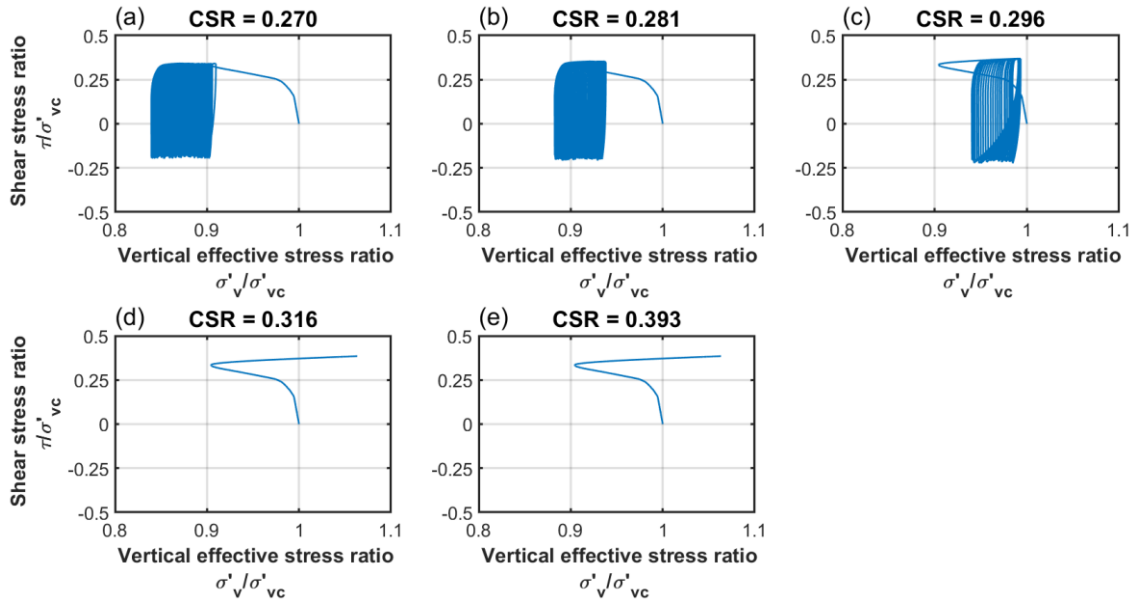


Figure 6.19: Stress path responses for undrained cyclic DSS loading for several CSR for the lower part of the Farneto del Principe dam core.

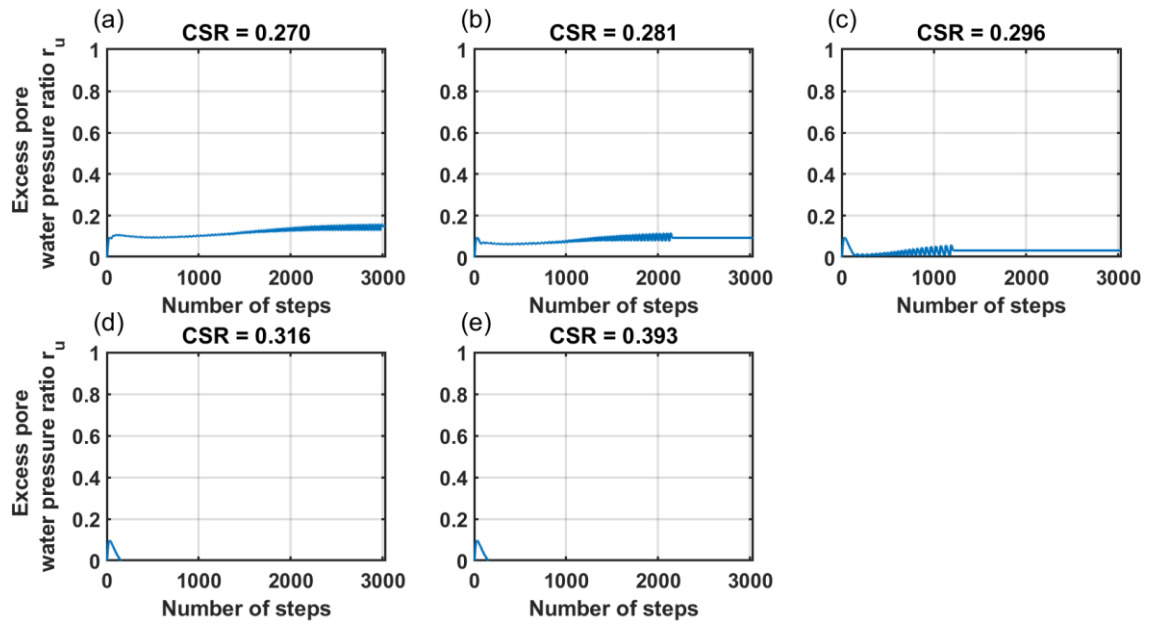


Figure 6.20: Excess pore water pressure ratio variation for the lower part of the Farneto del Principe dam core.

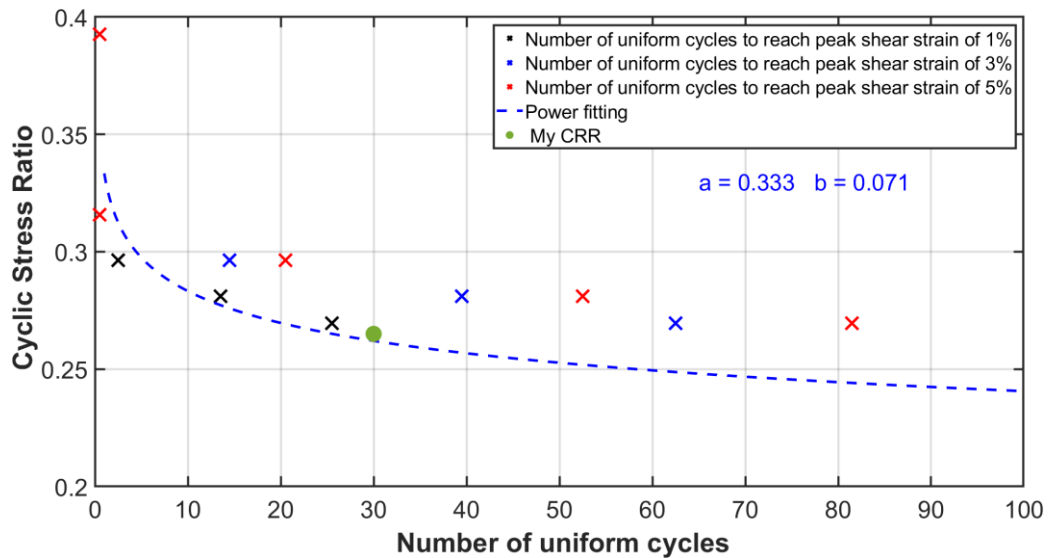


Figure 6.21: Cyclic stress ratio versus number of uniform loading cycles to cause 1%, 3%, and 5% shear strain in undrained cyclic DSS loading for the lower part of the core of the Farneto del Principe dam.

Step 9: if an initial static shear bias  $\alpha$  is present, the CRR curve should be estimated again, as in silty soils the cyclic strength reduces even with a low value of  $\alpha$ . The calibration performed in the absence of  $\alpha$  gives information about the capability of

the model to represent the stress-strain responses known from experimental data and from empirical relationships.

Steps 5 to 9 are repeated at least once to make sure that the stress-strain responses are still consistent after assigning the input parameters  $h_{p0}$  and the eventual fabric terms. If the soil behavior evaluated from single element simulations is not the one expected, even for  $\alpha = 0$ , then the capability of the model to estimate the undrained response should be questioned. For instance, this can happen if some parameters are given values that are outside the boundaries of the model for which they were built. For the Farneto del Principe dam, only one iteration of steps 5 to 9 was necessary.

## 6.5 Numerical model of the Angitola dam

### 6.5.1 Generalities

This section presents the numerical model of the Angitola dam, following the general considerations of § 6.3. As explained in Chapter 5, in this work only the secondary dam is of interest. The secondary dam has a longitudinal length of about 200 m, with three different cross section that can be identified (Figure 6.22). The first section is about 80 meters long, with a height of 27.75m, and it is where most of the in-situ tests were performed. The height and length of the other sections are lower compared to the first one. For these reasons, only the section one is analyzed and modelled, using a plane-strain assumption. While it is recognized that the overall geometry would require some 3D considerations, for the purpose of this work the 2D modelling is deemed sufficient.

The Farneto del Principe dam analyses proved that Seed et al. (1975) suggestion of using a lateral extension of the model equal to at least half the width works well. For the Angitola dam, the width is around 112 m; hence, the numerical model is extended for 55 m on the upstream and downstream side. The spatial distribution of the foundation layers is known only up to the points where the boreholes S4 and S5 were conducted (Figure 6.22); beyond that, a horizontal spacing is assumed for simplicity. The mesh is coarser near the external boundaries and finer beneath the dam and in the dam body. The upper limit of the mesh size is given by the Lysmar and Kuhlemeyer (1973) formula for accurate wave transmission in numerical models:



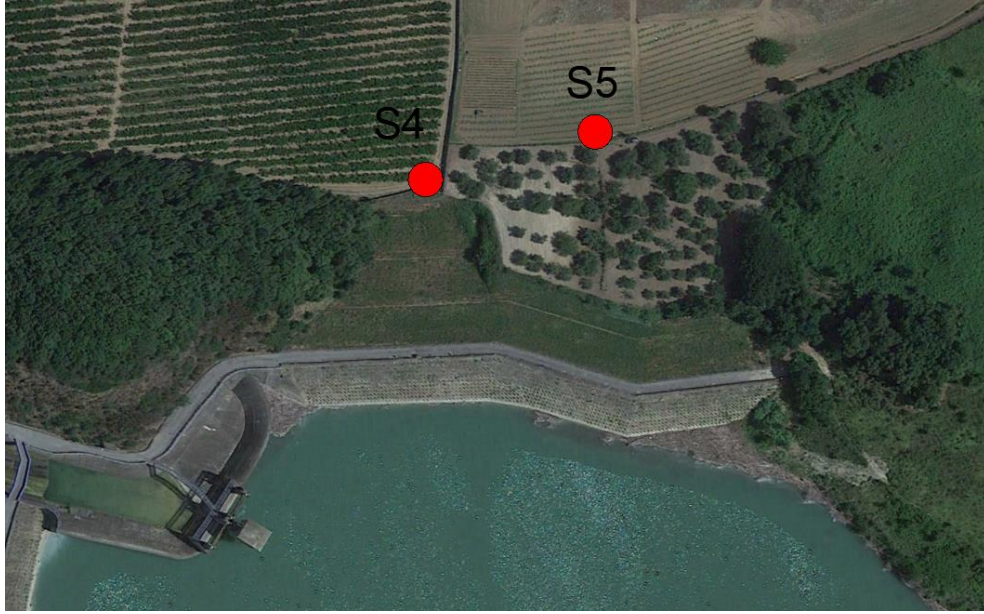


Figure 6.22: Aerial view of the secondary dam and location of the boreholes performed (from Google earth, 2021).

$$l_{max} < \frac{V_s}{10 f_{max}} \quad (6.21)$$

where the minimum shear wave velocity  $V_s$  and maximum frequency  $f_{max}$  of the input motion are taken as 200 m/s (from SPT empirical correlations) and 10 Hz. Thus, the maximum size of the mesh is 2 m, though it was used only towards the end of the model. The dimensions of the mesh adopted are smaller to represent better the interfaces between the foundation layers and the filters of the dam body. Figure 6.23 shows the mesh of the Angitola dam model.

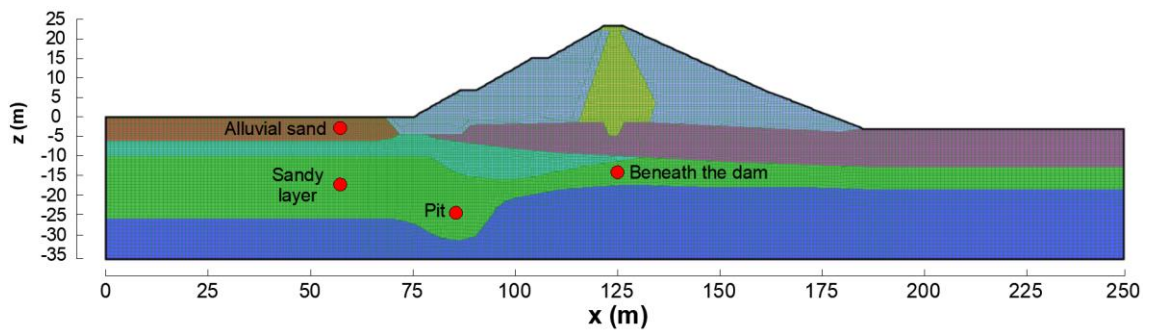


Figure 6.23: Numerical mesh of the Angitola dam used in FLAC.



The boundary condition used at the sides enforces the motion of a free-field condition (Itasca, 2019), and prevents the reflected waves to come back in to the model. At the base of the model, viscous dashpots are used to simulate the elastic halfspace beneath the foundation.

The constitutive models used in the analyses are different for some of the layers. The gneiss has been modelled as an elastic material, the dam body and the foundation layers with a Mohr Coulomb failure criterion. For the sands layers, the PM4Sand model is also used in a separate analysis. The differences between the classic and more advanced constitutive models are later discussed and analyzed. The properties and parameters of the various layers are described in the Angitola dam chapter (§ 5.5.2).

### 6.5.2 Construction process and groundwater flow

The seismic response and dynamic behavior of an earth dam depend on the initial static conditions. Thus, particular attention must be given to the first stages of the numerical model (i.e. evaluating the initial state of stress). The construction logs and monitoring data are extremely useful to verify the goodness of the model. A four-step construction process by gravity loading is conducted, based on the information on the building progression of the dam (Figure 6.24). The stages are: (1) from 22 m to 31 m a.s.l.; (2) from 31 m to 37 m; (3) from 37 m to 41 m; (4) from 41 m to 48.3 m a.s.l., which is the crest elevation. Two deformations monuments were installed in the dam, but they did not give significant results. Thus, the deformability of the dam body is assumed to be consistent with the one estimated from the down-hole tests.

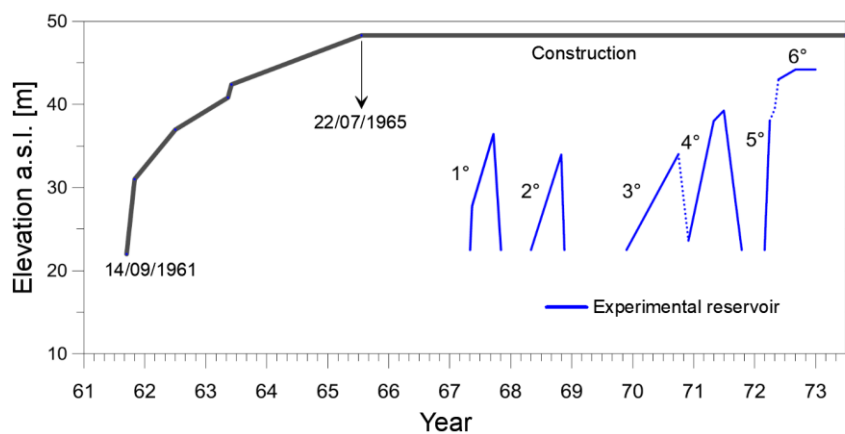


Figure 6.24: Construction log of the secondary dam and experimental reservoir (courtesy of Prof. Lanzo).

The piezometric data are used to check the groundwater flow in the dam body and in the foundation layers. Due to the complex stratigraphy in the foundation, piezometer levels were extremely useful to verify the numerical results versus the reality. Figure 6.25 shows a plane view and a cross section of the nine piezometers installed in the dam. Seven of them are standpipes, while the other two are Casagrande’s piezometers. The data were recorded during construction, filling, and operation. The piezometers in the foundation layer measured the water level at around 25 m a.s.l., which is where the high permeability filter is located. The Pz3, Pz4, Pz5, and Pz6 levels vary seasonally, depending on the rain. On the other hand, the piezometers in the core showed that the water level depends on the reservoir level. Finally, during “operation”, from 1996 to 2017, the mean level of the Pz3 piezometer found is 1.8 meters below the free surface. The Pz3 piezometer is in the cross section analyzed, thus the 1.8 m water table depth is used to calibrate the numerical groundwater flow (Figure 6.26).

The groundwater flow and the vertical effective stresses of the Angitola dam are shown in Figures 6.27 and 6.28. The reservoir level considered is the maximum allowable, which is 46.40 m a.s.l. The homogenous state-of-stress at the side boundaries is a proof that the model size works well also for static condition. The groundwater flow is hard to analyze, due to the complex geological setting. However, it is reasonable to assume that the water will flow in the sandy layer, due to its higher permeability. Some water is also certainly to flow in to the fractured gneiss, located immediately beneath the sandy layer. In addition, the water table obtained from the numerical analysis is consistent with the piezometer data, both in the core and in free field condition.

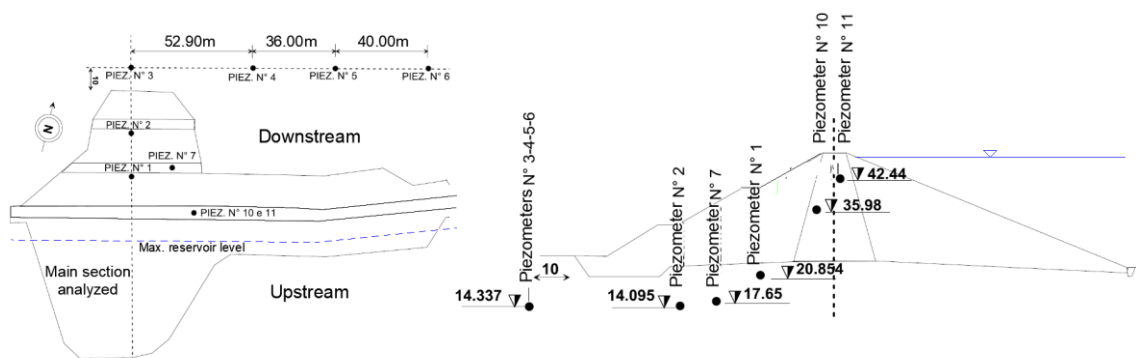


Figure 6.25: Plane view, cross-section, and location of the piezometers installed in the secondary dam.

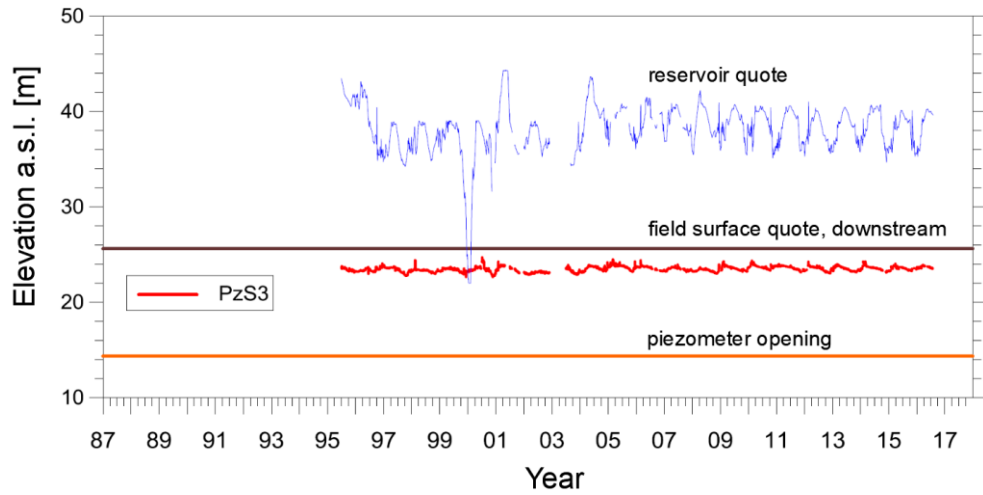


Figure 6.26: Downstream piezometer PzS3 measurements throughout the service life of the secondary dam.

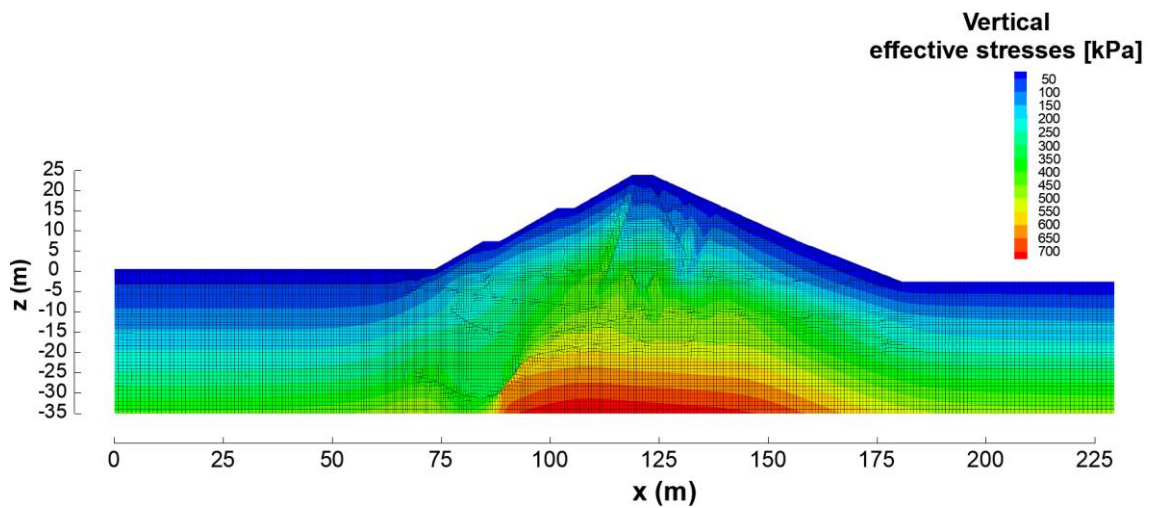


Figure 6.27: Vertical effective stresses after the application of the reservoir at the maximum level (Angitola dam).

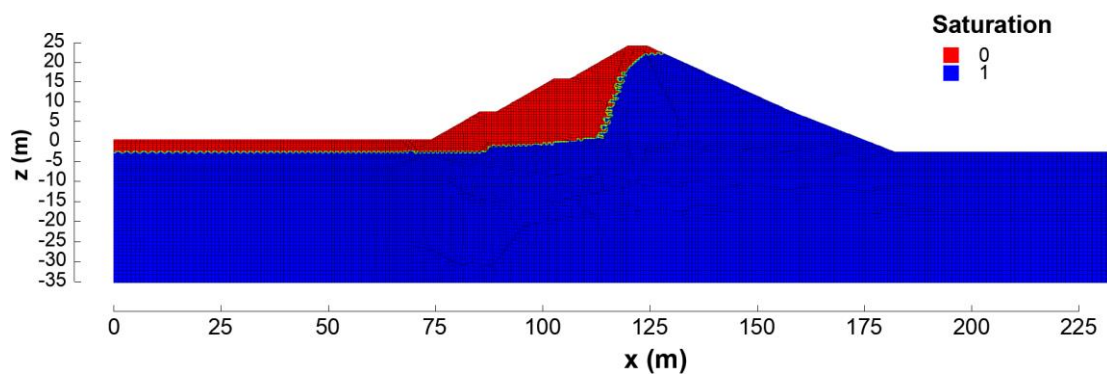


Figure 6.28: Groundwater flow and saturation contours of the Angitola dam for the reservoir at the maximum allowable level.

### 6.5.3 Dynamic properties and material damping

For the material damping of the Angitola dam, the same considerations for the Farneto del Principe dam can be made. The shear modulus reduction curves of the have been fitted with sigmoidal curves, using the empirical relationships of Menq (§6.4.2), Rollins, and Seed and Idriss (§ 5.5.2).

Just as the Farneto del Principe dam, the fundamental period has been estimated in from HVSR analyses (§ 5.5.3), from numerical analyses, and from analytical solutions. The microtremor analyses gave a fundamental period of about 0.2 s, while the damped free oscillation gave a value of 0.19 s and 0.16 s. The 0.19 s is related to a model where the shear modulus varies with mean effective stresses; the 0.16 s value is obtained when performing the analysis with mean values of shear modulus. This indicates that a more accurate modelling of stiffness parameters results in a better estimation of dynamic properties. Figure 6.29 shows the result of the damped oscillations after applying at the base of the model a sinusoidal shear stress time series. The fundamental period estimated from Gazetas and Dakoulas (1985) solution is 0.162 s, which is consistent with the HVSR and damped free oscillations analyses. Hence, for the Angitola dam, the value of 0.2 s is taken as the fundamental period.

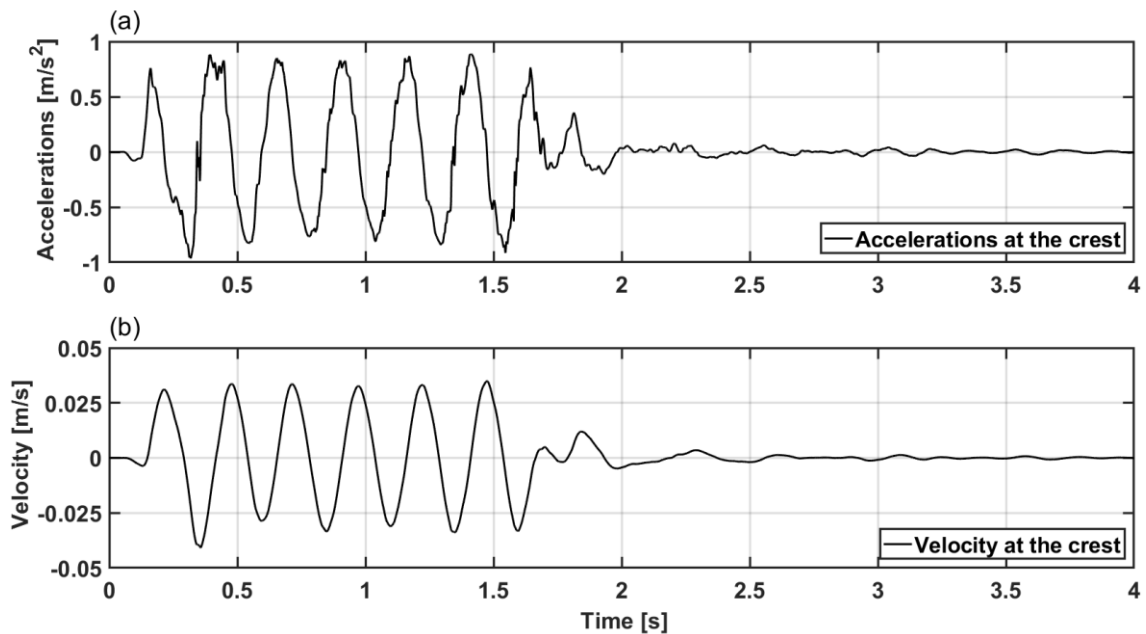


Figure 6.29: Results of the damped free oscillations of the Angitola dam with a shear modulus profile varying with mean effective stress.

The same amount of Rayleigh damping (0.5% with a central frequency of 3 Hz) is used for the Angitola dam. This is consistent because the two dams have similar vibration periods and input motions.

Figures 6.30 and 6.31 show the single-element simulations performed in FLAC for four zones: (1) core (2) silty clay foundation (3) shells (4) sandy layer. The numerical damping is overestimated at large strain compared to the empirical data.

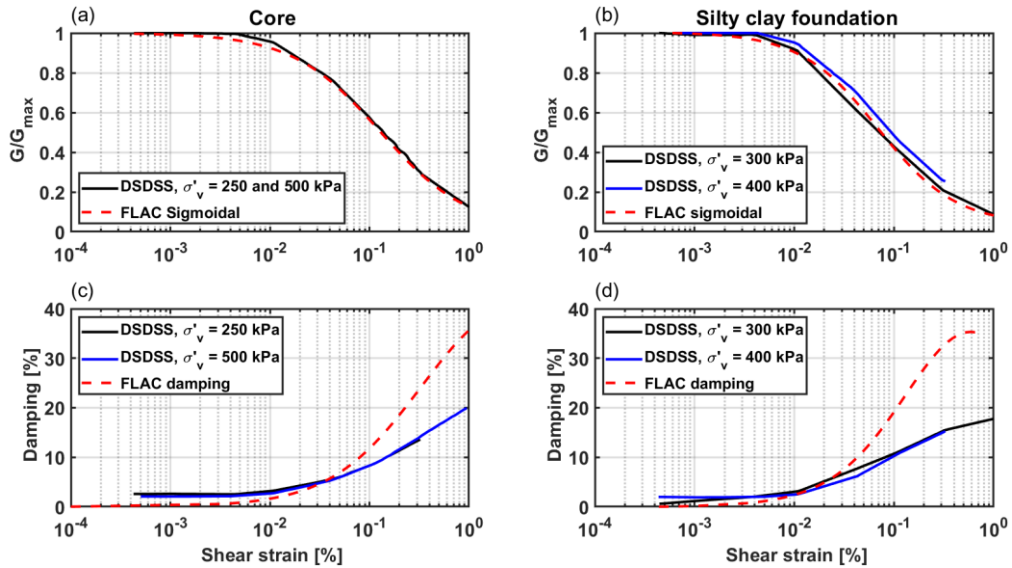


Figure 6.30: Comparison between the experimental modulus reduction and damping curves with single-element simulations in FLAC, for the core and silty clay foundation of the Angitola dam.

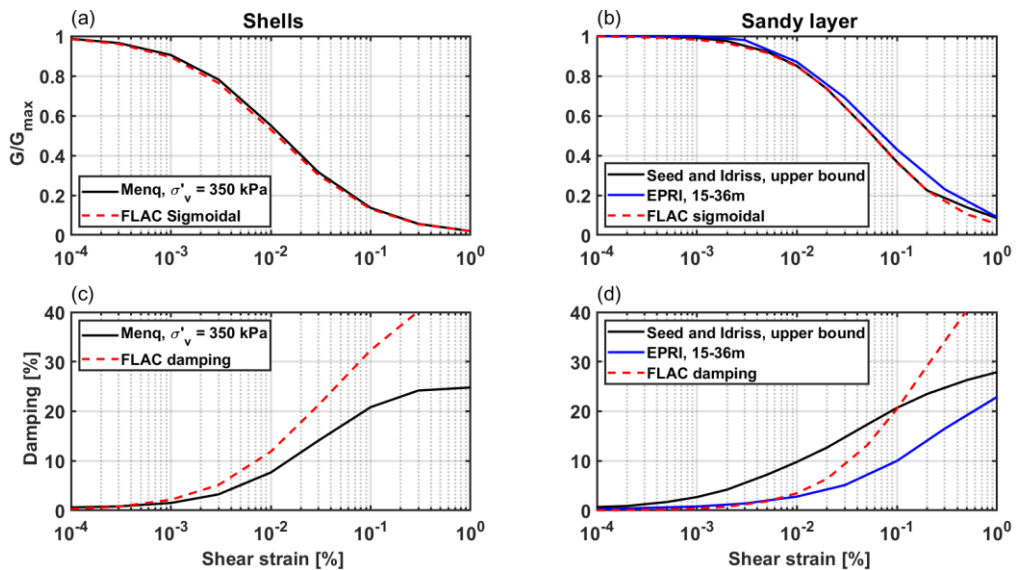


Figure 6.31: Comparison between the experimental modulus reduction and damping curves with single-element simulations in FLAC, for the shells and sandy layer of the Angitola dam.

#### 6.5.4 PM4Sand calibration for the Angitola dam foundation

The PM4Sand model calibration is an iterative procedure and it is done by performing single element simulations for all the condition of interest (e.g. different overburden stresses and initial static shear stresses). The calibration is first performed in the absence of initial static shear stresses, and in the end with the proper values. Figure 6.32 shows the flow chart of the calibration performed for the Angitola dam. Just as PM4Silt and any other advanced constitutive model, the calibration of PM4Sand depends on the data available and should consider the parameters' uncertainties. In addition, the initial conditions should be analyzed to make sure that the model is applicable to the case of interest (e.g. the initial  $\alpha = \frac{\tau}{\sigma_v}$  should not be too high, and the  $K_0$  should be consistent with the soil stratigraphy). Figure 6.33 shows the initial  $\alpha$  and  $K_0$  before applying the dynamic input. Then, the calibration is performed by following the steps below.

Step 1: The apparent relative density  $D_R$  is evaluated from SPT and CPT empirical relationships. For the sandy layer, the following correlation is used:

$$D_R = \sqrt{\frac{N_{160}}{C_d}} \quad (6.22)$$

where  $N_{160}$  is the  $N_{SPT}$  value corrected for energy efficiency and overburden stress, and  $C_d$  is equal to 46 (Idriss and Boulanger, 2008). An SPT was performed in free field condition, and another one from the downstream shell (Table 5.5). The mean value of the four  $N_{160}$  is considered for each SPT, resulting in a  $D_R$  value of 58.4% beneath the dam, and 67% in the sandy layer in free field condition. For the alluvial sand, a CPT correlation is used:

$$D_R = 0.465 \left( \frac{q_{c1N}}{C_{dq}} \right)^{0.264} - 1.063 \quad (6.23)$$

where  $q_{c1N}$  is the cone tip resistance corrected for confinement stress, and  $C_{dq}$  is equal to 0.9 (Idriss and Boulanger, 2008). The mean value in the first three meters of the CPT (which corresponds to the alluvial sand) is 39%.

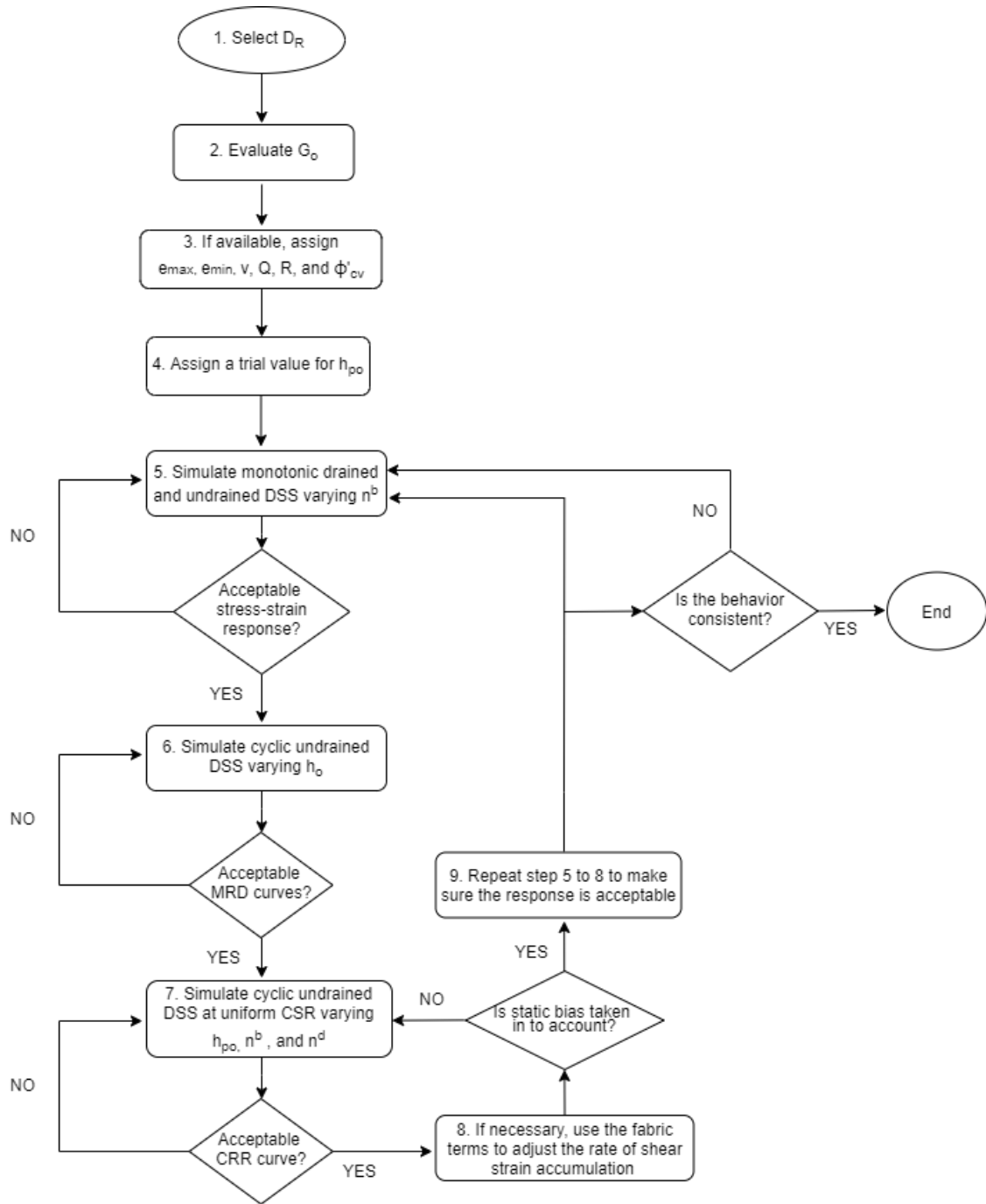


Figure 6.32: Flow chart for the calibration of the PM4Sand constitutive model calibration.



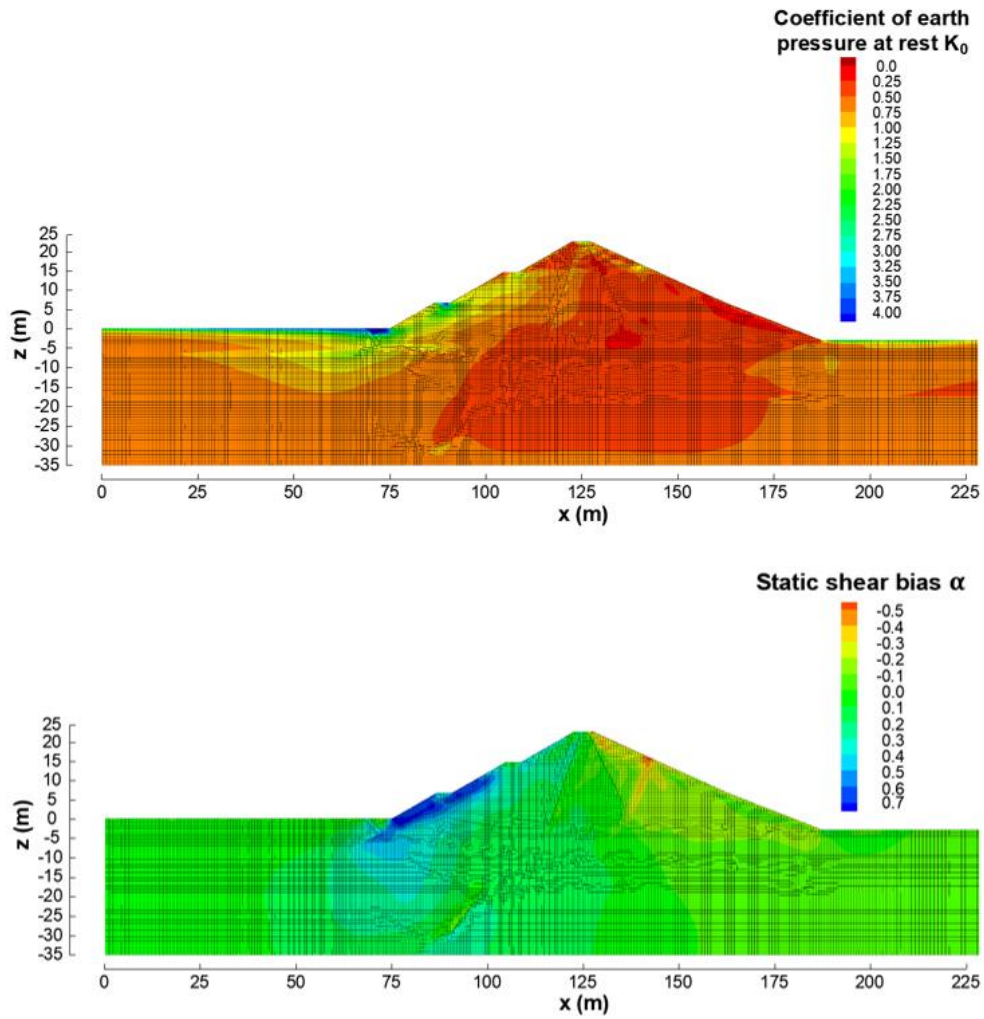


Figure 6.33: Coefficient of earth pressure at rest  $K_0$  and static shear stress ratio  $\alpha$  for the Angitola dam before applying the dynamic input.

Thus, the sandy layer is a medium-dense sand, while the alluvial sand is a medium-loose one. However, this information by itself does not tell if the soil will present a loose-of-critical or dense-of-critical state of stress (as defined by the classical theory of critical soil mechanics). The  $D_R$  is simply used to define a state parameter that define the critical state line; the position of the soil on interest depends on the in-situ mean effective stress (which are quite variable if the layer has a huge thickness). This will be accounted for in steps five, six, and seven of the flow chart, where the single element simulations will be performed for several confinement stresses.

Step 2: The  $G_0$  parameter that regulates the small strain shear modulus is evaluated. The PM4Sand functional form for the shear modulus is the following:



$$G = G_0 p_A \left( \frac{p'}{p_A} \right)^{\frac{1}{2}} \quad (6.24)$$

where  $p_a$  is the atmospheric pressure and  $p'$  the mean effective stress. An estimate of the  $G_0$  can be calculated as:

$$G_0 = \frac{\rho V_s^2}{p_A \left( \frac{p'}{p_A} \right)^{\frac{1}{2}}} \quad (6.25)$$

where  $\rho$  is the soil mass density, and  $V_s$  the mean shear wave velocity. Then, the variation of  $G$  with the mean effective stress is evaluated and compared with the real one (e.g. either a mean value, or the real trend with depth known from a geophysical test). For the sandy layer, three different areas can be defined: one in free-field condition, one in the trench beneath the downstream shell, and one beneath the dam. Hence, three different values of  $G_0$  will be used in the analyses. For the alluvial sand, a single  $G_0$  value is sufficient, as there is no spatial variation of that layer. Figure 6.34 shows the fitted shear modulus curves using the PM4Sand functional form, the mean value, and the one estimated from all the tests available (as shown in § 5.5.2, Figure 5.13). The fitted values of  $G_0$  are 800 for the alluvial sand, 810 for the sandy layer in free-field condition, 2250 for the pit, and 3400 beneath the dam.

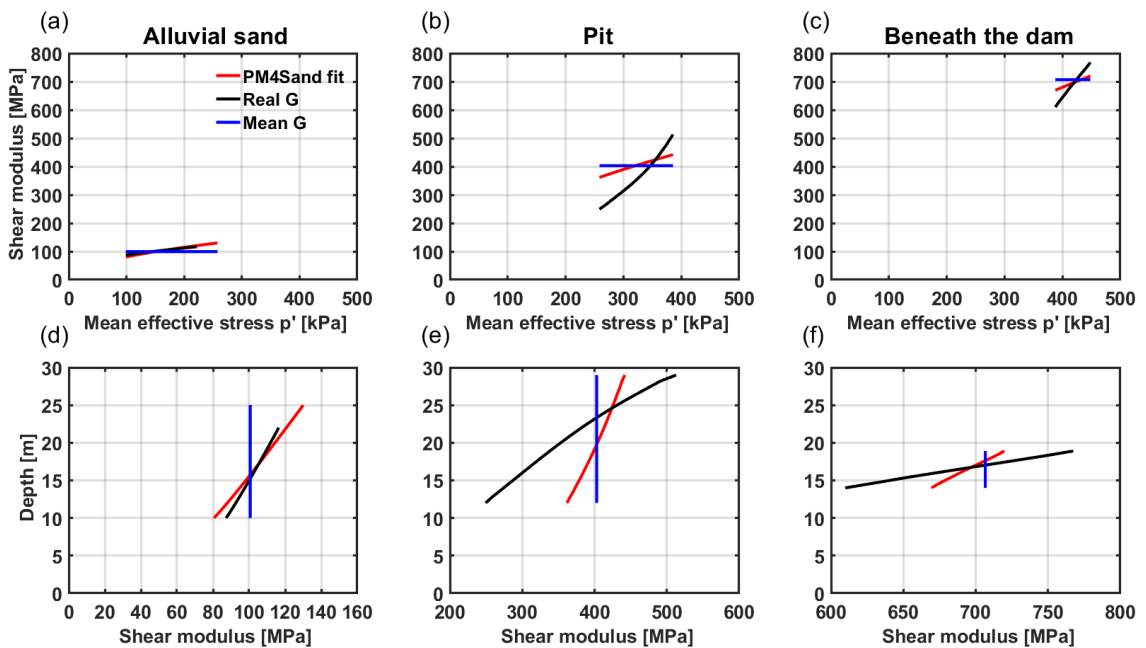


Figure 6.34: Calibration of the  $G_0$  parameter and profile of the shear modulus for three zones in the Angitola dam: alluvial sand (a) and (d); pit (b) and (e); beneath the dam (c) and (f).

Step 3: the secondary parameters  $e_{max}$ ,  $e_{min}$ ,  $\nu$ ,  $Q$ ,  $R$ , and  $\phi'_{cv}$  are assigned; these quantities are usually based on specific laboratory tests or empirical correlations. The maximum and minimum void index have been assumed as 1 and 0.5, and the initial void index from the following equation:

$$e_0 = e_{max} - D_R(e_{max} - e_{min}) \quad (6.26)$$

The critical state angle  $\phi'_{cv}$ , the Poisson ratio  $\nu$ , and the  $Q$  and  $R$  parameters retained their default values.

Step 4: a trial value for  $h_{po}$  is assigned (e.g. 10). Calibration of this parameter must be done last, because its value depends on the other parameters. The  $h_{po}$  regulates the contractiveness of the soil and thus the value of the CRR.

Step 5: The monotonic drained and undrained responses are estimated for five confining stresses. Overall, the same behavior was encountered for all the layers analyzed. This is because the sandy layer is characterized by a medium-high relative density, and the confining stresses are not large enough to fall on the right side of the CSL. This dense of critical behavior results in a dilatant material, which is reflected by the peak and post-peak response of Figure 6.35a-b, and the negative volumetric strains of figure 6.33c. For the alluvial sand, despite being a loose-medium soil ( $D_R = 38\%$ ), the same dense of critical behavior is found, due to the very low confining stresses (with a maximum value of around 100 kPa). These trends are consistent with the results obtained by Lee and Seed (1967) for monotonic drained response of loose and dense sands.

For the undrained monotonic response, the stress-strain curves and the stress-paths are consistent with the ICU results of the Toyoura sand (Ishihara, 1993). After a brief reduction of effective stresses, the soil presented a strain-hardening behavior (Figure 6.36c-d) and reached the critical strength at large strains.

Step 6: Single elements simulations of cyclic drained and undrained DSS are performed to estimate the shear modulus reduction and damping curves (MRD). The  $h_o$  parameter is modified until a reasonable fit of the MRD curves is obtained. For the sandy layer and alluvial sand, the Seed and Idriss curves and the EPRI curves are used as calibration comparison. Figure 6.37 shows the stress-strain curves obtained for the confining stresses considered, while Figure 6.38 shows the

comparison between the numerical MRD and the empirical ones. The results refer to the part of the sandy layer beneath the dam, but similar results were obtained for the other layers.

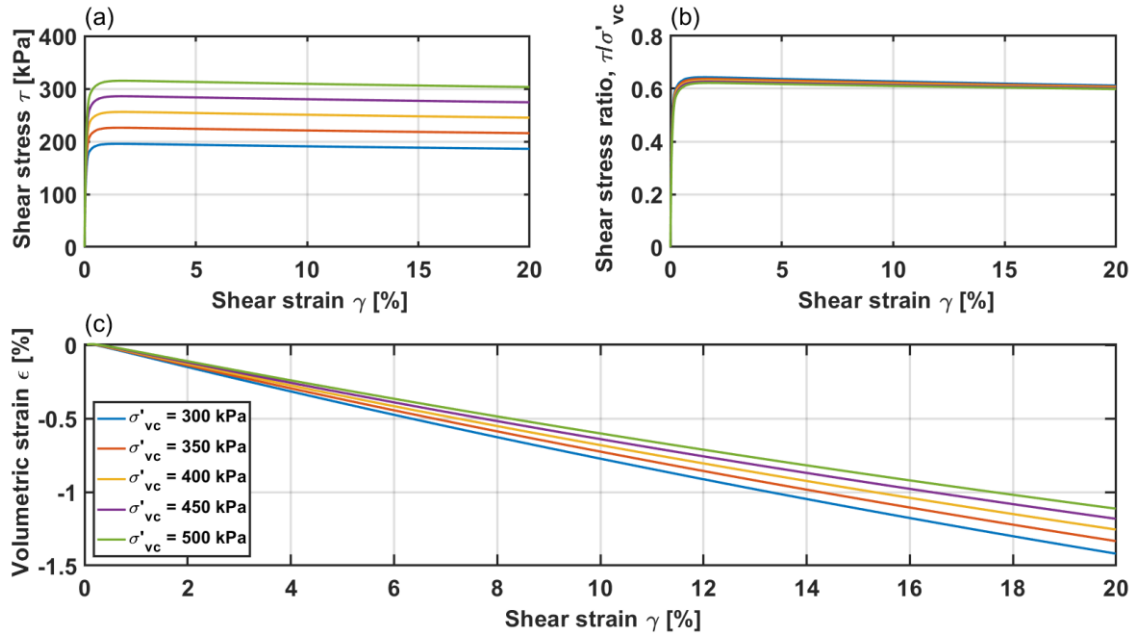


Figure 6.35: Drained monotonic loading response of the sandy layer beneath the dam ( $D_R = 58.4\%$ ). Stress-strain response (a) and (b); volumetric strains vs shear strain (c).

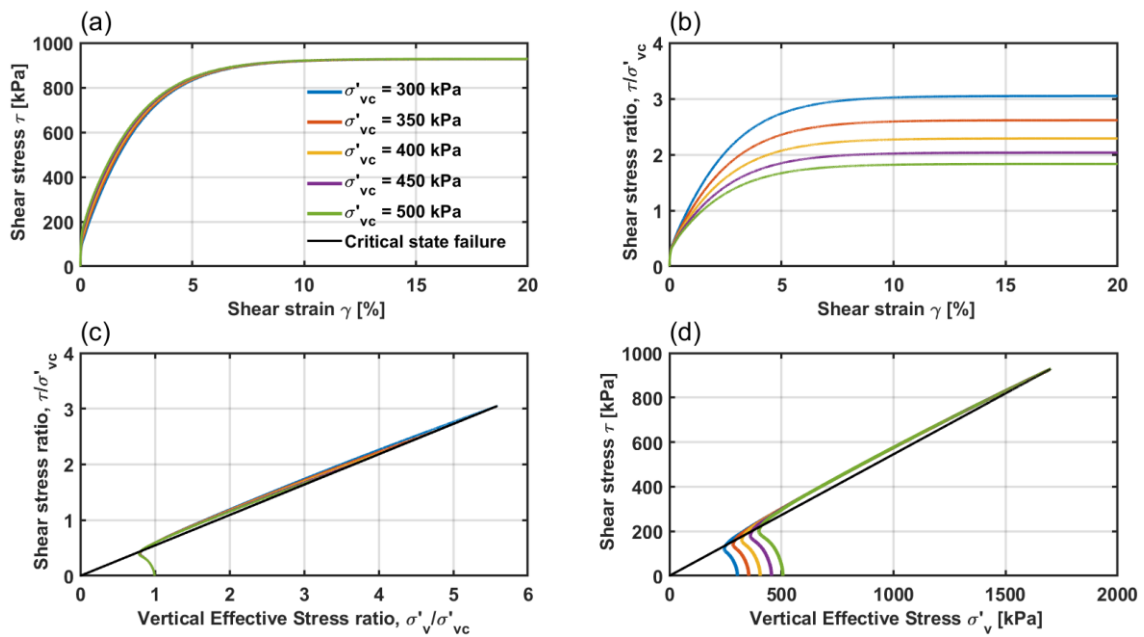


Figure 6.36: Undrained monotonic loading response of the sandy layer beneath the dam ( $D_R = 58.4\%$ ). Stress-strain response (a) and (b); stress-path (c) and (d).

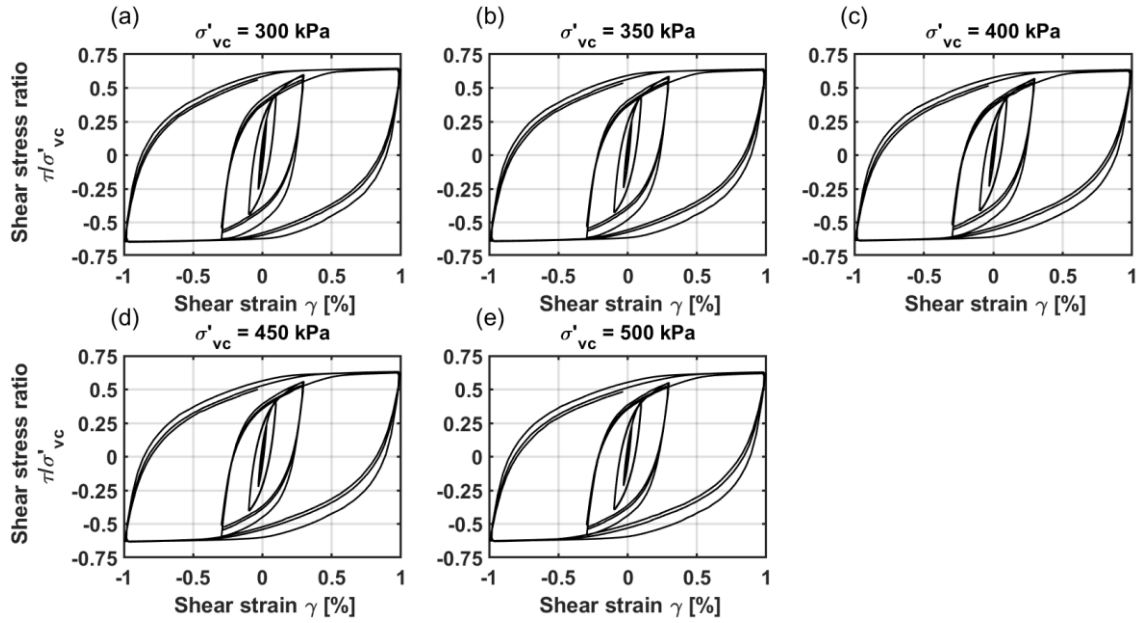


Figure 6.37: Drained cyclic loading response of the sandy layer beneath the dam for different confining pressures.

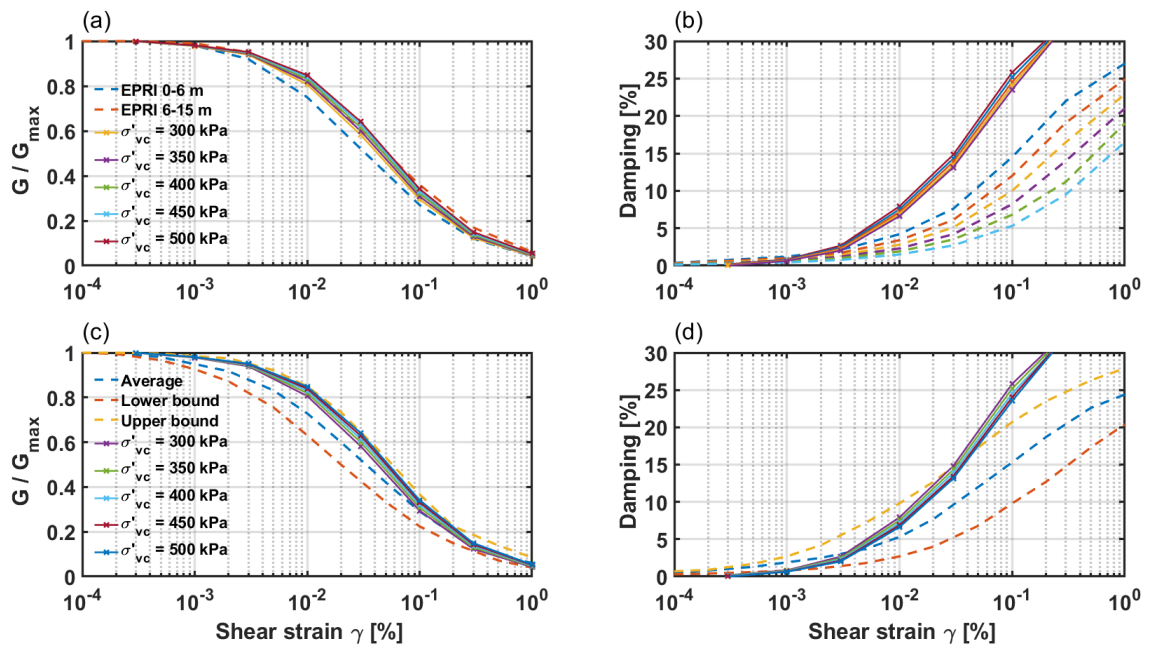


Figure 6.38: MRD from drained strain-controlled cyclic DSS loading in the sandy layer beneath the dam and comparison with well-known MRD found in literature.

The simulated MRD curves are in good agreement with the upper bound curve by Seed and Idriss and with the EPR1 curve for 6 to 15 m and for 15 to 36 m. The

resulting damping curves (calculated from the area of the hysteresis loops) are consistent with the upper limit of Seed and Idriss, but overestimated compared to the EPRI ones. For the alluvial sand, the MRD curves are all consistent; this is probably due to the slight variation in the confining stresses (Figure 6.39).

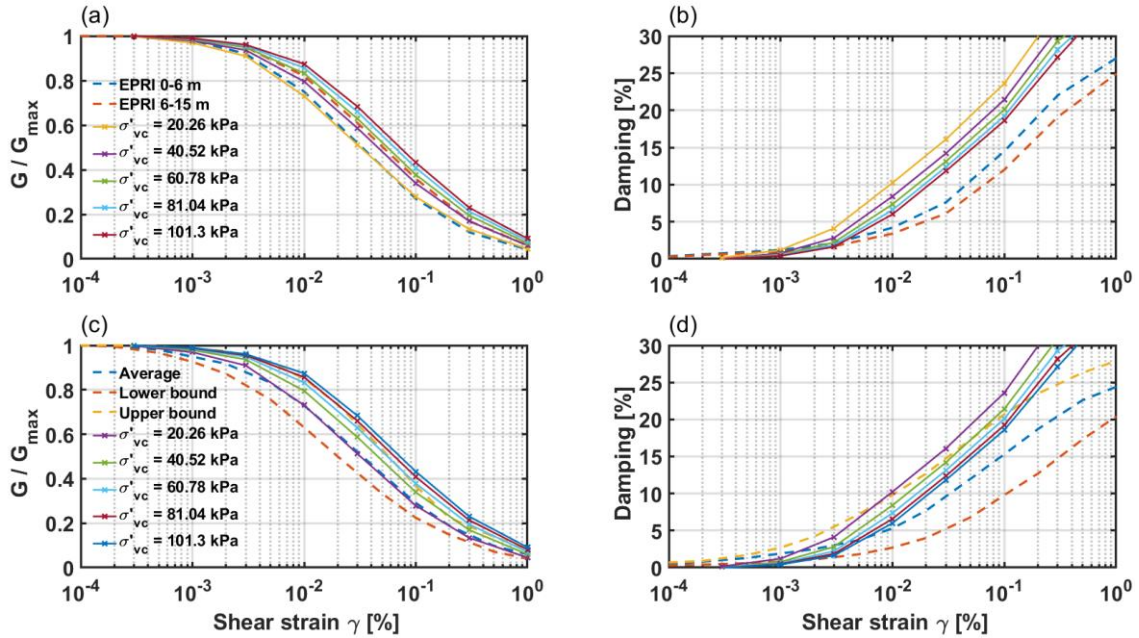


Figure 6.39: MRD from drained strain-controlled cyclic DSS loading in the alluvial sand and comparison with well-known MRD found in literature.

Step 7: Several cyclic undrained DSS loading at uniform CSR are simulated. The primary parameter  $h_{p0}$  is varied until the numerical CRR curve interpolates the soil's CRR at 15 uniform loading cycles. The failure criteria for liquefaction used are the onset of a peak shear strain of 1%, 3%, and 98% for the excess pore water pressure ratio  $r_u$  (in the analyses, the 1% peak shear strain used). Figures 6.40-42 show the response for the sandy layer beneath the dam, characterized by a CRR of 0.165, a relative density of 58.4%, and a static initial shear stress of 0.15 (or static bias  $\alpha$ ). The  $\alpha$  value determines the progressive accumulation of shear strain in one direction, but it does not influence the CRR (Figure 6.41). In fact, for medium dense sands, the CRR variation with  $\alpha$  is almost constant (Vaid and Finn 1979; Vaid and Chern, 1985). Thus, for the sandy layer, the  $h_{p0}$  parameter is found to insensitive to the static bias. The effect on confining stress on the CRR is also limited, though it is observed that higher values results in a slightly lower CRR curve. Hence, in the final

calibration, the mean value of confining stress is used (3.5 atm). Figure 6.43 also shows the curve that fits the simulated points, which is the power fitting:

$$CRR = aN^b \quad (6.27)$$

where  $a$  and  $b$  are fitting parameters, and  $N$  is the number of uniform loading cycles.

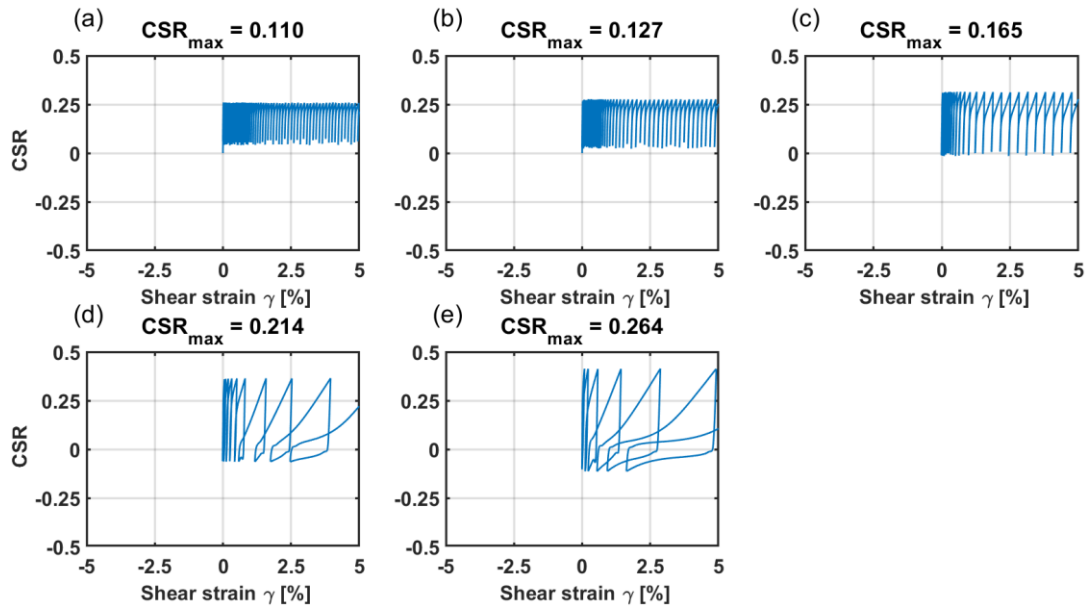


Figure 6.40: Undrained cyclic DSS loading response for the sandy layer beneath the dam ( $D_R = 58.4\%$ ).

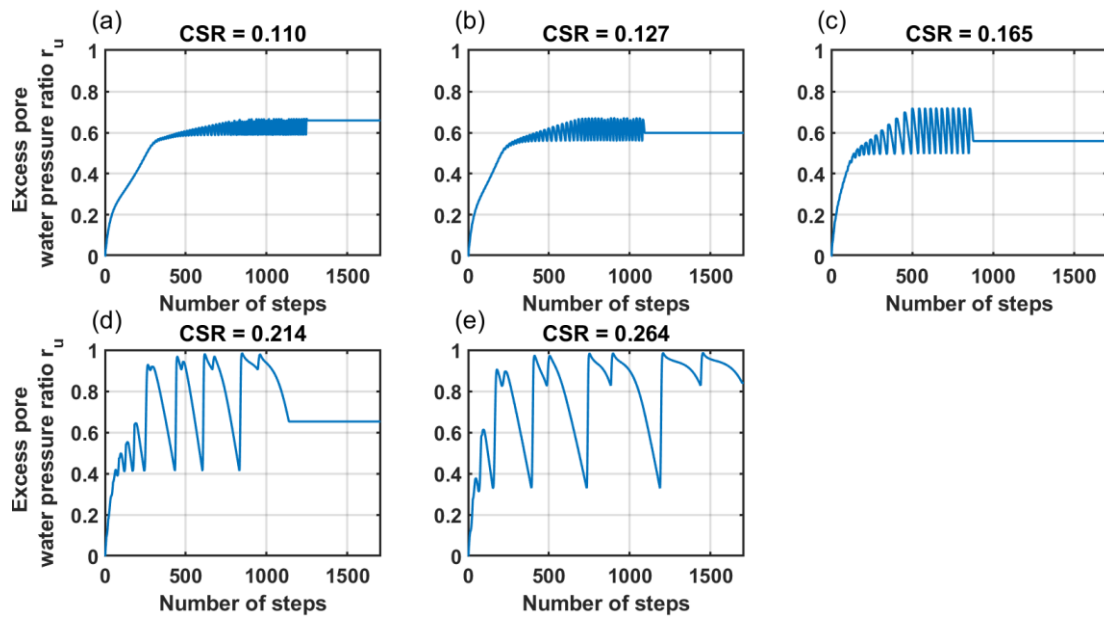


Figure 6.41: Excess pore water pressure ratio variation for the sandy layer ( $D_R = 58.4\%$ ) in undrained cyclic DSS loading.

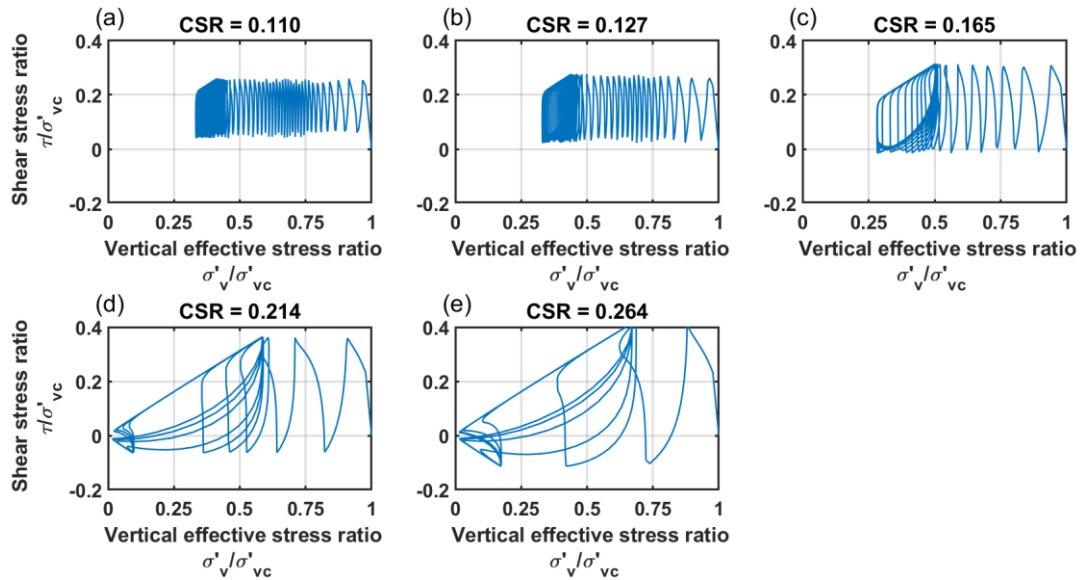


Figure 6.42: Stress path responses for undrained cyclic DSS simulation of the sandy layer ( $D_R = 58.4\%$ ).

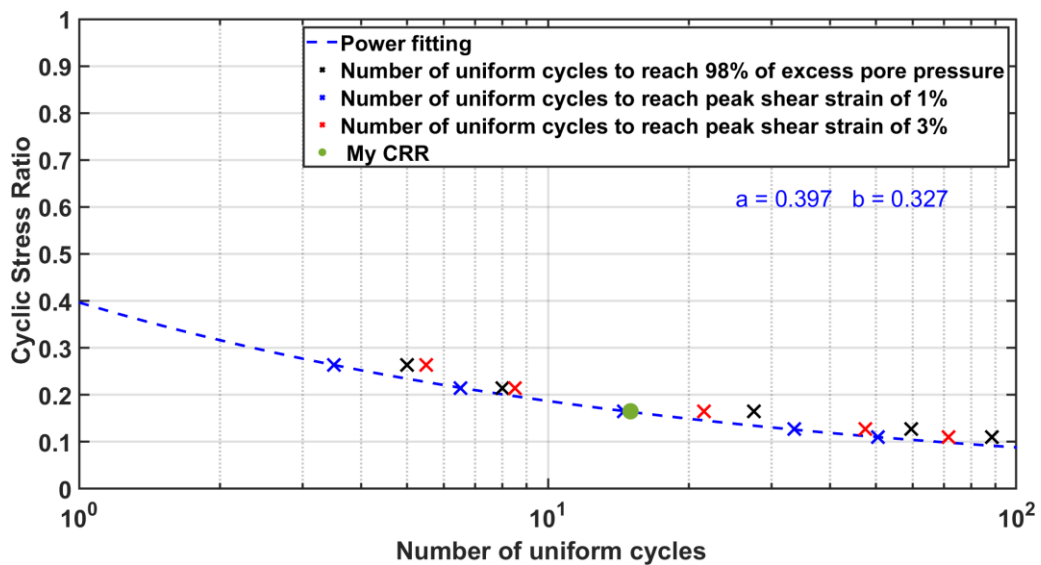


Figure 6.43: Cyclic stress ratios versus number of equivalent uniform loading cycles in undrained DSS loading to cause  $r_u=98\%$  or single-amplitude shear strains of 1% or 3% for the sandy layer ( $D_R = 58.4\%$ ,  $\sigma'_c = 3.5 \text{ atm}$ ).

For the sandy layer in free field condition, and for the alluvial sand, the static bias  $\alpha$  is close to 0. The cyclic stress strain response and the simulated CRR for the upper sand are shown in Figures 6.44-6.46. In this case, the mean confining stress of 0.7 atm is used, since for loose-medium sands the effect of  $\sigma'_c$  is almost negligible (Vaid and Sivathayalan, 1996).



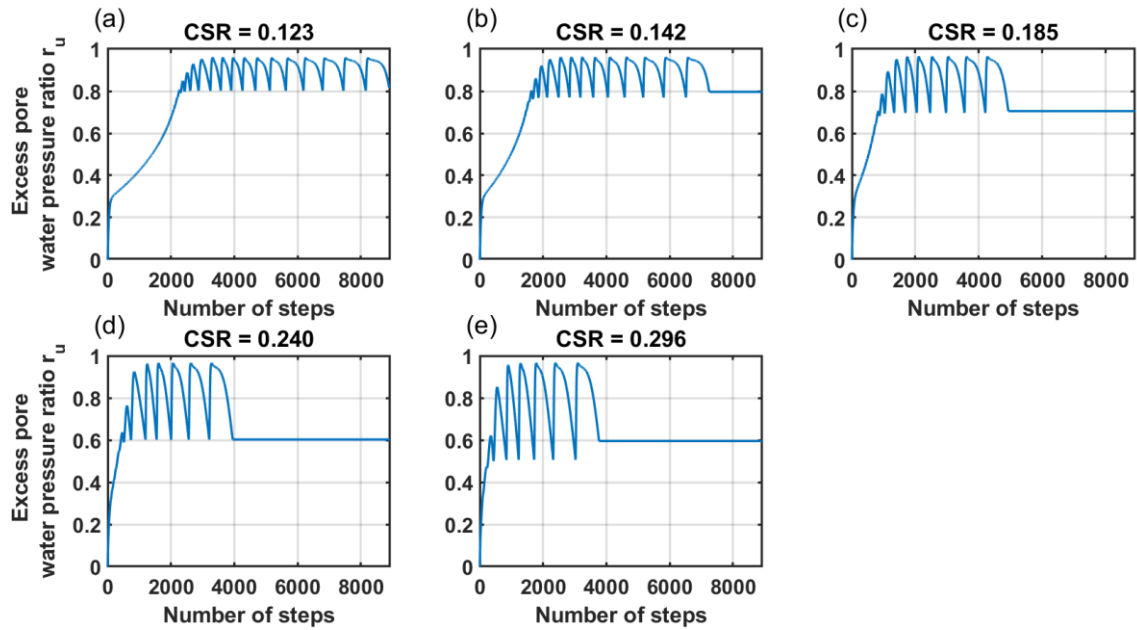


Figure 6.44: Excess pore water pressure ratio variation for the alluvial sand ( $D_R = 39\%$ ) in undrained cyclic DSS loading.

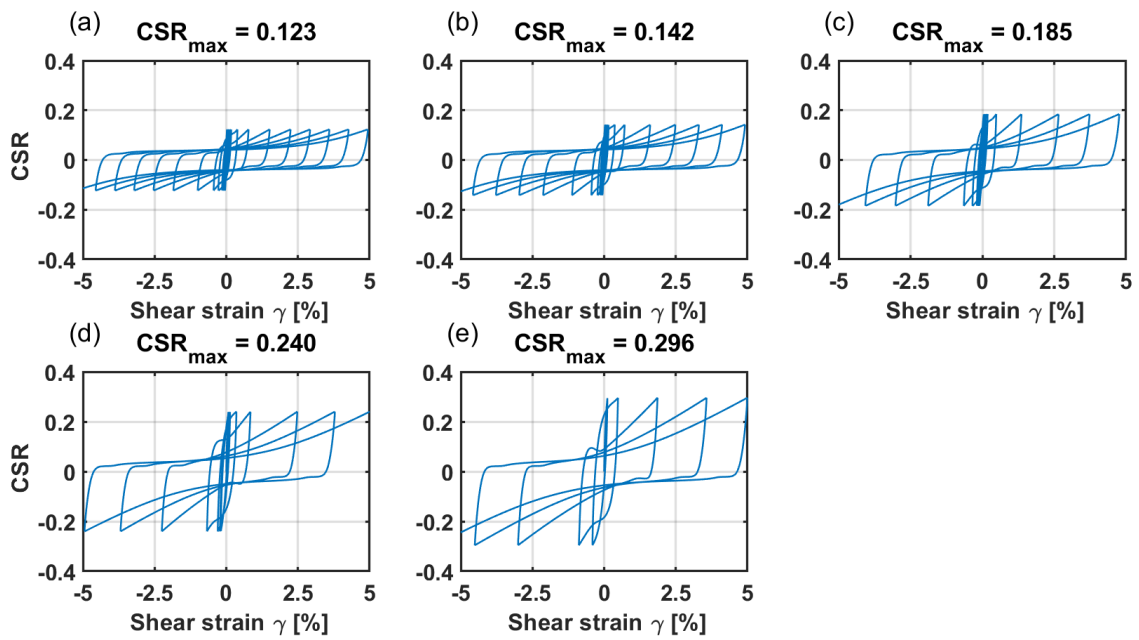


Figure 6.45: Undrained cyclic DSS loading response for the alluvial sand ( $D_R = 39\%$ ) with a vertical confining stress of 0.7 atm and no static bias.



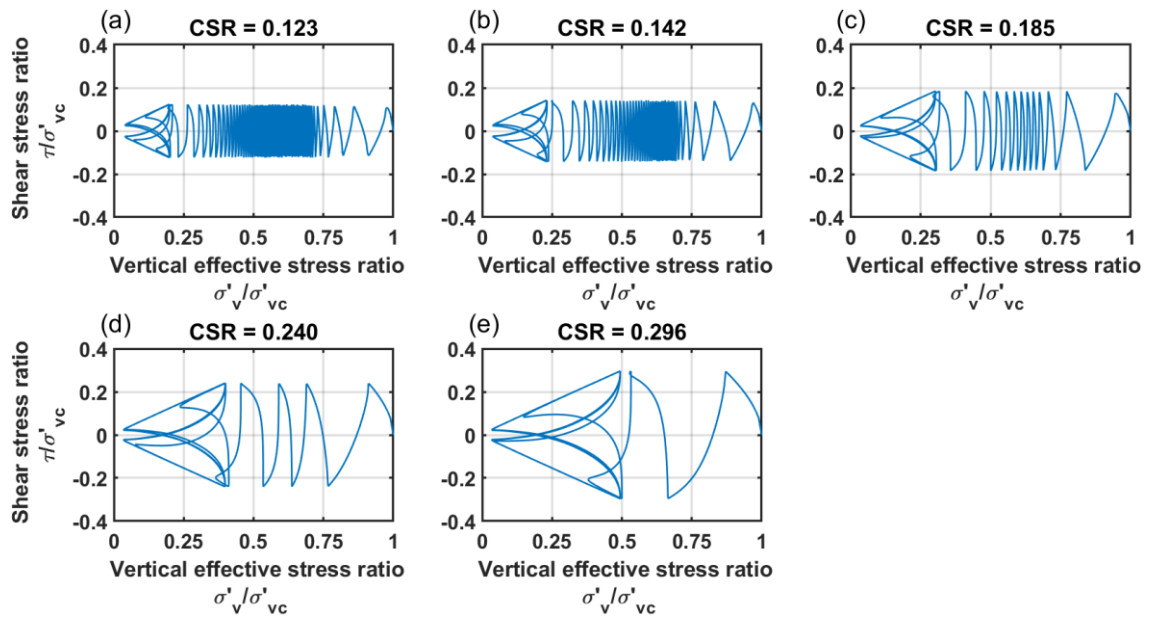


Figure 6.46: Stress paths responses for undrained cyclic DSS simulation for the alluvial sand ( $D_R = 39\%$ ) with a vertical confining stress of 0.7 atm and no static bias.

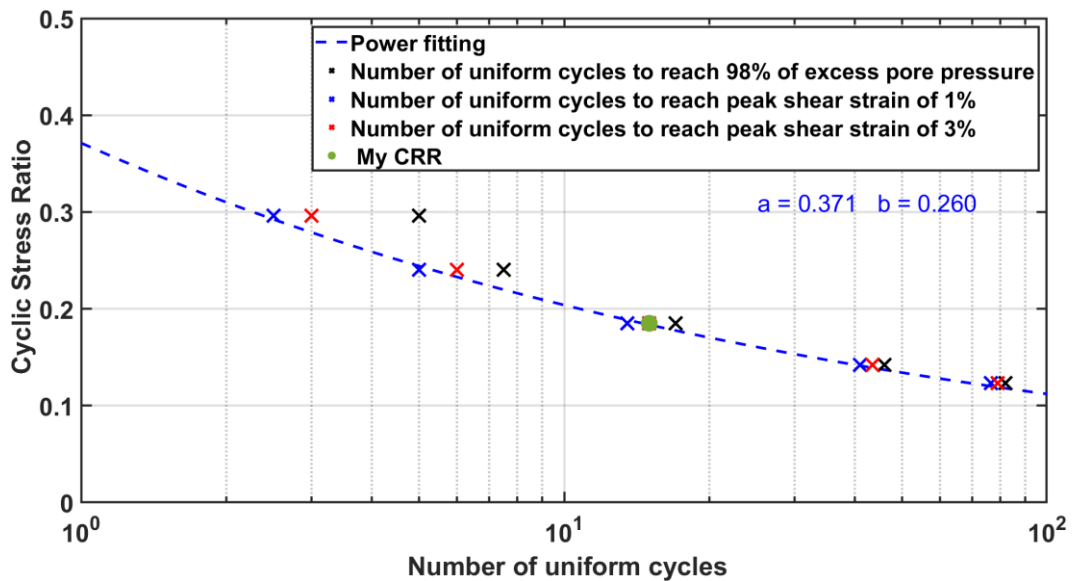


Figure 6.47: Cyclic stress ratios versus number of equivalent uniform loading cycles in undrained DSS loading to cause  $r_u=98\%$  or single-amplitude shear strains of 1% or 3% for the alluvial sand ( $D_R = 39\%$ ,  $\sigma'_c = 0.7$  atm).

Step 8: The stress-strain response obtained from the cyclic undrained DSS simulations are analyzed. For instance, the stress strain response of Figure 6.46 shows the progressive accumulation of shear strains, without locking up in a

repeating loop. This is a consequence of the fabric terms implemented in the PM4Sand model, whose response is consistent with experimental data. However, if laboratory data tests are available, the fabric terms can be used to adjust the rate of shear strain accumulation.

Step 9: if an initial static shear bias  $\alpha$  is present, the CRR curve should be estimated again, as the cyclic strength is related to  $\alpha$ . For the sandy layer, however, it was showed that the influence in negligible. Only the final calibration results were shown in this section, but two iterations of the procedure were still necessary to ensure that the model gave acceptable responses.

## 7. Nonlinear deformation analysis results

This chapter presents the results of Nonlinear Deformations Analyses (NDA) performed with the software FLAC, for the Farneto del Principe dam and the Angitola dam. First, an introduction to fragility functions is presented. This section is followed by a discussion on the choice of the damage measures, intensity measures, and ground motions used to derived analytical fragility functions (i.e., based on NDA). After these introductory sections, the chapter illustrates outcomes of the analyses for both dams, The last portion of the chapter contains quantitative analyses on efficiency and predictability of ground motion intensity measures used to constrain analytical fragility functions. A comparison with a recent similar study (Armstrong et al., 2020), but for earth dams in California, is also presented.

### 7.1 Introduction on analytical fragility functions

Fragility functions are defined as the probability of exceeding a certain Damage Measure (DM), given the occurrence of a particular Intensity Measure (IM). Mathematically, they represent the following conditional probability:

$$P(d > DM|IM = x) \quad (7.1)$$

There are three general approaches to build a fragility function: (1) analytically (i.e., based on the results of numerical models); (2) empirically (i.e., based on empirical data); (3) based on expert judgement. In this study, only analytical fragility functions are considered. Details about the other methodologies can be found in Porter (2017). The fragility function can also be defined as the cumulative distribution function (CDF) of the resistance to a certain damage state of the analyzed structure. A lognormal CDF is typically used to represent the above probability:

$$P(d > DM|IM = x) = \Phi\left(\frac{\ln \frac{x}{\theta}}{\beta}\right) \quad (7.2)$$

where  $\Phi$  is the standard normal CDF,  $x$  represent the IM,  $\theta$  is the IM that corresponds to 50% probability of exceedance (i.e., the median value), and  $\beta$  is the standard deviation of the natural logarithm of the IM (henceforth, the lognormal standard deviation). The real values of  $\theta$  and  $\beta$  are unknown, so they must be estimated using statistical procedures. Baker (2015) summarizes methods available to compute

fragility function. In this study, the Multiple Stripe Analysis (MSA) procedure, which is based on the method of maximum likelihood, is adopted. This approach is performed at discrete IM levels, typically corresponding to given return periods of the seismic action (each stripe represents an IM level). For each IM level, various ground motions are used in the analysis. The MSA method works well especially when ground motions are chosen to be consistent with a conditional spectrum. This is because the ground motion target properties change at each IM level and thus the representative ground motions do so as well (e.g., Bradley 2010; Iervolino et al. 2010; Lin et al. 2013). In the MSA, the number of ground motions that cause an exceedance of the DM of interest is computed from numerical analyses. Under the assumption that the exceedance of one DM is independent of the GM, the probability of having  $z_j$  exceedances in  $n_j$  GMs with  $IM = x_j$  is given by the following binomial distribution:

$$\text{Fraction of exceedances} = \binom{n_j}{z_j} p_j^{z_j} (1 - p_j)^{n_j - z_j} \quad (7.3)$$

The index  $j$  spaces on the number of IMs chosen to perform the MSA (i.e., the number of stripes). The fraction of exceedances are known from the analyses, and  $p_j$  is the probability of observing an exceedance with  $IM = x_j$ , which is the unknown fragility function. A lognormal CDF is used for the  $p_j$ , and the maximum likelihood method is exploited to estimate parameters  $\theta$  and  $\beta$ . Hence, finding the CDF that gives that highest probability of observing the exceedances computed from the analyses. When multiple IM levels are used, the likelihood is computed as the product of the binomial distributions. Finally, maximizing this function for  $\theta$  and  $\beta$  gives the fragility function:

$$\text{Likelihood} = \prod_{j=1}^m \binom{n_j}{z_j} \Phi\left(\frac{\ln x}{\beta}\right)^{z_j} \left[1 - \Phi\left(\frac{\ln x}{\beta}\right)\right]^{n_j - z_j} \quad (7.4)$$

## 7.2 Analytical fragility functions for the Farneto del Principe dam

### 7.2.1 Ground motions, intensity measures, and damage measures

This section presents the fragility functions for the Farneto del Principe dam calculated using results of MSA, for several damage classes and intensity measures.

The objectives of this section are to identify appropriate IMs that relates well with the predicted limit state (or damage state). Such appropriate IMs would be those producing low dispersions (i.e., lower values of  $\beta$ ). Input ground motions are chosen to be consistent with a CS computed from a site-specific PSHA. Six sets of ground motions are used, corresponding to the following return periods: 75, 475, 710, 1460, 1950, and 2475 years. Seven to ten site-specific ground motions are used (details in §4.2) for each return period set. This relatively high number of ground motions per IM level ensures that the ground motion uncertainties are captured.

Three IMs are used to construct analytical fragility functions for the Farneto del Principe dam: (1) PGA, (2) PGV, and (3) Arias Intensity (AI, Arias, 1970). For PGA, selected ground motions used in the analysis are scaled at the PGA level that comes from the M-R- $\epsilon$  disaggregation results (i.e. the PGA that is most likely to be expected at the corresponding M-R- $\epsilon$  scenario). Table 7.1 shows a summary of disaggregation results (more details about the disaggregation the seismic hazard at this sites are provided in § 4.2.2.1). To obtain another point in the upper part of the fragility function (high probability of damage), the set of ground motion corresponding to a return period of 1460 was scaled up to a value of PGA =1.5g. However, the return period associated with this PGA value is technically unknown and it only serves the purpose of constraining the fragility function at high level of probability of damage. All ground motions used in this section and their main characteristics used for the MSA of the Farneto del Principe dam are reported in Appendix A. Table 7.2 shows details about the sub-set of ground motions for which results are shown in this section.

Various DMs can be identified for earth dams. A comprehensive overview of them is provided in §2.5. As a result, in this study, the following DMs were considered to perform MSA and construct fragility functions for each of them:

*Table 7.1: Magnitude-Distance-Epsilon disaggregation for the Farneto del Principe dam.*

<b>Return period</b>	<b>M</b>	<b>R [Km]</b>	<b><math>\epsilon</math></b>	<b>PGA [g]</b>
75	6.56	50.25	1.16	0.21
475	6.96	50.20	1.47	0.51
710	7.05	51.18	1.54	0.62
1460	7.20	53.62	1.64	0.80
1946	7.27	54.81	1.67	0.88
2475	7.32	55.85	1.70	0.96

Table 7.2: Summary of the subset of ground motions for which results are shown in this section.

Earthquake				Station			Intensity Measure	Recording ID
Name	Year	M	Style of faulting	Name	R <sub>jb</sub> [Km]	V <sub>S30</sub> [m/s]	PGA [g]	
Loma Prieta	1989	6.93	Reverse oblique	Sunol - Forest Fire Station	47.4	400.6	0.08	1
Coalinga-05	1983	5.77	Reverse	Burnett Construction	8.3	352.2	0.34	2
Chalfant Valley-01	1986	5.77	Strike slip	Lake Crowley - Shehorn Res.	24.4	456.8	0.05	3
Lazio-Abruzzo Italy	1984	5.8	Normal	Cassino-Sant'Elia	20.0	436.8	0.11	4
Corinth Greece	1981	6.6	Normal oblique	Corinth	10.3	361.4	0.30	5

1) Filters displacement. Following Seed (1979) protocols, the limiting filter displacement value is defined as one time the filter thickness,  $t_f$ . For the Farneto del Principe dam, this limiting value would be equal to 1m. In the numerical model, this displacement value is taken as the displacement vector amplitude. Additional values of the limiting displacement for this damage mechanism were also considered (i.e., 50% and 25% of  $t_f$ ).

2) Global instability. This damage mechanism refers to permanent displacements that occur within the dam body and in the dam's foundation. In the numerical model, this displacement value is taken as the total displacement within the failure surface defined by maximum shear strains zone. The maximum allowable displacement is taken as 1 m. Additional values of the limiting displacement for this damage mechanism were also considered (i.e., 0.50, 0.25, and 0.15 m).

3) Free board reduction. This damage measure corresponds to the settlement of the upstream vertex of the crest. If it is greater than the free board, the collapse limit state is reached. Damage measures corresponding to 65%, 50%, and 25% of the free board settlement are also considered.

4) Fell damage classes. This damage measure is based on the empirical results obtained by Pells and Fell (2002, 2003). Their empirical methodology define five damage classes (DC), which are related to the vertical displacement of the crest. Table 7.3 reports all DCs considered in the analysis of the Farneto del Principe dam.

Table 7.3: Fell damage classes for the Farneto del Principe dam.

Damage Class		Maximum longitudinal crack width [mm]	Maximum relative crest settlement [cm]
Number	Description		
0	None or slight	< 10	≤ 1
1	Minor	10 < w ≤ 30	1 < d ≤ 6
2	Moderate	30 < w ≤ 80	6 < d ≤ 15
3	Major	80 < w ≤ 150	15 < d ≤ 45
4	Severe	150 < w ≤ 500	45 < d ≤ 150
5	Collapse	> 500	> 150

5) Normalized Crest Settlement (NCS). This damage measure is based on the Swaisgood (2014) empirical methodology (§ 2.5.2). The author analyzed the damage to several earth dams observed after strong earthquakes and related it to NCS, which is defined as:

$$NCS = \frac{\Delta}{H + s} \cdot 100\% \quad (7.5)$$

where  $\Delta$  is the mean vertical settlement of the crest,  $H$  is the dam height, and  $s$  is the foundation thickness. It should be noted that all dams that reported a value NCS greater than one are those where liquefaction occurred. Such conditions (liquefiable dam and/or dam's foundation material) are not met by the Farneto del Principe dam. As a result, this DM is not necessarily accurate to describe high displacements for this dam. This effect is visible in the lower part of fragility functions (populated with a relatively small number of data points) because even moderate earthquakes may produce high displacements in liquefiable materials, whereas such earthquakes would produce lower displacements in non-liquefiable materials such as those of the Farneto del Principe dam.

### 7.2.2 Numerical model results

This section shows the numerical results obtained for the Farneto del Principe dam, using the Mohr Coulomb (MC) and PM4Silt models. For the latter, only one set of analyses is performed (for constant PGA values) to verify if the response is similar to that produced by MC model. The Farneto del Principe dam materials are not susceptible to liquefaction (§3.5.1). Therefore, the results obtained using the PM4Silt model should be, in theory, similar to those obtained using the MC model. In this section, the term MC dam model will refer to NDAs performed with all materials modelled with a MC model. The term PM4Silt dam model, instead, will

refer to NDAs performed using the PM4Silt constitutive model for the core (whereas all other materials are still modeled using the MC model). Instead of showing results for all ground motions, in this chapter, only selected results involving relevant deformation patterns,  $r_u$  time series, and displacement fields are shown. These selected results refer to five recordings (IDs 1-5 in Table 7.2) for which differences are visible. For all other motions, no or little between-model differences were observed. These time series were selected using CS target spectra for two return periods: (1) 1460 years, and (2) 75 years. Ground motions consistent with the 1460-year return period are meant to capture nonlinear effects in the dam's materials. The more moderate ground motions consistent with the 75-year return period are shown for comparison as they produced a lower degree of nonlinearity in the dam's Figure 7.1 shows the maximum shear strain as estimated by FLAC (Eq. 7.6) for time series ID5 (PGA = 0.30g) for the MC model and PM4Silt model.

$$ssi = \frac{1}{2} \sqrt{(\varepsilon_{xx} - \varepsilon_{yy})^2 + 4\varepsilon_{xy}^2} \quad (7.6)$$

where  $\varepsilon_{xx}$ ,  $\varepsilon_{yy}$ , and  $\varepsilon_{xy}$  represent the horizontal, vertical, and shear strain component of the strain tensor.

Figure 7.1 shows slightly different strain patterns produced by the two models. The *ssi* amplitude is higher in the PM4Silt dam model. Furthermore, high *ssi* values are located in the landside shell and in the core in the PM4Silt model. In the MC model, high *ssi* values do not occur in the core. Figures 7.2 and 7.3 show horizontal and vertical displacements, respectively, for the same ground motion (time series ID5). Displacement patterns shown in these figures are consistent with what it was observed for the *ssi* spatial distribution. The PM4Silt dam model suffers higher overall displacements that involve a larger portion of the dam body and include a large portion of the core. Displacements are more limited, especially in the core, in the MC dam model.

Figures 7.4, 7.5, and 7.6 show *ssi*, horizontal, and vertical displacements, respectively, for time series ID3 (PGA = 0.05). This time series (consistent with the 75-year return period CS) produced more limited *ssi* values and displacements than those observed using time series ID5. All three figures show similar *ssi* and displacement values and spatial distributions for both numerical models. This is expected, as the ground motion is not intense and the dam does not experience high



degrees of nonlinearity. Figure 7.7 shows the  $r_u$  ratio in four zones of the core, near the upstream filter (upper, middle, lower, and central zone) for four different ground motions (time series ID = 1, 2, 3, and 4) estimated using the PM4Silt dam model. As expected, excess pore water pressures are mostly negative. This indicates a dilative behavior of the compacted core material. Only in the lower portion of the core, where pore pressure are greater and the confining stresses are higher, there is a slight tendency to develop positive  $r_u$  values.

Overall, differences between the MC and PM4Silt models in the amplitude and spatial distribution of displacements in the Farneto del Principe dam are typically negligible, with the exception of some ground motions characterized by long return periods for which some differences are visible (Figures 7.1-7.3 show these occurrences). For this reason, all fragility functions for the Farneto del Principe dam were derived using the MC model.

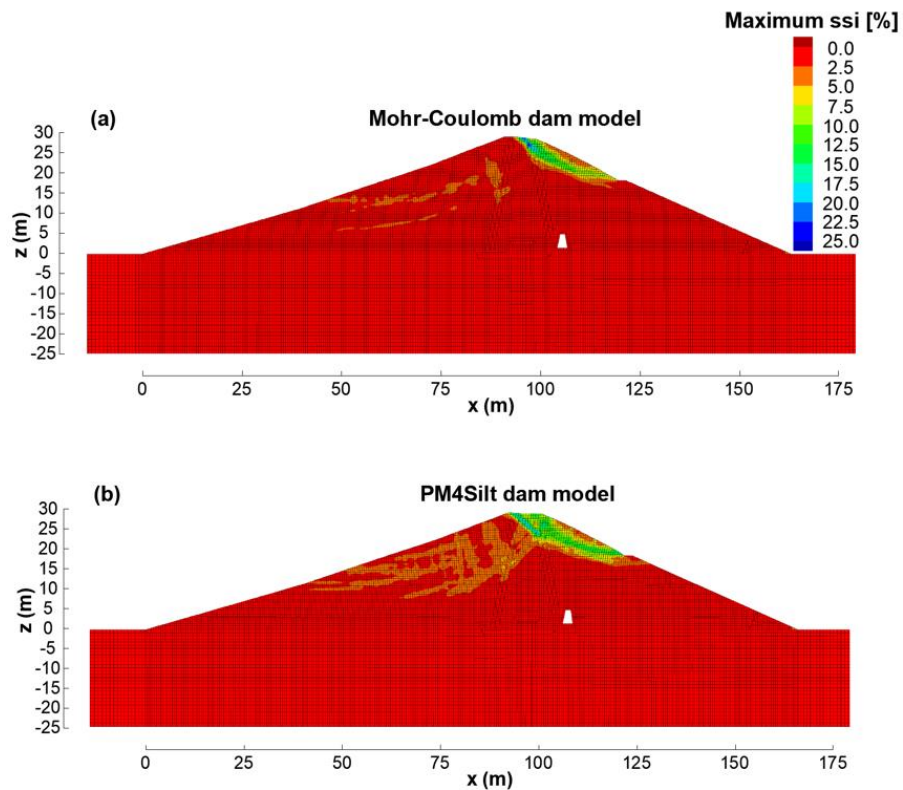


Figure 7.1: Contours of ssi for time series ID5 (return period of 1460 years).

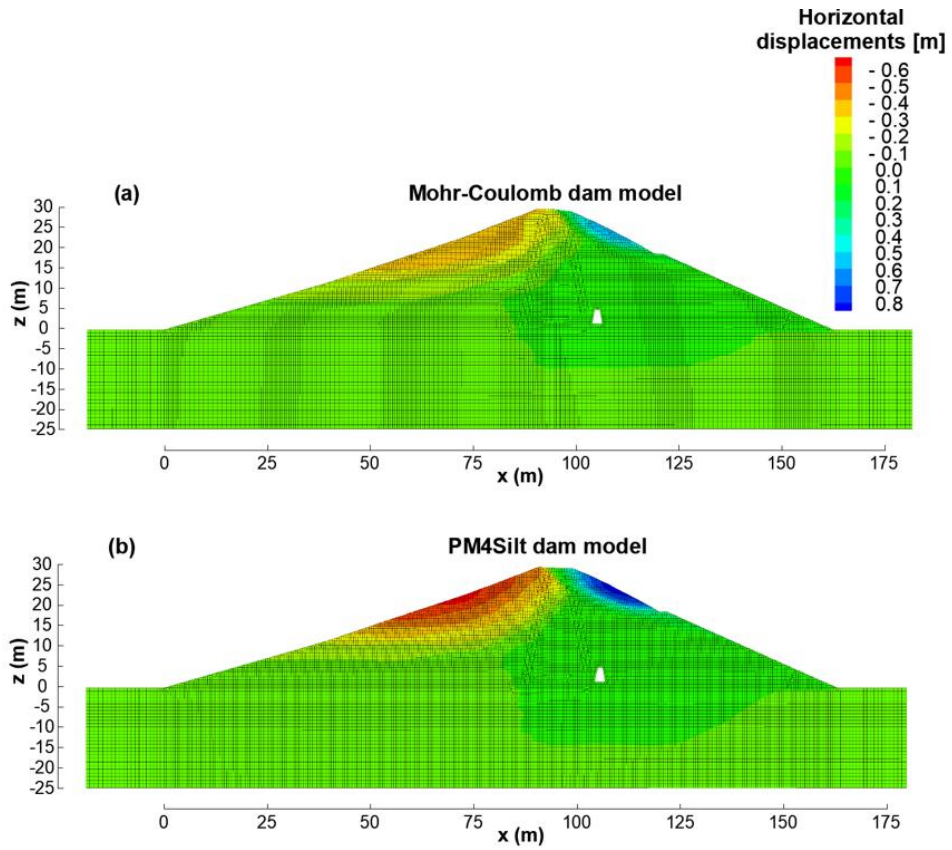


Figure 7.2: Contours of the horizontal displacements for time series ID5 (return period of 1460 years).

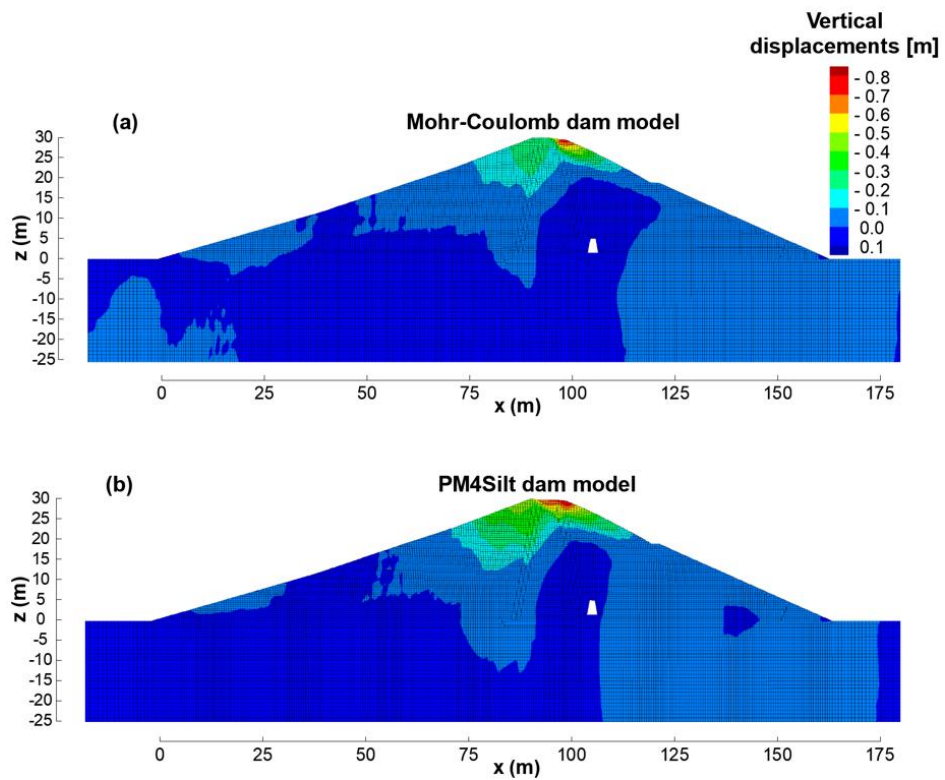


Figure 7.3: Contours of the vertical displacements for time series ID5 (return period of 1460 years).

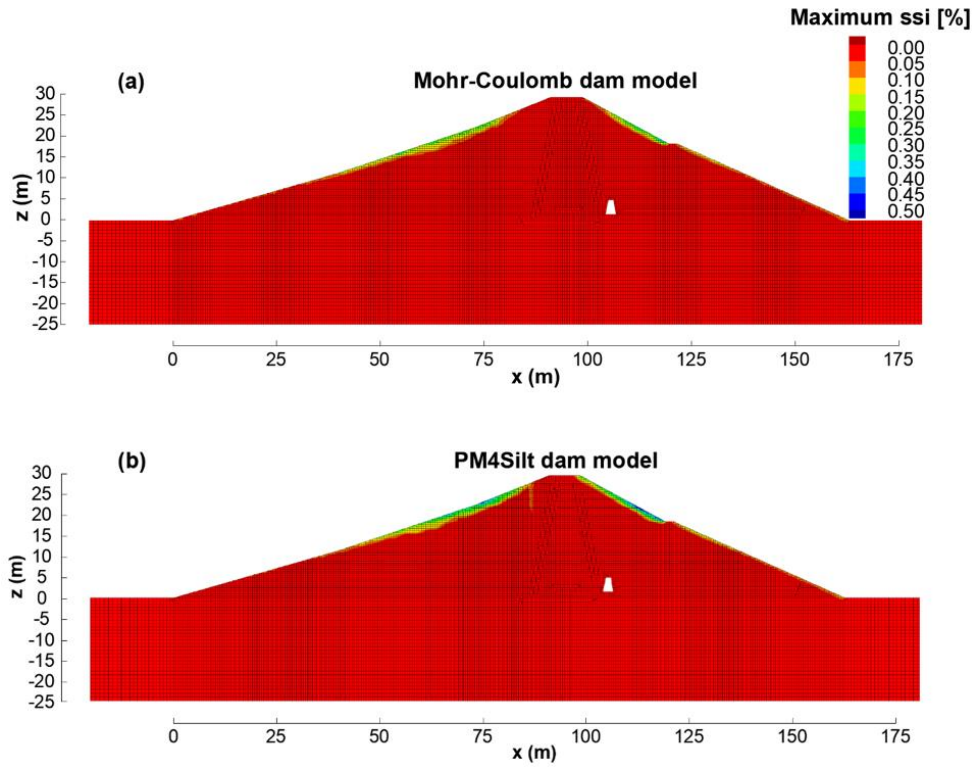


Figure 7.4: Contours of the shear strain increment for time series ID3 (return period of 75 years).

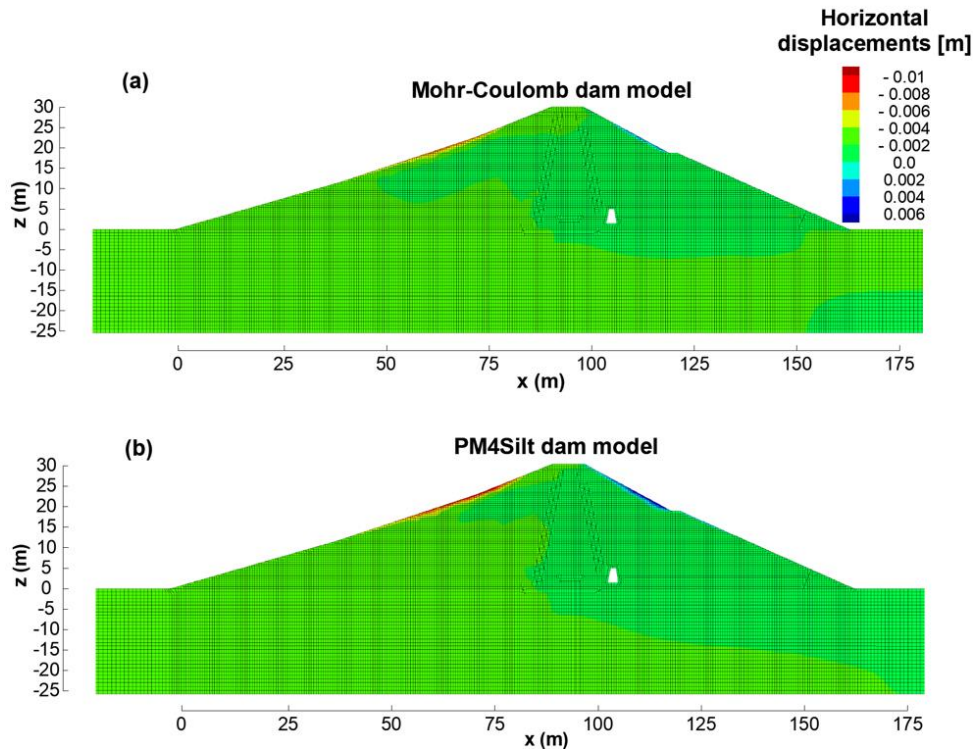


Figure 7.5: Contours of the horizontal displacements for time series ID3 (return period of 75 years).



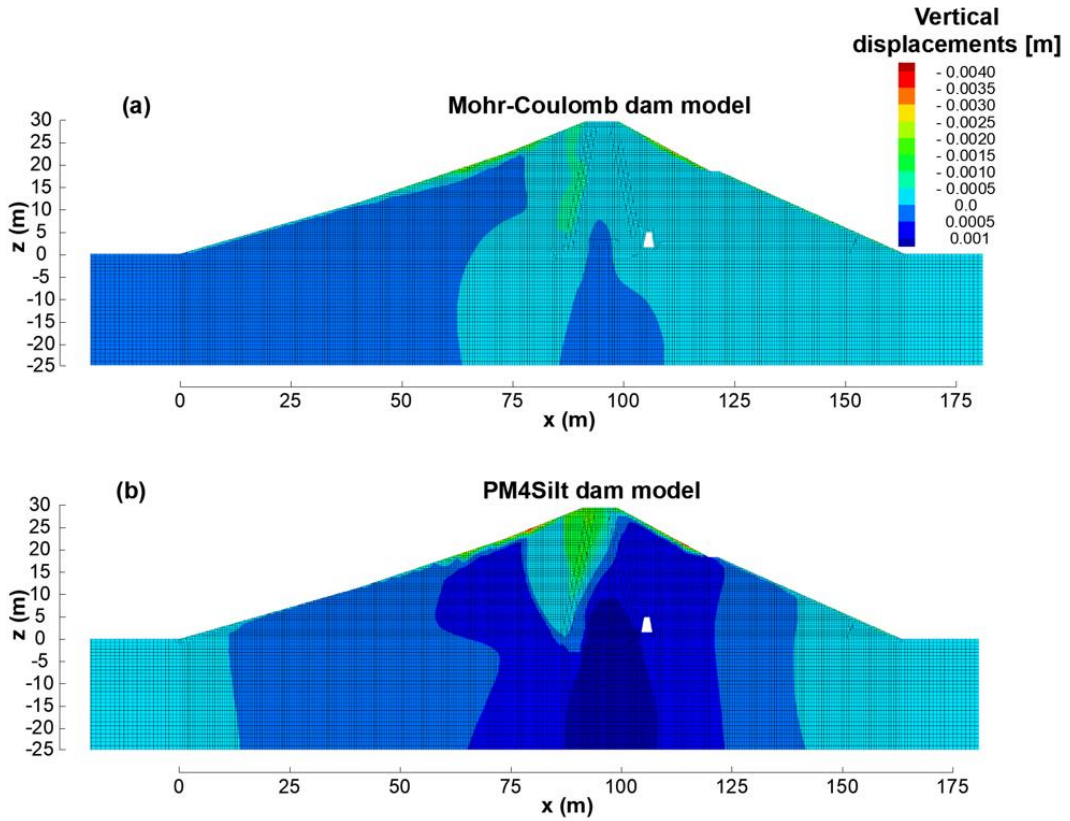


Figure 7.6: Contours of the vertical displacements for time series ID3 (return period of 75 years).

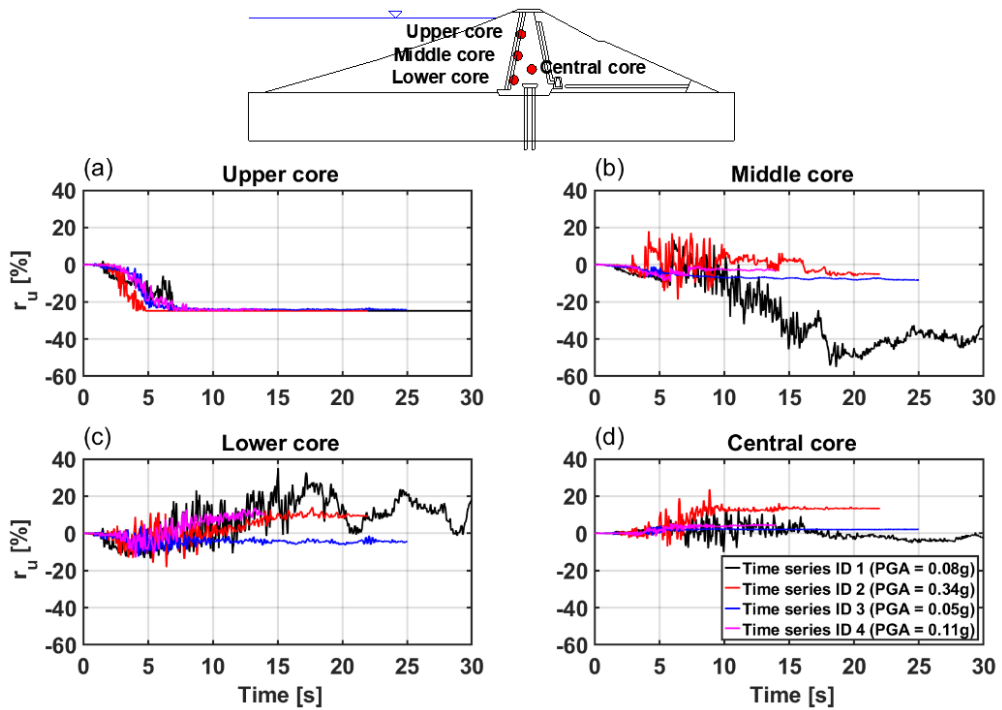


Figure 7.7: Locations of four control points within the dam core; excess pore water pressure ( $r_u$ ) time series for time series ID1-4 in four zones of the core of the Farneto del Principe dam: (a) upper core, (b) middle core, (c) lower core, and (d) central core.

Figure 7.8 shows FLAC-based NCS versus those estimated using Eq. 2.28. The plot shown in Figure 7.8 is the same as that in Figure 2.16 but with the addition of the limit states suggested by Silvestri and d’Onofrio (2014). It can be seen that the measured and estimated NCS are consistent with the limit states suggested by Silvestri and d’Onofrio (2014). For the 75-year return period, the ground motions resulting damage is negligible, while for return periods of 475 and 710 years the damage level is minor to moderate. For intense ground motions (i.e., return periods greater than 1460 years) the damage is moderate and/or severe. However, as pointed out by Silvestri and d’Onofrio (2014), damage thresholds are not unique, thus it is not possible to estimate the exact damage only with a single value of the NCS.

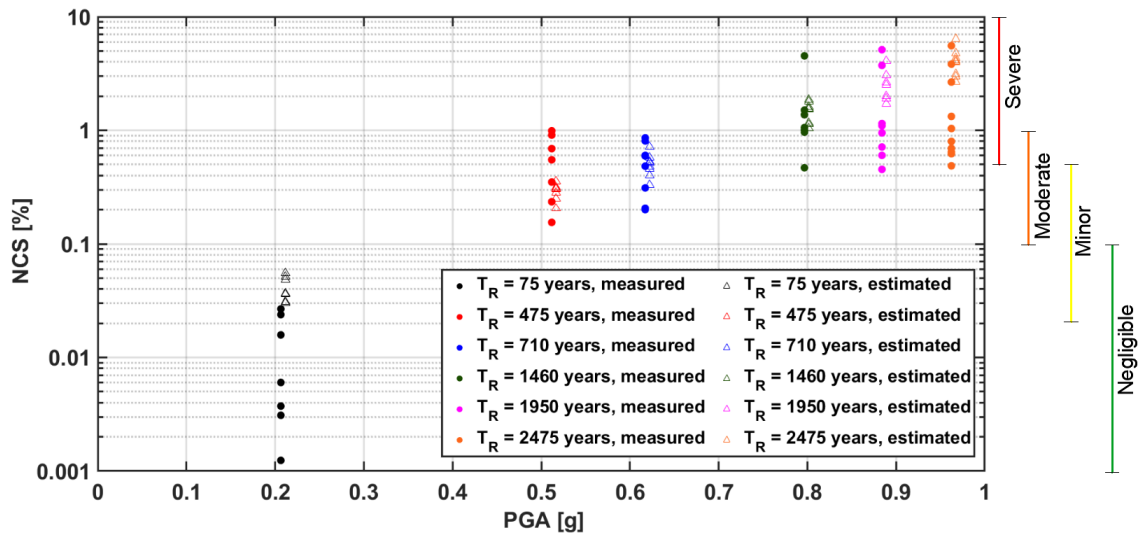


Figure 7.8: Measured and estimated NCS for the Farneto del Principe dam and comparison with the limit states suggested by Silvestri and d’Onofrio (2014).

## 7.2.3 Computed fragility functions

### 7.2.3.1 Peak Ground Acceleration

Figure 7.9 shows typical MSA results used to produce fragility functions. Each data point in Figure 7.9 represents the result of one numerical model simulation. Vertical dashed lines represent threshold for various damage states (i.e., Full damage classes 3 and 5 and freeboard reduction, labeled as Damage class 3, Damage class 5, and Freeboard, respectively in Figure 7.9), corresponding to different values of the maximum crest settlement. In Figure 7.9, various stripes of horizontally-aligned data points can be recognized. Each stripe corresponds to a different ground motion set (each of which is related to a return period value). Unlike traditional NDA approaches, within the MSA framework, higher values of the IM does not necessarily produce an increasing fraction of exceeding a given DMs. This is because each set of ground motions are scaled at the same value of the selected intensity measure. This scaling process can cause changes in the energy content of the scaled ground motion if compared against the unscaled motion. As an explicative example, an unscaled ground motion with an original low PGA value may need a high scale factor to become consistent with a high-return period target CS, causing the energy content of the earthquake to rise significantly. On the other hand, pulse-like ground motions (characterized by high PGA values occurring only at one moment in time), with an original high PGA, may need a low scaling factor to be consistent with the same target CS. This latter ground motion would have the same energy content in its scaled and unscaled versions. Furthermore, the performance of earth dams is highly dependent on the frequency content and duration of the motion and on the frequency content of the motion relative to the fundamental frequency of the dam. In the MSA framework, ground motions with the same IMs but different durations (i.e., motions characterized by different magnitude values) will most likely result in different damage levels (i.e., longer motions would cause more damage). These peculiar effects of the MSA framework on earth dam's performance are shown in Figure 7.10. There is a trend of increasing freeboard reduction as the significant duration of the motion,  $D_{595}$  (defined as the time interval between 5% and 95% of the AI, Trifunac and Brady, 1975) increases (Figure 7.9a). Figure 7.10b shows freeboard reduction vs ground motion frequency content. In this case, there is not evident trend of damage vs frequency and the data is scattered. Interestingly, low frequency motions result in higher damage, despite the fundamental frequency of the dam being around 5 Hz.

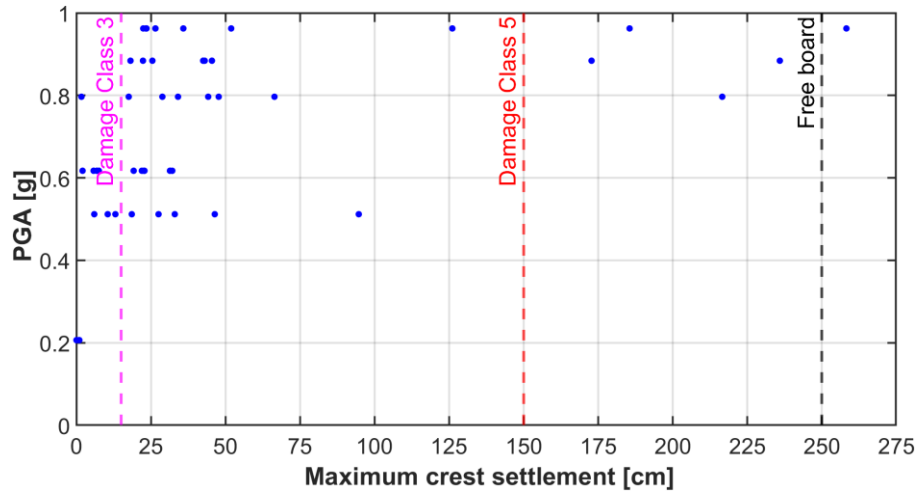


Figure 7.9: Typical results of the Multiple Stripe Analyses. The blue dots represent the damage observed and each stripe refers to a return period. The dashed vertical lines indicate the threshold used to define the damage measure and evaluate the fraction of ground motions that exceed that value.

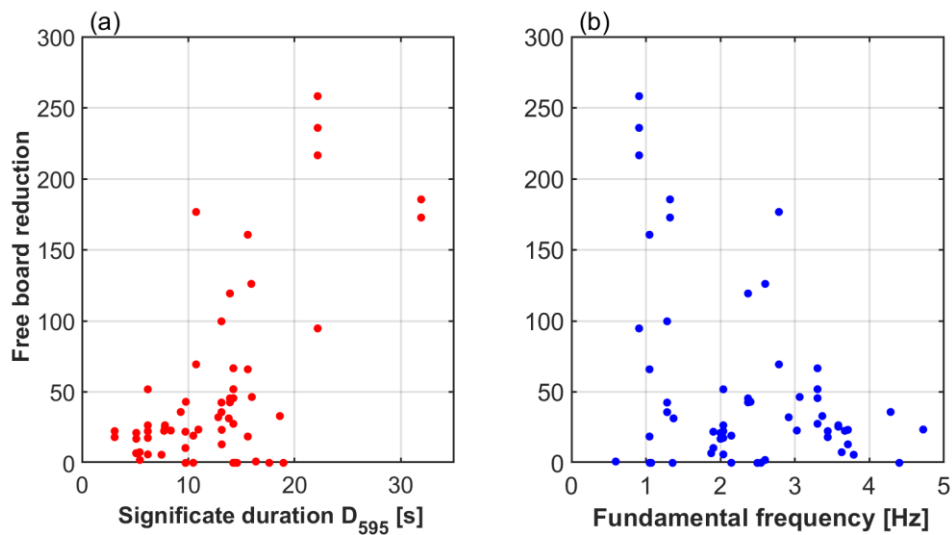


Figure 7.10: (a) Plot of the damage measure versus significant duration showing larger damage for long earthquakes; (b) Plot of the damage measure versus the fundamental frequency of the ground motions.

Figure 7.11 shows analytical fragility functions calculated for PGA. The model fitting to the data is relatively good and there seems to be a consistent trend of the fraction of ground motions that exceeds a certain threshold (i.e., open triangles) with increasing IM. The standard deviation  $\beta$  is an indicator of the goodness of fit. For PGA the  $\beta$  are relatively low for all analyzed DMs (ranging between 0.11-0.70). Figure 7.12a shows the DM that is most likely to be exceeded for a certain value of

the IM at the collapse limit state. This comparison shows that some damage states are more likely to be exceeded than others for the same level of PGA. Such differences should be carefully accounted for when using fragility functions for forward analyses. The filters and global instability DMs, have similar probabilities of exceedance given a certain level of PGA (i.e., fragility function are close to each other). They are much greater than for the freeboard reduction (which has a high standard deviation). This is somewhat expected, as the freeboard of the Farneto del Principe dam is 2.5 m, a displacement threshold significantly higher than the 1 m limit for filters and global instability. Fragility functions can also give information on how much damage the dam can still sustain before reaching collapse. In particular, the difference between the probability of exceeding a serviceability damage state and collapse state for a certain value of IM is estimated and shown in Figure 7.12. Figure 7.12b shows the probabilities of exceedance of lower damage measures (i.e., fragility functions are defined with lower damage thresholds). For these fragility functions, the return period of each stripe of ground motions is unknown. Figure 7.12b shows that it is more likely to get permanent a displacement of 25 cm in the shells than the same displacement value in the filters. This is consistent with the shear strain and displacement spatial patterns observed and shown in Figures 7.1-7.6, which hinted at collapse mechanisms concentrated near the abutments.

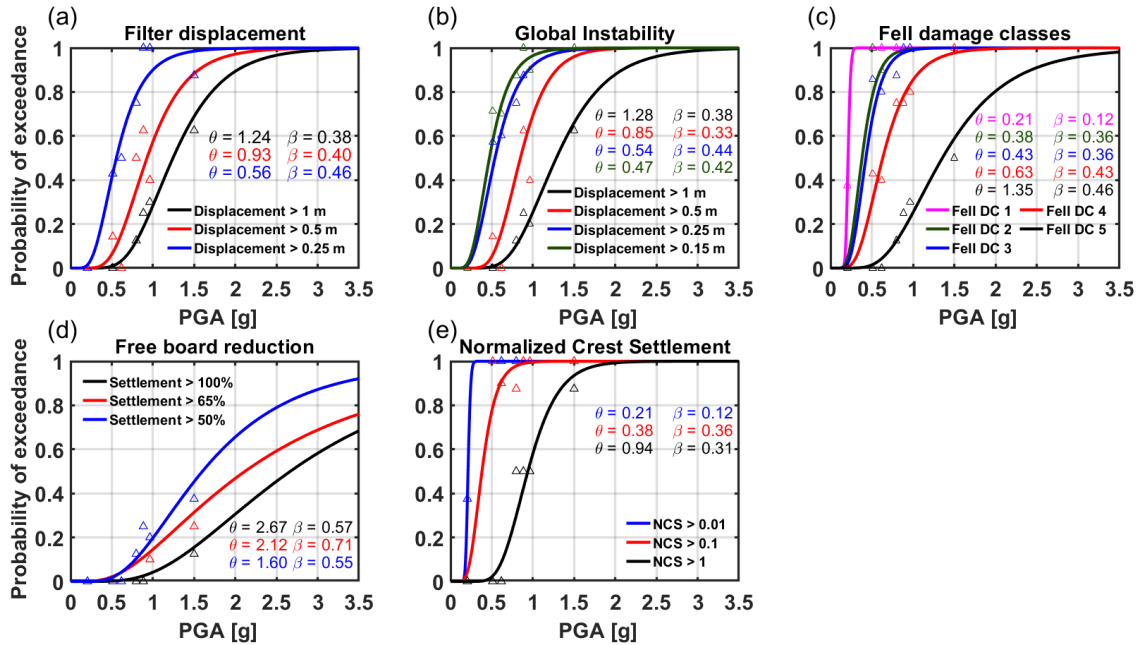


Figure 7.11: Fragility functions for the Farneto del Principe dam using the PGA as Intensity Measure.



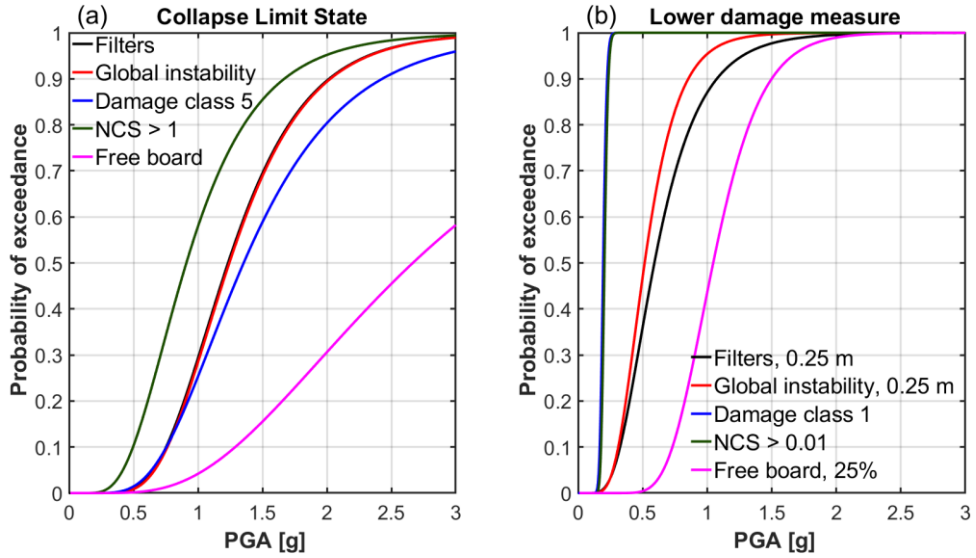


Figure 7.12: Comparison between fragility functions for the selected limit states: (a) Collapse Limit State; (b) Lower damage measures.

Another interesting result that can be obtained from fragility functions is the rate of collapse of the dam,  $\lambda_c$ . This can be done if a hazard curve describing the annual frequency of exceeding a certain IM is known. In fact, the fragility function gives the probability of a certain DM being exceeded when a certain value of IM is reached, but it does not specify the probability of that IM actually happening. The fragility function and hazard curve information can be joined to compute  $\lambda_c$  as:

$$\lambda_c = \int_x \Phi\left(\frac{\ln x}{\theta}\right) \cdot |d\lambda_{IM}(x)| \quad (7.7)$$

where  $d\lambda_{IM}(x)$  is the differential of the hazard curve. Assuming an occurrence of earthquakes in time with a Poisson model, the probability of one exceedance in  $t$  years can be estimated as:

$$P_{exceedance} = 1 - e^{-\lambda_c t} \quad (7.8)$$

Using these three results: the rate of collapse  $\lambda_c$ , the hazard curve, and the fragility function it is possible to estimate the intensity measure value that contributes the most to the collapse of the dam. This procedure is called collapse disaggregation (or deaggregation, Eads et al., 2013, Baker, 2015) and it provides the probability distribution of contributions of the IM level to the collapse:

$$\frac{P(x \leq IM < x + dx | C)}{dx} = \frac{P(C | IM = x) \cdot |d\lambda_{IM}(x)|}{\lambda_c} \quad (7.9)$$

Normalizing by the rate of collapse  $\lambda_c$  ensures that the area under the probability distribution curve is equal to one. The numerator of this expression for a specified value of IM is the contribution of that IM to the rate of collapse. When both the fragility function and the hazard curve are large, the contribution is high. This is why the most important IM levels are below to the median value of the fragility function (i.e., the annual frequencies of exceeding high IM levels are close to zero). Hence, the lower portion of the fragility function is the part of the curve that should be estimated more accurately (Baker, 2015). Figure 7.13 shows the results obtained for the Farneto del Principe dam. The PGA values contributing the most to the collapse of the dam, for all damage states considered, are reported in Table 7.4.

Table 7.4: PGA that contribute the most to the collapse as evaluated from the collapse disaggregation.

PGA values contributing the most to the rate of collapse					
IM	Filters	Global instability	Free board reduction	Fell damage class 5	Normalized Crest Settlement
PGA	0.869	0.876	0.879	0.776	0.784

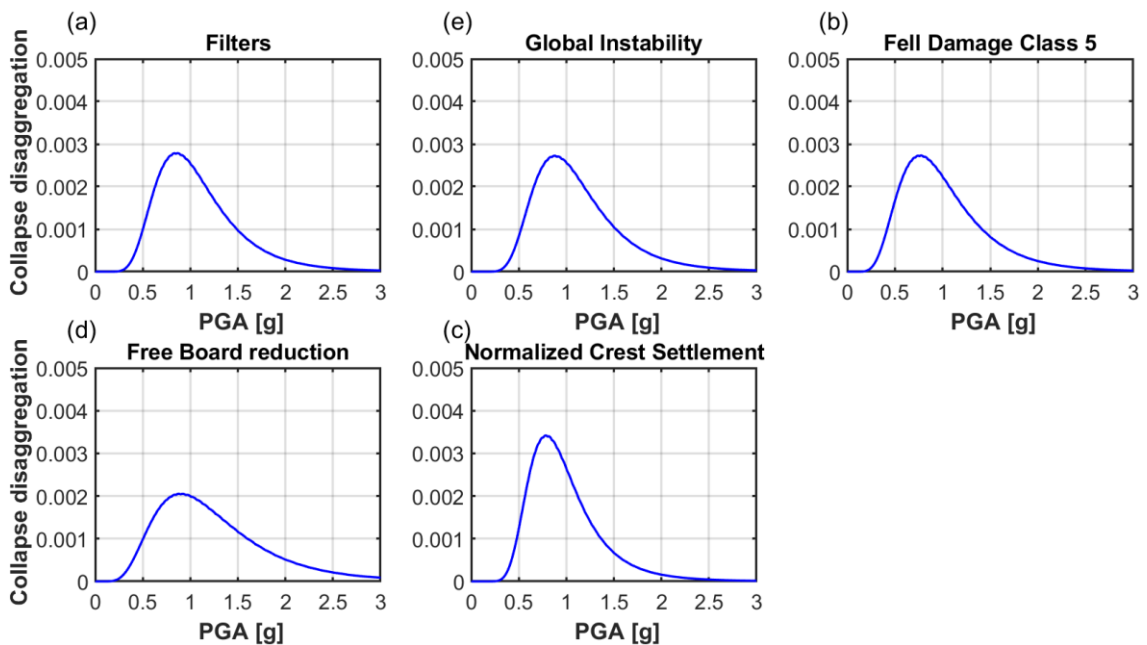


Figure 7.13: Collapse disaggregation for all DMs considered. The peak of these curves are used to evaluate PGA values contributing the most to the collapse of the dam.

### 7.2.3.2 Arias Intensity

The Ground Motion Models (GMMs) used in this study do not allow for the estimation of the Arias Intensity (AI). Hence, it is not possible to compute the mean values of this IM from disaggregation results. The AI used to perform the MSA were chosen based on the damage computed for the PGA-based analyses. This concept will be applied to the other IMs as well. The concept behind this choice is simple and is based on the search of the IM range that will produce significant results, while still being hazard-consistent (i.e., the new IMs are based on the PGA, for which disaggregation values are known). Figure 7.14 shows filter damage versus AI for the MSA performed with constant PGA values (i.e., constant PGA stripes). From the analysis of Figure 7.14, it can be seen that a range of 0-25 m/s of AI is necessary to capture most damage levels. The AI values adopted for the MSA are reported in Table 7.5, along with their corresponding PGA-based return periods.

Figure 7.15 shows the fragility functions obtained for the Farneto del Principe dam using the AI as IM. Some of them could not be estimated properly as the probability of exceedance of certain DMs was 100% for all considered ground motions (e.g., NCS of 0.01). The fragility functions evaluated from AI are more scattered (i.e., they have higher  $\beta$  values) than those obtained using PGA. This is due to the PGA range being relatively narrow, which can capture both collapse and low damage points. For AI, there are not many points (fraction of inputs exceeding threshold values) in the lower part of the curve. This is an undesired consequence of choosing AI ranges based on the damage expected from PGA results.

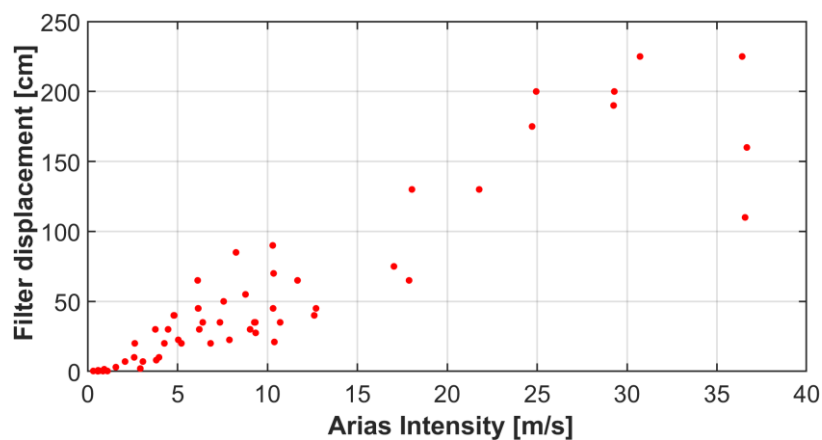


Figure 7.14: Filter displacement values versus AI for ground motions selected and scaled using PGA-based disaggregation results.

Table 7.5: AI used in this study for the MSA.

Return period	Arias Intensity [m/s]
75	1
475	5
710	10
1460	15
1946	20
2475	25

MSAs used to build AI-based fragility functions are performed at three different stripes, corresponding to low, intermediate, and high values of the IM. For embankment dams, however, inherent model and material uncertainties can result in scattered fraction of exceedances, which leads to unreliable fragility functions. If the IM range is large, it is likely to obtain results that are more scattered. The PGA range used in this case (0-1g) seems relatively small. However, that used for AI is wide. Hence, the choice of the IM range and the value of the stripes strongly affect computed analytical fragility functions. Sensitivity analyses may be performed to find the most appropriate IM range to build reliable fragility function. Figure 7.16 shows the limit state that is most likely to be exceeded when using the AI as IM. Unlike the comparison with PGA, the trend of fragility functions is slightly different, especially for freeboard reduction.

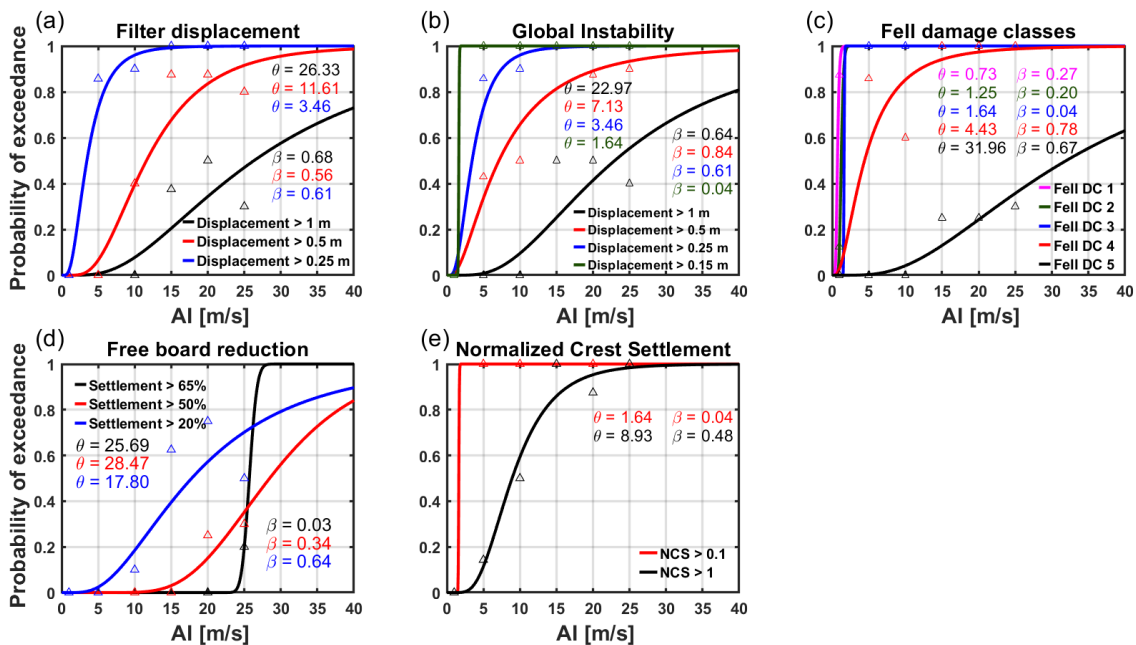


Figure 7.15: Fragility functions for the Farneto del Principe dam using the AI as IM.

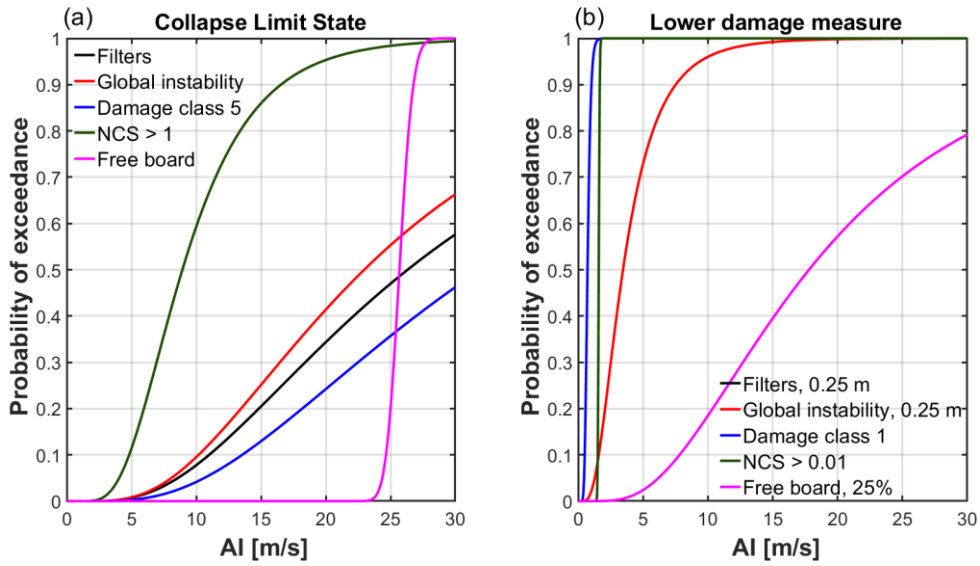


Figure 7.16: Comparison between fragility functions for the same limit state for (a) Collapse Limit State; (b) Lower damage measures.

### 7.2.3.3 Peak Ground Velocity

The PGV values used to scale the ground motions used in this analysis are reported in Table 7.6. They were selected based on the same considerations used for the AI scaling process and are based on PGA disaggregation results. This procedure produced a relatively narrow PGV range. The fragility functions obtained for the ground motions set scaled at different PGV levels are shown in Figure 7.17. The fragility functions for PGV produce lower standard deviation values than those for PGA and AI. This is an indication that the PGV is a good IM for fitting fragility functions for zoned earth dams, as they correlate well with the predicted damage. Figure 7.18 shows the limit state that is most likely to be exceeded when using the PGV as intensity measure. The trend observed for PGV is similar to that for PGA (Figure 7.4).

Table 7.6: Peak Ground Velocities used for the Multiple Stripe Analyses.

Return period	PGV [m/s]
75	0.1
475	0.35
710	0.5
1460	0.7
1946	0.85
2475	1

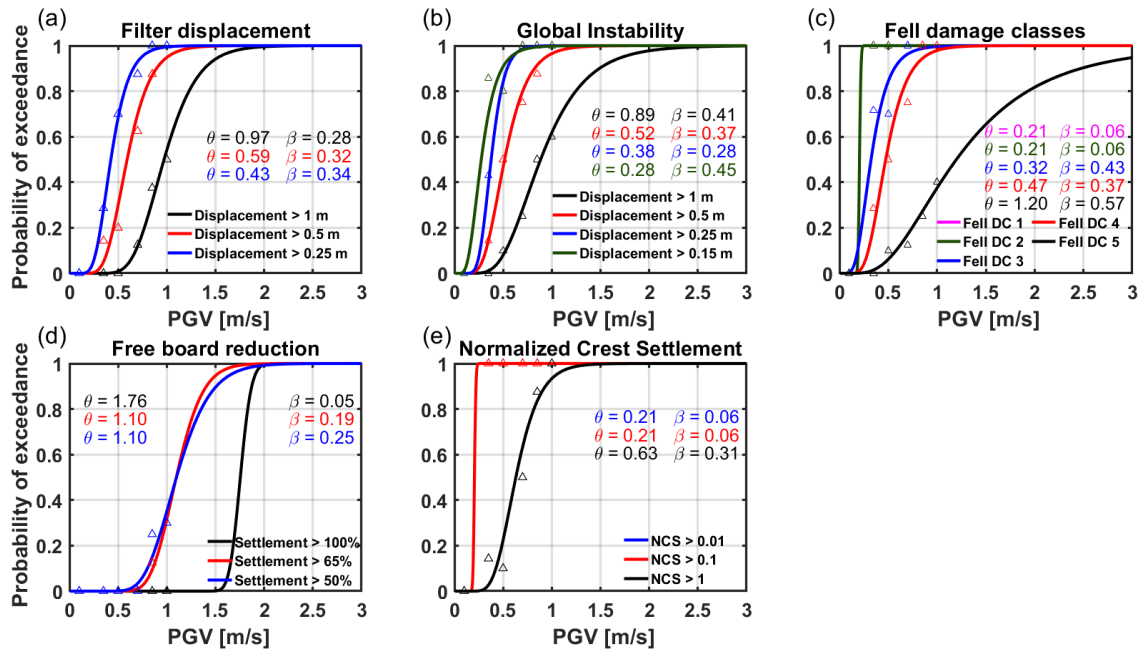


Figure 7.17: Fragility functions for the Farneto del Principe dam using PGV as IMs.

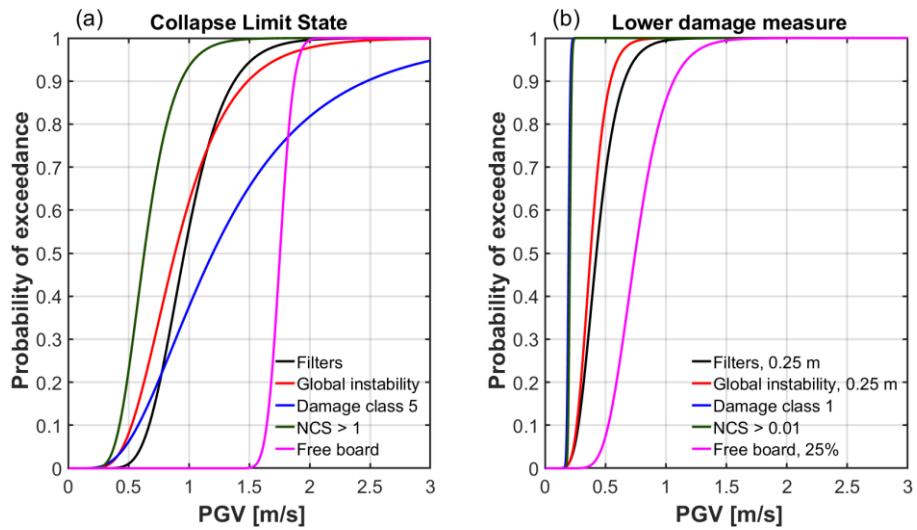


Figure 7.18: Comparison between fragility functions for the same limit state for (a) Collapse Limit State; (b) Lower damage measures.

#### 7.2.3.4 Between-IM fragility function comparison

The fragility functions computed with different intensity measures can be compared by normalizing the x-axis (i.e., dividing the IM by its maximum value  $IM_{max}$ ). Figure 7.19 shows the comparisons between fragility functions obtained for PGA and PGV.

Since the median IM values cannot be directly compared, in this analysis only the data scatter is analyzed by means of the  $\beta$  values. The curves, for both analyzed DMs (filter displacement and global instability) are quite similar because  $\beta$  values are comparable and both PGA and PGV fragility functions showed a good fit. Overall, PGA curves are more fragile (i.e., for the same value of  $IM/IM_{max}$  the probability of damage exceedance is higher for PGA) and  $\beta$  values are slightly smaller for PGV (i.e., PGV is a better predictor of damage than PGA).

Table 7.7 shows median and standard deviation values of all fragility curves obtained for the collapse limit state for different IMs for the Farneto del Principe dam. Standard deviation values are lower for PGV in all cases except for the global instability DM, where  $\beta$  for PGA is slightly lower. The median values for filters and global instability for PGV show that it is more likely to observe damage as a result of global instability than for filters damage (i.e. the  $\theta$  is lower for the global instability DM). This is something that was not captured for PGA, which showed equal and higher median values.

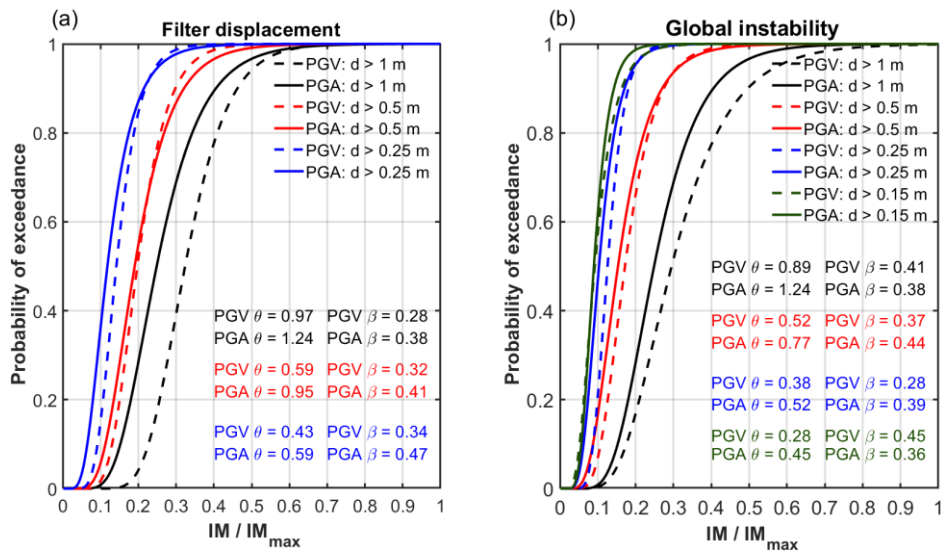


Figure 7.19: Comparison between fragility functions for PGA and PGV for (a) filter displacement; (b) global instability.

Table 7.7: Median and standard deviations of the Farneto del Principe dam fragility functions for the collapse limit state. *n.a.* means that no settlements greater than the freeboard were observed.

ULTIMATE LIMIT STATE CONDITION										
IM	Filters		Global instability		Free board reduction		Fell damage class 5		Normalized Crest Settlement	
	$\theta$	$\beta$	$\theta$	$\beta$	$\theta$	$\beta$	$\theta$	$\beta$	$\theta$	$\beta$
PGA [g]	1.24	0.38	1.28	0.38	2.67	0.57	1.35	0.46	0.94	0.31
AI [m/s]	26.33	0.68	22.97	0.64	n.a.	n.a.	31.96	0.67	8.93	0.48
PGV [m/s]	0.97	0.28	0.89	0.41	1.76	0.05	1.20	0.57	0.63	0.31

### 7.3 Analytical fragility functions for the Angitola dam

Dynamic analyses results for the Farneto del Principe dam provide information on the damage mechanisms that is most likely to happen for dams whose characteristics are similar to those of this dam (i.e., dams not susceptible to liquefaction). This section focuses on the calculation of fragility functions for the Angitola dam. This dam is founded on materials that are susceptible to liquefaction. Thus, fragility functions for the Angitola dam will capture deformation patterns and damage mechanisms that include liquefaction ground failure phenomena. Numerical analyses for this dam were performed using two different constitutive models: (1) MC, and (2) PM4Sand. The latter, as shown in Chapter 6, is able to faithfully describe sand-like material behavior during earthquakes, including excess pore pressure and liquefaction-related phenomena.

#### 7.3.1 Ground motions, intensity measures, and damage measures

Ground motions, IMs, and DMs for the Angitola dam were selected following the same procedures adopted for the Farneto del Principe dam. Table 7.8 shows ground motion characteristics for the selected time series for which results are shown in the remainder of this section. Main characteristics of all ground motions used in this Chapter are reported in Appendix A. For the Angitola dam, in addition to PGA, AI, and PGV, additional IMs were analyzed: the Cumulative Absolute Velocity (CAV) and the Cumulative Absolute Velocity above 5 cm/s<sup>2</sup> (CAV5; Kramer and Mitchell, 2006). These two additional IMs were selected as previous studies (e.g., Kramer and Mitchell, 2006; Khosravifar et al., 2014; Karimi and Dashti, 2017; Bray and Macedo, 2017; Armstrong et al., 2020) showed their ability in predicting liquefaction-related



damage. Table 7.9 shows the IM levels (and corresponding return periods) used in the MSA used to build all fragility functions shown in the remainder of this section.

Table 7.8: Summary of the subset of ground motions for which results are shown in this section.

Earthquake				Station			Intensity Measure	Recording ID
Name	Year	M	Style of faulting	Name	R <sub>jb</sub> [Km]	V <sub>s30</sub> [m/s]	PGA [g]	
Loma Prieta	1989	6.93	Reverse oblique	Gilroy Array #1	8.8	1428	0.42	1
Coyote Lake	1979	5.74	Strike slip	Gilroy Array #1	10.2	1428	0.12	2
N. Palm Springs	1986	6.06	Reverse oblique	Anza - Red Mountain	38.2	680	0.10	3
Whittier Narrows-01	1987	5.99	Reverse oblique	Mt Wilson - CIT Seis Sta	14.5	680	0.18	4
14095628	2004	5.03	Strike slip	Cattani Ranch	19.9	895	0.03	5
Northridge-01	1994	6.69	Reverse	Santa Susana Ground	1.7	715	0.29	6

Table 7.9: IMs adopted for the MSA of the Angitola dam.

Return period	PGA [g]	PGV [m/s]	AI [m/s]	CAV [m/s]	CAV <sub>s</sub> [m/s]
75	0.208	0.075	0.5	4	2
475	0.531	0.15	2	7.5	6
710	0.626	0.25	3	10	9
1460	0.820	0.4	4.25	13	12

An additional DM is also considered for the Angitola dam: the excess pore water pressure ratio  $r_u$  at the end of shaking:

$$r_u = \frac{\Delta u}{\sigma'_c} \quad (7.10)$$

where  $\Delta u$  is the excess pore water pressure that develops in the soil during shaking and  $\sigma'_c$  is the effective consolidation stress before shaking. This parameter describes the excess pore water pressures that can arise due to liquefaction. Thus, this is a liquefaction-related DM. Time series of  $r_u$  are calculated in four different zones of the model when performing the analyses with the PM4Sand constitutive model. Figure 7.20 shows these four locations within the dam body and foundation: (1) in the alluvial sand; (2) in the sandy layer, downstream; (3) in the pit zone of the sandy layer, where the pore pressure is higher; (4) in the sandy layer beneath the dam.

Four values of  $r_u$  are adopted to define the fragility functions, but in practice only the value equal to 100% is representative of the initiation of liquefaction. However, lower values of  $r_u$  are useful to appreciate shear strength reduction during shaking as a result of excess pore pressure generation mechanisms. The Fell damage classes for the Angitola dam are reported in Table 7.10.

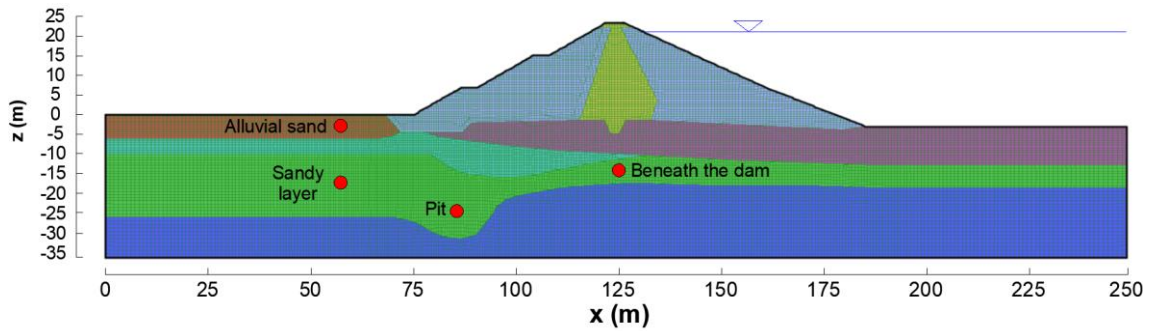


Figure 7.20: Locations of the Angitola dam where the excess pore water pressure ratio is calculated.

Table 7.10: Fell damage classes for the Angitola dam.

Damage Class		Maximum longitudinal crack width [mm]	Maximum relative crest settlement [cm]
Number	Description		
0	None or slight	$< 10$	$\leq 0.8$
1	Minor	$10 < w \leq 30$	$0.8 < d \leq 5.4$
2	Moderate	$30 < w \leq 80$	$5.4 < d \leq 13.5$
3	Major	$80 < w \leq 150$	$13.5 < d \leq 40.5$
4	Severe	$150 < w \leq 500$	$40.5 < d \leq 135$
5	Collapse	$> 500$	$> 135$

### 7.3.2 Numerical results and between-constitutive models differences

The numerical results of the MSA performed on the Angitola dam with two different constitutive models are analyzed. In the remainder of this Chapter, the terms “MC dam model” and “PM4Sand dam model” will be used. The former refers to MSA performed with all materials modelled with a Mohr-Coulomb model (except for the rock foundation that is modelled as an elastic material), while the latter refers to MSA performed using the PM4Sand model for all sandy soil layers. In general, the two constitutive models provide different results for long-return period motions. Figures 7.21-7.23 show  $ssi$ , horizontal, and vertical displacements for time series ID1 (return period of 1460 years). For this motion, there are some differences in the volume of soil influenced by the dynamic action. In particular, the downstream shell

displacements of the PM4Sand dam model often differs from those of the MC, the latter being slightly bigger, and comprising a portion of the foundation layers as well. This is due to the deformations and excess pore water pressures that take place in the foundation layers, which results in a smaller failure mechanism in the PM4sand dam model. Thus, in the MC dam model, the global instability and failure mechanism is larger. Figure 7.21 shows that the shear strains are greater at the interface of the alluvial sand and old alluvium, where the stiffness contrast is more important; these effects are less pronounced in the MC dam model. The two models provide comparable results when the seismic input is not intense (i.e. ground motions for short return periods - 75 and 475 years). This is expected because, for these relatively-low ground motion levels, soil nonlinearity and excess pore water pressure generation phenomena are not relevant. As an example of this, Figure 7.24-7.26 show comparable  $ss_i$ , horizontal, and vertical displacement patterns and spatial distributions for a short-return period motion (time series ID5). Analyzing deformation patterns, two general failures mechanisms can be identified: sliding of the upstream shell, and overall sliding and deformation in the downstream shell and foundation system. This complexity in the predicted deformation patterns are evident looking at the excess pore water pressure ratio  $r_u$  time series (Figure 7.27). These time series are different in different zones of the model, generating a variable pattern of pore pressure-induced shear strength reduction

For of the ground motions, excess pore water pressures are close to liquefaction conditions only in the pit zone, which is expected since the static pore water pressures are greater in this area. In addition, the calibration process performed in Chapter 6, showed that most of the cyclic behavior of sandy materials of the Angitola dam would be dilative, which explain the relative low values of  $r_u$  in the alluvial sand layer. The  $r_u$  is extremely sensitive to the various ground motion properties, not only peak amplitude values. This means that even a relatively weak motion can produce high  $r_u$  values Figure 7.28 shows the  $r_u$  trends with the CAV5 for a set of ground motions scaled at constant value of PGV. It can be seen that only the  $r_u$  in the pit zone and alluvial sand resemble a monotonic trend, while trends in the other control zones are rather erratic.

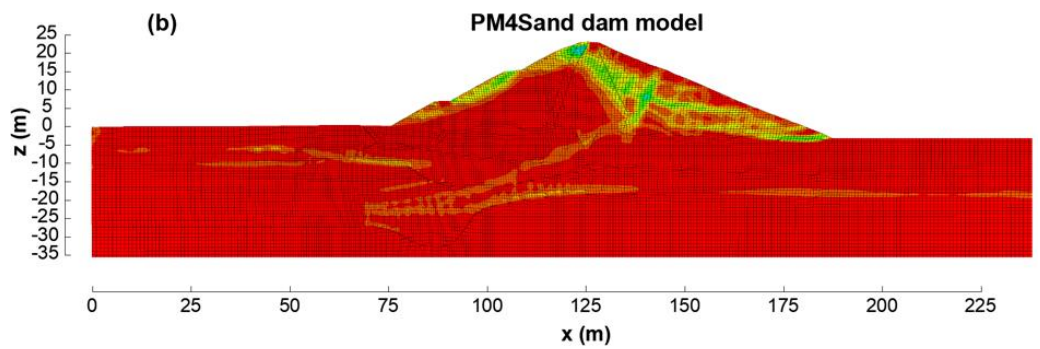
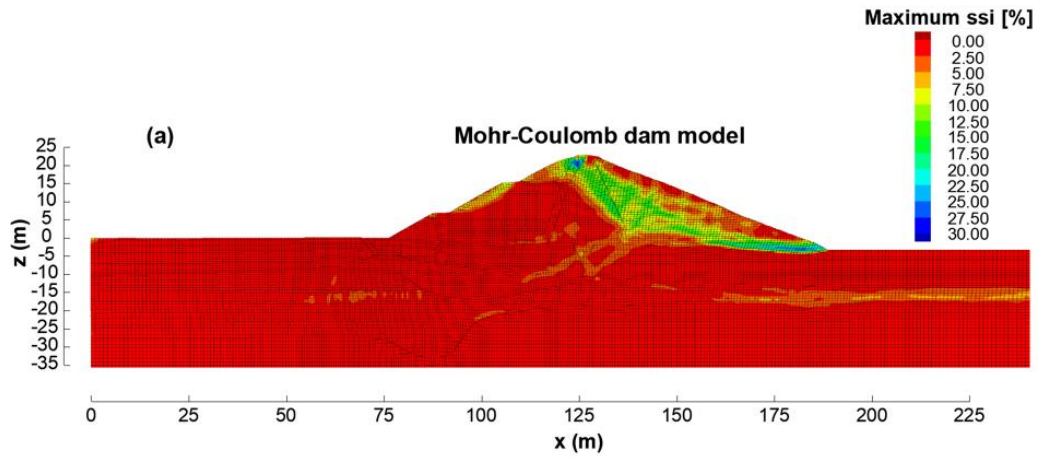


Figure 7.21: Contours of ssi for time series ID1 (return period of 1460 years).

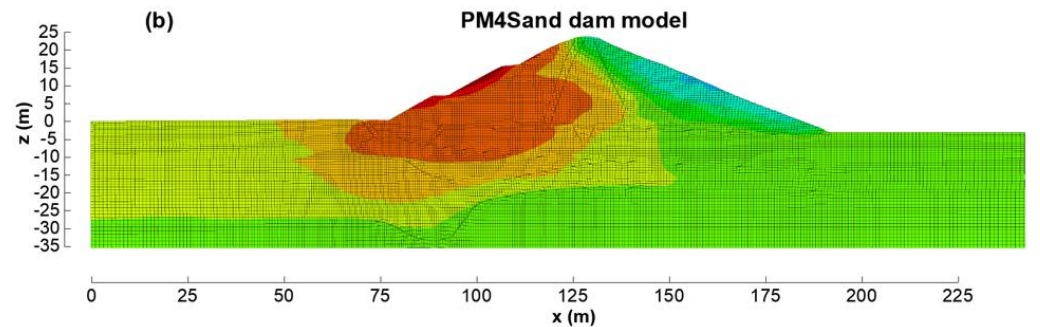
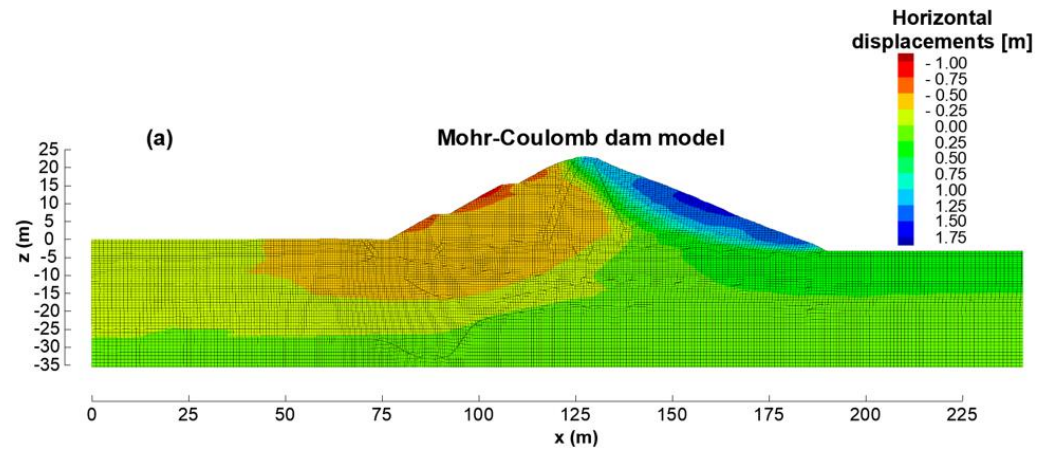


Figure 7.22: Contours of the horizontal displacements for time series ID1 (return period of 1460 years).

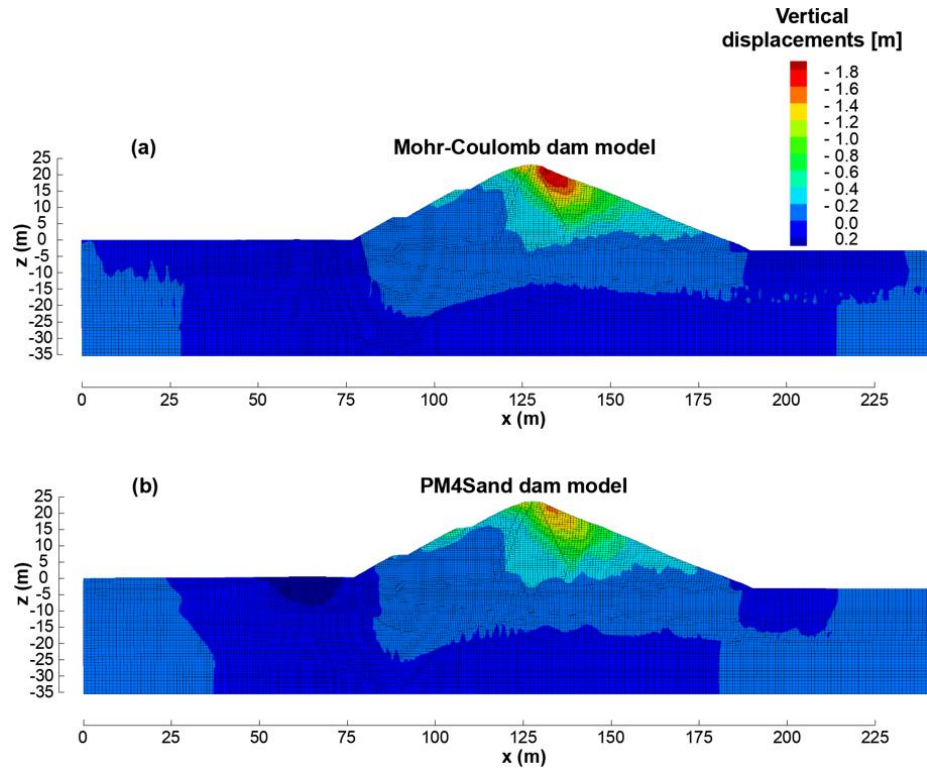


Figure 7.23: Contours of the vertical displacements for time series ID1 (return period of 1460 years).

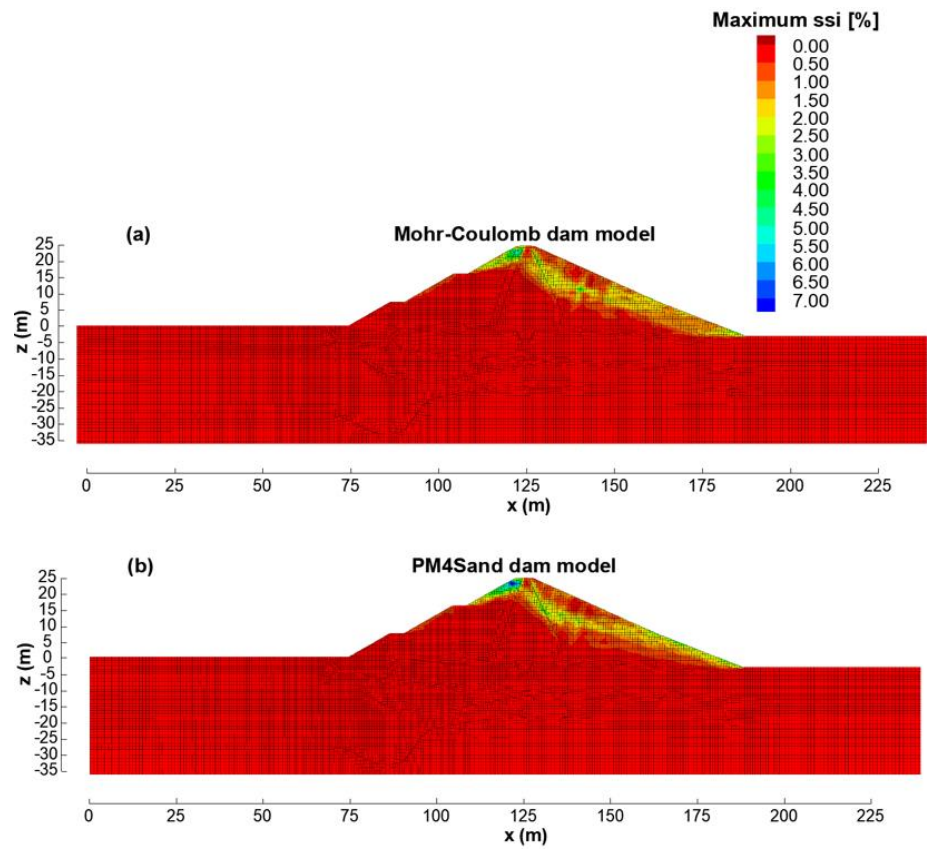


Figure 7.24: Contours of ssi for time series ID5 (return period of 75 years).



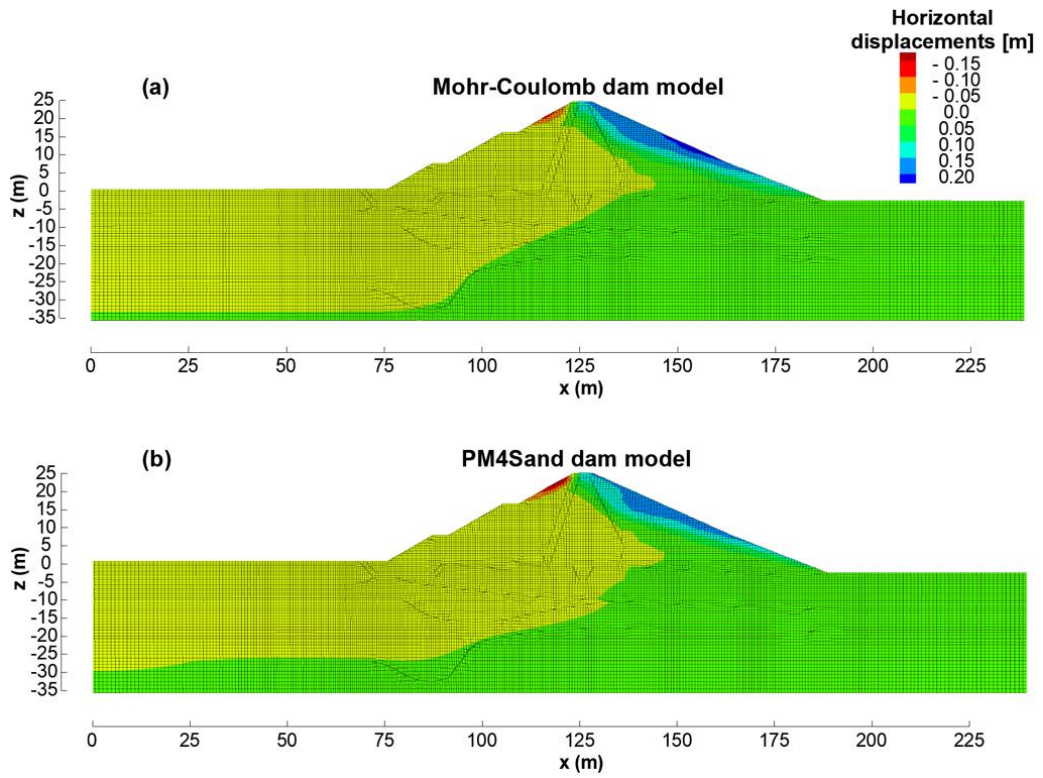


Figure 7.25: Contours of the horizontal displacements for time series ID5 (return period of 75 years).

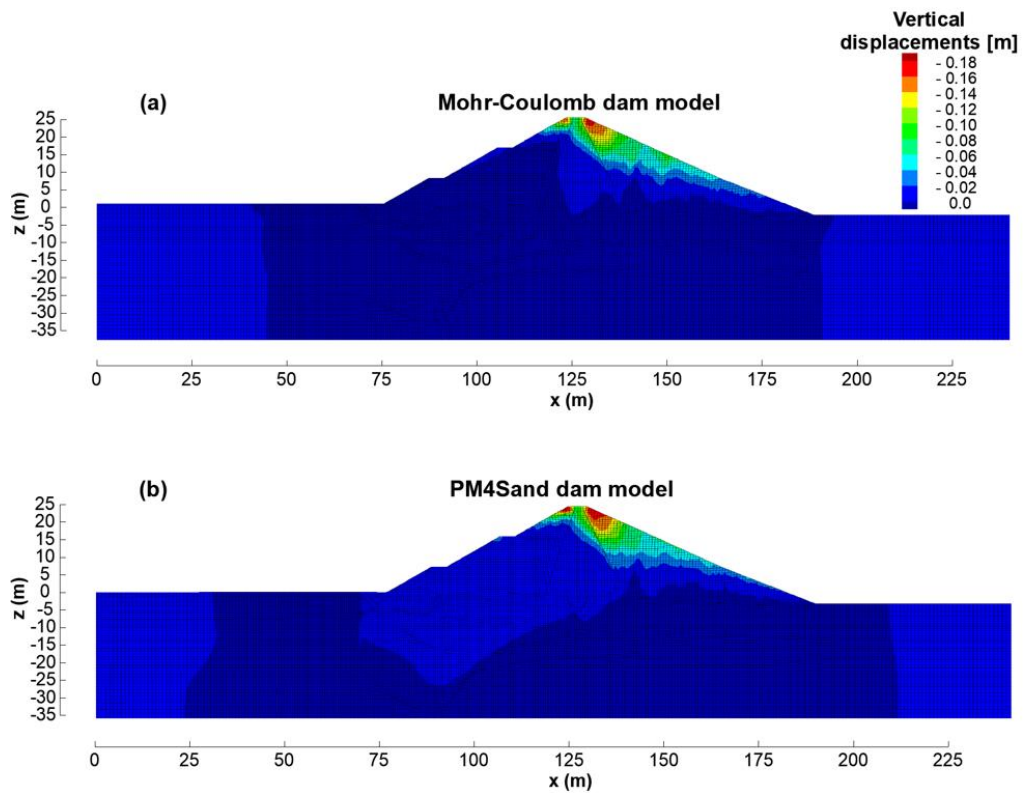


Figure 7.26: Contours of the vertical displacements for time series ID5 (return period of 75 years).

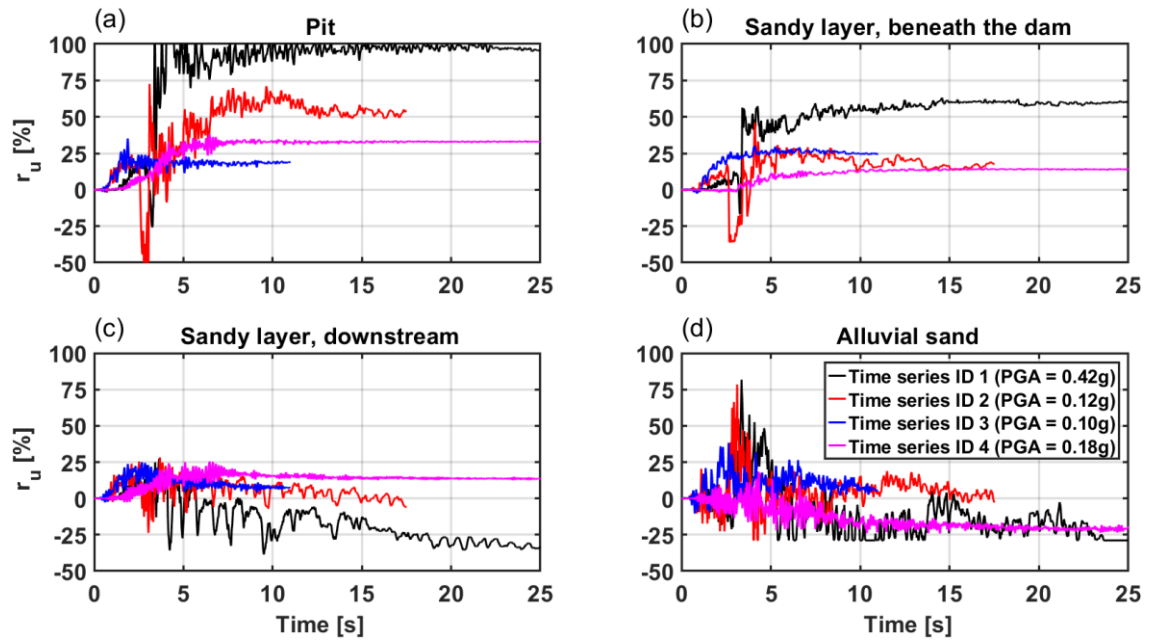


Figure 7.27: Excess pore water pressure ratio  $r_u$  time series for ground motions scales at the same PGA value, in four different zones of the model: (a) Pit, (b) sandy layer beneath the dam, sandy layer downstream, and alluvial sand.

This effect is due to the dilative behavior of the soil, which implies that a stronger ground motion does not necessarily result in positive and monotonic excess pore water pressure values (i.e., the volume of the zone has a tendency to expand instead of contracting). As explained later in §7.3.3, this has some consequences when trying to fit fragility functions.

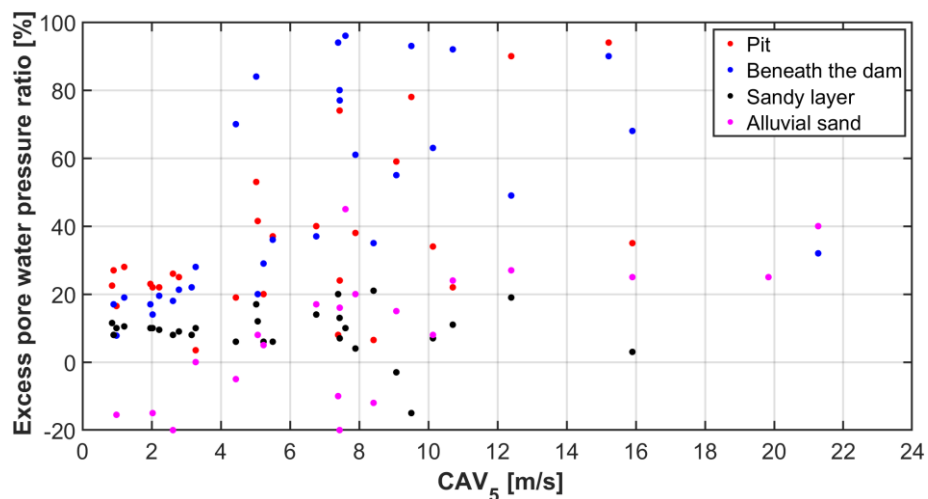


Figure 7.28: Variation of the excess pore water pressure ratio  $r_u$  in the pit, beneath the dam, in the sandy layer in free condition, and in the alluvial sand layer. The results refer to the set of ground motions scaled at a constant value of PGV.

The results of the PM4Sand dam model are also consistent with the stress-strain response obtained in the calibration procedure. Figure 7.29 shows the  $\tau$ - $\gamma$  plots in the four control zones where  $r_u$  is calculated, for time series ID6. The effect of the static shear bias can be seen in the progressive accumulation of shear strains in one direction. Overall, the PM4Sand model managed to represent well the dynamic behavior of the sandy layers in the Angitola dam foundation. However, due to the moderate deformation level (i.e., only few ground motions reached a  $r_u$  value of one, and only in some zones), the overall results are similar to those of the MC dam model. Nonetheless, the information acquired with the use of the PM4Sand model are quite useful to better understand details of the seismic response of earth dams similar to the Angitola dam (more detail are in § 7.3.4).

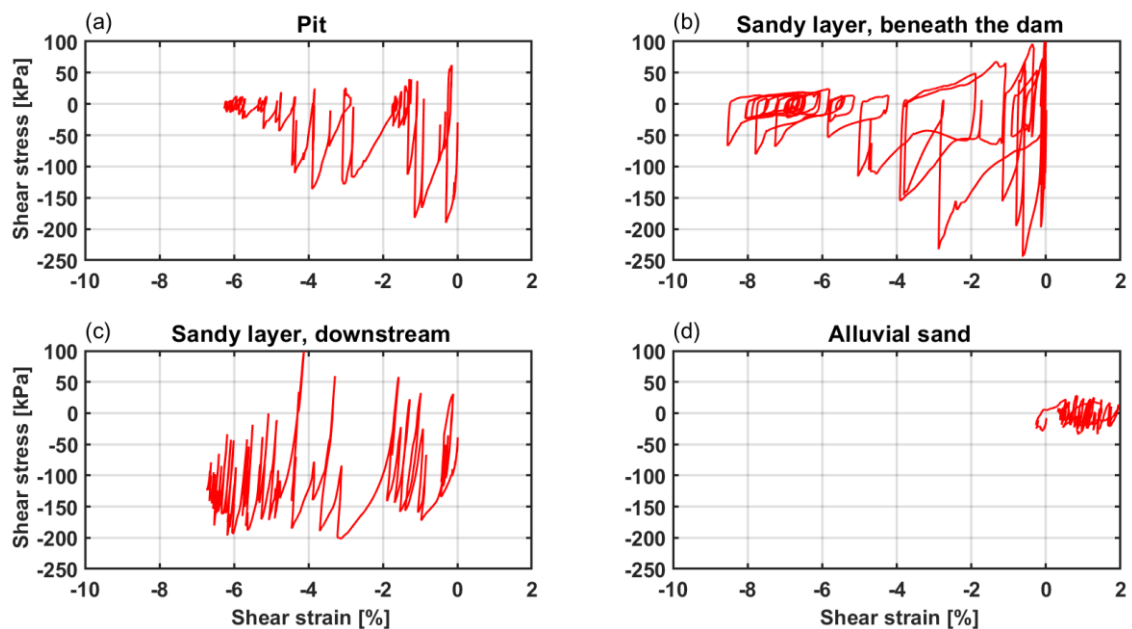


Figure 7.29: Shear stress vs shear strain showing the effects of the static shear stress ratio for time series ID6 at the following control zones: (a) pit, (b) sandy layer beneath the dam, (c) sandy layer downstream, and (d) alluvial sand.

### 7.3.3 Computed fragility functions

In this section, fragility functions evaluated for the Angitola dam are presented. Figure 7.30-7.34 show the results obtained for the MC dam model for several IMs, while There are consistent trends between fragility functions for different IMs. Most of them similar to those observed for the Farneto del Principe dam (§7.2.3). Overall, there are increasing fractions of exceeding DMs with increasing IM values. However,



some apparent numerical inconsistencies are present. For instance, for the free board reduction fragility function for PGV, the settlement greater than 100% curve (i.e., black curve in Figure 7.31) overlaps with the red curve at around 80% (i.e., settlement > 65%). This seems counterintuitive at first, but it is the result of the ground motion variabilities, that is, the set of ground motions used at the return periods adopted are not the same. Hence, a more intense ground motion can produce smaller effects of a lower intensity ground motion, but with particular characteristics. In general, long duration and high energy content ground motions resulted in higher damage. More detail about the relationships between ground motion intensity measure and observed damage for the Angitola dam are given in §7.4.

The CAV and CAV5 fragility functions are quite similar, as expected. For these two IMs the scale factors of the ground motions were very similar. The AI produces fragility functions with relatively high  $\beta$  values. Interestingly, this was not the case for the Farneto del Principe dam. This effect may be related to the chosen range of AI adopted. For the Angitola dam, a narrow AI range was sufficient to capture the observed damage from the PGA analyses. Thus resulting in less scattered fragility functions. A wider range of the IM influences the fragility function estimation, resulting in higher standard deviation values. More precisely, since the ground motions are all scaled linearly in the time domain, the scale factor (SF) strongly influences the overall fit. The mean scale factors adopted are summarized in Table 7.11. The lowest SF correspond to PGA and PGV, which are the best-fitted fragility functions. Table 7.12 shows the PGA values contributing the most to the rate of collapse of the Angitola dam. As expected, these values are pretty high for almost all DMs. The DMs for which PGAs are relatively low are based, as explained above, on observations made at dams prone to liquefaction.

*Table 7.11: Mean scale factors of the ground motions for the Intensity Measures used.*

<b>Intensity Measure</b>	<b>Mean scale factor</b>
PGA	3.81
PGV	3.34
AI	4.42
CAV	4
CAV <sub>5</sub>	4.33

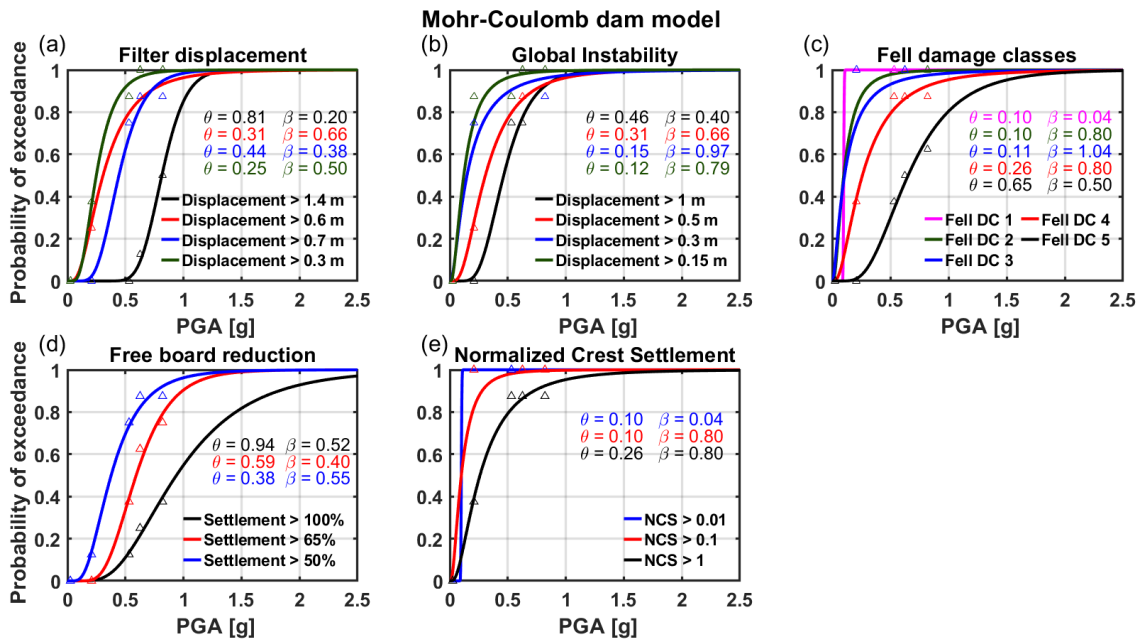


Figure 7.30: Fragility functions for the Angitola dam using the PGA as Intensity Measure (Mohr-Coulomb dam model).

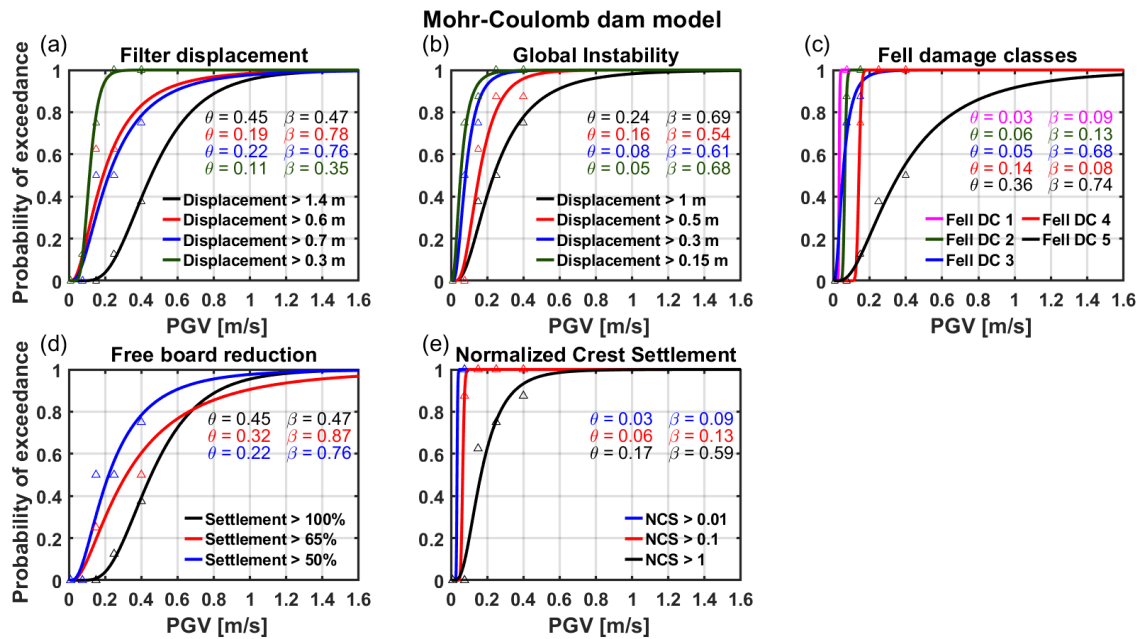


Figure 7.31: Fragility functions for the Angitola dam using the PGV as Intensity Measure (Mohr-Coulomb dam model).

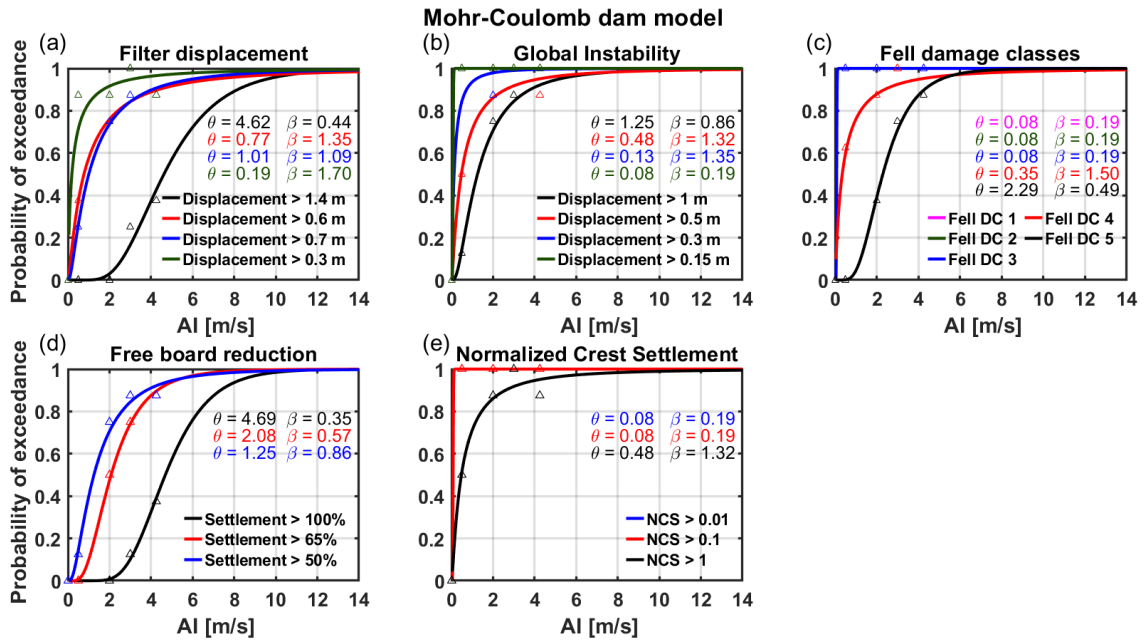


Figure 7.32: Fragility functions for the Angitola dam using the AI as Intensity Measure (Mohr-Coulomb dam model).

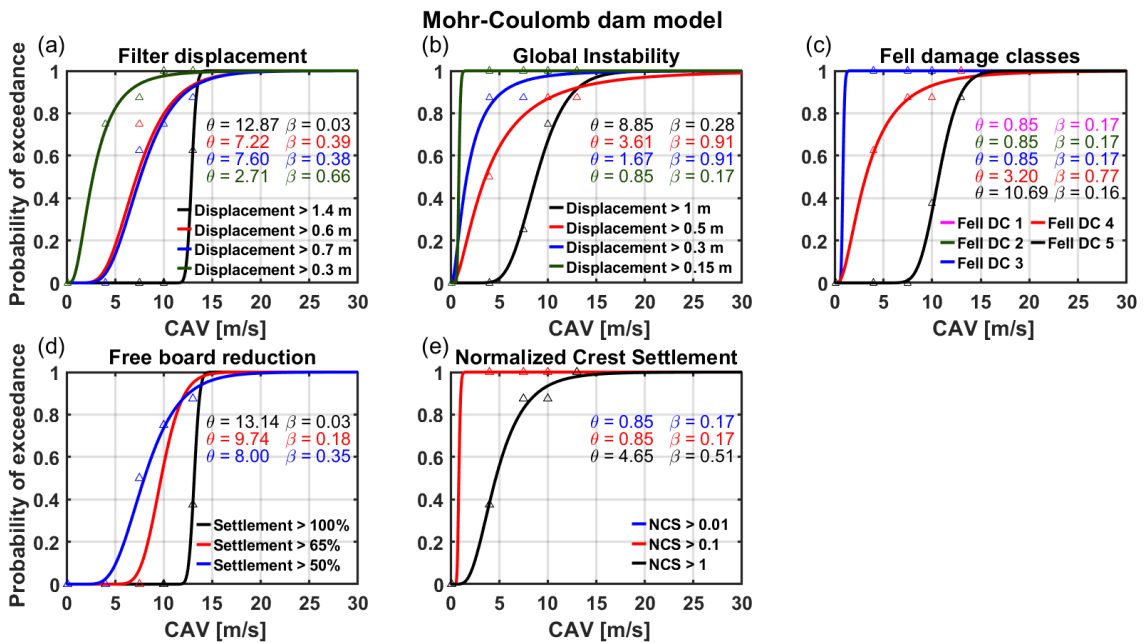


Figure 7.33: Fragility functions for the Angitola dam using the CAV as Intensity Measure (Mohr-Coulomb dam model).

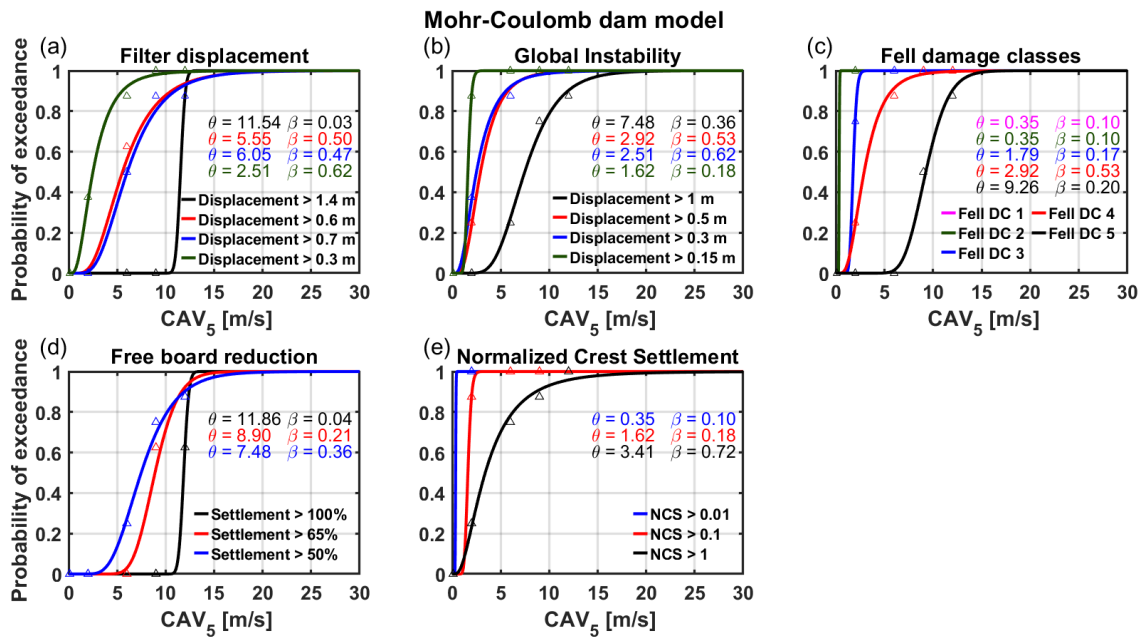


Figure 7.34: Fragility functions for the Angitola dam using the  $CAV_5$  as Intensity Measure (Mohr-Coulomb dam model).

Table 7.12: PGA values contributing the most contribute to the collapse of the Angitola dam.

Damage mechanism	PGA that most contribute to the rate of collapse [g]	
	MC dam model	PM4Sand dam model
Filters	0.834	0.866
Global instability	0.394	0.221
Free board reduction	0.551	0.866
Fell damage class 5	0.439	0.371
Normalized Crest Settlement	0.123	0.123

Collapse disaggregation results for both constitutive models are shown in Figure 7.35. Since the hazard curves for PGA are the same, the differences in the disaggregation are only due to differences in the fragility functions. For the filters, the PGAs that most contribute to collapse are almost the same. For the free board reduction, the PM4Sand dam model curve is shifted to the right, which is reflected in a lower probability of collapse for the same IM value. For global instability and Fell DC, the differences are not negligible. In general, the contribution to collapse is large when both the fragility function and hazard curve are high (Eq. 7.9). The hazard curve has large values only in the first part (i.e. low IM values) while fragility

function values depend on the median and standard deviation. If the median is high (i.e. fragility function is shifted to the right), then those values will multiply low annual frequency rates in the hazard curve, leading to low disaggregation values.

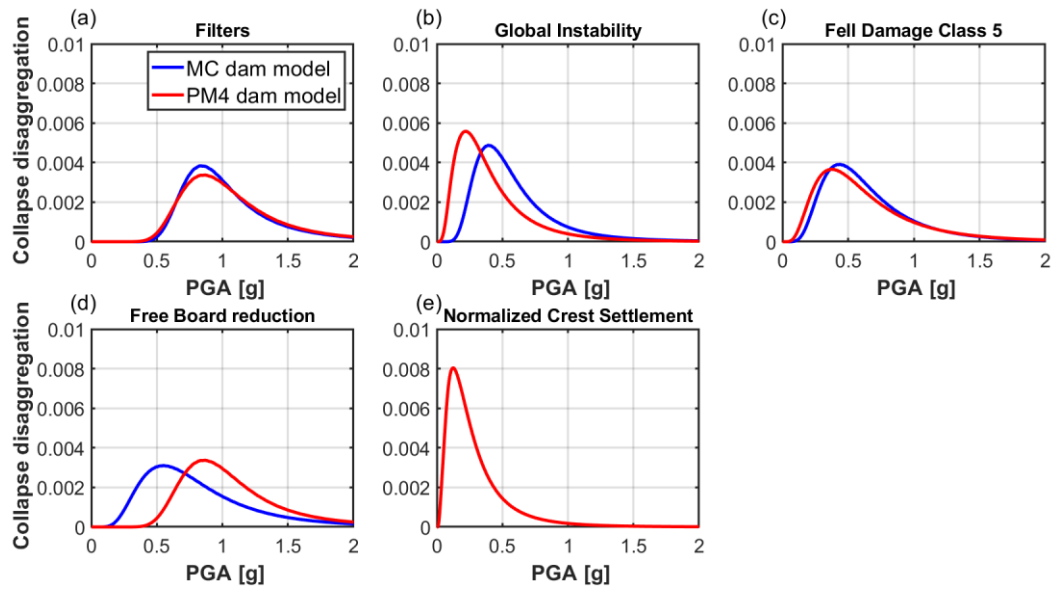


Figure 7.35: Collapse disaggregation for the Angitola dam for the Mohr-Coulomb dam model and the PM4Sand dam model.

The results obtained from the PM4Sand dam model are shown in Figures 7.36-7.40. Table 7.13 summarizes median and standard deviation values of the fitted fragility functions for all collapse limit state. For the PM4Sand dam model, fragility functions related to excess pore water pressure ratio values are also calculated. As reported in §7.3.1, four values of the  $r_u$  are adopted to define the fragility functions (i.e. 95%, 75%, 50%, and 30%). However, for some of these values it was not possible to build fragility functions. For instance, the  $r_u$  in the alluvial sand never exceeds 50%, and in the sandy layer it never exceeds 30%, even for intense ground motions. Therefore, it is not possible to build such fragility functions.

As shown in Figures 7.30-7.34, 7.36-7.40 and Table 13, CAV and CAV<sub>5</sub> produce the lowest values of  $\beta$  for both constitutive models. PGA and PGV values generally produce relatively low  $\beta$  values for all considered DMs, with PGA almost persistently producing lower  $\beta$  values than PGV. Overall, AI produces the highest  $\beta$  values.

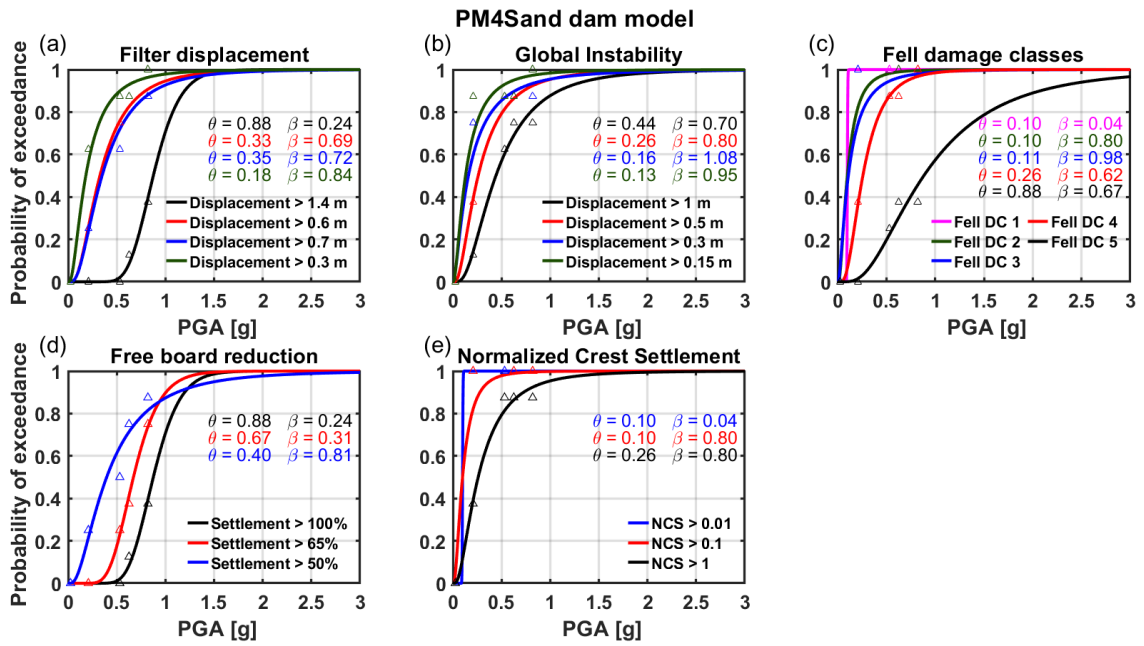


Figure 7.36: Fragility functions for the Angitola dam using the PGA as Intensity Measure (PM4Sand dam model).

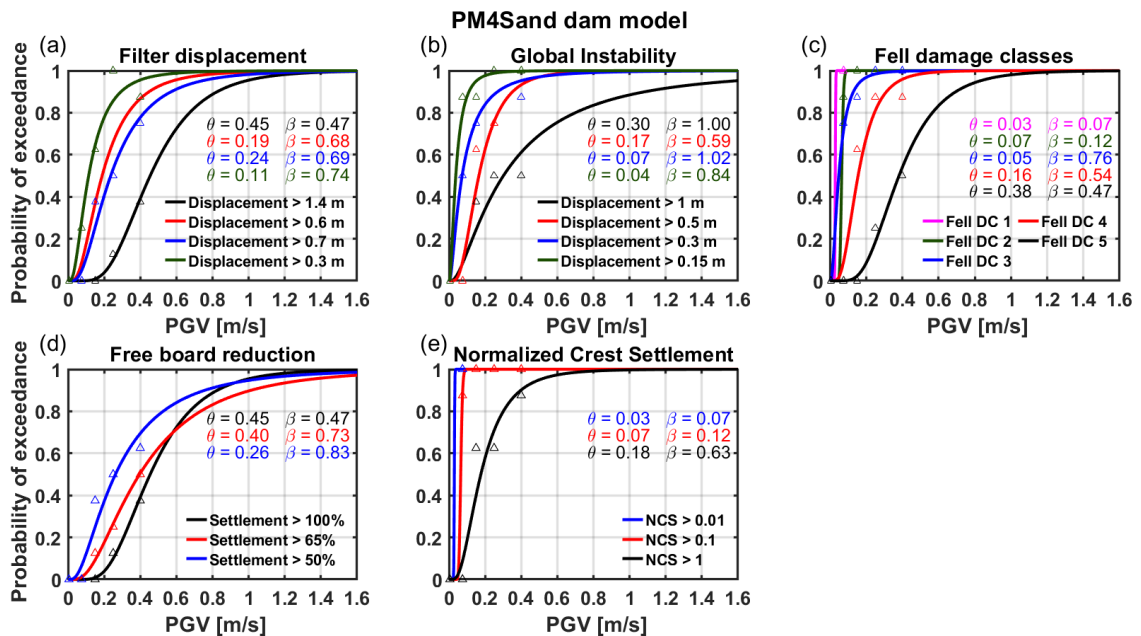


Figure 7.37: Fragility functions for the Angitola dam using the PGV as Intensity Measure (PM4Sand dam model).

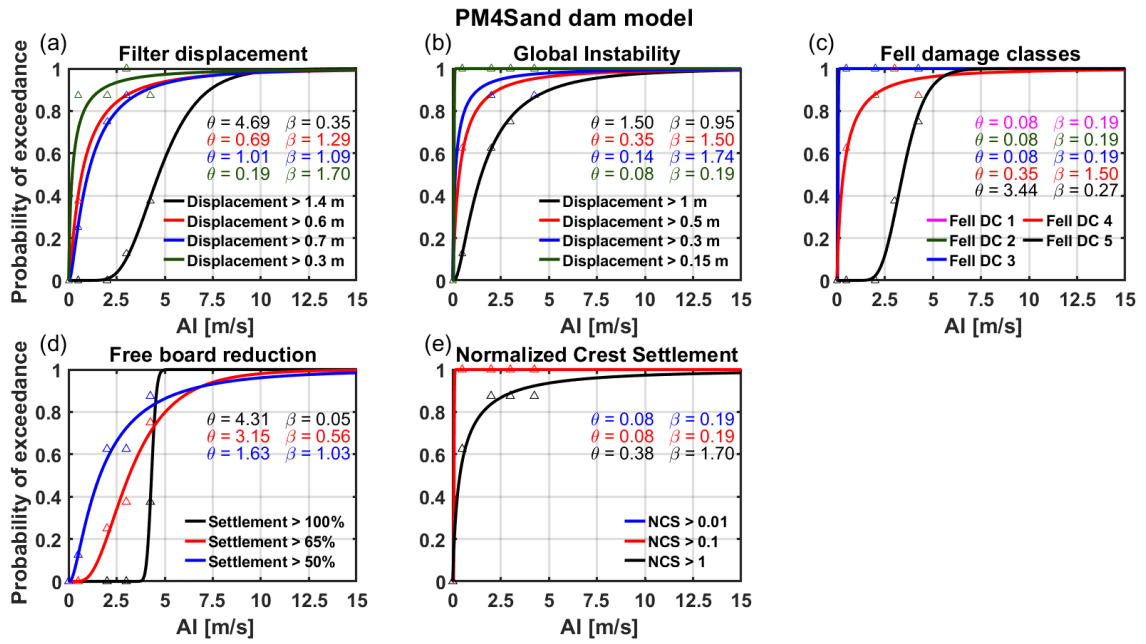


Figure 7.38: Fragility functions for the Angitola dam using the AI as Intensity Measure (PM4Sand dam model).

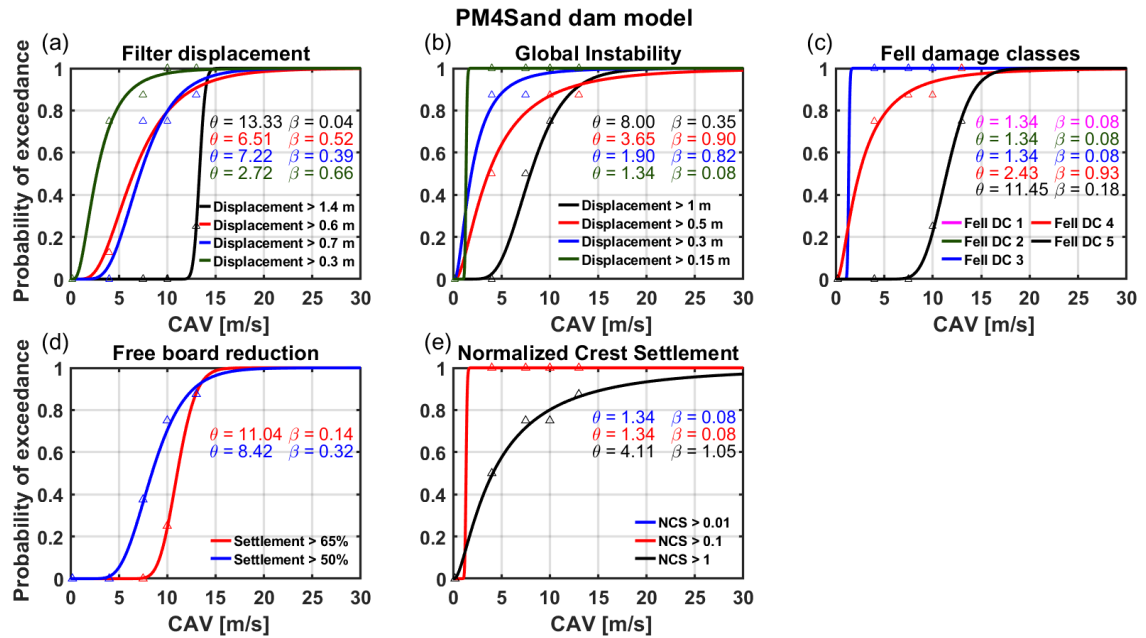


Figure 7.39: Fragility functions for the Angitola dam using the CAV as Intensity Measure (PM4Sand dam model).



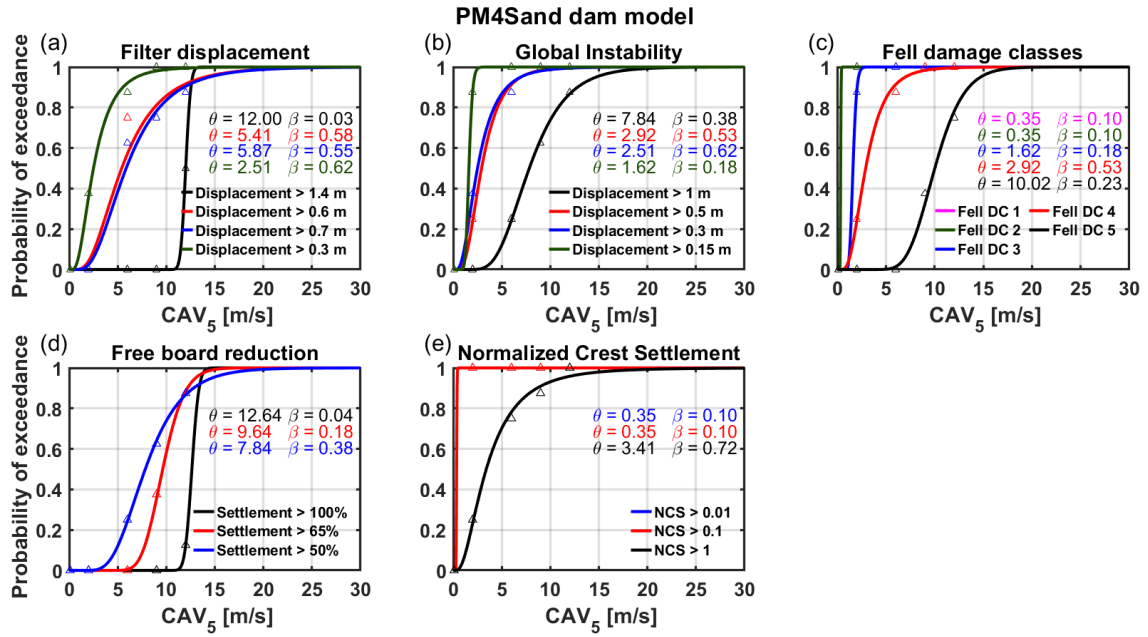


Figure 7.40: Fragility functions for the Angitola dam using the  $CAV_5$ s as Intensity Measure (PM4Sand dam model).

Table 7.13 Comparison between median and standard deviation values of the fragility functions for the MC dam model and PM4Sand dam model, for all considered collapse limit state (n.a. means that no exceedances were observed).

Collapse Limit State, Mohr-Coulomb dam model										
IM	Filters		Global instability		Free board reduction		Fell damage class 5		Normalized Crest Settlement	
	$\theta$	$\beta$	$\theta$	$\beta$	$\theta$	$\beta$	$\theta$	$\beta$	$\theta$	$\beta$
PGA [g]	0.81	0.20	0.46	0.40	0.94	0.52	0.65	0.50	0.26	0.80
AI [m/s]	4.62	0.44	1.25	0.86	4.69	0.35	2.29	0.49	0.51	1.52
PGV [m/s]	0.46	0.47	0.24	0.69	0.45	0.47	0.36	0.74	0.17	0.59
CAV [m/s]	12.87	0.03	8.85	0.28	13.14	0.03	10.69	0.16	4.75	0.61
$CAV_5$ [m/s]	11.54	0.03	7.48	0.36	11.86	0.04	9.26	0.20	3.62	0.83
Collapse Limit State, PM4Sand dam model										
IM	Filters		Global instability		Free board reduction		Fell damage class 5		Normalized Crest Settlement	
	$\theta$	$\beta$	$\theta$	$\beta$	$\theta$	$\beta$	$\theta$	$\beta$	$\theta$	$\beta$
PGA [g]	0.88	0.24	0.44	0.70	0.88	0.24	0.88	0.67	0.26	0.80
AI [m/s]	4.69	0.35	1.50	0.95	4.31	0.05	3.44	0.27	0.38	1.70
PGV [m/s]	0.45	0.47	0.30	1.00	0.45	0.47	0.38	0.47	0.18	0.63
CAV [m/s]	13.33	0.04	8.00	0.35	n.a.	n.a.	11.45	0.18	4.11	1.05
$CAV_5$ [m/s]	12.00	0.03	7.84	0.38	12.64	0.04	10.02	0.23	3.41	0.72



Figure 7.41 shows results of the MSA performed to build the  $r_u$ -based fragility functions. Figures 7.42-7.46 show fragility functions for  $r_u$  as DMs (this DM was not considered for the Farneto del Principe dam as it is related to liquefaction phenomena). The number of occurrences when  $r_u$  is  $> 0$  does not increase as IMs increase. As explained in §7.3.2, this is related to the dilative behavior of the sandy layers, which result in the development of negative pore pressure. This implies that only where positive excess pore pressure is observed (i.e., contractive behavior) fragility functions show good trends. The pit zone is the only case where there is a good fit of the fragility function, which is due to the fact that the material located in this area has a contractive behavior. This is confirmed by the low  $\beta$  value for this fragility function.

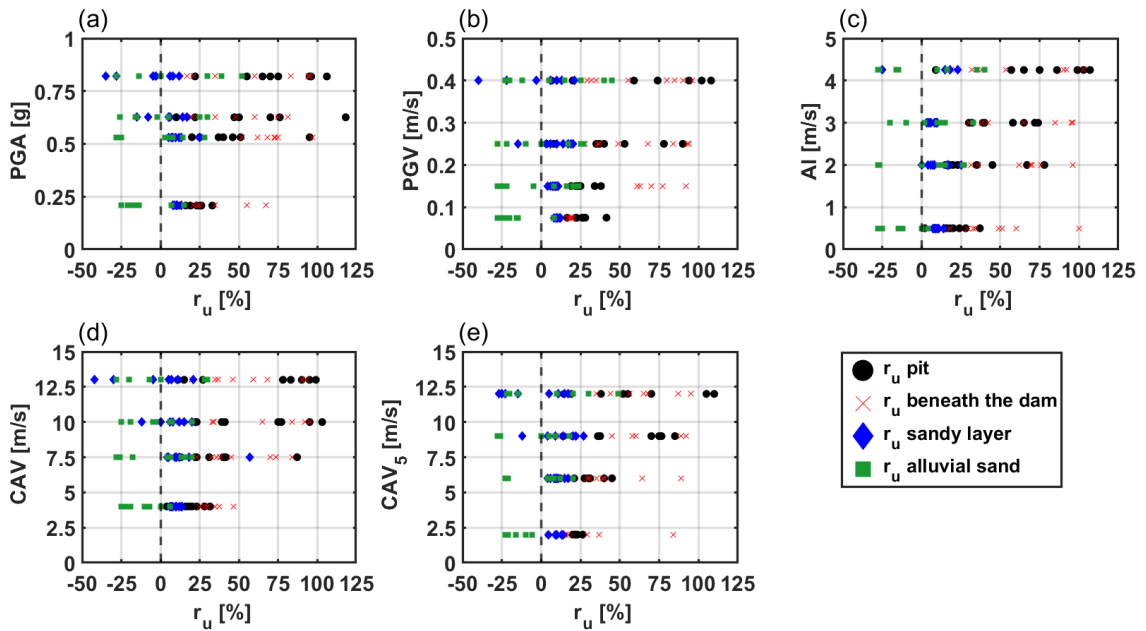


Figure 7.41: Variation of the excess pore water pressure ratio for the five IM adopted.

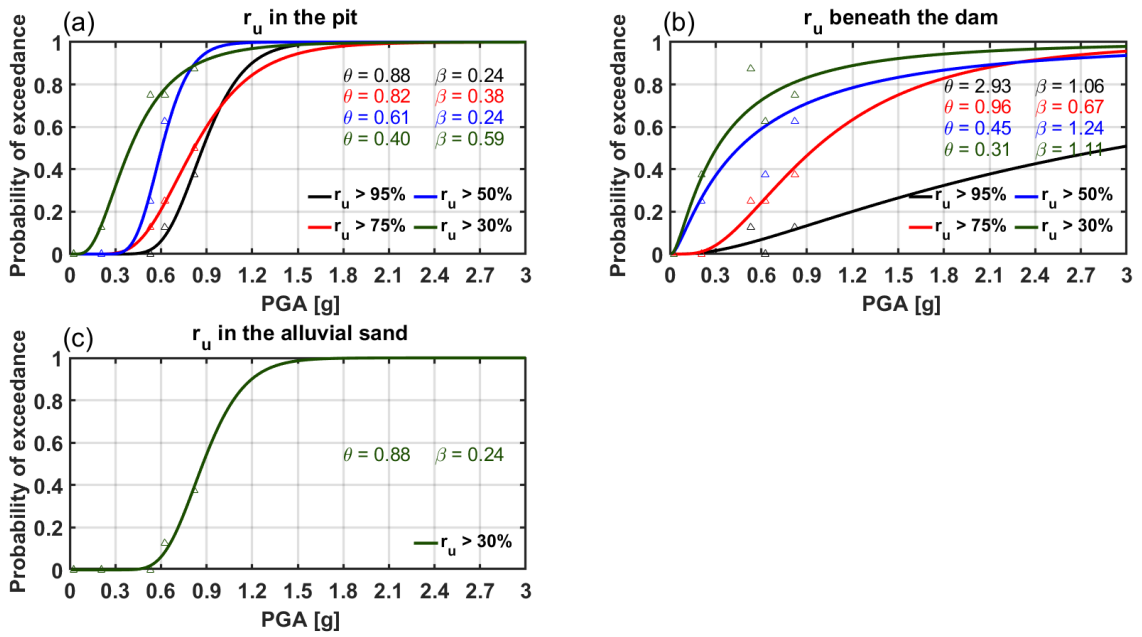


Figure 7.42: Fragility functions for the excess pore water pressure ratio  $r_u$  for the Angitola dam using PGA as Intensity Measure.

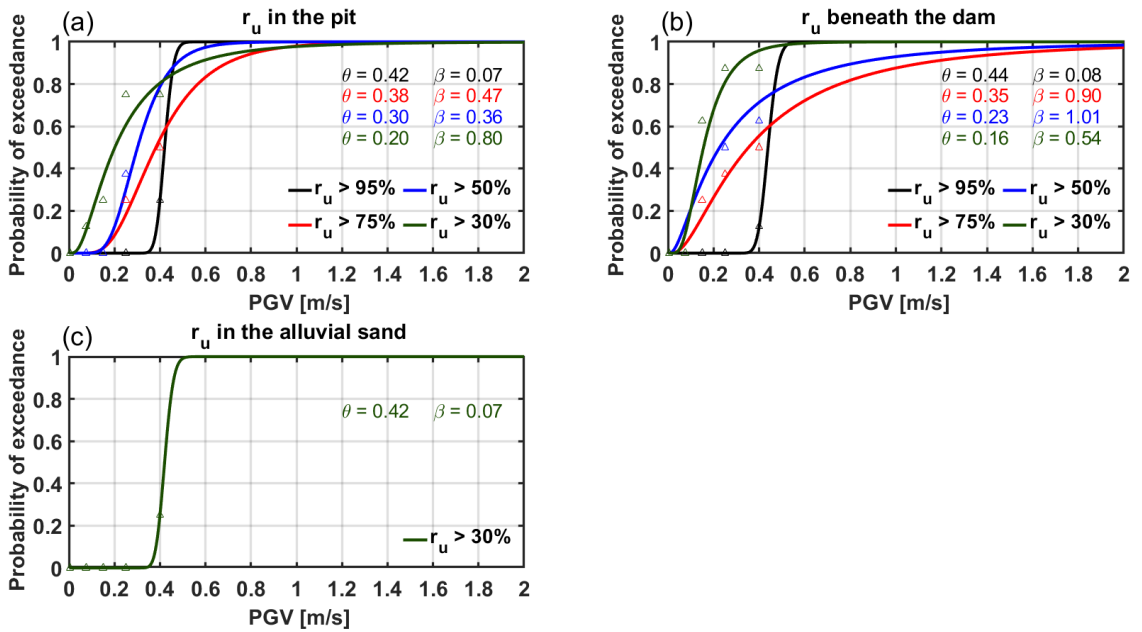


Figure 7.43: Fragility functions for the excess pore water pressure ratio  $r_u$  for the Angitola dam using PGV as Intensity Measure.

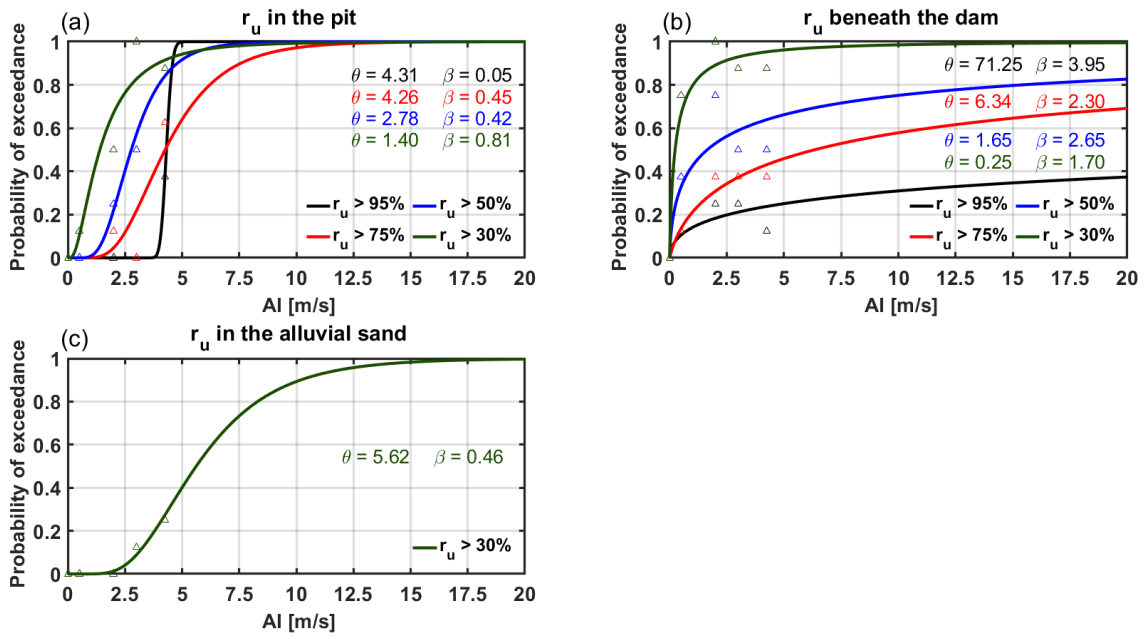


Figure 7.44: Fragility functions for the excess pore water pressure ratio  $r_u$  for the Angitola dam using AI as Intensity Measure.

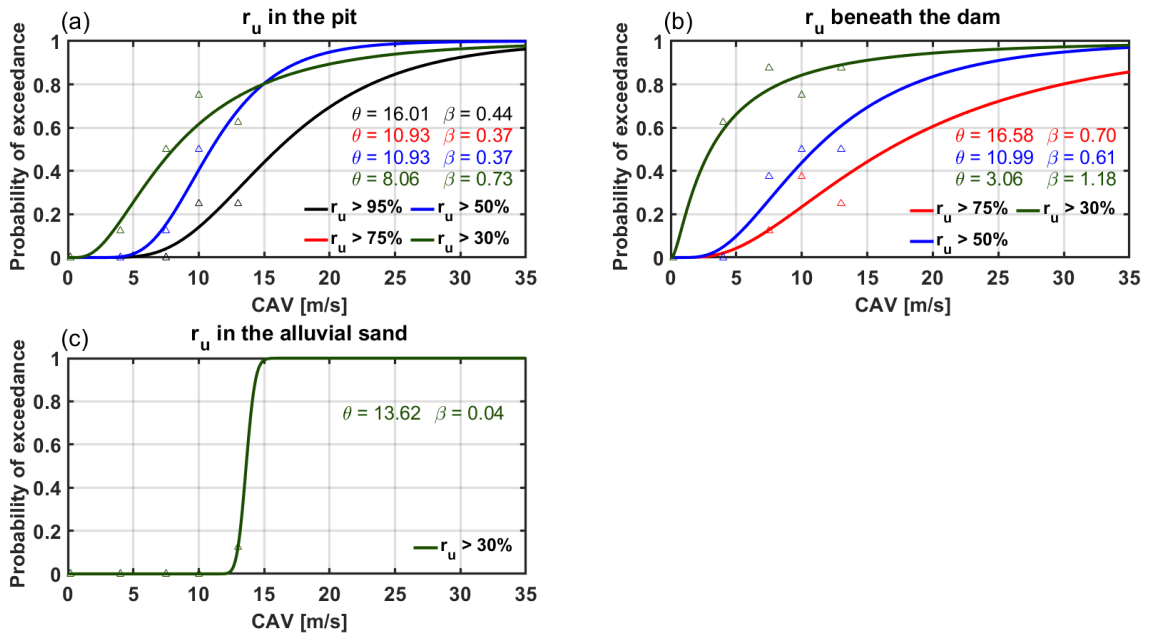


Figure 7.45: Fragility functions for the excess pore water pressure ratio  $r_u$  for the Angitola dam using CAV as Intensity Measure.

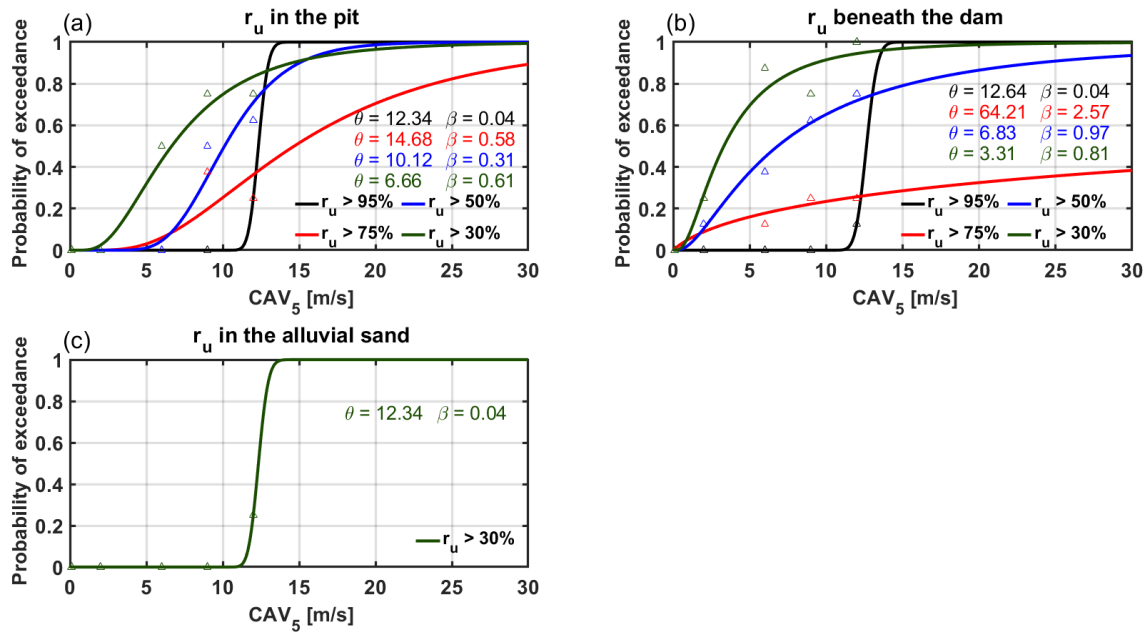


Figure 7.46: Fragility functions for the excess pore water pressure ratio  $r_u$  for the Angitola dam using  $CAV_5$  as Intensity Measure.

#### 7.3.3.4. Comparison between different IMs and limit states

Using the results shown in the previous section, it is possible to estimate the damage state that is most likely to be exceeded for the Angitola dam. Figure 7.47 shows the comparison between fragility functions for all analyzed IMs and DMs, for the Mohr-Coulomb dam model and the PM4Sand dam model. There seems to be some variability in the fragility functions shape, but some consistent trends can be identified. The damage state most likely to be exceeded is the NCS (Swaisgood methodology), followed by the global instability DM. The filters damage, free board reduction, and  $r_u$  fragility functions have different shapes for different IMs. For PGA (Figure 7.47a) the probability of exceedances are essentially the same for all three DMs. However, for PGV and AI (Figure 7.47b-c) they are quite different. Beyond a certain IM level, the  $r_u$  being greater than 95% in the pit is more likely to happen than other damage mechanisms, which is a result of the low standard deviation of its fragility function. The most important damage mechanism, however, also depends on the damage threshold used to define the fragility functions. For instance, if the filters thicknesses are different, the fragility function of the displacement of the thinnest will be shifted to the left (Figure 7.47 refers to the filter displacement being greater than 1.4 m, which is the thickness of the external filter). In addition, a  $r_u$  greater than 95% (and in general the onset of liquefaction) does not necessarily

imply collapse or extensive damage. For the Angitola dam, only the bottom part of the pit zone (which is around 20 m away from the dam body) suffers from liquefaction initiation, but not extensive deformations, as explained in § 7.3.2. Nonetheless, it seems clear that the standard deviation of the  $r_u$  fragility function is the lowest (less than 0.1 for all IM except PGA).

Figure 7.48 shows a comparison between fragility functions for the two models at the collapse limit state. Fragility functions for the filters are quite similar for both models, while fragility functions for the other DMs show some differences. As described in § 7.3.2, the dam body is modelled as a Mohr-Coulomb material in both models. Hence, at a certain IM level the filters will suffer similar displacements in both cases. For lower DM thresholds, the sandy layers modelled with PM4Sand and Mohr-Coulomb give the same results in terms of displacements and strain patterns. This is related to the fact that at lower strain levels, excess pore pressure phenomena are not as important as when strain levels (and thus excess pore pressures) are high. Figure 7.49 shows the fragility functions for DMs at lower thresholds than those used in the collapse states. In these cases, curves are similar with curves for the PM4Sand model being more fragile (as expected since excess pore pressures have effects on shear strength values also at relatively low  $r_u$  values).

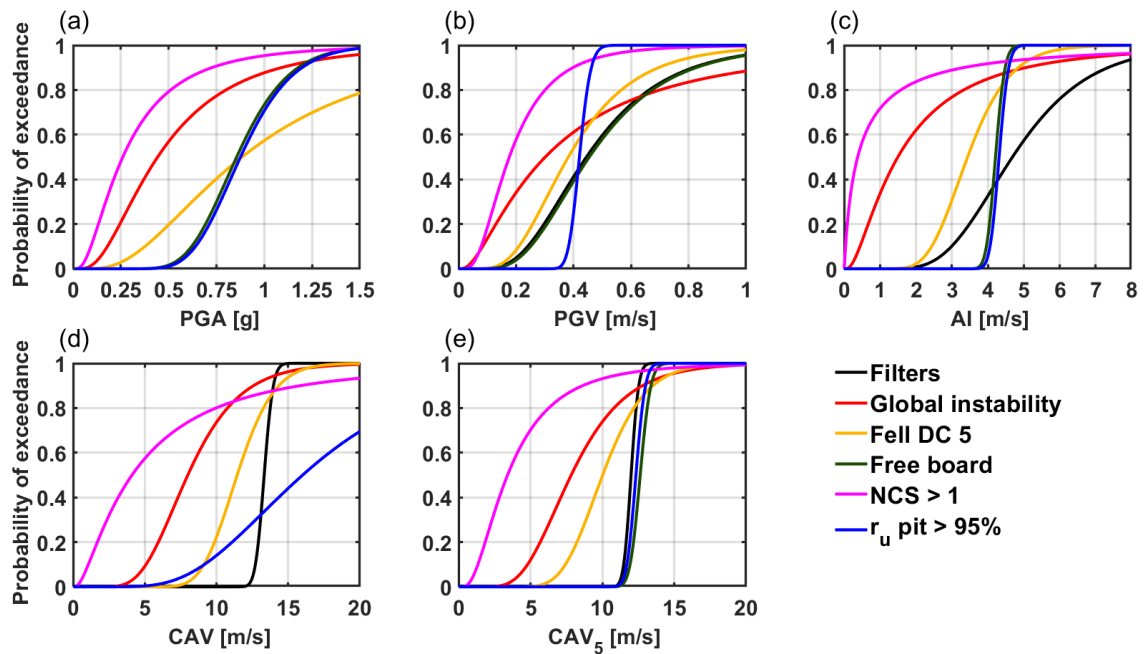


Figure 7.47: Comparison between fragility functions for different damage mechanisms for the PM4Sand dam model for (a) PGA, (b) PGV, (c) AI, (d) CAV, and (e) CAV<sub>5</sub>.

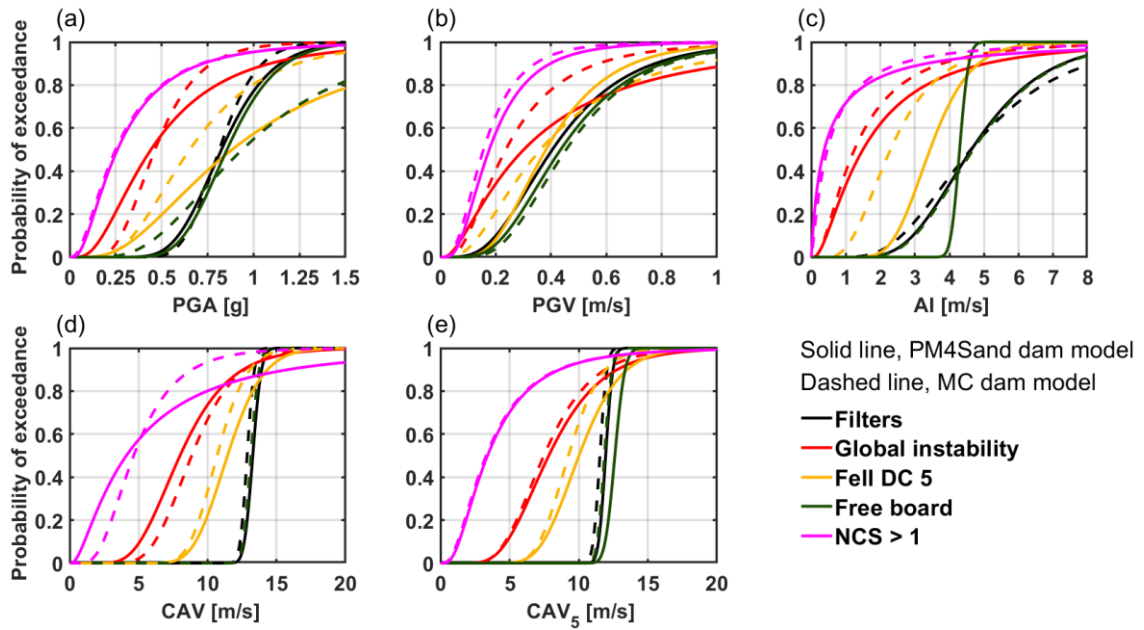


Figure 7.48: Comparison between fragility functions at the collapse limit state for the Mohr-Coulomb dam model and the PM4Sand dam model.

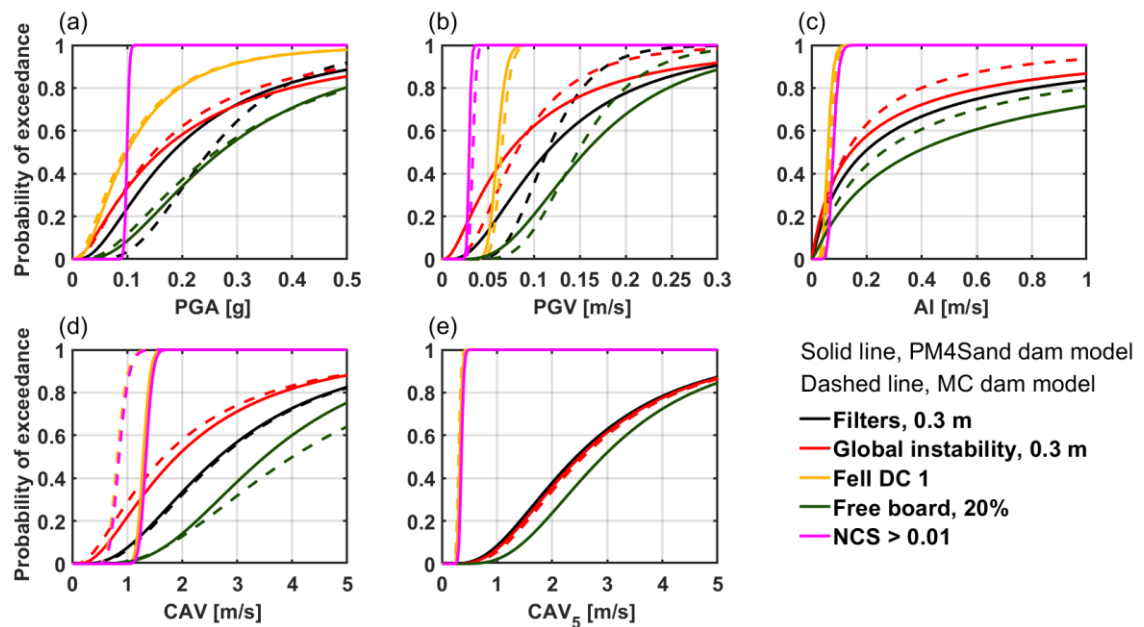


Figure 7.49: Comparison between fragility functions at DMs for thresholds lower than the collapse state for the Mohr-Coulomb dam model and the PM4Sand dam model.

#### 7.4 Efficiency of ground motion intensity measures

The efficiency of a given IM to predict a certain damage level is typically derived using fragility functions. The goodness of fit (i.e., how well the selected functional form fits data points based on observations or generated by numerical models) represented by the standard deviation of these curves ( $\beta$ ) is generally considered a good predictor of IM efficiency. However, this parameter by itself is not sufficient to define how well an IM is able to predict a given damage levels. This section presents the correlation between IMs and DMs for the two earth dams analyzed using other means by which to determine IM efficiency. Furthermore, after the most efficient IMs are identified, an analysis on IM predictability is performed. Such information is particularly useful when forward analyses are performed. Finally, both information: efficiency and predictability are used together to determine the total standard deviation of each considered IM. This last parameter is what it is believed to be the highest level synthetic parameter to guide the choice of an IM for forward deformation analysis.

The issue of determining the best IM to use in forward analysis is important for various reasons. Deterministic seismic hazard analyses are still widely used in dam engineering (Wong and Thomas, 2017). Thus, a target IM must be chosen to perform such analyses. For deterministic studies, it is of paramount importance that the selected IM correlates well with a DM (often-called Engineering Demand Parameter, EDP) because it is the only parameter that defines the seismic hazard level. If the IM and DM are poorly related, a small variation in the IM level (and thus a small variation of the seismic hazard level), could lead to a huge variation in the expected DM. IM-DM relationships are also crucial for coupled analyses of earth dams, which comprise the hazard estimation and seismic response evaluation procedures with probabilistic approaches (i.e. site-specific PSHA and fragility functions).

Another important concept when choosing the optimal IM to perform seismic evaluation of earth dams is the sufficiency (Luco and Cornell, 2001). This parameter measures the dependence of the DM, for a given IM, on the magnitude  $M$  and source-to-site distance  $R$  of the ground motion. If the IM is sufficient, the information on  $M$  and  $R$  does not reduce the variability of the DM. In such case, the efficiency of a ground motion IM is solely evaluated by the standard deviation in the DM for a given IM. In particular, the natural logarithm of the IM and DM are first calculated, and then a least-square linear regression is performed. The Root-Mean-Square Error

(RMSE) of the regression is the logarithmic standard deviation  $\sigma_{\ln DM|\ln IM}$  and it represents the efficiency of the IM. The  $\sigma_{\ln DM|\ln IM}$  is estimated from the MSA results performed on the Farneto del Principe and the Angitola dam, for a constant value of the PGA (i.e., the only IM estimated from the disaggregation analyses). Hence, the efficiency of the PGA will not be estimated. Results are then compared against a recent study on two earth dams in California (Armstrong et al., 2020): the Lenihan and Anderson dams. The latter is susceptible to liquefaction, while the former is not (Kuhl, 2011, Dorsey, 2011). In addition to focusing on different earth dams located in different regions, this study is different from that of Armstrong et al. (2020) as they did not perform MSA but a more traditional type of NDAs with unscaled ground motions, chosen to be consistent with the seismic hazard of several dams in California. The number of ground motions used by Armstrong et al. (2020) is 342, corresponding to 48 different earthquakes events.

Figure 7.50 shows the correlation between several IMs (PGV, AI, D595, CAV, and CAV<sub>5</sub>) and the crest settlement for the Farneto del Principe dam. The red points represent the damage observed, the black straight line is the linear regression, and the blue lines are the mean  $\pm$  one standard deviation (i.e., 67% confidence interval bounds). Low values of the IMs (75 years of return period) are far from the mean, which leads to a potentially biased correlation.

Table 7.14 summarizes the standard deviation obtained for the Farneto del Principe dam, for two DMs: (1) crest settlement, and (2) filter displacements. The  $\sigma_{\ln DM|\ln IM}$  for the filters displacements is slightly lower compared to that of the crest displacement. However, similar trends can be observed in the IMs for both DMs. The significant duration D595 is the least efficient IM, as it results in high values of standard deviation. The most efficient IM is AI, followed by CAV. This trend is the same reported by Armstrong et al. (2020). The authors suggested that the evolutionary nature of AI and CAV (both being integral intensity measures) is the reason for this good efficiency.

Results obtained for the Angitola dam are illustrated in Figures 7.51-7.53, and Table 7.15, for the PM4Sand dam model and the Mohr-Coulomb dam model. The IM-DM correlation is better than for the Farneto del Principe dam, which is reflected in the lower values of the  $\sigma_{\ln DM|\ln IM}$ .



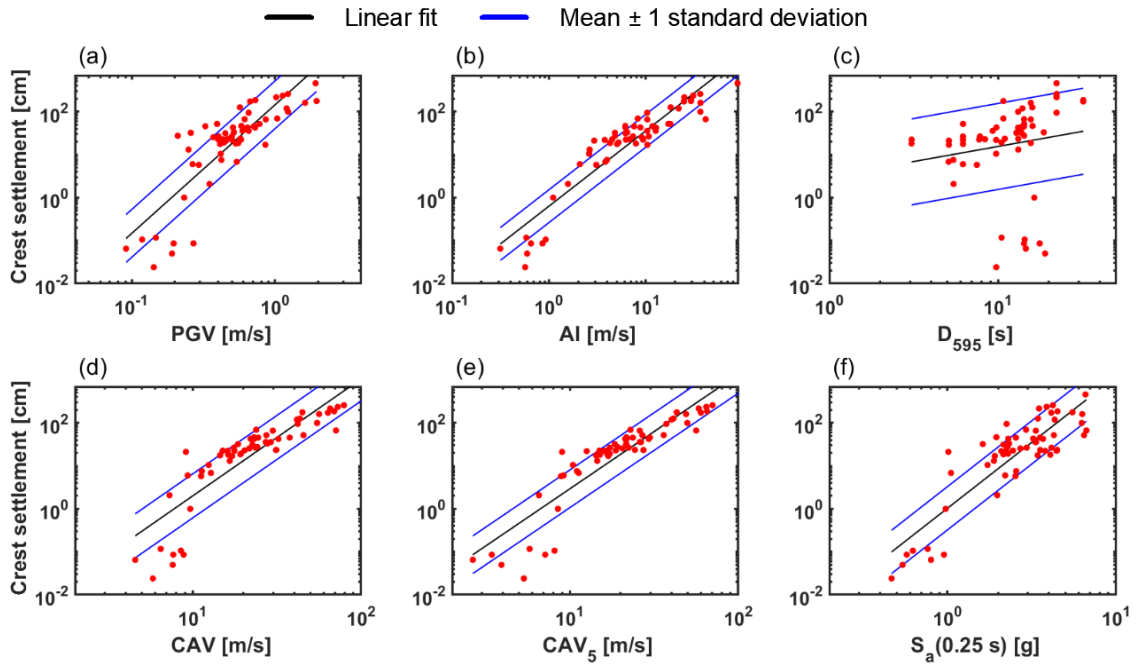


Figure 7.50: Ground Motion Intensity Measure Efficiency for the crest settlement (Farneto del Principe dam).

Table 7.14:  $\sigma_{\ln DM|\ln IM}$  from regression analysis for several IM and DM for the Farneto del Principe dam.

Farneto del Principe dam, $\sigma_{\ln DM \ln IM}$		
IM	Filter displacement	Right crest displacement
PGV [m/s]	1.211	1.280
AI [m/s]	0.819	0.880
D595 [s]	1.990	2.305
CAV [m/s]	1.010	1.180
CAV <sub>5</sub> [m/s]	0.905	1.008
S <sub>a</sub> (0.25s) [g]	1.000	1.159

For the PM4Sand dam model, the most efficient IM are AI, PGV, and CAV. Among them, CAV seems to be the most consistent, as it always stays in the range 0.50-0.53. The  $\sigma_{\ln DM|\ln IM}$  values for the MC dam model, on the other hand, are slightly lower for almost all IM, especially CAV. This is also consistent with findings by Armstrong et al. (2020), who found more variability in the case study where liquefaction occurred. This is a direct result of the complexity of damage mechanisms and damage patterns occurring when excess pore pressure-related phenomena occur. For the Angitola dam, only some zones experienced a  $r_u$  greater than 95%, but they were still sufficient to cause shear strength reduction and complex shear strain and deformation patterns (§7.3.2), and thus a different response.

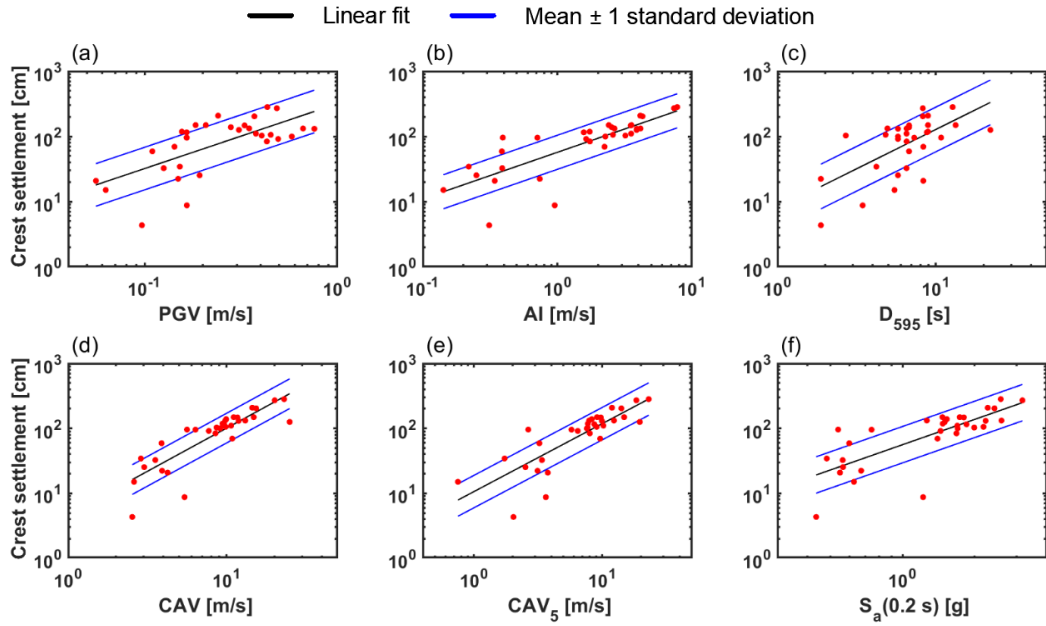


Figure 7.51: Ground Motion Intensity Measure Efficiency for the crest settlement for the PM4Sand dam model (Angitola dam).

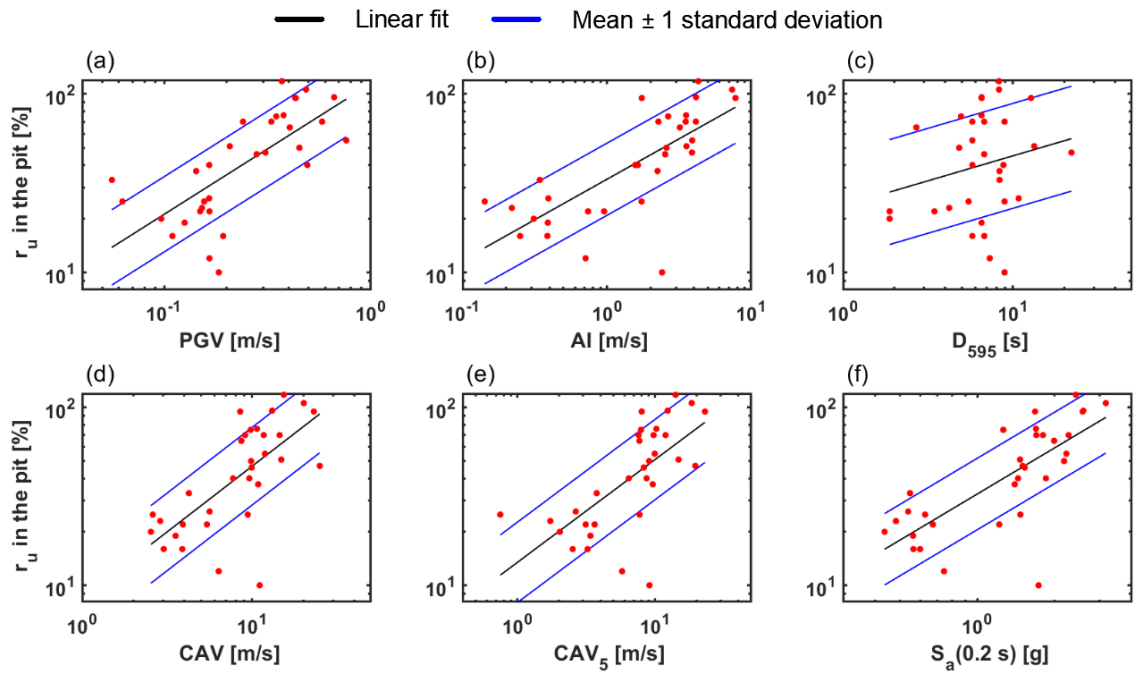


Figure 7.52: Ground Motion Intensity Measure Efficiency for the  $r_u$  in the pit for the PM4Sand dam model (Angitola dam).

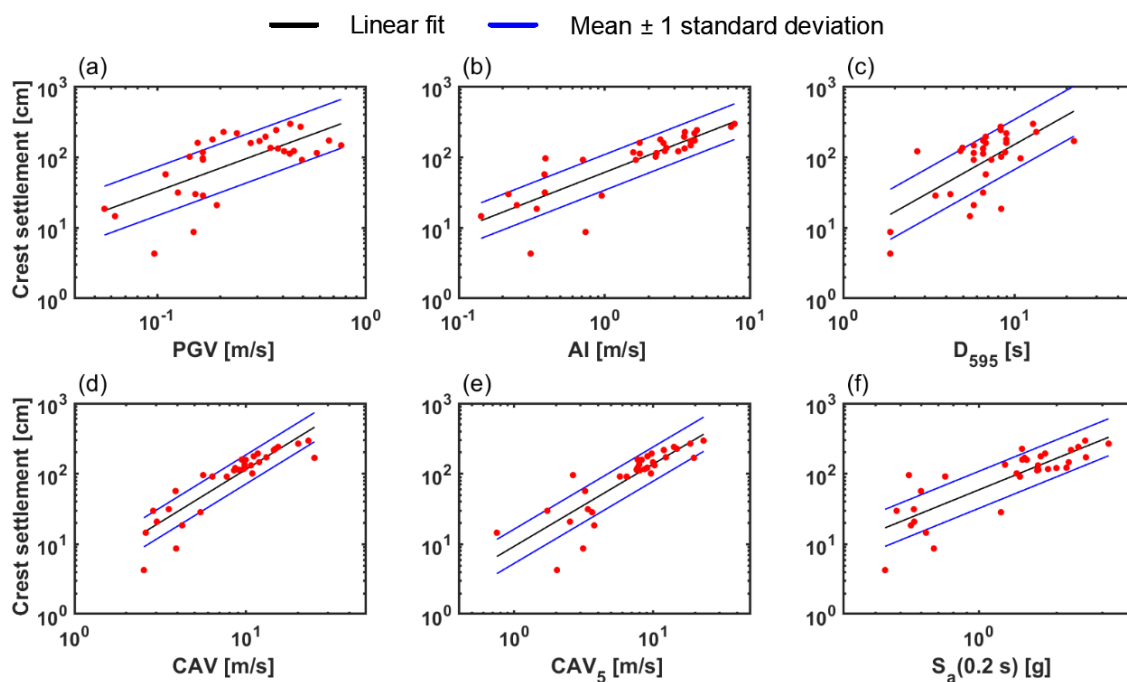


Figure 7.53: Ground Motion Intensity Measure Efficiency for the crest settlement for the Mohr-Coulomb dam model (Angitola dam).

Table 7.15:  $\sigma_{\ln DM|\ln IM}$  from regression analysis for various IM and DM, for the PM4Sand dam model of the Angitola dam.

Angitola dam, PM4Sand dam model, $\sigma_{\ln DM \ln IM}$				
IM	Filter displacement	Right crest displacement	Excess pore water pressure in the pit	Excess pore water pressure beneath the dam
PGV [m/s]	0.728	0.752	0.486	0.614
AI [m/s]	0.613	0.602	0.466	0.538
D595 [s]	0.729	0.789	0.677	0.597
CAV [m/s]	0.533	0.526	0.503	0.517
CAV <sub>5</sub> [m/s]	0.574	0.575	0.520	0.524
S <sub>a</sub> (0.2s) [g]	0.648	0.645	0.463	0.552

As mentioned before, the efficiency of the IM cannot be the only parameter of reference when selecting an optimal IM for the estimation of earth dams deformation. This is especially so when recording stations are not available in the vicinity of the dam and IMs should be predicted using an empirical model. The analysis of IM sufficiency is outside the scope of this work, while IM predictability is incorporated in this study as suggested by Armstrong et al. (2020) by computing the total standard deviation as:

Table 7.16:  $\sigma_{\ln DM|\ln IM}$  from regression analysis for various IM and DM, for the Mohr-Coulomb dam model of the Angitola dam.

Mohr-Coulomb dam model		
IM	Filter displacement	Right crest displacement
PGV [m/s]	0.751	0.795
AI [m/s]	0.591	0.580
D595 [s]	0.783	0.815
CAV [m/s]	0.490	0.476
CAV <sub>5</sub> [m/s]	0.574	0.560
S <sub>a</sub> (0.2s) [g]	0.597	0.605

$$\sigma_{\ln EDP|M,R,S} = \sqrt{\sigma_{\ln EDP|\ln IM}^2 + b^2 \sigma_{\ln IM|M,R,S}^2} \quad (7.11)$$

where  $\sigma_{\ln IM|M,R,S}^2$  is the standard deviation of a GMM, which represents its predictability, and  $b$  is the slope of the least-square linear regression in a log-log scale. Tables 7.17 and 7.18 show efficiency, predictability, and total standard deviation for various IMs and the left crest displacement. GMM standard deviation values are from: (1) Boore et al. (2014), BSSA14; Akkar et al. (2014), AEA14; Zhao et al. (2016), ZEA16. GMM, total standard deviations are estimated for the M and R that contribute the most to the seismic hazard for a return period of 1460 years. For the standard deviation of AI and CAV, the Campbell and Bozorgnia, CB, (2019) is exploited, for CAV<sub>5</sub> the Kramer and Mitchell relationship, KM (2006), is used, while for the significant duration (D595) the Asfhari and Stewart GMM, AS (2016). For the CB and AS models, the total standard deviation is estimated for the M and R that contributes the most to the seismic hazard for a return period of 1460 years.

For the Farneto del Principe dam, CAV is always the best IM (i.e., the IM with the lowest total standard deviation values). The second best IM is AI. CAV<sub>5</sub> is the second best IM in terms of efficiency for both DMs. However, it has a poor predictability. As a result, CAV<sub>5</sub> should only be used when forward analyses are performed for dams similar to the Farneto del Principe dam having available recording stations at the site. These results are generally consistent with those of Armstrong et al. (2018b and 2020).

Table 7.17: Efficiency, predictability, and total standard deviation for PGV, AI, CAV, CAV<sub>5</sub>, and S<sub>a</sub>(0.25s) for some well-known Ground Motion Models in literature. Farneto del Principe dam, MC dam model, Left crest displacement.

<b>Farneto del Principe dam</b>			
	<b>Efficiency</b> $\sigma_{\ln DM \ln IM}$	<b>Predictability</b> $\sigma_{\ln IM \ln M,R,S}$	<b>Total standard deviation</b> $\sigma_{\ln DM \ln M,R,S}$
<b>IM</b>	Left crest displacement		
PGV [m/s]	1.380	0.652 (BSSA14) 0.687 (AEA14)	2.470 (BSSA14) 2.562 (AEA14)
AI [m/s]	0.913	0.919 (CB)	1.943 (CB)
D595 [s]	2.443	0.419 (AS)	2.463 (AS)
CAV [m/s]	1.223	0.470 (CB)	1.834 (CB)
CAV <sub>5</sub> [m/s]	1.070	0.708 (KM)	2.267 (KM)
S <sub>a</sub> (0.25s) [g]	1.132	0.621 (BSSA14) 0.768 (AEA14) 0.780 (ZET16)	2.361 (BSSA14) 2.799 (AEA14) 2.837 (ZET16)

Table 7.18: Efficiency, predictability, and total standard deviation for PGV, AI, CAV, CAV<sub>5</sub>, and S<sub>a</sub>(0.25s) for some well-known Ground Motion Models in literature. Farneto del Principe dam, MC dam model, Filter displacement.

<b>Farneto del Principe dam</b>			
	<b>Efficiency</b> $\sigma_{\ln DM \ln IM}$	<b>Predictability</b> $\sigma_{\ln IM \ln M,R,S}$	<b>Total standard deviation</b> $\sigma_{\ln DM \ln M,R,S}$
<b>IM</b>	Filter displacement		
PGV [m/s]	1.171	0.652 (BSSA14) 0.687 (AEA14)	1.993 (BSSA14) 2.064 (AEA14)
AI [m/s]	0.715	0.919 (CB)	1.564 (CB)
D595 [s]	1.949	0.419 (AS)	1.979 (AS)
CAV [m/s]	0.893	0.470 (CB)	1.444 (CB)
CAV <sub>5</sub> [m/s]	0.782	0.708 (KM)	1.822 (KM)
S <sub>a</sub> (0.25s) [g]	0.942	0.621 (BSSA14) 0.768 (AEA14) 0.780 (ZET16)	1.907 (BSSA14) 2.254 (AEA14) 2.284 (ZET16)

Table 7.19: Efficiency, predictability, and total standard deviation for PGV, AI, CAV, CAV<sub>5</sub>, and S<sub>a</sub>(0.2s) for some well-known Ground Motion Models in literature. Angitola dam, PM4Sand dam model, right crest displacement.

Angitola dam, PM4Sand dam model			
	Efficiency $\sigma_{\ln DM} / \ln IM$	Predictability $\sigma_{\ln IM} / \ln M,R,S$	Total standard deviation $\sigma_{\ln DM} / \ln M,R,S$
IM	Right crest displacement		
PGV [m/s]	0.752	0.652 (BSSA14) 0.687 (AEA14)	0.992 (BSSA14) 1.015 (AEA14)
AI [m/s]	0.602	0.919 (CB)	0.891 (CB)
D595 [s]	0.789	0.419 (AS)	0.937 (AS)
CAV [m/s]	0.526	0.470 (CB)	0.817 (CB)
CAV <sub>5</sub> [m/s]	0.575	0.708 (KM)	0.938 (KM)
S <sub>a</sub> (0.2s) [g]	0.645	0.621 (BSSA14) 0.768 (AEA14) 0.780 (ZET16)	1.030 (BSSA14) 1.183 (AEA14) 1.196 (ZET16)

Table 7.20: Efficiency, predictability, and total standard deviation for PGV, AI, CAV, CAV<sub>5</sub>, and S<sub>a</sub>(0.2s) for some well-known Ground Motion Models in literature. Angitola dam, PM4Sand dam model, filter displacement.

Angitola dam, PM4Sand dam model			
	Efficiency $\sigma_{\ln DM} / \ln IM$	Predictability $\sigma_{\ln IM} / \ln M,R,S$	Total standard deviation $\sigma_{\ln DM} / \ln M,R,S$
IM	Filter displacement		
PGV [m/s]	0.728	0.652 (BSSA14) 0.687 (AEA14)	0.944 (BSSA14) 0.965 (AEA14)
AI [m/s]	0.613	0.919 (CB)	0.857 (CB)
D595 [s]	0.729	0.419 (AS)	0.885 (AS)
CAV [m/s]	0.533	0.470 (CB)	0.788 (CB)
CAV <sub>5</sub> [m/s]	0.574	0.708 (KM)	0.895 (KM)
S <sub>a</sub> (0.2s) [g]	0.648	0.621 (BSSA14) 0.768 (AEA14) 0.780 (ZET16)	0.978 (BSSA14) 1.113 (AEA14) 1.124 (ZET16)

Table 7.21: Efficiency, predictability, and total standard deviation for PGV, AI, CAV, CAV<sub>5</sub>, and S<sub>a</sub>(0.2s) for some well-known Ground Motion Models in literature. Angitola dam, PM4Sand dam model, excess pore water pressure in the pit zone.

Angitola dam, PM4Sand dam model			
	Efficiency $\sigma_{\ln DM \ln IM}$	Predictability $\sigma_{\ln IM \ln M,R,S}$	Total standard deviation $\sigma_{\ln DM \ln M,R,S}$
IM	Excess pore water pressure in the pit		
PGV [m/s]	0.486	0.652 (BSSA14) 0.687 (AEA14)	0.681 (BSSA14) 0.699 (AEA14)
AI [m/s]	0.466	0.919 (CB)	0.625 (CB)
D595 [s]	0.677	0.419 (AS)	0.687 (AS)
CAV [m/s]	0.503	0.470 (CB)	0.611 (CB)
CAV <sub>5</sub> [m/s]	0.520	0.708 (KM)	0.662 (KM)
S <sub>a</sub> (0.2s) [g]	0.463	0.621 (BSSA14) 0.768 (AEA14) 0.780 (ZET16)	0.707 (BSSA14) 0.807 (AEA14) 0.816 (ZET16)

Table 7.22: Efficiency, predictability, and total standard deviation for PGV, AI, CAV, CAV<sub>5</sub>, and S<sub>a</sub>(0.2s) for some well-known Ground Motion Models in literature. Angitola dam, PM4Sand dam model, excess pore water pressure beneath the dam.

Angitola dam, PM4Sand dam model			
	Efficiency $\sigma_{\ln DM \ln IM}$	Predictability $\sigma_{\ln IM \ln M,R,S}$	Total standard deviation $\sigma_{\ln DM \ln M,R,S}$
IM	Excess pore water pressure beneath the dam		
PGV [m/s]	0.614	0.652 (BSSA14) 0.687 (AEA14)	0.667 (BSSA14) 0.673 (AEA14)
AI [m/s]	0.539	0.919 (CB)	0.630 (CB)
D595 [s]	0.597	0.419 (AS)	0.646 (AS)
CAV [m/s]	0.517	0.470 (CB)	0.604 (CB)
CAV <sub>5</sub> [m/s]	0.524	0.708 (KM)	0.644 (KM)
S <sub>a</sub> (0.2s) [g]	0.552	0.621 (BSSA14) 0.768 (AEA14) 0.780 (ZET16)	0.679 (BSSA14) 0.738 (AEA14) 0.743 (ZET16)

Table 7.23: Efficiency, predictability, and total standard deviation for PGV, AI, CAV, CAV<sub>5</sub>, and S<sub>a</sub>(0.2s) for some well-known Ground Motion Models in literature. Angitola dam, MC dam model, right crest displacement.

Angitola dam, Mohr-Coulomb dam model			
	Efficiency $\sigma_{\ln DM \ln IM}$	Predictability $\sigma_{\ln IM \ln M,R,S}$	Total standard deviation $\sigma_{\ln DM \ln M,R,S}$
IM	Right crest displacement		
PGV [m/s]	0.795	0.652 (BSSA14) 0.687 (AEA14)	1.063 (BSSA14) 1.089 (AEA14)
AI [m/s]	0.580	0.919 (CB)	0.940 (CB)
D595 [s]	0.815	0.419 (AS)	0.996 (AS)
CAV [m/s]	0.476	0.470 (CB)	0.851 (CB)
CAV <sub>5</sub> [m/s]	0.560	0.708 (KM)	0.999 (KM)
S <sub>a</sub> (0.2s) [g]	0.605	0.621 (BSSA14) 0.768 (AEA14) 0.780 (ZET16)	1.107 (BSSA14) 1.296 (AEA14) 1.312 (ZET16)

Table 7.24: Efficiency, predictability, and total standard deviation for PGV, AI, CAV, CAV<sub>5</sub>, and S<sub>a</sub>(0.2s) for some well-known Ground Motion Models in literature. Angitola dam, MC dam model, filter displacement.

Angitola dam, Mohr-Coulomb dam model			
	Efficiency $\sigma_{\ln DM \ln IM}$	Predictability $\sigma_{\ln IM \ln M,R,S}$	Total standard deviation $\sigma_{\ln DM \ln M,R,S}$
IM	Filter displacement		
PGV [m/s]	0.751	0.652 (BSSA14) 0.687 (AEA14)	1.026 (BSSA14) 1.052 (AEA14)
AI [m/s]	0.591	0.919 (CB)	0.915 (CB)
D595 [s]	0.783	0.419 (AS)	0.961 (AS)
CAV [m/s]	0.490	0.470 (CB)	0.831 (CB)
CAV <sub>5</sub> [m/s]	0.574	0.708 (KM)	0.968 (KM)
S <sub>a</sub> (0.2s) [g]	0.597	0.621 (BSSA14) 0.768 (AEA14) 0.780 (ZET16)	1.069 (BSSA14) 1.248 (AEA14) 1.263 (ZET16)



Table 7.25: Percentage variation of the total standard deviation for the Angitola dam between the two models. Positive values corresponds to larger  $\sigma_{\ln DM|\ln M,R,S}$  for the MC dam model.

<b>Angitola dam</b>		
<b>IM</b>	<b>% Variation of the total standard deviation <math>\sigma_{\ln DM \ln M,R,S}</math> between the two models</b>	
	<b>Filter displacement</b>	<b>Right crest displacement</b>
PGV [m/s]	7.98 (BSSA14) 8.27 (AEA14)	6.65 (BSSA14) 6.72 (AEA14)
AI [m/s]	6.35 (CB)	5.27 (CB)
D595 [s]	7.87 (AS)	5.88 (AS)
CAV [m/s]	5.13 (CB)	3.98 (CB)
CAV <sub>5</sub> [m/s]	7.13 (KM)	6.08 (KM)
S <sub>a</sub> (0.2s) [g]	8.56 (BSSA14) 10.85 (AEA14) 11.00 (ZET16)	7.01 (BSSA14) 8.70 (AEA14) 8.82 (ZET16)

## Conclusion

In this dissertation, a fully-probabilistic approach to evaluate the seismic response of two earth dams in Southern Italy is presented. These dams (the Farneto del Principe dam and the Angitola dam) are located in the same region and tectonic environment. However, the Angitola dam is founded on potentially liquefiable soils, whereas the Farneto del Principe dam only comprises non-liquefiable materials. For the Farneto del Principe dam site, a non-ergodic PSHA was performed. This analysis was done by first performing a numerical seismic ground response analysis (GRA) program to build amplification functions for the site of interest. The limits of numerical GRA approaches were discussed and sources of uncertainty in the ground response were addressed. Then, the results of the GRA were merged into the PSHA framework to perform a non-ergodic analysis. The resulting non-ergodic seismic hazard at the site was compared to hazard predictions obtained using simplified methods. It was found that, in this case, the modified hybrid approach produces results similar to those obtained using the non-ergodic PSHA.

For both dams, comprehensive field and laboratory geotechnical investigation programs were performed. All results from these programs were presented and discussed. The availability of this large amount of high-quality data enabled the possibility of calibrating both simplified and advanced constitutive models. For both dams, simplified (i.e., using the Mohr–Coulomb failure criterion coupled with a simplified hysteretic procedure) and advanced (i.e., PM4Sand and PM4Silt, Boulanger and Ziotopoulou, 2017 and 2018) constitutive models were calibrated. These calibration processes were fully documented, enabling future studies on similar dams for which geotechnical data might be available. Furthermore, this effort may be used to help planning future geotechnical investigation programs in Italy and elsewhere where similar dam types exist.

In the last part of this study, MSA were performed for the Farneto del Principe and Angitola dams. Fragility functions for different IMs and DMs were built and differences between constitutive models results were shown. When nonlinearity is important and soils are potentially liquefiable, advanced constitutive models capture some nuances of complex damage mechanisms that simplified models fails to identify. There are significant differences in data scatter and standard deviation values for different IMs. Results from this study clearly show that for both dams and practically all DMs, CAV- and CAV5-based fragility functions have the lowest

standard deviation values. The availability of a large number of fragility functions for two typical earth dams in Italy will likely be used in the future to perform screening analyses on existing dams. Such simple preliminary studies on dams' vulnerability may be used to define priorities for future mitigation strategies of the entire national large dams inventory.

Fragility functions may also be a useful tool for rapid post-earthquake damage assessments. Near real-time damage estimates can be performed using IMs predicted by readily available ShakeMaps or measured by existing recording stations at the dam site. If the latter is available, fragility functions may be implemented as part of EEW systems. Such EEW systems are capable of predicting damage levels based on the data interpretation of a continuous monitoring of the dam. If a strong ground motion occurs, the IM of the event is recorded and thus the probability that a certain damage will be exceeded can be promptly estimated and used in combination with other data available as part of the monitoring system (e.g., pore water pressures, crest settlements, etc.) to identify the performance of the structure.

Although fragility function standard deviations values can provide insights on the best IM to be used to predict a given DM, in the last part, the correlation between IMs and DMs were addressed for the both dams and all investigated IMs and DMs. This correlation is described by IM efficiency values. Furthermore, the predictability of all analyzed IMs is also calculated. Velocity-based ground motion intensity measures were the most efficient in predicting earth dam damage. In particular, CAV, CAV5, AI, and PGV provided low values of efficiency. However, they do not have the same level of predictability. As a result, they can all be used in forward analyses only if recording stations are available at dams' sites. If input records for forward analyses need to be derived from global time series databases, efficiency and predictability need to be merged into one synthetic parameter to guide the selection of the best IM. This synthetic parameter was evaluated for all IMs and DMs. CAV provided the lowest values of the total standard deviation for all IMs and DMs. Hence, it should be used for forward applications when recording stations are not available at the dam site.

## References

- Abrahamson, N.A., Al Atik, L. (2010). Scenario Spectra for Design Ground Motions and Risk Calculation. 9th US National and 10th Canadian Conference on Earthquake Engineering, Toronto, Canada, 12.
- Abrahamson, N.A, Gregor N, Addo KBC. (2015). Hydro ground motion prediction equations for subduction earthquakes. *Earthq. Spectra*, 32, 23-44.
- Abrahamson, N.A. Gülerce, Z. (2020). Regionalized Ground-Motion Models for Subduction Earthquakes Based on the NGA-SUB Database. PEER Report No. 2020/25 Pacific Earthquake Engineering Research Center Headquarters at the University of California, Berkeley.
- Afshari, K., Stewart, J.P. (2016). Physically parameterized prediction equations for significant duration in active crustal regions. *Earthquake Spectra*, 32(4):2057-2081
- Akkar S., Bommer J.J. (2010). Empirical equations for the prediction of PGA, PGV and spectra accelerations in Europe, the Mediterranean region and the Middle East, *Seism. Res. Lett.*, 81, 195-206.
- Akkar, S., Sandikkaya, M. A., Bommer, J. J. (2014). Empirical ground-motion models for point-and extended-source crustal earthquake scenarios in Europe and the Middle East. *Bulletin of Earthquake Engineering*, 12(1), 359-387.
- Albano, M., Modoni, G., Croce, P., Russo, G. (2015). Assessment of the seismic performance of a bituminous faced rockfill dam. *Soil Dyn Earthq Eng*, 75, pp. 183-198.
- Ambraseys, N., (1974). Notes on engineering seismology. in J. Solnes (ed.), *Engineering Seismology and Earthquake Engineering*, NATO Advanced study, 33-54.
- Ancheta, T. D., Darragh, R. B., Stewart, J.P., Seyhan, E., Silva, W.J., Chiou, B. S. J., Wooddell, K. E., Graves, R. W., Kottke, A. R., Boore, D. M., Kishida, T., Donahue, J.L. (2014). NGA-West2 database, *Earthquake Spectra* 30, 989–1005.
- Anderson, J. G., Brune, J.N. (1999). Probabilistic seismic hazard analysis without the ergodic assumption, *Seismol. Res. Lett.* 70, no. 1, 19–28.
- Andrus, R.D., Stokoe, K.H. (2000). Liquefaction resistance of soils from shear-wave velocity. *J. Geotechnical and Geoenvironmental Eng.*, ASCE 126(11), 1015–025.
- Arias, A. (1970). A measure of earthquake intensity. R.J. Hansen, ed. *Seismic Design for Nuclear Power Plants* Cambridge, Massachusetts: MIT Press: 438-483.
- Armstrong, R.J, Kishida, T., Park, D.S. (2018a). Efficiency of ground motion intensity measures with earthquake-induced earth dam deformations. In: *Proceedings of the 2018 California strong motion instrumentation program seminar*, Sacramento, CA, USA, 25 October 2018.

- Armstrong RJ, Park DS, Guillen, A. (2018b). Cyclic soil behavior of common constitutive models used in nonlinear deformation analyses of embankment dams. In: Proceedings of the 2018 annual United States society of dams conference, Miami, FL, USA, 30 April–4 May 2018.
- Armstrong, R., Kishida, T., Park, D., (2020). Efficiency of ground motion intensity measures with earthquake-induced earth dam deformations. In: Earthquake Spectra.
- Assimaki, D., W. Li (2012). Site- and ground motion-dependent nonlinear effects in seismological model predictions. *Soil Dynamics and Earthquake Engineering* 32: 143-151.
- Athanasopoulos, G.A. (1995). Empirical Correlations  $V_{so}$ - $N_{spt}$  For Soils Of Greece: A Comparative Study Of Reliability. *Soil Dynamics and Earthquake Engineering*, 15.
- Atkinson G.M., Boore D.M. (2003). Empirical ground-motion relations for subduction zone earthquakes and their application to Cascadia and other regions, *Bull. Seis. Soc. Am.*, 93, 1703-1729.
- Ausilio, E., Dente G., Zimmaro, P. (2013). Osservazioni sul monitoraggio geotecnico della diga di Farneto del Principe. *Incontro Annuale dei Ricercatori di Geotecnica 2013*.
- Ausilio, E., Dente, G., Zimmaro, P. (2016). Geotechnical investigation and field performance of a zoned earth dam in Italy. In: 1st IMEKO TC-4 International Workshop on Metrology for Geotechnics, Benevento, Italy, pp. 281-287.
- Baker, J.W., Cornell, C. A. (2006b). Spectral shape, epsilon and record selection. *Earthquake Engineering & Structural Dynamics*, 35(9), 1077–1095.
- Baker, J.W. (2013). Probabilistic Seismic Hazard Analysis. White Paper Version 2.0.1, 79 pp.
- Baker, J.W. (2011). Conditional mean spectrum: tool for ground motion selection. *ASCE, J. Struct. Eng.*, 137(3): 322–333.
- Baker, J.W., Lin, T. (2013). Proposed terminology for conditional spectra and related concepts.
- Baker, J.W. (2015). Efficient Analytical Fragility Function Fitting Using Dynamic Structural Analysis. *Earthquake Spectra: February 2015, Vol. 31, No. 1*, pp. 579-599.
- Baker J.W., Lee C. (2018). An Improved Algorithm for Selecting Ground Motions to Match a Conditional Spectrum, *Journal of Earthquake Engineering*, 22:4, 708-723
- Baturay, M.B., Stewart J.P. (2003). Uncertainty and bias in ground motion estimates from ground response analyses, *Bull. Seismol. Soc. Am.*, 93(5): 2025–2042.
- Bazzurro, P., Cornell C.A. (1999). Disaggregation of seismic hazard, *Bull. Seis. Soc. Am.* 89: 501-520.
- Bazzurro, P., Cornell, C. A. (2004a). Nonlinear soil-site effects in probabilistic seismic-hazard analysis, *Bull. Seismol. Soc. Am.* 94, 2110–2123.

- Beaty, M.H., Byrne, P.M. (2001). Observations on the San Fernando Dams. In Proceedings of 4<sup>th</sup> International Conference on Recent Advances in Geotechnical Earthquake Engineering and Soil Dynamics, San Diego, California, March 26-31, University of Missouri-Rolla, pp. 339-347.
- Bernier C., Monteiro R., Paultre P. (2016). Using the Conditional Spectrum Method for Improved Fragility Assessment of Concrete Gravity Dams in Eastern Canada. *Earthquake Spectra*, 32, 1449-1468
- Bolton, M. D. (1986). The strength and dilatancy of sands. *Géotechnique* 36(1), 65–78.
- Bommer, JJ., Acevedo, A.B. (2004). The use of real earthquake accelerograms as input to dynamic analysis. *Journal of Earthquake Engineering*, 8, special issue 1: 43-91.
- Bommer, JJ., Scott, S.G., Sarma, SK. (2000). Hazard-consistent earthquake scenarios. *Soil Dynamics and Earthquake Engineering*; 19:219–231.
- Bommer, JJ., Douglas, J., Scherbaum, F., Cotton, F., Bungum, H., Fäh, D. (2010). On the selection of ground-motion prediction equations for seismic hazard analysis. *Seismological Research Letters*, 81(5):783-793
- Boore D.M., Stewart J.P., Seyhan E., Atkinson G.M (2014). NGA-West 2 equations for predicting PGA, PGV, and 5%-damped PSA for shallow crustal earthquakes, *Earthq. Spectra*, 30(3): 1057–1085.
- Boulanger, R. W. (2003a). Relating  $K\alpha$  to relative state parameter index. *Journal of Geotechnical and Geoenvironmental Engineering*, ASCE, 129(8), 770-773.
- Boulanger, R. W. (2003b). High overburden stress effects in liquefaction analyses, *J. Geotechnical and Geoenvironmental Eng.*, ASCE 129(12), 1071–082.
- Boulanger, R. W., Idriss, I. M. (2004). Evaluating the potential for liquefaction or cyclic failure of silts and clays. Rep. UCD/CGM-04/01, Univ. of Calif., Davis, Calif.
- Boulanger, R. W., Idriss, I. M. (2006). Liquefaction susceptibility criteria for silts and clays. *J. Geotech. Geoenviron. Eng.*, 132(11), 1413–1426.
- Boulanger, R.W., Idriss, I.M. (2007). Evaluation of cyclic softening in silts and clays. *J. Geotechnical and Geoenvironmental Eng.*, ASCE 133(6), 641–52.
- Boulanger, R.W., Idriss, I.M. (2012a). Probabilistic SPT-based liquefaction triggering procedure. *Journal of Geotechnical and Geoenvironmental Engineering*, ASCE, 138(10), 1185-1195.
- Boulanger, R.W., Idriss, I.M. (2014). CPT and SPT based liquefaction triggering procedures. Rep. No. UCD/CGM-14/01, Univ. of California, Davis, CA.
- Boulanger R.W., Montgomery J., Ziotopoulou K. (2015). Nonlinear Deformation Analyses of Liquefaction Effects on Embankment Dams. In: Ansal A., Sakr M. (eds) *Perspectives on*

Earthquake Geotechnical Engineering. Geotechnical, Geological and Earthquake Engineering, vol 37. Springer, Cham.

Boulanger, R.W., Idriss, I.M. (2016). CPT-based liquefaction triggering procedure. *J. Geotech. Geoenviron. Eng.*, 142, 04015065.

Boulanger, R.W. Beaty, M. H. (2016). Seismic deformation analyses of embankment dams: A reviewer's checklist. Proceedings, Celebrating the Value of Dams and Levees – Yesterday, Today and Tomorrow, 36th USSD Annual Meeting and Conference, United States Society on Dams, Denver, CO, 535-546.

Boulanger, R. W., Montgomery, J. (2016). Nonlinear deformation analyses of an embankment dam on a spatially variable liquefiable deposit. *Soil Dynamics and Earthquake Engineering*, 91, 222–233.

Boulanger, R. W., Price, A. B., Ziotopoulou, K. (2018). Constitutive modeling of the cyclic loading response of low plasticity fine-grained soils. GSIC 2018, Proceedings of GeoShanghai 2018 International Conference: Fundamentals of Soil Behaviours, A. Zhou et al. (Eds.), Springer Nature Singapore Pte Ltd., pp. 1–13,

Boulanger, R. W., Ziotopoulou, K. (2013). Formulation of a sand plasticity plane-strain model for earthquake engineering applications. *Journal of Soil Dynamics and Earthquake Engineering*, Elsevier, 53, 254-267, [dx.doi.org/10.1016/j.soildyn.2013.07.006](https://doi.org/10.1016/j.soildyn.2013.07.006).

Boulanger, R. W., Ziotopoulou, K. (2017). PM4Sand (Version 3.1): A sand plasticity model for earthquake engineering applications. Report No. UCD/CGM-17/01, Center for Geotechnical Modeling, Department of Civil and Environmental Engineering, University of California, Davis, CA.

Boulanger, R. W., Ziotopoulou, K. (2018). PM4Silt (version 1): A silt plasticity model for earthquake engineering applications. Rep. No. UCD/CGM-18/01. Davis, CA: Center for Geotechnical Modeling, Dept. of Civil and Environmental Engineering, Univ. of California.

Boulanger, R. W., Ziotopoulou, K. (2019). A constitutive model for clays and plastic silts in plane-strain earthquake engineering applications. *Soil Dynamics and Earthquake Engineering*, 127(2019): 105832, [10.1016/j.soildyn.2019.105832](https://doi.org/10.1016/j.soildyn.2019.105832).

Boulanger, R. W., Wijewickreme D. (2019). Calibration of a constitutive model for the cyclic loading response of Fraser River Delta Silt. In *Earthquake Geotechnical Engineering for Protection and Development of Environment and Constructions: Proc., 7th Int. Conf. on Earthquake Geotechnical Engineering*, edited by F. Silvestri and N. Moraci, 121–137. Rome: Associazione Geotecnica Italiana.

Boulanger, R. W. (2019). Nonlinear dynamic analyses of Austrian dam in the 1989 Loma Prieta earthquake. *Journal of Geotechnical and Geoenvironmental Engineering*, 145(11), 05019011.

Bozorgnia Y., Crouse C.B., Hamburger R.O., Klemencic R., Krawinkler H., Malley J.O., Moehle J.P., Naeim F., Stewart J.P. (2010). Guidelines for performance-based seismic design of tall

buildings, PEER Report No.2010/05, Pacific Earthquake Engineering Research Center, University of California, Berkeley, CA.

Bozorgnia, Y., Abrahamson, N.A., Atik, L.A., Ancheta, T.D., Atkinson, G.M., Baker, J.W., Baltay, A., Boore, D.M., Campbell, K.W., Chiou, B.S.J., Darragh, R., Day, S., Donahue, J., Graves, R.W., Gregor, N., Hanks, T., Idriss, I.M., Kamai, R., Kishida, T., Kottke, A., Mahin, S.A., Rezaeian, S., Rowshandel, B., Seyhan, E., Shahi, S., Shantz, T., Silva, W., Spudich, P., Stewart, J.P., Watson-Lamprey, J., Wooddell, K., Youngs, R. (2014). NGA-west2 research project. *Earthquake Spectra* 30 (3), 973–987.

Bradley, B. A., (2010). A generalized conditional intensity measure approach and holistic ground motion selection, *Earthquake Engineering & Structural Dynamics* 39, 1321–1342.

Bradley, B. A. (2012). A ground motion selection algorithm based on the generalized conditional intensity measure approach. *Soil Dynamics and Earthquake Engineering*, 40, 48–61.

Brandenberg, S.J., Zimmaro, P., Stewart, J.P., Kwak, D.Y., Franke, K.W., Moss, R.E.S., Cetin, K.O., Can, G., Ilgac, M., Stamatakos, J., Weaver, T., Kramer, S.L. (2019). Next generation liquefaction database. *Earthquake Spectra*, 36, 939-959.

Bray, J.D., Rathje, E.M. (1998). Earthquake-induced displacements of solid-waste landfills. *J Geoenviron Eng* 124(3):242–253.

Bray, J. D., Sancio, R. B. (2006). Assessment of the liquefaction susceptibility of fine-grained soils. *J. Geotech. Geoenviron. Eng.*, 132(9), 1165–1177.

Bray, J. D., Travasarou, T. (2007). Simplified procedure for estimating earthquake-induced deviatoric slope displacements. *Journal of Geotechnical and Geoenvironmental Engineering*, ASCE 133(4), 381-392.

Bray, J.D., Macedo, J., (2017). 6th Ishihara lecture: Simplified procedure for estimating liquefaction-induced building settlement. *Soil Dynamics and Earthquake Engineering* 102, 215–231.

Campbell, K. W., Bozorgnia, Y. (2019). Ground motion models for the horizontal components of Arias intensity (AI) and cumulative absolute velocity (CAV) using the NGA-West2 database. *Earthquake Spectra*, 35(3): 1289-1310, Aug 2019.

Campanella, R.G., Gillespie, D., Robertson, P.K. (1982). Pore pressure during cone penetration testing. *Proc. Of the 2nd European Symposium on Penetration Testing, ESPOT II. Amsterdam. A.A. Balkema*, 507 - 512.

Cancani, A. (1904). Sur l'emploi d'une double echelle sismique des intensités, empirique et absolue. *Gerlands Beitr Geophys* 2:281–283

Carlton, B., Abrahamson N.A. (2014). Issues and Approaches for Implementing Conditional Mean Spectra in Practice, *Bull. Seism. Soc. Am*, 104(1).



- Cascone E., Rampello S. (2003). Decoupled seismic analysis of an earth dam. *Soil Dynamics and Earthquake Engineering*, 23, 349-365.
- Castellani A., Faccioli, E. (2008). *Costruzioni in zona sismica*. Ulrico Hoepli Editore
- Cavallaro, A., Maugeri, M., Lo Presti, D.C., Pallara, O. (1999). Characterising Shear Modulus and Damping from in Situ and Laboratory Tests for the Seismic Area of Catania. In: 2nd International Symposium on Pre-failure Deformation Characteristics of Geomaterials, Torino, Italy, pp. 51-58.
- Cetin, K.O., Seed, R.B., Kayen, R.E., Moss, R.E.S., Bilge, H.T., Ilgac, M., Chowdhury, K. (2018). SPT-based probabilistic and deterministic assessment of seismic soil liquefaction triggering hazard. *Soil Dynamics and Earthquake Engineering* 115: 698–709.
- Chopra, A. K., Zhang, L. (1991). Earthquake-induced base sliding of concrete gravity dams. *Journal of Structural Engineering*, ASCE 117(12), 3698-3719.
- Chowdhury, K., Seed, R.B., Dreger, D.S., Perlea, V., Beaty, M., Ma, F., Wang, Z. (2018). Re-evaluation of the Lower San Fernando Dam: A seismic performance case history involving liquefaction flow failures conditions. In: *Proceedings of the geotechnical earthquake engineering and soil dynamics V*. ASCE, Austin, TX, 10–13 June.
- Chu, D.B, Stewart, J.P., Youd, T.L., Chu, B.L (2006). Liquefaction-induced lateral spreading in near-fault regions during the 1999 Chi-Chi, Taiwan earthquake. *J. Geotech. and Geoenv. Eng.* 2006; 132(12): 1549-1565.
- Coatsworth, A. M. (1985). A rational approach to consolidated undrained triaxial testing, *Proceedings for the 20th Regional Meeting, Engineering Group, Guildford, U.K., Geological Society, Vol. 1.*
- Committee on seismic risk (1984). Glossary of terms for probabilistic seismic-risk and hazard analysis. *Earthquake Spectra*, Vol. 1, No. 1, pp. 33-40
- Conte, E., Dente, G. (1986). Seismic response of an earth dam and foundations system. *Proceedings of the 8th European conference on earthquake engineering, Lisbon.*
- Coppersmith, K., Bommer, J., Hanson, K., Coppersmith, R., Unruh, J., Wolf, L, Youngs, B., Al Atik, L, Rodriguez-Marek, A., Toro, G., (2014). Hanford Site-wide Probabilistic Seismic Hazard Analysis, Prepared for the U.S. Department of Energy Under Contract DE-AC06076RL01830, and Energy Northwest, Pacific Northwest National Lab Report PNNL-23361, November
- Cornell, C.A. (1968). Engineering Seismic Risk Analysis. *Bulletin of the Seismological Society of America*, 58(5), 1583–1606.
- Cornell, C.A., Luco, N. (2001). Ground motion intensity measures for structural performance assessment at near-fault sites. *Proceedings for the U.S. Japan joint workshop and third grantees 20.*

- Costanzo, A., Sica, S., Silvestri, F. (2011). Verifica della sicurezza in condizioni sismiche della diga sul fiume Melito (CZ). *Rivista Italiana di Geotecnica*, 2, 38-67.
- Costigliola, R.M., Mancuso, C., Pagano, L., Silvestri, F. (2019). Seismic safety evaluation of an existing bituminous faced rockfill dam. In: Silvestri, F., Moraci, N. (eds.) *Proceedings of the VII ICEGE 7th International Conference on Earthquake Geotechnical Engineering*. Rome 17–20 June 2019. *Proceedings in Earth and geosciences*, pp. 1887–1894.
- Cotton, F., Scherbaum, F., Bommer, J.J., Bungum, H. (2006). Criteria for selecting and adjusting ground-motion models for specific target regions: Application to central Europe and rock sites. *Journal of Seismology*, 10(2): 137-156, Apr 2006.
- CPTI Working Group (1999). *Catalogo Parametrico dei Terremoti Italiani, versione 1 (CPTI99)*, INGV, Milano. Available at <http://emidius.mi.ingv.it/CPTI99/> (last accessed January 2021). In Italian
- CPTI Working Group (2004). *Catalogo Parametrico dei Terremoti Italiani, version 2004 (CPTI04)*, INGV, Milano. Available at <http://emidius.mi.ingv.it/CPTI04/> (last accessed January 2021). In Italian.
- Cramer C.H. (2003). Site-specific seismic-hazard analysis that is completely probabilistic, *Bull. Seismol. Soc. Am.*, 93(4): 1841–1846.
- Cremen, G., Baker, J. W. (2020). Variance-based Sensitivity Analyses and Uncertainty Quantification for FEMA P-58 Consequence Predictions. *Earthquake Engineering & Structural Dynamics*, (in press).
- Cua, G., Wald, D. J., Allen, T. I., Garcia, D., Worden, C. B., Gerstenberger, M., Lin, K., Marano, K. (2010). Best practices for using macroseismic intensity and ground motion intensity conversion equations for hazard and loss models in GEM1. *Technical Report 2010-4*, GEM Foundation, Pavia, Italy, Oct 2010.
- Dafalias, Y. F., Manzari, M. T. (2004). Simple plasticity sand model accounting for fabric change effects. *Journal of Engineering Mechanics*, ASCE, 130(6), 622-634.
- Dakoulas, P., Gazetas, G. (1985). A class of inhomogeneous shear models for seismic response of dams and embankments. *Soil Dynamics and Earthquake Engineering*, Vol. 4, No. 4, 166-182.
- Dakoulas, P., Gazetas, G. (1987). Vibration characteristics of dams in narrow canyons. *Journal of Geotechnical Engineering* 113(8), 899-904.
- Decanini, L., Gavarini, C. e Mollaioli, F. (1995). Proposta di definizione delle relazioni tra intensita' macrosismica e parametri del moto del suolo, *Atti 70 Convegno L'ingegneria sismica in Italia*, 1, 63-72.
- Lliboutry, L., 2000. *Quantitative Geophysics and Geology*, Springer, London

- De Mello, V.F.B. (1971). The Standard Penetration Test. State of the Art Report, 4th Panamerican Conference Soil Mechanics Found. Eng., Dan Juan, Puerto Rico, V.1, pp.1-86.
- Duncan, J. M., Wright, S. G. (2005). Soil strength and slope stability, Wiley, Hoboken, N.J.
- Dorsey, C. (2011). Memorandum of Design Review Leroy Anderson Dam No.72-9 Santa Clara County. Sacramento, CA: California Division of Safety of Dams.
- Douglas, J. (2019). Ground motion prediction equations 1964-2019.
- Eads, L., Miranda, E., Krawinkler, H., and Lignos, D. G., (2013). An efficient method for estimating the collapse risk of structures in seismic regions, *Earthquake Engineering & Structural Dynamics* 42, 25–41.
- Electric Power Research Institute EPRI (1993). Guidelines for determining design basis ground motions. Final Rep. No. TR-102293, Palo Alto, Calif.
- Elgamal, A. W., Abdel-Ghaffar, A. M., Prevost, J. H. (1987b). 2D Elastoplastic Seismic Shear Response of Earth Dams: Theory. *Journal of Engineering Mechanics* 113(5), 689{701.
- Elia G., Amorosi A., Chan A.H.C., Kavvadas M.J. (2011). Fully coupled dynamic analysis of an earth dam. *Geotechnique*, 61, 549-563.
- Faccioli, E., Paolucci, R. (2005). *Elementi di sismologia applicate all'ingegneria*, Pitagora Ed., Bologna, Italy, 280 pp. (in Italian).
- Fazio, L. (2019). Definizione delle curve di fragilità per la diga in materiali sciolti nel comune di Arignano. Politecnico di Torino.
- Fell, R., Foster, M., Cyganiewicz, J., Sills, G., Vroman, N., Davidson, R. (2008). *Risk Analysis for Dam Safety: A Unified Method for Estimating Probabilities of Failure of Embankment Dams by Internal Erosion and Piping*. URS Australia Pty. Ltd., Sydney, New South Wales, Australia.
- Fell, R., Fry, J.J. (2013). State of the art on the likelihood of internal erosion of dams and levees by means of testing. Chapter 1 In *Erosion in Geomechanics applied to dams and levees*. Edited by S. Bonelli. Wiley, Hoboken, and ISTE, London. 1–100
- Fell, R., MacGregor, P., Stapledon, D., Bell, G., Foster, M. (2014). *Geotechnical engineering of dams*, 2<sup>nd</sup> edition. Taylor & Francis Group.
- FEMA P-1032 (2015). *Evaluation and Monitoring of Seepage and Internal Erosion*. Interagency Committee on Dam Safety (ICODS)
- Field, E. H., Jordan, T.H., Cornell, C.A. (2003). OpenSHA - A developing Community- Modeling Environment for Seismic Hazard Analysis. In: *Seism. Res. Lett.* 74, pages 406– 419 (cited on pages 11, 17).
- Field, E. H., Biasi, G. P., Bird, P., Dawson, T. E., Felzer, K. R., Jackson, D. D., Johnson, K. M., Jordan T.H., Madden, C., Michael, A.J., Milner, K.R., Page, M.T., Parsons, T., Powers, P.M., Shaw, B.E., Thatcher, W.R., Weldon II, R.J., Zeng, Y. (2015). Long-term, time-dependent

probabilities for third Uniform California Earthquake Rupture Forecast (UCERF3). *Bulletin of the Seismological Society of America*, 105, 511– 543

Figura, F. (2020). Comportamento dinamico della diga in terra nel comune di Briaglia: definizione delle curve di fragilità. Politecnico di Torino.

Finn, WDL., Wu, G (2013). Dynamic analyses of an earthfill dam on over-consolidated silt with cyclic strain softening. Seventh international conference on case histories in geotechnical earthquake engineering, Chicago, April 29-May 4.

Foster, M.A., Fell, R. (1999a). Assessing embankment dam filters which do not satisfy design criteria. UNICIV Report No. R-376, ISBN 85841 343 4, ISSN 0077-880X, School of Civil and Environmental Engineering, The University of New South Wales, Sydney.

Foster, M., Fell, R., Spannagle, M. (2000a). The statistics of embankment dam failures and accidents, *Canadian Geotechnical Journal*, Vol. 37, No. 5, National Research Council Canada, Ottawa, 1000–1024.

Foster, M., Fell, R. (2001). Assessing embankment dam filters that do not satisfy design criteria. *Journal of Geotechnical and Geoenvironmental Engineering*, ASCE, Vol. 127, No. 5, 398–407.

Franklin, A.G., Chang, F.K. (1977). Earthquake resistance of earth and rock-fill dams: permanent displacements of earth embankments by Newmark sliding block analysis. US Army Engineer Waterways Experiment Station, CE, Vicksburg. Miscellaneous Paper S-71-17, Report 5.

Gaudio, D., Rauseo, R., Masini, L., Rampello, S. (2020). Semi-empirical relationships to assess the seismic performance of slopes from an updated version of the Italian seismic database. *Bulletin of Earthquake Engineering*, 18, 6245–6281.

Gazetas, G., Dakoulas, P. (1992). Seismic analysis and design of rockfill dams: state-of-the-art. *Soil Dynamics and Earthquake Engineering* 11, 27-61.

GEM (2019). The OpenQuake-engine User Manual. Global Earthquake Model (GEM) Open-Quake Manual for Engine version 3.4.0.

Gospe T., Zimmaro P., Wang P., Buckreis T., Ahdi S.K., Yong A.K., Brandenberg S.J., Stewart J.P. (2020). Supplementing shear wave velocity profile database with microtremor-based H/V spectral ratios. 17th World Conference on Earthquake Engineering (WCEE), Sendai (Japan).

Goulet, C.A., Stewart, J.P. (2009). Pitfalls of deterministic application of nonlinear site factors in probabilistic assessment of ground motions *Earthq. Spectra*, 25(3): 541–555.

Groholski, D., Hashash, Y., Kim, B., Musgrove, M., Harmon, J., and Stewart, J. (2016). Simplified Model for Small-Strain Nonlinearity and Strength in 1D Seismic Site Response Analysis. *J. Geotech. Geoenviron. Eng.*

- Grünthal, G. (Ed.) (1998). European Macroseismic Scale 1998, Cahiers du Centre Européen de Géodynamique et de Seismologie, 15, Conseil de l'Europe, Luxembourg, 99 pp.
- Ha, S. J., Han, S. W. (2016a). A method for selecting ground motions that considers target response spectrum mean and variance as well as correlation structure. *Journal of Earthquake Engineering* 20(8), 1263–1277.
- Ha, S. J., Han, S. W. (2016b). An efficient method for selecting and scaling ground motions matching target response spectrum mean and variance. *Earthquake Engineering and Structural Dynamics*, 45(8), 1381–1387.
- Harder, F. L. Jr, Kelson, I. K., Kishida, T., Kayen, R. (2011). Preliminary Observations of the Fujinuma Dam Failure Following the March 11, 2011 Tohoku Offshore Earthquake, Japan. *Geotechnical Extreme Events Reconnaissance (GEER)*, Berkeley, California.
- Hashash Y.M.A., Musgrove M.I., Harmon J.A., Groholski D.R., Phillips C.A., Park D. (2016). DEEPSOIL 6.1, User Manual.
- Hatanaka, M., Uchida, A. (1996). Empirical correlation between penetration resistance and effective friction angle of sandy soil. *Soils Found*, 36(4): 1–9.
- Hegazy, A.Y., Mayne W.P. (1995). Statistical correlations between VS and cone penetration data for different soil types. In: *Proceedings of International Symposium on Cone Penetration Testing, CPT '95, Linkoping, Sweden, Vol. 2*, pp. 173–178.
- Hynes-Griffin, M.E., Franklin A.G. (1984). Rationalizing the seismic coefficient method, Miscellaneous paper GL-84-13, U.S. Army corps of engineers, Waterways experiment station, Vicksburg, Mississippi.
- ICOLD(2020). [https://www.icold-cigb.org/article/GB/world\\_register/general\\_synthesis/general-synthesis](https://www.icold-cigb.org/article/GB/world_register/general_synthesis/general-synthesis). (last accessed, January 2021).
- Idriss, I.M., (1999). An update to the Seed-Idriss simplified procedure for evaluating liquefaction potential, in *Proceedings, TRB Workshop on New Approaches to Liquefaction*, Publication No. FHWA-RD-99-165, Federal Highway Administration, January.
- Idriss, I.M., Boulanger, R.W., (2003a). Estimating  $K_\alpha$  for use in evaluating cyclic resistance of sloping ground, in *Proceedings, 8<sup>th</sup> US-Japan Workshop on Earthquake Resistant Design of Lifeline Facilities and Countermeasures against Liquefaction*, Hamada, O'Rourke, and Bardet, eds., Report MCEER-03-0003, MCEER, SUNY Buffalo, NY, pp. 449–68.
- Idriss, I.M., Boulanger, R.W., (2003b). Relating  $K_\alpha$  and  $K_\sigma$  to SPT blow count and to CPT tip resistance for use in evaluating liquefaction potential, in *Proceedings of the 2003 Dam Safety Conference, ASDSO, September 7–10, Minneapolis, MN*.
- Idriss, I. M., Boulanger, R. W. (2006). Semi-empirical procedures for evaluating liquefaction potential during earthquakes. *Soil Dyn. Earthquake Eng.*, 26, 115–130.

- Idriss, I. M., Boulanger, R. W. (2008). Soil liquefaction during earthquakes. Monograph MNO-12, Earthquake Engineering Research Institute, Oakland, CA, 261 pp.
- Idriss, I. M., Boulanger, R. W. (2010). SPT-based liquefaction triggering procedures. Report UCD/CGM-10/02, Department of Civil and Environmental Engineering, University of California, Davis, CA, 259 pp.
- Iervolino, I., Giorgio, M., Galasso, C., Manfredi, G., (2010). Conditional hazard maps for secondary intensity measures, *Bulletin of the Seismological Society of America* 100, 3312–3319.
- Ishihara, K. (1993). Liquefaction and flow failure during earthquakes. *Geotechnique* 43(3), 351–415.
- Ishihara, K. (1996). *Soil Behavior in Earthquake Geotechnics*. The Oxford Engineering Science Series, No. 46.
- Ishihara, K. (2010). Performances of rockfill dams during recent large earthquakes. Fifth International Conference on Recent Advances in Geotechnical Earthquake Engineering and Soil Dynamics, (p. 1-11). San Diego, California.
- Italian Ministry of Infrastructures (2004). Testo del decreto-legge 29 marzo 2004, n. 79 (in *Gazzetta Ufficiale - serie generale - n. 75 del 30 marzo 2004*), coordinato con la legge di conversione 28 maggio 2004, n. 139, recante: Disposizioni urgenti in materia di sicurezza di grandi dighe e di edifici istituzionali. (in Italian).
- Itasca (2019) - *FLAC – Fast Lagrangian Analysis of Continua – Version 8.1, User’s Guide*, Itasca Consulting Group, Minneapolis, USA.
- Jamiolkowski, M., Ladd, C. C., Germaine, J. T., Lancellotta, R. (1985). New developments in field and laboratory testing of soils, *Proceedings of 11th International Conference on Soil Mechanics and Foundation Engineering*, Vol. 1, San Francisco, pp. 57–153.
- Jappelli R. (2003) Le costruzioni geotecniche per le grandi dighe in Italia, Terza conferenza “Arrigo Croce”. *Italian Geotechnical Journal*, 3, 17-78.
- Jafari, MK, Shafiee, A., Ramzkhah, A. (2002). Dynamic properties of the fine grained soils in south of Tehran. *Journal of Seismology and Earthquake Engineering*, 4 (1), pp. 25–35.
- Jayaram, N., Lin, T., and Baker, J. W. [2011] A computationally efficient ground-motion selection algorithm for matching a target response spectrum mean and variance. *Earthquake Spectra*, 27 (3), 797–815.
- Jin, C., Chi, S. (2019). Seismic fragility analysis of high earth-rockfill dams considering the number of ground motion records. *Mathematical Problems in Engineering* 6958643: 12.
- Kaklamanos, J., Baise, L. G., Boore, D. M., (2011). Estimating unknown input parameters when implementing the NGA ground motion prediction equations in engineering practice, *Earthquake Spectra* 27, 1219–1235

- Kaklamanos, J., L. G. Baise, E. M. Thompson, L. Dorfmann (2015). Comparison of 1D linear, equivalent-linear, and nonlinear site response models at six KiK-net validation sites. *Soil Dynamics and Earthquake Engineering* 69: 207-219.
- Karimi, Z., Dashti, S. (2017). Ground motion intensity measures to evaluate II: The performance of shallow-founded structures on liquefiable ground, *Earthquake Spectra* 33, 277-298.
- Kayen, R.E., Moss, R. E. S., Thompson, E. M., Seed, R. B., Cetin, K. O., Kiureghian, A. D., Tanaka, Y., & Tokimatsu, K. (2013). Shear-wave velocity-based probabilistic and deterministic assessment of seismic soil liquefaction potential. *Journal of Geotechnical and Geoenvironmental Engineering*, 139(3), 407-419.
- Khosravifar, A., Boulanger, R.W., Kunnath, S.K., (2014). Effects of liquefaction on inelastic demands on extended pile shafts. *Earthquake Spectra*, 30, 1749-1773.
- Kim, J-T., Kim, D-S., Park, H-J., Kwon, H-K. (2009). Estimation of dynamic material properties for fill dam: I. In-situ shear wave velocity profiles. *Journal of the Korean Geotechnical Society*, 25, pp. 69-85.
- Kim, B., Hashash, Y. M. A. (2013). Site Response Analysis Using Downhole Array Recordings during the March 2011 Tohoku-Oki Earthquake and the Effect of Long-Duration Ground Motions. *Earthquake spectra* 29: S37-S54.
- Kim, B., Y. M. Hashash, J. P. Stewart, E. M. Rathje, J. A. Harmon, M. I. Musgrove, K. W. Campbell, W. J. Silva (2016). Relative differences between nonlinear and equivalent-linear 1-D site response analyses, *Earthquake Spectra* 32, 1845-1865.
- Kottke, A., and Rathje, E. M. (2008). A semi-automated procedure for selecting and scaling recorded earthquake motions for dynamic analysis. *Earthquake Spectra*, 24(4), 911-932.
- Kramer S.L. (1996) *Geotechnical earthquake engineering*, Upper Saddle River, N.J.: Prentice Hall.
- Kramer, S.L. and Mitchell, R.A. (2006). An Efficient and Sufficient Scalar Intensity Measure for Soil Liquefaction. *Earthquake Spectra*, Vol. 22, No. 2, pp. 1-26.
- Krawinkler, H., E. Miranda. (2004). Chapter 9 - Performance-Based Earthquake Engineering. *Earthquake Engineering*, Y. Bozorgnia, V. V. Bertero, eds. CRC Press.
- Kuhl, J (2011) Memorandum of design review James J. Lenihan Dam No. 72-8 Santa Clara County. California Division of Safety of Dams, pp. 1-27.
- Kuhlemeyer, R.L. Lysmer, J. (1973). Finite element method accuracy for wave propagation problems. *Journal of the Soil Mechanics and Foundations Division* 99(SM5): 421-427.
- Kulhawy, F.H., Mayne, P.H., (1990). Manual on estimating soil properties for foundation design, Report EL-6800 Electric Power Research Institute, EPRI, August 1990

- Kwok, A.O., Stewart, J.P., Hashash, Y.M.A, Matasovic, N., Pyke, R., Wang, Z., Yang, Z. (2007). Use of exact solutions of wave propagation problems to guide implementation of nonlinear seismic ground response analysis procedures, *J. Geotech. & Geoenviron. Engr., ASCE* 133 (11), 1385- 1398.
- Ladd, C. C., DeGroot, D. J. (2003). Recommended practice for soft ground site characterization: Arthur Casagrande lecture. Proc., Soil and Rock America, P. J. Culligan, H. H. Einstein, and A. J. Whittle, eds., Verlag Gluckauf GMBH, Essan, Germany, Vol. 1, 3-57.
- Ladd, C. C., and Foott, R. (1974). New design procedure for stability of soft clays. *J. Geotech. Engrg. Div.*, 100(7), 763-786.
- Ladd, C. C., Foott, R., Ishihara, K., Schlosser, F., and Poulos, H. G. (1977). Stress-deformation and strength characteristics, Proceedings of 9th International Conference on Soil Mechanics and Foundation Engineering, Tokyo, pp. 421-494.
- Lanzo, G. (2018). Alcune considerazioni sulla rivalutazione della sicurezza sismica delle dighe di materiali sciolti. In Proceedings of Conferenze di Geotecnica di Torino - XXV Ciclo, Analisi e Progetto delle Opere Geotecniche in Zona Sismica. Politecnico di Torino (In Italian).
- Lee, K. L., and Seed, H. B., (1967). Drained strength characteristics of sands, *J. Soil Mechanics and Foundations Div., ASCE* 93(SM6), 117-41.
- Lee, S.HH. (1992). Analysis of the multicollinearity of regression equations of shear wave velocities. *Soils and Foundations*, 32(1), pp. 205-214.
- Li, W., Assimaki, D. (2011). Site and motion-dependent parametric uncertainty of site-response analyses in earthquake simulations, *Bull. Seismol. Soc. Am.*, 100, 954-968.
- Liao, S. C., and Whitman, R. V. (1986). Overburden correction factors for SPT in sand, *J. Geotechnical Eng., ASCE* 112(3), 373-77.
- Licata, V., Forte, G., Ebrahimian, H., d’Onofrio, A., Jalayer, F., Santo, A., Silvestri, F. (2019). Evaluation of the seismic ground amplification considering the variability of the bedrock depth and random shear wave velocity profiles. Proc., 7th Int. Conf. on Earthquake Geotechnical Engineering, edited by F. Silvestri and N. Moraci, 3601-3608. Rome: Associazione Geotecnica Italiana.
- Lin, T., Harmsen, S. C., Baker, J. W., Luco, N. (2013a). Conditional spectrum computation incorporating multiple causal earthquakes and ground motion prediction models. *Bulletin of the Seismological Society of America*, 103(2A), 1103-1116.
- Lin, T., Haselton, C. B., Baker, J. W. (2013b). Conditional spectrum-based ground motion selection. Part I: Hazard consistency for risk-based assessments. *Earthquake Engineering and Structural Dynamics*, 42(12), 1847-1865.
- Lowe, J., Karafiath, L. (1959). Stability of earth dams upon drawdown. Proc., 1st PanAmerican Conference on Soil Mechanics and Foundation Eng., Mexico City, Vol. 2, 537-552.



- Lowe, J., Karafiath, L. (1960). Effect of anisotropic consolidation on the undrained shear strength of compacted clays. Proc., Research Conference on Shear Strength of Cohesive Soils, Boulder, Colo., June, 837-858.
- Lunne, T., Robertson, P.K. Powell, J.J.M. (1997) Cone Penetration Testing in Geotechnical Practice. Blackie Academic & Professional, London, 312 p.
- Lupoi A., Callari C. (2011). A probabilistic method for the seismic assessment of existing concrete gravity dams. *Structure and Infrastructure Eng*, 8, 985–998.
- Lysmer, J., Kuhlemeyer, L. (1969). Finite dynamic model for infinite media. *Journal of Geotechnical engineering mechanics*, 95(EM4), 859-877.
- Madabhushi, S. P. G., Haigh, S. K. (2001). The Bhuj, India Earthquake of 26th January 2001, Technical Report A Field Report by EEFIT, Society for Earthquake and Civil Engineering Dynamics, Institution of Structural Engineers, London.
- Makdisi F. I., Seed, H.B. (1977). A simplified procedure for estimating earthquake induced deformations in dams and embankments. Report n EERC 79—19. University of California, Berkeley.
- Makdisi, F. I., Seed, H. B. (1978). Simplified procedure for estimating dam and embankment earthquake-induced deformations. *Journal of Geotechnical Engineering, ASCE* 104(7), 849-867.
- Malvick, E.J., Kutter, B.L., Boulanger, R.W., Kulasingam, R. (2006). Shear localization due to liquefaction-induced void redistribution in a layered infinite slope, *J. Geotech. & Geoenv. Eng., ASCE*, 132 (10). 1293-1303.
- Masini, L., Rampello, S., Donatelli, R. (2020). Seismic performance of two classes of earth dams. *Earthquake Engineering and Structural Dynamics*.
- Masini, L., Rampello, S. (2020). Influence of Input Assumptions on the Evaluation of the Seismic Performance of Earth Dams. *Journal of Earthquake Engineering*.
- Matsumoto, N., Sasaki, T., Ohmachi, T. (2011). The 2011 Tohoku Earthquake and Dams. ICOLD 89th Annual Meeting in Lucerne. Japan Commission on Large Dams. June 1, 2011.
- Mayne, W.P., Rix, J.G. (1995). Correlations between shear wave velocity and cone tip resistance in natural clays. *Soils and Foundations*, 35(2), pp. 107–110.
- Mayne, W.P. (2006). Undisturbed sand strength from seismic cone tests. The 2nd James K. Mitchell Lecture. *J. Geomech. and Geoenng*, 1(4)L 239-258.
- Mayne, W.P. (2006) In situ test calibrations for evaluating soil parameters. In: *Proceedings of Characterization and Engineering Properties of Natural Soils II*, Singapore.
- Mayne, W.P. (2007). Cone penetration testing state-of-practice. NCHRP Project 20-05 Topic 37-14.

- McGuire, R. K. (1995). Probabilistic Seismic Hazard Analysis and Design Earthquake: Closing the Loop. In: *Bulletin of the Seismological Society of America* 85.5, pages 1275–1284 (cited on page 18).
- Menq, Farn-Yuh (2003). *Dynamic Properties of Sandy and Gravelly Soils*, Department of Civil, Architectural and Environmental Engineering, The University of Texas, Austin, Texas.
- Michelini, A., Faenza, L., Lauciani, V., Malagnini, L. (2008). ShakeMap implementation in Italy. *Seism. Res. Lett.*, 79, 688-697.
- Ministero delle Infrastrutture e dei Trasporti (2014). *Norme tecniche per la progettazione e la costruzione degli sbarramenti di ritenuta (dighe e traverse)*, NTD. Decreto Ministeriale, D.M. 26 giugno 2014. *Gazzetta Ufficiale della Repubblica Italiana* 156.
- Ministero delle Infrastrutture e dei Trasporti (2018). *Aggiornamento delle Norme Tecniche per le Costruzioni*, D.M. 17 Gennaio 2018. *Gazzetta Ufficiale della Repubblica Italiana*, 42.
- Ministero delle Infrastrutture e dei Trasporti, Dipartimento per le infrastrutture, i sistemi informativi e statistici, Direzione generale per le dighe e le infrastrutture idriche ed elettriche (2019). *Verifiche Sismiche delle Grandi dighe, degli Scarichi e delle opere Complementari e Accessorie*; Circ. D.G. Dighe 18 marzo 2019, n. 6660.
- Mitchell, K.J. (2008). *Recent Developments in Ground Improvement for Mitigation of Seismic Risk to Existing Embankment Dams*. In: *Geotechnical Earthquake Engineering and Soil Dynamics Congress IV*, Sacramento, California.
- Moho s.r.l. (2021). Tromino, available at: <https://moho.world/en/>, last accessed February, 2021.
- Montgomery, J., R. W. Boulanger, R. J. Armstrong, E. J. Malvick. (2014). Anisotropic undrained shear strength parameters for non-linear deformation analyses of embankment dams. In *Geo-Congress 2014: Geo-Characterization and Modeling for Sustainability*, Geotechnical Special Publication 234, 1294–1306. Reston, VA: ASCE.
- Moss, R.E.S., Seed, R.B., Kayen, R.E., Stewart, J.P., Der Kiureghian, A., Cetin, K.O. (2006). CPT-based probabilistic and deterministic assessment of in situ seismic soil liquefaction potential. *Journal of Geotechnical & Geoenvironmental Engineering* 132: 1032–1051.
- MPS working group (2004). *Redazione della mappa di pericolosità sismica prevista dall'Ordinanza PCM del 20 marzo 2003 n. 3274, All. 1. Rapporto conclusivo per il Dipartimento della Protezione Civile, Istituto Nazionale di Geofisica e Vulcanologia (INGV), Milano-Roma, Italy*, available at <http://zonesismiche.mi.ingv.it/> (last accessed January 2021), 163 pp. In Italian.
- Musson, R.M.W. (2000). Intensity-based seismic risk assessment. *Soil Dynamics and Earthquake Engineering*. 20 (5–8): 353–360.
- Musson, R. M. W., Grünthal, G. Stucchi, M. (2010). The comparison of macroseismic intensity scales. *J. Seismol.*, 14, 413-428.

- Musson, R. M., Cčić, I. (2012). Intensity and Intensity Scales. - In: Bormann, P. (Ed.), *New Manual of Seismological Observatory Practice 2 (NMSOP-2)*, Potsdam: Deutsches GeoForschungsZentrum GFZ, 1-41.
- Naeim, F., Lew, M. (1995). On the use of design spectrum compatible time histories. *Earthquake Spectra*; 11: 111–127.
- Naeim, F., Alimoradi, A., Pezeshk, S. (2004). Selection and scaling of ground motion time histories for structural design using genetic algorithms. *Earthquake Spectra* 20(2):413–426
- Nakamura, Y. (1989). A method for dynamic characteristics estimates of subsurface using microtremor on the ground surface. *QR of RTRI*, 30, 25–33.
- Newmark N.M. (1965) Effects of Earthquakes on Dams and Embankments, *Géotechnique*, 15(2): 139-160.
- Ono, K., Kazama S., Kawagoe, S., Yokoo, Y., Gunawardhana, L. (2011). Possible earthen dam failure mechanisms of Fujinuma reservoir due to the Great East Japan Earthquake of 2011. *Hydrol Res Lett* 2011;5:69–72.
- Ohta, Y., Goto, N. (1978). Empirical shear wave velocity equations in terms of characteristic soil indexes. *Earthquake Engineering Structural Dynamics*, 6: pp. 167–187.
- Padgett J., DesRoches, R. (2007). Sensitivity of seismic response and fragility to parameter uncertainty. *Journal of Structural Engineering*, 133, 1710–1718.
- Pagano, L., Fontanella E., Sica S., Desideri A. (2010). Pore water pressure measurements in the interpretation of the hydraulic behaviour of two earth dams, *Soils and Foundations*, 50, 295-307.
- Pagano, L., Sica, S. (2012). Earthquake early warning for earth dams: Concepts and objectives. *Nat. Hazards* 66, 303–318.
- Pagano, L., Russo, C., Sica, S., Costigliola, R. (2019). Limit states in earth dams during seismic and post-seismic stages. In: Silvestri, F., Moraci, N. (eds.) *Proceedings of the VII ICEGE 7th International Conference on Earthquake Geotechnical Engineering (Theme Lecture)*. Rome 17–20 June 2019. *Proceedings in Earth and geosciences*, vol. 4, pp. 600–616.
- Pagani, M., Monelli, D., Weatherill, G. A., Garcia, J. (2014). *The OpenQuake-engine Book: Hazard*. Global Earthquake Model (GEM) Technical Report 2014-08, doi: 10.13117/-GEM.OPENQUAKE.TR2014.08, 67 pages.
- Pagani, M., Monelli, D., Weatherill G.A., Danciu L., Crowley H., Silva V., Henshaw P., Butler L., Nastasi M., Panzeri L., Simionato M., Viganò D. (2014). OpenQuake Engine: An Open Hazard (and Risk) Software for the Global Earthquake Model, *Seismological Research Letters*, 85, 692-702.

- Papaspiliou, M., Kontoe, S., Bommer, J.J. (2012). An exploration of incorporating site response into PSHA-Part II: Sensitivity of hazard estimates to site response approaches. *Soil Dyn & Earthquake Eng.*, 42, 316–330.
- Park, D.S., Kishida, T. (2019). Shear modulus reduction and damping ratio curves for earth core materials of dams. *Canadian Geotechnical Journal*, 56, pp. 14-22.
- Park, D.S., Kishida, T. (2019) Seismic response of embankment dams based on recorded strong motion data in Japan. *Earthquake Spectra* 35(2): 955–976.
- Parker, G.A., Stewart, J.P., Boore, D.M., Atkinson, G.M., Hassani, B. (2020). NGA-Subduction Global Ground-Motion Models with Regional Adjustment Factors. PEER Report 2020/03 Pacific Earthquake Engineering Research Center Headquarters, University of California at Berkeley.
- Pelecanos, L. (2013). Seismic response and analysis of earth dams. PhD dissertation, Imperial College London, London, UK.
- Phillips, C., and Hashash, Y. M. A. (2009). Damping formulation for nonlinear 1D site response analyses. *Soil Dyn. Earthquake Eng.*, 29(7), 1143–1158.
- PEER ground motion database working group. (2010). Ground motion database and associated works [http://peer.berkeley.edu/peer\\_ground\\_motion\\_database](http://peer.berkeley.edu/peer_ground_motion_database). (B. University of California).
- PEER ground motion database working group. (2010). Technical report. (B. University of California).
- Pells, S., Fell, R. (2002). Damage and cracking of embankment dams by earthquakes, and the implications for internal erosion and piping. UNICIV Report R 406. The University of New South Wales, ISBN 85841 3752.
- Pells, S., Fell, R. (2003). Damage and cracking of embankment dams by earthquake and the implications for internal erosion and piping. Proc., 21st Internal Congress on Large Dams, Montreal. ICOLD, Paris Q83-R17, International Commission on Large Dams, Paris.
- Penman, A. D. M. (1986). On the embankment dam. *Geotechnique*, 36, pp. 301–348.
- Perlea, V.G., Beaty, M.H. (2010). Corps of Engineers practice in the evaluation of seismic deformation of embankment dams. Fifth international conference on recent advances in geotechnical earthquake engineering and soil dynamics, San Diego, paper SPL-6
- Pietrantonio, M., Tagliaferri, A., Petrangeli, M. (2013). Valutazione dell'affidabilità delle prove SPT per la caratterizzazione sismica dei terreni (Evaluation of the SPT test reliability in the seismic characterization of soils), *Rivista Italiana di Geotecnica*, 1, pp. 17-31.
- Piratheepan, P. (2002). Estimating Shear-Wave Velocity from SPT and CPT Data. Master of Science Thesis, Clemson University.

- Pitilakis, K., Raptakis, D., Lontzetidis, K., Tika-Vassilikou, Th, Jongmans, D. (1999). Geotechnical and geophysical description of Euro-Seistests, using field, and laboratory tests and moderate strong ground motions. *Journal of Earthquake Engineering*, 3(3), pp. 381–409.
- Porter, K., (2017). *A Beginner's Guide to Fragility, Vulnerability, and Risk*. University of Colorado Boulder, 103 pp.
- Pradel, D., Wartman, J., Tiwari, B. (2012). Failure of Fujinuma dam during the 2011 Tohoku earthquake. *Joint Conference Proceedings of the 9th International Conference on Urban Earthquake/ 4th Asia Conference on Earthquake Engineering (2012)* 6pp.
- Prevost, J. H. (1977). Mathematical modelling of monotonic and cyclic undrained clay behavior. *International Journal of Numerical and Analytical Methods in Geomechanics* 1(2), 195-216.
- Rathje, E. M., Bray, J. D. (1999). An examination of simplified earthquake-induced displacement procedures for earth structures. *Canadian Geotechnical Journal* 36, 72-87.
- Rathje, E. M., Kottke, A. R., Trent, W.L., (2010). Influence of input motion and site property variabilities on seismic site response analysis, *J. Geotech. Geoenv. Eng.*, 136, 607–619.
- Rathje, M. E., Saygili, G. (2011). Estimating Fully Probabilistic Seismic Sliding Displacements of Slopes from a Pseudoprobabilistic Approach. *Journal of Geotechnical and Geoenvironmental Engineering*, Volume 137 Issue 3 – March 2011.
- Rathje, E. M., Pehlivan, M., Gilbert, R., Rodriguez-Marek, A. (2015). Incorporating site response into seismic hazard assessments for critical facilities: A probabilistic approach. In *Perspectives on Earthquake Geotechnical Engineering*, Springer International Publishing, 93–111.
- Regina G., Cairo R., Zimmaro P. (2019). Risposta sismica locale di una diga in terra. *Proceedings Incontro Annuale dei Giovani Ingegneri Geotecnici (IAGIG)*, Naples (Italy), May 10-11.
- Regina G., Cairo R., Zimmaro P. (2019). Ground response analyses for a zoned earth dam site in Southern Italy. *7th Italian National Congress of Geotechnical Researchers (CNRIG2019)*, Lecco (Italy), July 3-5. *Lecture Notes in Civil Eng*, 40, 148-154.
- Reiter, L. (1990). *Earthquake Hazard Analysis: Issues and Insights*. Columbia University Press: New York, 254.
- Reséndiz, D., Romo, M. P., Moreno, E. (1982). El Infernillo and La Villita dams: seismic behavior', *Journal of the Geotechnical Engineering Division, ASCE* 108(GT1), 109-131.
- Robertson, P.K., Wride, C.E. (1998). Evaluating cyclic liquefaction potential using the cone penetration test. *Canadian Geotechnical Journal* 35(3): 442–459.

- Robertson, PK. (2009). Interpretation of cone penetration tests – a unified approach, *Canadian Geotech. J.*, 46(11):1337–1355.
- Robertson, PK. (2010). Estimating in-situ soil permeability from CPT & CPTu, 2nd International Symposium on Cone Penetration Testing, Huntington Beach, CA, USA, May 2010.
- Rodriguez-Marek, A., Cotton, F., Abrahamson, N. A., Akkar, S., Al Atik, L., Edwards, B., Montalva, G. A., Dawood, H.M. (2013). A model for single-station standard deviation using data from various tectonic regions, *Bull. Seismol. Soc. Am.* 103, 3149–3163.
- Rodriguez-Marek, A., Rathje, E.M., Bommer, JJ., Scherbaum, F., Stafford, P. J., (2014). Application of single-station sigma and site response characterization in a probabilistic seismic hazard analysis for a new nuclear site, *Bull. Seismol. Soc. Am.* 104: 1601–1619.
- Rollins, K., Evans, M., Diehl, N., & Daily, W. (1998). Shear Modulus and Damping Relationships for Gravels. *Journal of Geotechnical and Geoenvironmental Engineering*, 396-405.
- Sabetta, F., Pugliese A. (1996). Estimation of response spectra and simulation of nonstationary earthquake ground motions, *Bull. Seismol. Soc. Am.*, 86, 337-352.
- Sarma, S. K. (1973). Stability analysis of embankments and slopes. *Geotechnique* 23(3), 423-433.
- Saygili, G., Rathje, M. E. (2008). Empirical predictive models for earthquake-induced sliding displacements of slopes. *Journal of Geotechnical and Geoenvironmental Engineering*, Volume 134 Issue 6 – June 2008.
- Scasserra G., Pagliaroli A., Lanzo G. (2014). Verifica sismica di una diga in terra: confronto tra analisi dinamiche complete e agli spostamenti. *Incontro Annuale Ricercatori di Geotecnica, Chieti e Pescara*, Luglio 14-16.
- Scherbaum, F., Kuehn, N.M., Ohrnberger, M., Koehler, A. (2010). Exploring the proximity of ground-motion models using high-dimensional visualization techniques. *Earthquake Spectra* 26 (4), 1117–1138.
- Schwartz, D.P., Coppersmith, K.J. (1984). Fault behavior and characteristic earthquakes: examples from the Wasatch and San Andreas fault zones. *Journal of Geophysical Research*, Vol. 89, No. B7, pp. 5681-5698.
- Sêco e Pinto P. (2015). Lessons Learned From Dams Behavior Under Earthquakes. In: Ansal A., Sakr M. (eds) *Perspectives on Earthquake Geotechnical Engineering. Geotechnical, Geological and Earthquake Engineering*, vol 37. Springer, Cham.
- Seed, H. B., Martin, G. R. (1966). The seismic coefficient in earth dam design. *Journal of the Soil Mechanics and Foundations Division, ASCE*92(SM3), 25-58.

- Seed, H. B., Lee, K. L., Idriss, I. M. (1969). Analysis of Sheffield Dam failure. *J. Soil Mech. Fdn Div., Am. Soc. Civ. Engrs* 9.5, No. SM6, Proceedings Paper 6906, 1453-1490.
- Seed, H.B, Idriss IM (1970). Soil moduli and damping factors for dynamic response analyses. Technical Report EERRC-70-10, University of California, Berkeley
- Seed, H.B., Idriss, I. M. (1971). Simplified procedure for evaluating soil liquefaction potential, *J. Soil Mechanics and Foundations Div., ASCE* 97(SM9), 1249–273.
- Seed, H.B., Martin P.P. and Lysmer J. (1975). The Generation and Dissipation of Pore Water Pressures during Soil Liquefaction, University of California, Berkeley, Earthquake Engineering Research Center, NSF Report, 252 648.
- Seed, H.B., Idriss, I.M., Lee, K.L., Makdisi, F.I. (1975). Dynamic Analysis of the Slide in the Lower San Fernando Dam during the Earthquake of February 9, 1971 – ASCE, *J of the Geotechnical Engineering Division, GT9*, pp. 889-911.
- Seed, H. B., Idriss, I. M. (1982). Ground motions and soil liquefaction during earthquakes. Earthquake Engineering Research Institute (EERI), MNO-05 Berkeley, CA.
- Seed, H.B. (1979). Soil liquefaction and cyclic mobility evaluation for level ground during earthquakes. *J. Geotech. Engrg. Div.*, 105(2), 201–255.
- Seed, H.B. (1979a). Consideration in the earthquake resistant design of earth and rockfill dams. *Geotechnique* 29, 215–263.
- Seed, H. B. (1981). Earthquake-Resistant Design of Earth Dams. In: First International Conference on Recent Advances in Geotechnical Earthquake Engineering & Soil Dynamics, Rolla, Missouri.
- Seed, H. B. (1983). Earthquake resistant design of earth dams. In Proceedings, Symposium on Seismic Design of Embankments and Caverns, Pennsylvania, ASCE, NY, pp. 41–64.
- Seed, H. B., et al. (2003). Recent advances in soil liquefaction engineering: A unified and consistent framework. Keynote Presentation, 26<sup>th</sup> Annual ASCE Los Angeles Geotech. Spring Seminar, Long Beach, Calif.
- SESAME (2004). Guidelines for the Implementation of the H/V spectral ratio technique on ambient vibrations—Measurements, processing and interpretation: European Commission, Project No. EVG1-CT-2000-00026.
- Seyhan, E., Stewart, J. P. (2014). Semi-empirical nonlinear site amplification from NGAWest2 data and simulations, *Earthquake Spectra* 30, 1241–1256.
- Sherard, J. L. (1967). Earthquake considerations in earth dam design. *J. Soil Mech. Dir., Am. Soc. Civ. Engrs* 93, No. SM4, Proceedings Paper 5322, 377-401.
- Sherard, J.L. (1973). Embankment Dam Cracking. *Embankment Dam Engineering*, S. Poulos and R. Hirschfeld, Eds., John Wiley and Sons, New York, N.Y., pp. 272–353.

- Sherard, J.L., Dunnigan, L.P. (1985). Filters and leakage control, in embankment dams, in Seepage and Leakage from Dams and Impoundments. ASCE Geotechnical Engineering Division Conference, 1–30.
- Shewbridge, S. (2019). Undrained Strengths and Long-Term Stability of Slopes. *Journal of Geotechnical and Geoenvironmental Engineering* Vol. 145, Issue 11.
- Sica, S., de Magistris Santucci, F., Vinale, F. (2002). Seismic behaviour of geotechnical structures. *Ann Geophys* 45(6):799–815
- Sieberg, A. (1923). *Geologische, physikalische und angewandte Erdbebenkunde*. Verlag Gustav Fischer, Jena, 572 S.
- Sieberg, A. (1932). *Geologie der Erdbeben*. Handbuch der Geophysik, Gebrüder Bornträger, Berlin, vol. 2, pt 4, 550-555.
- Silvestri, F., d’Onofrio, A. (2014). Risposta sismica e stabilità di centri abitati e infrastrutture. In: XXV Convegno Nazionale di Geotecnica, Baveno, 4-6 giugno, *La geotecnica nella difesa del territorio e delle infrastrutture dalle calamità naturali*, 5-60.
- Sponheuer, W., Karnik, V. (1964). Neue seismische Skala, In: Sponheuer, W., (Ed.), Proc. 7th Symposium of the ESC, Jena, 24-30 Sept. 1962, Veröff. Inst. f. Bodendyn. u. Erdbebenforsch. Jena d. Deutschen Akad. d. Wiss., No 77, 69-76.
- Stewart J.P, Chiou S.J., Bray J.D., Graves R.W., Somerville P., Abrahamson N.A. (2002). Ground motion evaluation procedures for performance-based design. *Soil Dynamics and Earthquake Engineering*, 22, 765–772.
- Stewart, J. P., Lanzo, G., Pagliaroli, A., Scasserra, G., Di Capua, G., Peppoloni, S., Darragh, R. B., and Gregor, M. (2012). Ground motion recordings from the Mw 6.3 2009 L’Aquila earthquake in Italy and their engineering implications. *Earthquake Spectra* 28, 317–345.
- Stewart, J.P., Afshari K., Hashash Y.M.A. (2014). Guidelines for performing hazard-consistent one-dimensional ground response analysis for ground motion prediction. PEER Report No. 2014/16, Pacific Earthquake Engineering Research Center, UC Berkeley, CA.
- Stewart, J.P., Douglas, J., Javanbarg, M., Abrahamson, N.A., Bozorgnia, Y., Boore, D.M., Campbell, K.W. Delavaud, E., Erdik, M., Stafford, P.J. (2015). Selection of ground motion prediction equations for the Global Earthquake Model. *Earthquake Spectra*, 31(1):19-45
- Stewart, J.P., Afshari, K., Goulet, C. A. (2017b). Non-ergodic site response in seismic hazard analysis. *Earthquake Spectra*, 33, 1385–1414.
- Stewart, J. P., Wang, P., Teague, D., Vecchiotti, A. (2019). Applications of non-ergodic site response in ground motion modeling. In Proc. 7<sup>th</sup> Int. Conf. Earthquake Geotechnical Engineering. Rome: Associazione Geotecnica Italiana.
- Stucchi M., Meletti C., Montaldo V., Crowley H., Calvi G.M., Boschi E. (2011) Seismic hazard assessment (2003–2009) for the Italian building code, *Bull Seismol Soc Am* 101:1885–1911.



- Swaisgood, J. R. (1998). Seismically-induced deformation of embankment dams, Proc., 1998 U.S. National Conference on Earthquake Engineering, Seattle, Washington.
- Swaisgood, J. R. (2003). Embankment dam deformations caused by earthquakes, Proc., 2003 Pacific Conference on Earthquake Eng., Christchurch, New Zealand.
- Swaisgood, J. R. (2014). Behavior of embankment dams during earthquake, Journal of Dam Safety, ASDSO, 12(2): 35-44.
- Tekie P.B., Ellingwood B. (2003). Seismic fragility assessment of concrete gravity dams. Earthquake Engineering and Structural Dynamics, 32, 2221–2240.
- Thompson, E.M., Baise L.G., Tanaka Y., Kayen R.E. (2012). A taxonomy of site response complexity, Soil Dyn. Earthquake. Eng., 41: 32–43.
- Toro G.R. (1995). Probabilistic models of site velocity profiles for generic and site-specific ground-motion amplification studies, Technical Report No. 779574, Brookhaven National Laboratory, Upton, NY.
- Tropeano, G., Ausilio, E., Costanzo, A., Silvestri, F. (2008). Previsioni di spostamenti sismici di pendii omogenei con diverse procedure semplificate. Incontro Annuale dei Ricercatori di Geotecnica, IARG, Catania.
- Tropeano, G., Silvestri, F., Ausilio, E. (2017). An uncoupled procedure for performance assessment of slopes in seismic conditions Bull Earthq Eng, 15 (9), pp. 3611-3637.
- Trifunac, M.B., Brady, A.G. (1975). A study on the duration of strong earthquake ground motion. Bulletin of the Seismological Society of America, 65(3): 581-626
- U.S. Department of the Interior, Bureau of Reclamation (2011). Design Standards No. 13 Embankment Dams, Chapter 5: Protective Filters. Design Standards No. 13, chapter 5, revision 9.
- USACE (2011). Safety of dams-policy and procedures. ER 110-2-1156, US Army Corps of Engineers, Washington, October 28, p 430.
- USSD (2014). Observed performance of dams during earthquakes. Volume III, USSD Committee on Earthquakes ed., United States Society on Dams, Denver, CO, USA.
- Vaid, Y. P., Finn, W. D. L., (1979). Static shear and liquefaction potential, J. Geotechnical Div., ASCE
- Vaid, Y. P., Chern, J. C., (1985). Cyclic and Monotonic Undrained Response of Saturated Sands, Advances in the Art of Testing Soils under Cyclic Conditions, ASCE, NY, 120–47.
- Vaid, Y. P., and Sivathayalan, S., (1996). Static and cyclic liquefaction potential of Fraser Delta sand in simple shear and triaxial tests, Canadian Geotechnical J. 33, 281–89. 105(GT10), 1233–246.

- Vecchietti, A., Stewart, J.P., Cecconi, M., Pane, V., Russo, G. (2019). Non-ergodic site response model based on local recordings for Menta Dam site. Proc. 7th International Conference on Earthquake Geotechnical Engineering, Rome, 17-20 June 2019.
- Vecchietti, A., Cecconi, M., Russo, G., Pane, V. (2019). Seismic vulnerability of a rockfill dam through different displacement-based approaches. *J Earthq Eng.*
- Vick, S., Dorey, R., Finn, W., Adams, R. (1993). Seismic Stabilization of St. Joe State Park Tailings Dams. In *Geotechnical Practice in Dam Rehabilitation* (L. Anderson, ed.), Geotechnical Special Publication 35, American Society of Civil Engineers, New York, pp. 402-415.
- Vucetic, M., Dobry, R. (1991). Effect of Soil Plasticity on Cyclic Response. *Journal of Geotechnical Engineering*, 117, pp. 89-107.
- Wald, D. J., Worden, C. B., Quitoriano, V., Pankow, K.L. (2005). ShakeMap manual: Technical manual, user's guide, and software guide. U.S. Geological Survey, Techniques and Methods 12-A1. Available at: <http://pubs.usgs.gov/tm/2005/12A01/>
- Wan, C.F., Fell, R. (2004c). Experimental investigation of internal instability of soils in embankment dams and their foundations. UNICIV Report No. 429, School of Civil and Environmental Engineering, The University of New SouthWales, Sydney.
- Wan, C.F., Fell, R. (2007). Investigation of internal erosion by the process of suffusion in Embankment dams and their foundations. In *Internal Erosion of Dams and their Foundations*. Editors R. Fell and J.J. Fry. Taylor and Francis, London. 219-234.
- Wan, C.F., Fell, R. (2008). Assessing the Potential of Internal erosion and Suffusion in Embankment Dams and Their Foundations. *Journal of Geotechnical and Geoenvironmental Engineering*, ASCE, Vol. 134, No. 3, 410-407.
- Wair, R. B., DeJong, T.J., Shantz, T. (2012). Guidelines for Estimation of Shear Wave Velocity Profiles. Pacific Earthquake Engineering Research Center (PEER), Berkeley, California, Rep. 08.
- Wartman, J, JD Bray, and RB Seed (2005). Shaking table modeling of seismically induced deformations in slopes, *J. Geotech. & Geoenviron. Engrg.*, ASCE, 131 (5), 610-622.
- Wang, W. (1979). Some findings in soil liquefaction, Water Conservancy and Hydroelectric Power Scientific Research Institute, Beijing, China.
- Wells D.L., Coppersmith K.J. (1994). New empirical relationships among magnitude, rupture length, rupture width, rupture area, and surface displacement, *Bull. Seismol. Soc. Am.*, 84, 974-1002.
- Wilson, R. C., Keefer, D. K. (1985), Predicting areal limits of earthquake-induced landslides, in J. I. Ziony, ed., *Evaluating earthquake hazards in the Los Angeles region - An earth sciences perspective*, USGS Professional, Paper 1360, pp. 317-345.

- Wong, I., Thomas, P. (2017) Comparing seismic hazard estimates for dams in the U.S. and their implications to risk. In: Proceedings of the 2017 association of state dam safety officials conference, San Antonio, TX, 10–14 September.
- Worden, C. B., Wald, D.J. (2016). ShakeMap manual online: Technical manual, user's guide, and software guide. U.S.1022 Geological Survey. Available at: <http://usgs.github.io/shakemap>
- Xu, T., Zhang, L. (2013). Simulation of Piping in Earth Dams Due to Concentrated Leak Erosion. Geo-Conference 2013.
- Yiagos, A. N., Prevost, J. H. (1991b). Two-phase elasto-plastic seismic response of earth dams: theory. *Soil Dynamics & Earthquake Engineering* 10(7), 357{370.
- Youd, T. L., Perkins, M. (1978). Mapping liquefaction-induced ground failure potential, *J. Geotechnical Eng. Div., ASCE* 104(GT4), 433–46.
- Youngs, R.R., Coppersmith, K.J. (1985). Implications of fault slip rates and earthquake recurrence models to probabilistic seismic hazard assessments. *Bulletin of the Seismological Society of America*, Vol. 75, No. 4, pp. 939-964.
- Youngs, RR., Power, MS., Wang, G., Makdisi, F., Chin, CC (2007). Design ground motion library (DGML) – tool for selecting time history records for specific engineering applications. In: Proceedings of SMIP07 seminar on utilization of strong-motion data, Sacramento
- Zhao, J.X., Liang, X., Jiang, F., Xing, H., Zhu, M., Hou, R., Zhang, Y., Lan, X., Rhoades, D.A., Irikura, K., Fukushima, Y., and Somerville, P.G. (2016a). Ground-motion prediction equations for subduction interface earthquakes in Japan using site class and simple geometric attenuation functions: *Bulletin of the Seismological Society of America*, 106, 1518-1534.
- Zhao, J.X., Jiang, F., Shi, P., Xing, H., Huang, H., Hou, R., Zhang, Y., Yu, P., Lan, X., Rhoades, D.A., Somerville, P.G., Irikura, K., and Fukushima, Y. (2016b). Ground-motion prediction equations for subduction slab earthquakes in Japan using site class and simple geometric attenuation functions: *Bulletin of the Seismological Society of America*, 106, 1535-1551.
- Zhao, J.X., Zhou, S.L., Gao, P.J., Zhang, Y.B., Zhou, J., Lu, M., and Rhoades, D.A. (2016c). Ground-motion prediction equations for shallow crustal and upper mantle earthquakes in Japan using site class and simple geometric attenuation functions: *Bulletin of the Seismological Society of America*, 106, 1552-1569.
- Zimmaro P. (2015). Seismic response of the Farneto del Principe dam in Italy using hazard-consistent and site-specific ground motions. PhD Dissertation, University Mediterranea, Reggio Calabria.
- Zimmaro P., Stewart J.P. (2017). Site-specific seismic hazard analysis for Calabrian dam site using regionally customized seismic source and ground motion models. *Soil Dynamics and Earthquake Engineering*, 94, 179-192.

Zimmaro P., Kwak D.Y., Stewart J.P., Brandenberg S.J., Balakrishnan A., Jongejan R., Ausilio E., Dente G., Xie J., Mikami A. (2017). Procedures from international guidelines for assessing seismic risk to flood control levees. *Earthquake Spectra*, 33 (3), 1191-1218.

Zimmaro P., Scasserra G., Stewart J.P., Kishida T., Tropeano G., Castiglia M., Pelekis, P. (2018). Strong ground motion characteristics from 2016 Central Italy earthquake sequence. *Earthquake Spectra*, 34, 1611-1637.

Zimmaro, P., Brandenberg, S.J., Stewart, J.P., Kwak, D.Y., Franke, K.W., Moss, R.E.S., Cetin, K.O., Can, G., Ilgac, M., Stamatakis J., Juckett, M., Mukherjee, J., Murphy, Z., Ybarra, S., Weaver, T., Bozorgnia, Y., Kramer, S.L. (2019). Next-Generation Liquefaction Database. Next-Generation Liquefaction Consortium.

Zimmaro P., Ausilio E. (2020). Numerical Evaluation of Natural Periods and Mode Shapes of Earth Dams for Probabilistic Seismic Hazard Analysis Applications. *Geosciences* 10 (12), 499.

Ziotopoulou, K., and Boulanger, R. W. (2013). Calibration and implementation of a sand plasticity plane-strain model for earthquake engineering applications. *Journal of Soil Dynamics and Earthquake Engineering*, 53, 268-280

Ziotopoulou K. and Boulanger, R.W. (2016). Plasticity modeling of liquefaction effects under sloping ground and irregular cyclic loading conditions. *J. Soil Dynamics and Earthquake Engineering*; 84:269-283.

## Appendix A: Ground motions adopted for the Multiple Stripe Analyses

The following Tables report the ground motions and their characteristics used to perform the Multiple Stripe Analyses, for the Farneto del Principe and the Angitola dam.

### Ground Motions for the Farneto del Principe dam

Return period, 75 years											
Earthquake				Station			Ground Motion Intensity Measure				
Name	Year	M	Style of faulting	Name	R <sub>jb</sub> [Km]	V <sub>S30</sub> [m/s]	PGA [g]	PGV [m/s]	AI [m/s]	CAV [m/s]	D5-95 [s]
14383980	2008	5.39	Reverse oblique	Los Angeles - Hollywood Blvd & Hillhurst	48.6	394.1	0.03	0.03	0.02	1.3	19.0
40204628	2007	5.45	Strike slip	Campbell	25.4	365.8	0.02	0.02	0.01	0.9	17.6
Chalfant Valley-01	1986	5.77	Strike slip	Lake Crowley - Shehorn Res.	24.4	456.8	0.05	0.02	0.02	1.1	14.6
Dinar, Turkey	1995	6.4	Normal	Burdur	35.6	468.4	0.04	0.04	0.04	1.9	16.4
Lazio-Abruzzo Italy	1984	5.8	Normal	Cassino-Sant'Elia	20.0	436.8	0.11	0.08	0.17	3.2	9.7
Livermore-01	1980	5.8	Strike slip	San Ramon - Eastman Kodak	15.2	377.5	0.06	0.08	0.08	2.4	14.2
Northridge-01	1994	6.69	Reverse	San Gabriel - E Grand Ave	38.9	401.4	0.14	0.08	0.44	5.8	14.3
San Simeon_ CA	2003	6.52	Reverse	Cambria - Hwy 1 Caltrans Bridge	7.0	362.4	0.18	0.13	0.44	5.6	10.5

Return period, 475 years											
Earthquake				Station			Ground Motion Intensity Measure				
Name	Year	M	Style of faulting	Name	R <sub>jb</sub> [Km]	V <sub>S30</sub> [m/s]	PGA [g]	PGV [m/s]	AI [m/s]	CAV [m/s]	D5-95 [s]
Big Bear-01	1992	6.46	Strike slip	Joshua Tree	41.0	379.3	0.06	0.06	0.10	3.4	18.6
Coalinga-05	1983	5.77	Reverse	Burnett Construction	8.3	352.2	0.34	0.17	0.90	6.1	6.2
Loma Prieta	1989	6.93	Reverse oblique	Sunol - Forest Fire Station	47.4	400.6	0.08	0.09	0.11	3.1	15.6
Morgan Hill	1984	6.19	Strike slip	Corralitos	23.2	462.2	0.08	0.07	0.06	2.0	9.7
Niigata-Japan	2004	6.63	Reverse	NIG024	29.1	375.2	0.22	0.09	0.91	10.5	14.2
Northridge-01	1994	6.69	Reverse	Leona Valley #5 - Ritter	37.5	375.2	0.09	0.10	0.20	4.1	16.0
Tottori-Japan	200	6.61	Strike slip	SMNH01	5.8	446.3	0.73	0.36	5.38	23.7	13.1

Return period, 710 years											
Earthquake				Station			Ground Motion Intensity Measure				
Name	Year	M	Style of faulting	Name	R <sub>jb</sub> [Km]	V <sub>S30</sub> [m/s]	PGA [g]	PGV [m/s]	AI [m/s]	CAV [m/s]	D5-95 [s]
Big Bear-01	1992	6.46	Strike slip	Highland Fire Station	26.2	362.4	0.11	0.08	0.20	4.1	13.8
Chi-Chi_ Taiwan-03	1999	6.2	Reverse	TCU078	0.0	443.0	0.27	0.19	0.77	5.0	5.4
Duzce_ Turkey	1999	7.14	Strike slip	Lamont 375	3.9	454.2	0.89	0.37	9.97	26.8	12.8
L'Aquila_ Italy	2009	6.3	Normal	GRAN SASSO (Assergi)	6.4	488.0	0.15	0.10	0.40	4.9	8.4
Mammoth Lakes-03	1980	5.91	Strike slip	Convict Creek	2.7	382.1	0.19	0.16	0.35	3.9	5.1
Morgan Hill	1984	6.19	Strike slip	Corralitos	23.2	462.2	0.08	0.07	0.06	2.0	9.7
New Zealand-01	1984	5.5	Normal	Turangi Telephone Exchange	3.8	356.4	0.07	0.03	0.04	1.3	7.5
Northridge-01	1994	6.69	Reverse	Beverly Hills - 12520 Mulhol	12.4	545.7	0.45	0.31	2.38	11.0	7.7
Parkfield	1966	6.19	Strike slip	Temblor pre-1969	16.0	527.9	0.27	0.15	0.31	3.2	5.4
San Simeon_ CA	2003	6.52	Reverse	Cambria - Hwy 1 Caltrans Bridge	7.0	362.4	0.18	0.13	0.44	5.6	10.5

Return period, 1460 years											
Earthquake				Station			Ground Motion Intensity Measure				
Name	Year	M	Style of faulting	Name	R <sub>jb</sub> [Km]	V <sub>S30</sub> [m/s]	PGA [g]	PGV [m/s]	AI [m/s]	CAV [m/s]	D5-95 [s]
Coalinga-05	1983	5.77	Reverse	Burnett Construction	8.3	352.2	0.34	0.17	0.90	6.1	6.2
Corinth_ Greece	1981	6.6	Normal oblique	Corinth	10.3	361.4	0.30	0.24	0.85	8.2	13.9
Darfield_ New Zealand	2010	7	Strike slip	SPFS	29.9	389.5	0.16	0.20	1.01	13.1	22.2
Loma Prieta	1989	6.93	Reverse oblique	Sunol - Forest Fire Station	47.4	400.6	0.08	0.09	0.11	3.1	15.6
Mammoth Lakes-06	1980	5.94	Strike slip	Fish & Game (FIS)	6.5	373.2	0.33	0.19	0.51	3.8	5.1
Niigata_ Japan	2004	6.63	Reverse	NIG024	29.1	375.2	0.22	0.09	0.91	10.5	14.2
Northridge-01	1994	6.69	Reverse	LA - Brentwood VA Hospital	12.9	416.6	0.19	0.24	0.45	5.5	10.7
Parkfield-02_ CA	2004	6	Strike slip	PARKFIELD - UPSAR 01	9.6	357.8	0.18	0.15	0.55	6.7	13.1

Return period, 1950 years											
Earthquake				Station			Ground Motion Intensity Measure				
Name	Year	M	Style of faulting	Name	R <sub>jb</sub> [Km]	V <sub>S30</sub> [m/s]	PGA [g]	PGV [m/s]	AI [m/s]	CAV [m/s]	D5-95 [s]
Chi-Chi_ Taiwan	1981	7.62	Reverse oblique	CHY087	28.8	505.2	0.14	0.10	0.58	9.7	31.9
Coalinga-05	1983	5.77	Reverse	Burnett Construction	8.3	352.2	0.34	0.17	0.90	6.1	6.2
Corinth_ Greece	1981	6.6	Normal oblique	Corinth	10.3	361.4	0.30	0.24	0.85	8.2	13.9
Darfield_ New Zealand	2010	7	Strike slip	SPFS	29.9	389.5	0.16	0.20	1.01	13.2	22.2
Joshua Tree_ CA	1992	6.1	Strike slip	Whitewater Trout Farm	29.0	425.0	0.19	0.08	0.43	4.7	7.8
Parkfield-02_ CA	2004	6	Strike slip	PARKFIELD - UPSAR 01	9.6	357.8	0.18	0.15	0.55	6.7	13.1
Northridge-01	1994	6.69	Reverse	LA – Cypress Ave	12.9	416.6	0.18	0.15	0.55	6.7	13.1
Whittier Narrows-01	1987	5.99	Reverse oblique	Arcadia - Campus Dr	4.5	367.5	0.29	0.18	0.87	5.4	3.1

Return period, 2475 years											
Earthquake				Station			Ground Motion Intensity Measure				
Name	Year	M	Style of faulting	Name	R <sub>jb</sub> [Km]	V <sub>S30</sub> [m/s]	PGA [g]	PGV [m/s]	AI [m/s]	CAV [m/s]	D5-95 [s]
Chi-Chi_ Taiwan	1981	7.62	Reverse oblique	CHY087	28.8	505.2	0.14	0.10	0.58	9.7	31.9
Chuetsu-oki_ Japan	2007	6.8	Reverse	NIG021	24.3	418.5	0.28	0.17	0.80	9.2	11.0
Coalinga-05	1983	5.77	Reverse	Burnett Construction	8.3	352.2	0.34	0.17	0.90	6.1	6.2
Darfield_ New Zealand	2010	7	Strike slip	SPFS	29.9	389.5	0.16	0.20	1.01	13.2	22.2
Joshua Tree_ CA	2010	6.1	Strike slip	Whitewater Trout Farm	29.0	425.0	0.19	0.08	0.43	4.7	7.8
Niigata_ Japan	1992	6.63	Reverse	NIG024	29.1	375.2	0.22	0.09	0.91	10.5	14.2
Northridge-01	2004	6.69	Reverse	Topanga - Fire Sta	10.3	506.0	0.19	0.12	0.50	5.4	9.3
Parkfield-02_ CA	1994	6	Strike slip	PARKFIELD - UPSAR 06	9.1	440.6	0.23	0.13	1.00	10.2	15.9
Tottori_ Japan	2000	6.61	Strike slip	SMNH01	5.8	446.3	0.73	0.36	5.38	23.7	13.1
Whittier Narrows-01	1987	5.99	Reverse oblique	Arcadia - Campus Dr	4.5	367.5	0.29	0.18	0.87	5.4	3.1



### Ground Motions for the Angitola dam

Return period, 75 years											
Earthquake				Station			Ground Motion Intensity Measure				
Name	Year	M	Style of faulting	Name	R <sub>jb</sub> [Km]	V <sub>S30</sub> [m/s]	PGA [g]	PGV [m/s]	AI [m/s]	CAV [m/s]	D5-95 [s]
14095628	2004	5.03	Strike slip	Cattani Ranch	19.9	895	0.03	0.01	0.002	0.3	5.5
14383980	2008	5.39	Reverse oblique	Pleasants Peak	19.0	699	0.04	0.03	0.01	1.0	10.8
40204628	2007	5.45	Strike slip	Lick Observatory_ Mt.Hamilton_CA_ USA	12.8	710	0.05	0.04	0.01	0.7	4.2
Coyote Lake	1979	5.74	Strike slip	Gilroy Array #1	10.2	1428	0.12	0.11	0.08	1.7	5.8
Northridge-01	1994	6.69	Reverse	Vasquez Rocks Park	23.1	996	0.14	0.11	0.32	4.3	7.3
N. Palm Springs	1986	6.06	Reverse oblique	Anza - Red Mountain	38.2	680	0.10	0.06	0.08	1.7	6.5
Umbria-03_ Italy	1984	5.6	Normal	Gubbio	14.7	922	0.07	0.04	0.04	1.3	6.8
Whittier Narrows-01	1987	5.99	Reverse oblique	Mt Wilson - CIT Seis Sta	14.5	680	0.18	0.05	0.26	3.7	8.3

Return period, 475 years											
Earthquake				Station			Ground Motion Intensity Measure				
Name	Year	M	Style of faulting	Name	R <sub>jb</sub> [Km]	V <sub>S30</sub> [m/s]	PGA [g]	PGV [m/s]	AI [m/s]	CAV [m/s]	D5-95 [s]
14151344	2005	5.2	Strike slip	Pinon Flats Observatory_Ca_Usa	12.82	763	0.49	0.09	0.26	2.3	1.9
Coyote Lake	1979	5.74	Strike slip	Gilroy Array #1	10.21	1428	0.12	0.11	0.08	1.7	5.8
Duzce_ Turkey	1999	7.14	Strike slip	IRIGM 496	4.21	760	1.03	0.40	13.37	28.8	13.3
Loma Prieta	1989	6.93	Reverse oblique	Gilroy Array #1	8.84	1428	0.42	0.34	1.06	6.6	6.5
Morgan Hill	1984	6.19	Strike slip	Gilroy Array #1	14.9	1428	0.10	0.03	0.06	1.8	8.9
Northridge-01	1994	6.69	Reverse	Mt Wilson - CIT Seis Sta	35.53	680	0.23	0.07	0.30	4.2	8.8
Umbria-03_ Italy	1984	5.6	Normal	Gubbio	14.67	922	0.07	0.04	0.04	1.3	6.8
Whittier Narrows-01	1987	5.99	Reverse oblique	Mt Wilson - CIT Seis Sta	14.5	680	0.18	0.05	0.26	3.7	8.3

Return period, 710 years											
Earthquake				Station			Ground Motion Intensity Measure				
Name	Year	M	Style of faulting	Name	R <sub>jb</sub> [Km]	V <sub>S30</sub> [m/s]	PGA [g]	PGV [m/s]	AI [m/s]	CAV [m/s]	D5-95 [s]
14151344	2005	5.2	Strike slip	Red Mountain_ Riverside Co._ Ca_ Usa	26.0	704	0.16	0.04	0.06	1.4	3.5
Coyote Lake	1979	5.74	Strike slip	Gilroy Array #1	10.2	1428	0.12	0.11	0.08	1.7	5.8
Loma Prieta	1989	6.3	Reverse oblique	Gilroy - Gavilan Coll.	9.2	730	0.33	0.24	0.70	5.1	4.8
Morgan Hill	1984	6.19	Strike slip	Gilroy Array #1	14.9	1428	0.10	0.03	0.06	1.8	8.9
Northridge-01	1994	6.69	Reverse	Santa Susana Ground	1.7	715	0.29	0.17	0.89	7.0	8.3
N. Palm Springs	1986	6.06	Reverse oblique	Anza - Red Mountain	38.2	680	0.10	0.06	0.08	1.7	6.5
Tottori_ Japan	2000	6.61	Strike slip	OKYH08	24.8	694	0.24	0.12	0.58	9.6	22.1
Umbria-03_ Italy	1984	5.6	Normal	Gubbio	14.7	922	0.07	0.04	0.04	1.3	6.8

Return period, 1460 years											
Earthquake				Station			Ground Motion Intensity Measure				
Name	Year	M	Style of faulting	Name	R <sub>jb</sub> [Km]	V <sub>S30</sub> [m/s]	PGA [g]	PGV [m/s]	AI [m/s]	CAV [m/s]	D5-95 [s]
14151344	2005	5.2	Strike slip	Pinon Flats Observatory_ Ca_ Usa	12.8	763	0.49	0.09	0.26	2.3	1.9
Coyote Lake	1979	5.74	Strike slip	Gilroy Array #1	10.2	1428	0.12	0.11	0.08	1.7	5.8
Duzce_ Turkey	1999	7.14	Strike slip	IRIGM 496	4.2	760	0.75	0.40	6.52	21.1	12.8
Loma Prieta	1989	6.93	Reverse oblique	Gilroy Array #1	8.8	1428	0.42	0.34	1.06	6.6	6.5
Morgan Hill	1984	6.19	Strike slip	Gilroy Array #1	14.9	1428	0.10	0.03	0.06	1.8	8.9
Northridge-01	1994	6.69	Reverse	Santa Susana Ground	1.7	715	0.29	0.17	0.89	7.0	8.3
Sierra Madre	1991	5.61	Reverse	Cogswell Dam - Right Abutment	17.8	680	0.30	0.15	0.43	3.2	2.7
Umbria Marche (aftershock 1)_ Italy	1997	5.5	Normal	Nocera Umbra-Salmata	11.7	694	0.16	0.07	0.11	1.9	5.0